

NAVAL POSTGRADUATE SCHOOL

Monterey, California



THESIS

**EFFECTS OF SHIBOARD COMPARTMENT FUEL FIRE
AND FIRE EXTINGUISHING ON RF SIGNAL
PROPAGATION IN THE 2.4 GHz ISM BAND**

by

Christos Deyannis
Dimitrios Xifaras

June 2000

Thesis Advisor:
Thesis Co-advisor:

Jovan Lebaric
James Luscombe

Approved for public release; distribution is unlimited.

THIS QUALITY INSPECTED &

20000919 146

REPORT DOCUMENTATION PAGE

Form Approved
OMB No. 0704-0188

Public reporting burden for this collection of information is estimated to average 1 hour per response, including the time for reviewing instruction, searching existing data sources, gathering and maintaining the data needed, and completing and reviewing the collection of information. Send comments regarding this burden estimate or any other aspect of this collection of information, including suggestions for reducing this burden, to Washington headquarters Services, Directorate for Information Operations and Reports, 1215 Jefferson Davis Highway, Suite 1204, Arlington, VA 22202-4302, and to the Office of Management and Budget, Paperwork Reduction Project (0704-0188) Washington DC 20503.

1. AGENCY USE ONLY (Leave blank)

2. REPORT DATE
June 2000

3. REPORT TYPE AND DATES COVERED
Master's Thesis

4. TITLE AND SUBTITLE

Effects of Shipboard Compartment Fuel Fire and Fire Extinguishing on RF Signal Propagation in the 2.4 GHz ISM Band

5. FUNDING NUMBERS

6. AUTHORS: LT Christos Deyannis, LT Dimitrios Xifaras

7. PERFORMING ORGANIZATION NAME(S) AND ADDRESS(ES)

Naval Postgraduate School
Monterey, CA 93943-5000

8. PERFORMING
ORGANIZATION REPORT
NUMBER

9. SPONSORING / MONITORING AGENCY NAME(S) AND ADDRESS(ES)

10. SPONSORING /
MONITORING
AGENCY REPORT NUMBER

11. SUPPLEMENTARY NOTES

The views expressed in this thesis are those of the author and do not reflect the official policy or position of the Department of Defense or the U.S. Government.

12a. DISTRIBUTION / AVAILABILITY STATEMENT

Approved for public release; distribution unlimited.

12b. DISTRIBUTION CODE

13. ABSTRACT (maximum 200 words)

The objective of this research was to quantify the effects of fuel fire and the follow-on fire extinguishing actions on wireless shipboard communications in the 2.4 GHz ISM band. Directional and non-directional antennas with horizontal and vertical polarization, and a PC-controlled scalar network analyzer, were used onboard ex-USS SHADWELL to measure the attenuation of 2.4 - 2.485 GHz signals transmitted through diesel and heptane fire, water mist created by the fire extinguishing system, and subsequently developed steam. A MATLAB code has been used to analyze the data statistically.

The attenuation for directional antennas exhibits relatively small variations with time and frequency, but fire and the follow-on fire-extinguishing phases create severe non-stationary frequency selective fading for non-directional antennas. Therefore standard communication techniques effective against frequency selective fading (non-stationary but slowly varying with time) are recommended for use with communication systems intended for shipboard indoors use. Even in normal conditions, without fire, water mist, or steam, we have determined that frequency selective fading would be a problem for non-directional antennas used in shipboard compartments and thus a system with anti-fading capability should be considered for shipboard use.

14. SUBJECT TERMS

Instrumentation Scientific Medical (ISM) band, Radio Frequency (RF) propagation, Attenuation, Fire extinguishing system, Plasma, MATLAB

15. NUMBER OF
PAGES

410

16. PRICE CODE

17. SECURITY CLASSIFICATION OF
REPORT

Unclassified

18. SECURITY CLASSIFICATION OF
THIS PAGE

Unclassified

19. SECURITY CLASSIFICATION
OF ABSTRACT

Unclassified

20. LIMITATION
OF ABSTRACT

UL

Approved for public release; distribution is unlimited

**EFFECTS OF SHIBOARD COMPARTMENT FUEL FIRE AND FIRE
EXTINGUISHING ON RF SIGNAL PROPAGATION IN THE 2.4 GHz ISM BAND**

Christos Deyannis
Lieutenant, Hellenic Navy
B.S., Hellenic Naval Academy, 1989

Dimitrios Xifaras
Lieutenant, Hellenic Navy
B.S., Hellenic Naval Academy, 1989

Submitted in partial fulfillment of the
requirements for the degrees of

**MASTER OF SCIENCE IN APPLIED PHYSICS,
AND MASTER OF SCIENCE IN ELECTRICAL ENGINEERING**

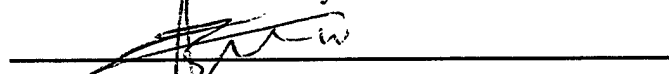
from the

**NAVAL POSTGRADUATE SCHOOL
June 2000**

Authors:

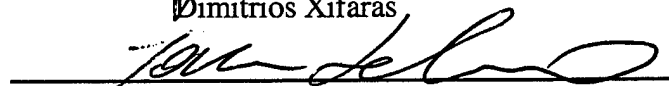


Christos Deyannis

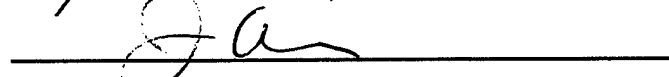


Dimitrios Xifaras

Approved by:



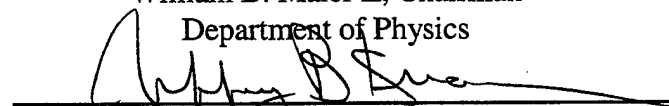
Jovan Lebaric, Thesis Advisor



James Luscomb, Thesis Co-Advisor



William B. Maier II, Chairman
Department of Physics



Jeffrey B. Knorr, Chairman
Department of Electrical and Computer Engineering

ABSTRACT

The objective of this research was to quantify the effects of fuel fire and the follow-on fire extinguishing actions on wireless shipboard communications in the 2.4 GHz ISM band. Directional and non-directional antennas with horizontal and vertical polarization, and a PC-controlled scalar network analyzer, were used onboard ex-USS SHADWELL to measure the attenuation of 2.4 - 2.485 GHz signals transmitted through diesel and heptane fire, water mist created by the fire extinguishing system, and subsequently developed steam. A MATLAB code has been used to analyze the data statistically.

The attenuation for directional antennas exhibits relatively small variations with time and frequency, but fire and the follow-on fire-extinguishing phases create severe non-stationary frequency selective fading for non-directional antennas. Therefore standard communication techniques effective against frequency selective fading (non-stationary but slowly varying with time) are recommended for use with communication systems intended for shipboard indoors use. Even in normal conditions, without fire, water mist, or steam, we have determined that frequency selective fading would be a problem for non-directional antennas used in shipboard compartments and thus a system with anti-fading capability should be considered for shipboard use.

TABLE OF CONTENTS

I. INTRODUCTION.....	1
A. DAMAGE CONTROL AUTOMATION FOR REDUCED MANNING (DC-ARM).....	1
B. THESIS OBJECTIVE AND PROBLEM APPROACH	3
C. THESIS OUTLINE.....	4
II. REVIEW OF PREVIOUS RESEARCH SPONSORED BY THE NAVY RELATED TO RF PROPAGATION WITHIN SHIPBOARD COMPARTMENTS.....	7
A. MEASUREMENTS OF PROPAGATION OF RF ENERGY IN CONFINED NAVAL SHIPBOARD ENVIRONMENT...7	
1. <i>Experimental Setup</i>	8
2. <i>Antenna Placement and Measurement Procedures</i>	10
3. <i>Results</i>	12
B. MEASUREMENTS OF PROPAGATION OF RF ENERGY THROUGH LIVE FIRE IN OPEN SPACE	14
1. <i>Experimental Setup</i>	14
2. <i>Antenna Placement and Measurement Procedures</i>	16
3. <i>Results</i>	17
III. THEORETICAL PRINCIPLES FOR MEASUREMENTS OF PATH LOSS	21
A. DIFFERENTIAL METHOD OF MEASUREMENT.....	21
B. MEASUREMENTS OF PATH LOSS	22
1. <i>Free Space Propagation</i>	22
2. <i>Waveguide Measurements of Path Loss</i>	26
3. <i>Single Path Propagation Measurements</i>	28
4. <i>Multipath Propagation (Fading) Measurements</i>	30
IV. PHYSICS OF BASIC PROPAGATION MECHANISMS	41
A. REFLECTION	42
1. <i>Electromagnetic Waves in Conductors</i>	42
2. <i>Reflection for Normal Incidence to a Conducting Surface</i>	46
B. DIFFRACTION OVER OBSTACLES.....	51
C. SCATTERING AND ABSORPTION FROM PARTICLES.....	54
1. <i>Energy Absorption</i>	54
2. <i>Energy Scattering</i>	55
V. PHYSICS OF ELECTROMAGNETIC WAVES PROPAGATION THROUGH FIRE	59
A. BASIC PLASMA CONCEPTS	59
1. <i>Electron Debye Length</i>	60
2. <i>Plasma Frequency</i>	61
3. <i>Electromagnetic Wave Propagation in Plasmas</i>	64
4. <i>Electromagnetic Wave Propagation in Collisional Plasma</i>	69
B. FLAMES AND PLASMA	73
1. <i>Ionization Due to Flames</i>	73
2. <i>Dilute Plasma Created During SCFE and its Effect on Propagation of RF Energy</i>	76
VI. INSTRUMENTATION USED FOR SCFE.....	81
A. HARDWARE USED AND MEASUREMENT SETUP	81
B. DATA ACQUISITION/CONTROL SOFTWARE DESIGN	88
1. <i>General Purpose Interface Bus (GPIB)</i>	88
2. <i>LabView Program for Controlling the SNA and Acquiring the Measured Data</i>	91
VII. MEASUREMENT PROCEDURE.....	97

A.	FUEL TYPE AND ANTENNA CONFIGURATIONS USED	97
B.	MEASUREMENT SCENARIOS	98
1.	Day One (Thursday, May 13) Measurements	99
2.	Day Two (Friday, May 14) Measurements	100
VIII.	CODE DEVELOPMENT FOR DATA ANALYSIS.....	103
A.	INITIAL REQUIREMENTS	103
B.	CODE DEVELOPED ON SITE.....	103
C.	DEVELOPMENT OF THE STATISTICAL ANALYSIS CODE	106
1.	Selection of the Measurements Set According to the Type of Fire, Type of Antennas and Polarization.....	107
2.	Initialization Phase.....	108
3.	Estimation of the Path Loss / Attenuation	108
4.	Surface Plots.....	109
5.	Estimation of Frequency Averages.....	110
6.	Estimation of Time Averages.....	111
7.	Estimation of the Density and Distribution Functions	111
8.	Estimation of the Frequency Response Autocorrelation Functions	112
9.	Estimation of Frequency Difference with Least Total Attenuation.....	112
10.	Temperature Plots	113
11.	Correlation Between Temperature and Attenuation.....	113
IX.	RESULTS FOR DIRECTIONAL ANTENNAS	115
A.	DIESEL FIRE	115
1.	Vertical Polarization	115
2.	Horizontal Polarization.....	146
B.	HEPTANE FIRE.....	176
1.	Vertical Polarization	177
2.	Horizontal Polarization.....	210
X.	NON DIRECTIONAL ANTENNAS.....	245
A.	DIESEL FIRE	245
1.	Vertical Polarization	245
2.	Horizontal Polarization.....	273
XI.	CONCLUSIONS AND RECOMMENDATIONS	301
A.	CONCLUSIONS	301
B.	RECOMMENDATIONS	306
	APPENDIX A. ANTENNAS SPECIFICATION SHEETS	309
	APPENDIX B. LABVIEW VI CODE.....	311
	APPENDIX C. EX-USS SHADWELL AND SCFE MEASUREMENT COMPARTMENT	323
	APPENDIX D. MATLAB DATA PROCESSING CODE.....	329
	LIST OF REFERENCES.....	331
	INITIAL DISTRIBUTION LIST	333

LIST OF SYMBOLS, ACRONYMS AND/OR ABBREVIATIONS

cdf	Cumulative Distribution Function
CW	Continuous Wave
DC-ARM	Damage Control-Automated for Reduced Manning
EMI	Electromagnetic Interference
GPIB	General Purpose Interface Bus
HPIB	Hewlett Packard Interface Bus
ISM	Instrumentation-Scientific-Medical
LabVIEW	Laboratory Virtual Instrument Engineering
LAN	Local Area Network
NRL	Naval Research Laboratory
NRL CBD	Naval Research Laboratory's Chesapeake Bay
ONR	Office of Naval Research
PC	Personal Computer
pdf	Probability density Function
RF	Radio Frequency
RSVP	Reduced Ships-crew by Virtual Presence
SCFE	Shipboard Compartment Fire Experiment Detachment Workbench
SNA	Scalar Network Analyzer
WFE	Waveguide Flame Experiment
A	Effective area of an antenna, or amplitude of
A'	Scaling Factor
α	Radius of a droplet
B	Magnetic flux density
B_0	Amplitude of the magnetic field
β	Complex conjugate of β
c	Speed of light in vacuum
d	distance, or skin depth
$\Delta \Phi$	Phase shift
Δt	time delay
E	Electric field intensity vector
E_0	Amplitude of the electric field under free-space conditions
E_m	Amplitude of the electric field at a given point under specified conditions (medium, environment)
ϵ	Permittivity of a material
ϵ_0	Permittivity of the free space
e	Electron charge
F	Ratio E_m/E_0
f	Frequency
Φ	Phase of a random signal
G	Power gain of an antenna
G_T	Transmitting antenna gain in decibels
G_R	Receiving antenna gain in decibels

g_T	Gain of the transmitting antenna
g_R	Gain of the receiving antenna
h	Planck's constant
i	equal to $\sqrt{-1}$
J	Current density
J_f	Free current density
K	Parameter for Rician distribution
K	Complex wave number
K_+	Real part of K
K_-	Imaginary part of K
K_f	Free surface current at the boundary of the interface of two mediums
k	Wavelength ($k = 2\pi / \lambda$)
K_B	Boltzmann constant
L	Length of an object
Λ	Ratio of the minimum and maximum impact parameter
λ	Wavelength
λ_{abs}	Absorption length
L_p	Loss due to the medium in decibels
L_0	Free space loss in decibels
λ_{De}	Debye length
λ_μ	Free-space wavelength of the light in units of micrometers
m_j	Mass of a particles of species j
m_e	Electron mass
μ	Permeability of a material
μ_0	Permeability of the free space
N_D	Number of electrons in the Debye sphere
n_e	Electron density
n_j	Density of particles of species j
n	Index of refraction, or charge density
\hat{n}	Unit vector perpendicular to the surface of the interface of two mediums, pointing from medium (2) to medium (1)
n_{refr}	Index of refraction for plasma
n_{cr}	Critical density of plasma
ν_{ei}	Collision frequency
ν_{dmp}	Energy damping rate
p_T	Total transmitted power a random signal
p_R	Available power at the receiving antenna
p_j	Pressure of particles of species j
p_e	Pressure of electrons
P_R	Received power in decibels referred to 1 W
P_T	Transmitted power in decibels referred to 1 W
PL	Signal path loss
q_j	Charge of a particles of species j

r_s	Signal's dominant component
R	Reflection coefficient
σ_a	Absorption cross section of a droplet
σ	Standard deviation, or conductivity of a material
σ_f	Free space surface charge
σ_s	Scattering cross section of a droplet
T	Absolute temperature K
t	time
u_j	Mean velocity of particles of species j
u_e	Mean velocity of electrons
v_{th}	Electron thermal velocity
v	Wave propagation speed
v_e	Electron speed
W	Power per unit area (power density)
ω_p	Electron plasma frequency
ω	angular frequency
ω_{real}	Real part of ω
Z	Atomic number
\tilde{j}, \tilde{k}	Unit vectors in y and z directions respectively

subscripts 1,2 indicate the E , B , μ , ϵ , K and v within mediums 1 and 2 respectively

subscripts \parallel, \perp indicate the components of E , B , which are parallel and perpendicular, respectively, to the interface of the two mediums

subscripts I, R, T indicate the incident, reflected and transmitted E , B fields and their amplitudes (E_0 , B_0) respectively

ACKNOWLEDGEMENTS

The authors would like to acknowledge the financial support of this study by the Naval Surface Warfare Center, Carderock division, Philadelphia, PA.

We would especially like to express our gratitude to Professor Jovan Lebaric for his help, patience and especially the numerous hours of counseling, that led to the timely and successful completion of this thesis.

To our thesis co-advisor, Professor James Luscombe a special thanks for your cooperation and your consideration.

Finally we would like to thank our wives Elina and Elena for their understanding, patience and the moral support they provided us during the course of writing this thesis. A special mention goes to the Hellenic Navy for giving us the opportunity to be intellectually challenged at the Naval Postgraduate School.

I. INTRODUCTION

A. DAMAGE CONTROL AUTOMATION FOR REDUCED MANNING (DC-ARM)

Reduced manning and affordability have become crucial factors in production planning for the ships of the 21st century. These benefits can be achieved in the area of damage control by utilizing technologies that demonstrate the viability of automating functions of detection, reasoning and casualty response operations. The benefits will be life-cycle cost reduction resulting from reduced manning, improved personnel safety and ship survivability, reduced exposure of personnel and quicker responses in casualty control efforts. To meet the challenges to damage control efforts by a reduced manned combatant, the Office of Naval Research has funded the Damage Control-Automated for Reduced Manning (DC-ARM) program. [Ref.1]

The objective of the Damage Control-Automation for Reduced Manning (DC-ARM) program is to demonstrate advanced technologies for the detection, decision making, control, actuation, and system integration required to decrease shipboard damage control manning requirements and casualty response time. The primary DC-ARM goal is a greater than 50% reduction in General Quarters surge manning for future ships, particularly DD-21. To achieve a manning reduction down to a crew of 95 people for DD-21 the Reduced Ships-crew

by Virtual Presence (RSVP) initiative was assumed by the U.S. Navy, Office of Naval Research (ONR). Under the RSVP initiative Draper Labs is developing a system, which has as its goal the reduction of manpower and maintenance costs necessary to operate a ship. The idea is to replace human functions by a system, which will provide sense, fusion and assessment of information. The system is based upon large number of wireless sensors distributed throughout the ship, which inter-network with the ship's backbone via a wireless local area network (LAN). The data collected by the sensors will be processed by an information fusion system, and actionable information will be provided to the ship's crew in the control centers.

The operability and effectiveness of a communication system like the one described above is based upon the propagation of radio frequency (RF) energy in confined ship spaces. The system must have the ability to transfer large amounts of sensor data related to a ship's condition, damage control operation, C³ functions, must be survivable in the event of damage and must be resistant to electromagnetic interference (EMI) from other ship's RF sources. As a result, thorough examination of factors that can degrade a RF signal in confined ship spaces must be considered. For example, it is known that single-frequency communication systems suffer from multipath interference in confined

spaces, where spread spectrum and frequency-hopping systems, currently used in wireless LANs have been proved to operate effectively [Ref.2]. To ensure reliable operation and effectiveness of a communication system at any time throughout the ship, it is of great importance to investigate the mechanisms of propagation of RF energy within confined shipboard spaces, during several operational situations and conditions. In other words, it is extremely important to know when a communication system will work and when problems can be expected.

In a related area, consideration should be given to the performance of a communication system in the event of shipboard fire. To ensure reliable data transmissions in a situation like this, the effects of the fire including suppression means, chemical byproducts and the flame itself should be examined.

B. THESIS OBJECTIVE AND PROBLEM APPROACH

The objective of this thesis is to quantify the effects of fire on wireless communications in the 2.4 GHz to 2.485 GHz Instrumentation-Scientific-Medical (ISM) frequency range including suppression means (water mist) and chemical byproducts, in standard system engineering terms, such as path loss and attenuation. The two main questions answered are:

a) Is a 2.4 GHz ISM band signal attenuated when transmitted through a fuel fire in a shipboard compartment?

b) Does water mist, produced by a high-pressure fire extinguishing system, introduce additional appreciable attenuation?

To accomplish the above goals, a Shipboard Compartment Fire Experiment (SCFE) with live shipboard compartment fires was conducted onboard ex-USS SHADWELL stationed at Mobile, AL, within the second week of May of 1999. The attenuation of 2.4 - 2.485 GHz signals through diesel and heptane fire was measured, using pairs of directional and omnidirectional antennas and a scalar network analyzer. Comparative measurements of signal attenuation between the same transmitting and receiving antennas, with and without fire and also with water mist created by the fire extinguishing system were conducted. To acquire results for both horizontal and vertical polarizations two sets of measurements were conducted. Finally, the results of the experiments have been processed to extract the statistical averages.

C. THESIS OUTLINE

Chapter II presents background material on propagation of radio frequency (RF) energy in confined ship spaces, and through live fire. Two sets of previous related experiments

are discussed. The first one, regarding propagation of RF energy in confined shipboard environment, was conducted onboard ex-USS SHADWELL (23-25 February 1998) in Mobile, AL [Ref.2]. A broadband (800 MHz - 3 GHz) bistatic measurement system was developed, and measurements for different shipboard indoor configurations were taken. The second one, regarding propagation of RF energy through fire, was conducted (December 23, 1996 and January 8, 1997) at the Naval Research Laboratory's Chesapeake Bay Detachment (NRL CBD) in Calvert County, Maryland [Ref.3]. Again a broadband (50 MHz - 1 GHz) bistatic measurement system was developed, this time in an open area, and measurements of RF signals transmitted through a heptane pool fire were taken.

Chapter III discusses the theoretical principles for measurements of path loss. The "differential method" of measurement is described and comparisons between waveguide measurements, single path propagation measurements and multipath propagation (fading) measurements are presented. Chapter IV describes the physics of the propagation mechanisms during the SCFE. Reflection, diffraction, scattering and absorption are depicted because they are the basic propagation mechanisms which impacted propagation of the RF energy during the experiments conducted onboard ex-USS SHADWELL. Chapter V is devoted to the physics of the electromagnetic waves propagation through fire. Plasma

theory is presented, and the issue of hot plasma creation is discussed. Chapter VI describes the instrumentation used for the experiment. The software program that was developed in LabVIEW to automate the experiment's measurements, and the hardware used are presented.

Chapter VII discusses the measurement procedure and the set-up of the experiment that was performed onboard ex-USS SHADWELL. The different configurations of antennas, polarizations and fuel types used, in addition to the different compartment conditions (pre-fire, fire, mist, steam, ventilation) under which measurements were conducted are described. Chapter VIII describes the development of MATLAB code used for the statistical analysis of the results. Chapter IX discusses the statistical analysis of the data acquired for the directional antennas during the experiment. The frequency dependence of the path loss, its time dynamics, autocorrelation functions and frequency diversity effectiveness are presented. Chapter X discusses the statistical analysis of the data acquired for the non-directional antennas during the experiment. The frequency dependence of the path loss, its time dynamics, autocorrelation functions and frequency diversity effectiveness are presented. Finally, Chapter XI contains a summary, conclusions and recommendations for future research.

II. REVIEW OF PREVIOUS RESEARCH SPONSORED BY THE NAVY RELATED TO RF PROPAGATION WITHIN SHIPBOARD COMPARTMENTS

This section briefly outlines the procedures and results of previous work, related to RF propagation measurements, performed for the Navy under the DC-ARM program.

The propagation of RF energy below deck aboard naval ships has been a concern of shipboard personnel and test teams for many years. Surveys on below deck EMI were conducted onboard USS OAK HILL (LSD 51) from 23 September through 4 October 1996 and on USS PONCE (LPD 15) from 27 through 28 August 1997 [Ref.2]. Under the initiative of the program on Damage Control-Automation for Reduced Manning (DC-ARM), Naval Research Laboratory (NRL) has conducted two experiments so as to understand and characterize the underlying propagation mechanisms of RF signals within confined ship spaces and through live fire.

A. MEASUREMENTS OF PROPAGATION OF RF ENERGY IN CONFINED NAVAL SHIPBOARD ENVIRONMENT

To address the issue of propagation of RF energy in a shipboard environment and to examine the transfer characteristics of RF signals relative to bulkheads, watertight doors, compartment penetrations and obstructions,

ducts, mask cable transits, and steel deckplates, NRL conducted measurements onboard ex-USS SHADWELL, its Advanced Fire Research Vessel (23-25 February, 1998) in Mobile AL. [Ref.2]

1. Experimental Setup

A broadband (800 MHz-3 GHz) bistatic measurement system was developed for the experiment's purposes. The system consisted of an HP8592L spectrum analyzer, an HP83752A synthesized signal source (10 MHz-20 GHz), an HP8347A RF amplifier (100 kHz-3 GHz), a broadband discone transmitting antenna, a laptop computer, a broadband "batwing" receiving dipole and a small coaxially-tipped receiving probe. The system setup is shown in Figure 2.1.

The stationary part of the measurement system consisted of the transmitting antenna attached to the RF amplifier, which was connected to the signal source. The signal source generated a stepped CW signal from 800 MHz to 3 GHz, in 100 MHz frequency increments.

The transportable part of the measurement system consisted of the receiving antenna, either the broadband dipole or the coaxial probe, attached to the spectrum analyzer, which was controlled by the laptop computer through an HP-IB interface. The broadband dipole was used as the receiving antenna, except for the cases of measurements

taken close to an object's surface, such as close to cables and hard-to-reach places, where the coaxial probe was used.

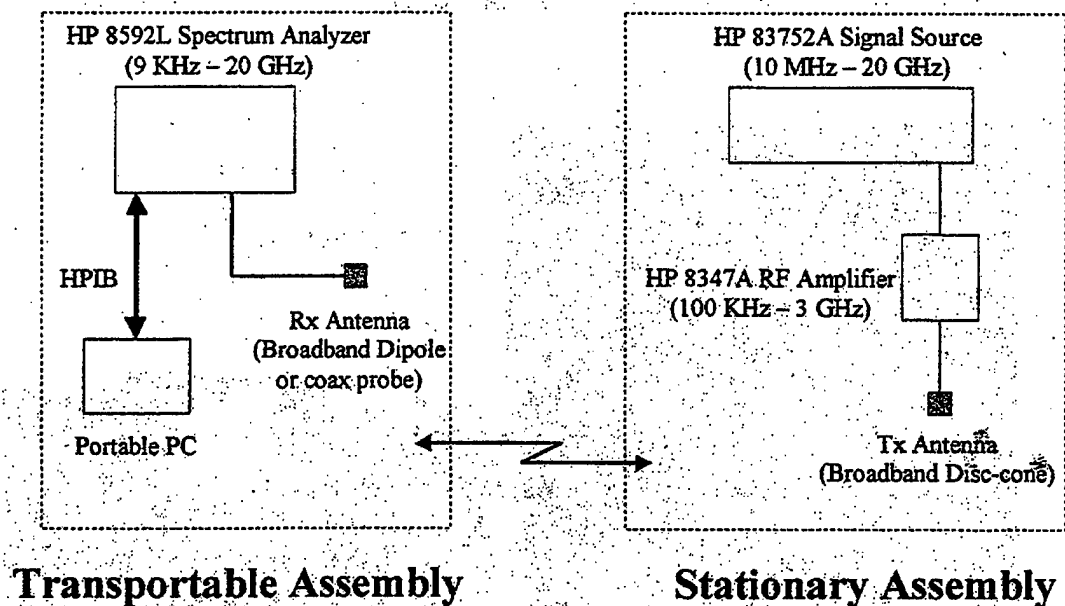


Figure 2.1: Block Diagram of Bistatic Measurement System. From Ref.[2].

Both the disc-cone and the batwing dipole were repositioned so that both vertical and Horizontally Polarized could be measured. The spectrum analyzer measured the absolute signal-amplitude levels, and the data were transferred to a file in the laptop computer. Data acquisition and control software used for the experiment was developed in LabVIEW.

2. Antenna Placement and Measurement Procedures

Altogether 113 data sets (23 frequencies) were sampled, and the received power levels were collected for various open/closed door configurations, selected locations of the transmitter and receiver on three levels of the ex-USS SHADWELL and for different signal polarizations. A schematic of the main deck of ex-USS SHADWELL with the locations of the transmitting and receiving antennas in the different compartments is shown in Figure 2.2. The measurements were taken in the forward half of the ship between frames 13 and 29, on the main deck (level 1), the deck bellow the main deck (level 2) and the deck above the main deck (level 01). In Figure 2.2, the frame numbers appear at the bottom, the levels 1, 2 and 01 of the ship are identified with decks 1, 2 and 3 respectively, and the compartments of each deck are designated $D_{L,n}$ with $L=1,2,3$ for the three decks and "n" for compartment number.

For most of the measurements, the transmitting antenna was placed in compartment $D_{1,3}$ (shown in Figure 2.2) on the main deck of the ship, and the receiving antenna was moved to different compartments of the main deck. However, for some measurements the receiving antenna was moved to the other two decks to test inter-deck propagation, and there were also some cases in which transmitting antenna was moved to compartments other than $D_{1,3}$ as shown in Figure 2.2.

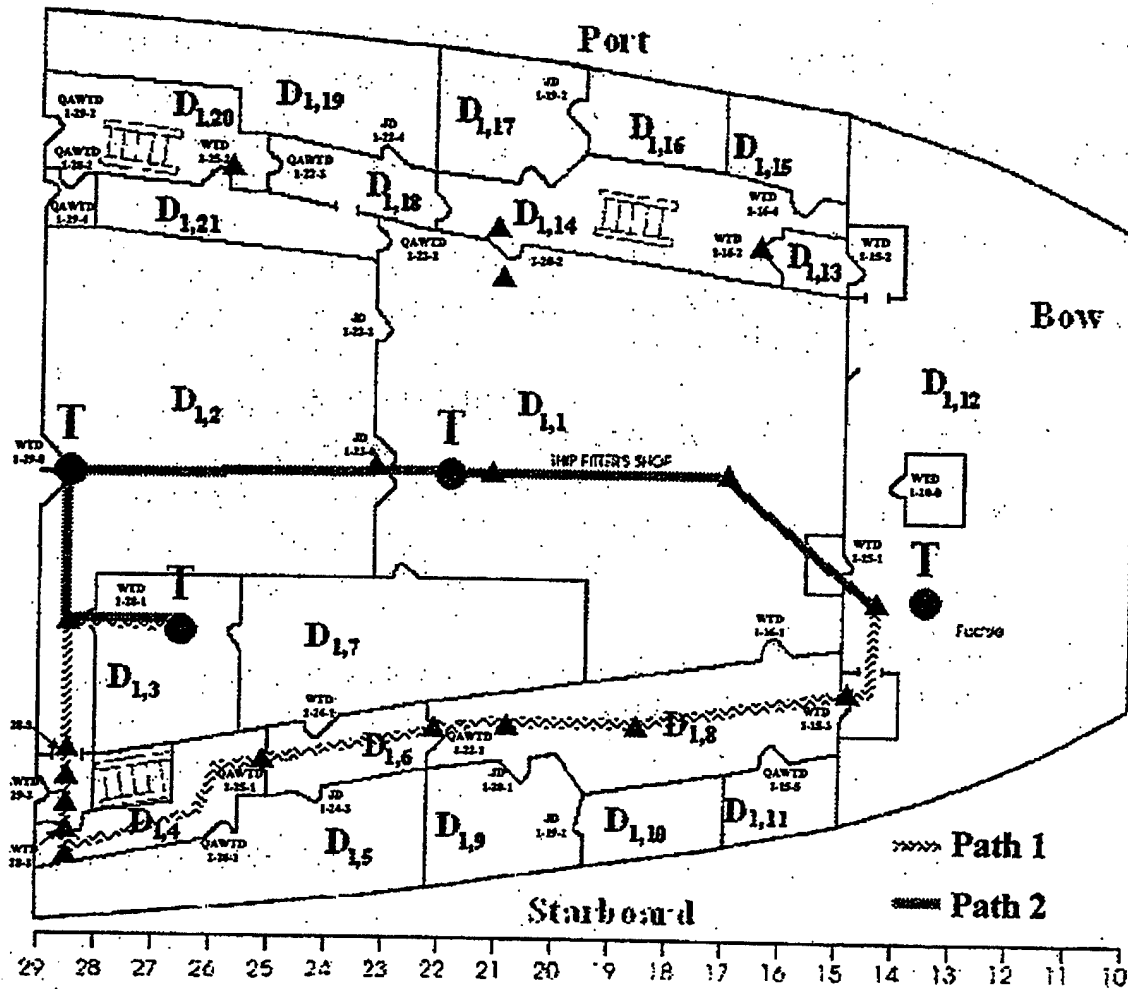


Figure 2.2: Locations of Receiver (triangles) and Transmitter (Circles) Positions in Compartments ($D_{1,n}$) on the Main Deck of the ex-USS SHADWELL. From Ref.[2]. The Rest of the Symbols on the Figure Are from the Blue-Prints of ex-USS SHADWELL and do not Have any Relevance to this Thesis.

The different positions of the transmitting and receiving antennas and open/close door configurations were chosen so as to determine if energy escaped through the door

seals, if energy propagated along the cables running through the compartments and to test inter-deck propagation as well as propagation along different paths. In addition to these, measurements of the background noise on ex-USS SHADWELL were made, which were used as reference for analyzing the rest of the data sets.

3. Results

To analyze the data, an algorithm was developed using a variation of the Friis Transmission Equation. Through this algorithm, the effective propagation loss was extracted from the measured received power at each of the 23 transmission frequencies. The effective propagation loss embodied the losses from all modes of propagation that were generated in the complex electromagnetic environment of the confined ship spaces, and because it is essentially independent of the measurement system, the results can be applied to any radar, communication or surveillance system on ex-USS SHADWELL.

The propagation modes of the electromagnetic energy during the experiment, included multipath scattering from the bulkheads, scattering from compartment penetrations and obstructions, surface waves along cables, waveguide effects from the nature of the ship spaces like corridors, free-space propagation and possibly coaxial cable effects [Ref.2]. The equipment limitations, including the use of a

spectrum analyzer instead of a network analyzer, did not allow well-controlled measurements that would lead to the clear separation of the propagated modes. As a result, definitive conclusions on the essence of the electromagnetic modes actually propagated in the confined spaces of ex-USS SHADWELL during the experiment could not be drawn.

The authors state that the most significant result derived from the experiment was that the received power levels over reasonably long propagation distances were sufficient to ensure communication, even when all passageway doors were closed. The fact that most of the measurements for the various open/closed door configurations, selected locations of the transmitter/receiver on the three levels of the ex-USS SHADWELL and different signal polarizations, that were examined, were above the background noise level (-90 dBm) over the entire frequency interval (800 MHz - 3 GHz), strongly suggest that power levels (-80 dBm to -55 dBm) were sufficient to ensure inter-deck and intra-deck communications.

Additionally, the authors state that measurements indicated that intra-deck propagation of RF energy occurred through central-room compartments as well as passageways. The study concluded that although evidence of some of the suggested modes of propagation of RF energy in confined ship spaces was observed, such as the multipath effects caused by

scatter from the steel bulkheads, more rigidly controlled testing is needed to gain a better understanding of the various modes of propagation in the specific environment and their relative impact on RF signals.

B. MEASUREMENTS OF PROPAGATION OF RF ENERGY THROUGH LIVE FIRE IN OPEN SPACE

To address the issue of propagation of RF energy through a live turbulent hydrocarbon pool fire, and examine the effects on attenuation of RF signals transmitted through this fire, NRL conducted measurements at the Naval Research Laboratory's Chesapeake Bay Fire Test Facility in Calvert County, Maryland. [Ref.3]

1. Experimental Setup

A broadband (50 MHz - 1 GHz) bistatic measurement system was developed for the experiment's purposes. The system consisted of a Tektronix TDS784A digitizing oscilloscope, an HP8648C signal generator, an ENI/607L power amplifier, one transmitting and two receiving log phaseic/biconical antennas LPB-2520 (25 MHz-2 GHz), and a personal computer (PC). The system setup is shown in Figure 2.3.

The PC controlled the signal generator through a GPIB interface. The transmitted waveform consisted of a sinusoid of varying frequencies from 50 MHz to 1 GHz in 10 MHz

increments. After being amplified by the power amplifier, the signal was sent to the transmitting biconical antenna. The signal was then transmitted through a four-foot square heptane pool fire.

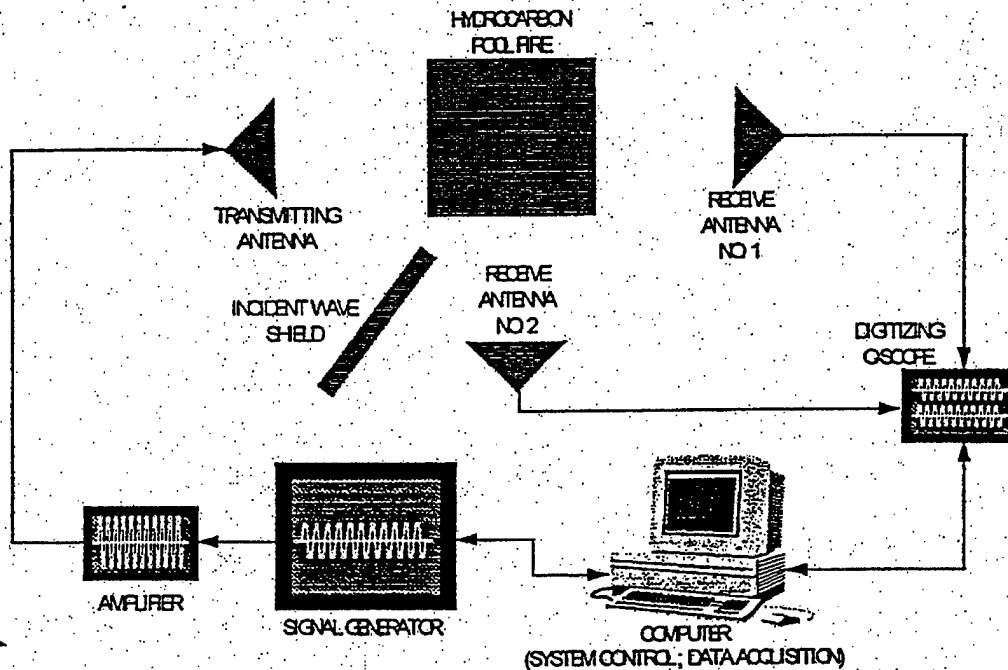


Figure 2.3: Block Diagram of Bistatic Measurement System. From Ref.[3].

The signal received by the two receiving biconical antennas was forwarded to the digitizing oscilloscope and recorded. The PC was also connected to the digitizing oscilloscope through the GPIB interface and the data recorded by the oscilloscope were transferred to a PC file.

Data acquisition and control software used for the experiment was developed in LabVIEW.

2. Antenna Placement and Measurement Procedures

The experiment consisted of eight separate tests. Each test was run twice, once without fire and once with fire. Upon the completion of the experiment the data acquired during measurements without fire was compared with the respective ones acquired during measurements with fire. In this manner, the effects of fire on the propagated waveforms could be observed.

The antenna configuration for each of the eight fire tests was varied in order to obtain information on the transmitted signal. Horizontal and vertical polarizations were tested and different positions of the receiving antennas allowed measurements of reflected power and signal losses and gains. The antenna separation was maintained at 10 meters during the experiment so as to be sufficient for the measurements at wavelengths from 0.3 to 10 meters, in order to cover the whole desired frequency band (30 MHz - 1 GHz). Figure 2.4 depicts the general set up and the antenna placement for the first fire test.

The "raw" data recorded by the measurement system consisted of 500 voltage points per waveform. Since the incremental frequency step of 10 MHz was chosen to cover the frequency band from 30 MHz to 1 GHz, each test set that was

conducted consisted of 95 different frequency waveforms. A total number of 760,000 data points were collected throughout the experiment and the respective time domain

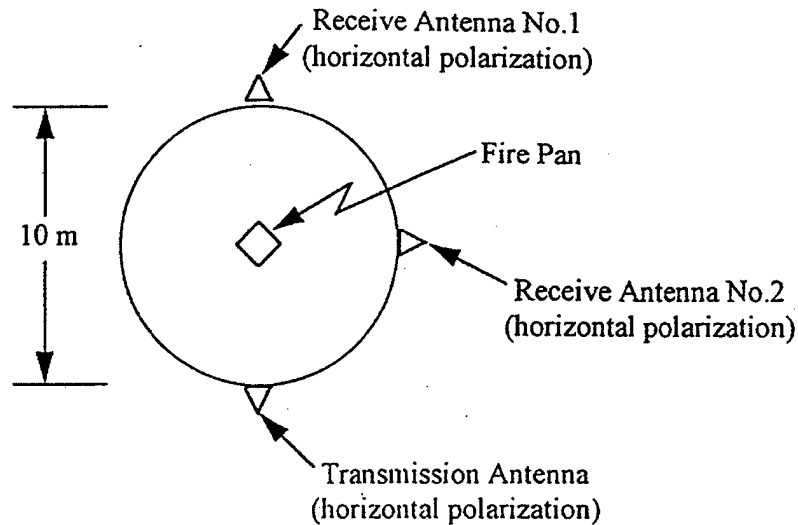


Figure 2.4: Antenna Placements for Fire Test 1. From Ref.[3].

waveforms were created. To analyze the experimental data in the frequency domain the power spectrum was computed, the peak powers for each frequency with and without fire were compared, and the losses (or gains) for the signals transmitted through fire were calculated.

3. Results

According to the experiment's report (Ref.3), the analysis of the experimental data led to two main

conclusions. The first was that a hydrocarbon pool fire rotates vertically and horizontally polarized RF signals. When transmitting in one polarity, a decrease in signal strength was measured for the same polarity, and an increase in signal strength was measured for the orthogonal polarity. According to the authors, this rotation was in essence a form of transmission loss for the communication system, and provided evidence that a turbulent hydrocarbon pool fire displays characteristics typically found in plasmas [Ref.3]. However, it must be noted that other mechanisms (like scattering from a "rough" surface) may have contributed to the polarization rotation. As a result, this rotation, in our opinion, does not provide conclusive evidence of plasma existence.

The second conclusion was that signal reflection was not observed and total signal losses were not significant enough so as to obstruct communication between the antennas. It was estimated that losses due to particles within the fire could have contributed to the total signal loss, because it was observed that the signal losses tended to be higher at higher frequencies.

Finally, signal gains were observed at various random frequencies. The authors attributed these gains,, to signal phase shifting and energy scattering caused by the fire. Definitive conclusion could not be drawn because the

experiment configuration used did not allow detection and measurement of signal phase shifting. In addition to these, the erratic wind that prevailed during the experiment tended to blow the fire from the vertical resulting in intangible effects on the strength of the signals that were transmitted through the fire.

III. THEORETICAL PRINCIPLES FOR MEASUREMENTS OF PATH LOSS

This Chapter presents theoretical concepts for measurements of path loss. The "differential method" of measurement is described and comparisons between waveguide measurements, single path propagation measurements and multipath propagation (fading) measurements are presented.

A. DIFFERENTIAL METHOD OF MEASUREMENT

The objective of the SCFE conducted onboard ex-USS SHADWELL was to measure the attenuation through actual ship compartment fire in the 2.4 GHz to 2.485 GHz ISM band. To achieve the objective, the "differential method" of measurement was used.

First, the path loss between the transmitting and receiving antennas in the ship's compartment was measured without fire. Next the measurements in the compartment continued with "live" fire and water mist created by the fire extinguishing system. The differences between the path losses measured without fire and those measured with fire and water mist were used to calculate the attenuation of the signal due to fire and the fire suppression system.

B. MEASUREMENTS OF PATH LOSS

In order to examine the effects of fire on propagation of RF energy, three different methods of path loss measurements have been considered:

- waveguide measurements
- single path propagation measurements
- multipath propagation (fading) measurements

However, before addressing the fundamentals of each method, we will briefly review the RF propagation in "free space".

1. Free Space Propagation

The free space propagation model is used to predict received signal strength when the transmission takes place in vacuum between antennas so remote from all other objects such that these objects exert no measurable influence on transmission.

If a transmitting antenna is located in free space, i.e., remote from the earth or any obstructions, and has a gain g_t (over an isotropic antenna) in the direction of a receiving antenna, the power per unit area (power density) at a distance d in the chosen direction is:

$$W = \frac{P_T g_T}{4\pi d^2} \quad (3.1)$$

where p_t is the total transmitted power. The effective area A of an antenna and its power gain G are related by:

$$A = \frac{\lambda^2 G}{4\pi} \quad (3.2)$$

where λ is the wavelength in meters. The available power p_r at the receiving antenna, which has an effective area A , is therefore:

$$p_R = \frac{p_T g_T}{4\pi d^2} \cdot A = \frac{p_T g_T}{4\pi d^2} \cdot \frac{\lambda^2 g_R}{4\pi} \quad (3.3)$$

where g_R is the gain of the receiving antenna. Thus we obtain:

$$p_R = p_T g_T g_R \left[\frac{\lambda}{4\pi d} \right]^2 \quad (3.4)$$

which is a fundamental relationship known as the free-space or Friis Equation. [Ref. 4,5,6]

However, the concept of free space channel characterizes an ideal RF propagation path; in practice, propagation through atmosphere, near the ground or in confined spaces results in absorption, reflection, refraction and diffraction, factors which modify the free space transmission. Detailed analysis of the mechanisms behind the electromagnetic wave propagation in the confined

shipboard environment of ex-USS SHADWELL is presented in the next Chapter. For purposes of formulation, when the propagation path is not free space, it is convenient to group the medium's effect into a single correction factor F such that, [Ref.7]:

$$P_R = \frac{P_T G_T G_R \lambda^2}{(4\pi d)^2} |F|^2 \quad (3.5)$$

The correction factor F can be defined as the ratio of the amplitude of the electric field E_m at a given point under specified conditions (medium, environment), to the amplitude of the electric field E_o under free space conditions:

$$F = \frac{E_m}{E_o} \quad (3.6)$$

For practical engineering applications Equation (3.5) can be written in the form:

$$P_R = P_T + G_T + G_R - L_o - L_p \quad (3.7)$$

where:

P_R = received power in decibels referred to 1 W

P_T = transmitted power in decibels referred to 1 W

G_T = transmitting antenna gain in decibels

G_R = receiving antenna gain in decibels

L_o = free space loss in decibels

L_p = loss due to the medium in decibels

The free space loss is given by:

$$L_o = 10 \log \left(\frac{4\pi d}{\lambda} \right)^2 \quad (3.8)$$

and the loss L_p due to the medium is related to the F factor by:

$$L_p = -10 \log |F|^2 \quad (3.9)$$

In RF propagation the medium almost invariably behaves as an attenuator, so the factor F is less than unity in magnitude. It follows that L_p is generally a positive number. The combination of free space loss L_o and loss due to the medium L_p gives the signal path loss. The path loss PL , which represents signal attenuation as a positive quantity measured in dB, is defined as the difference (in dB) between the effective transmitted power and the received power as shown in Equation (3.10):

$$PL = P_T - P_R \quad (3.10)$$

We next consider the three methods of path loss measurements.

2. Waveguide Measurements of Path Loss

The first approach considered for measuring the path loss of an RF signal transmitted through fire was the Waveguide Flame Experiment (WFE). The idea was to modify a standard rectangular waveguide for the 2.4 GHz band, and manufacture a custom-designed waveguide apparatus. Non-radiating slots for the dominant TE_{01} mode would be cut at the bottom of the waveguide, so that the flame could be introduced through the slots into the waveguide using nozzles. In this way, it would be possible to create a flame volume; i.e., an almost uniform flame distribution over the entire cross-section and over a certain length of the waveguide. Using a signal generator at one end and a power meter at the other end of the waveguide, insertion loss measurements would be conducted. As a result, the transmission coefficient for the waveguide would be measured with and without fire, for certain flame temperature and transparency (soot content), and over a range of frequencies.

Initially, the signal source would transmit a signal (level 1) into the flame-free waveguide, as shown in Figure 3.1. The power meter at the receiving end of the waveguide would record the received signal's strength (level 2). Next, we would saturate the waveguide with flame and transmit again the same signal (level 1) as before into the waveguide

as shown in Figure 3.2. The power meter at the receiving end of the waveguide would again record the received signal's strength (level 3). Subtracting the received power with the flame in the waveguide (level 3)

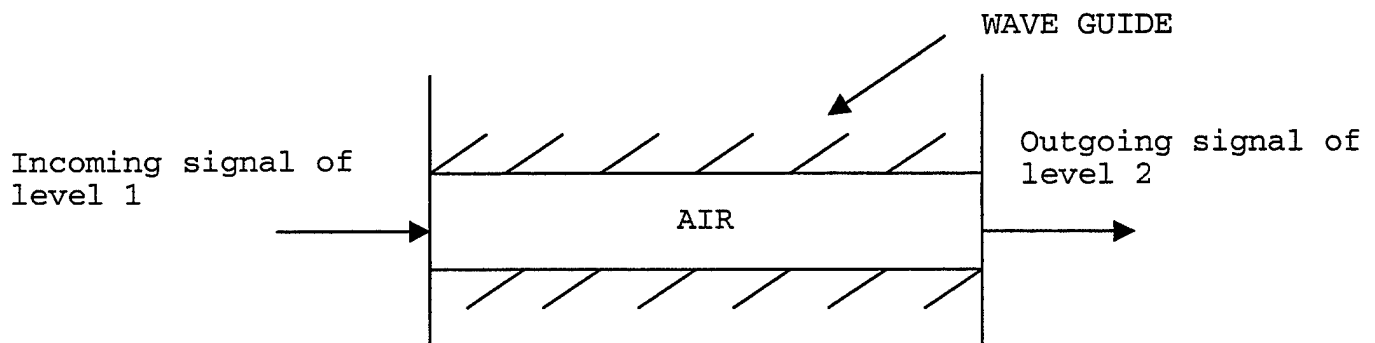


Figure 3.1: Waveguide Measurement Setup Without Flames Introduced.

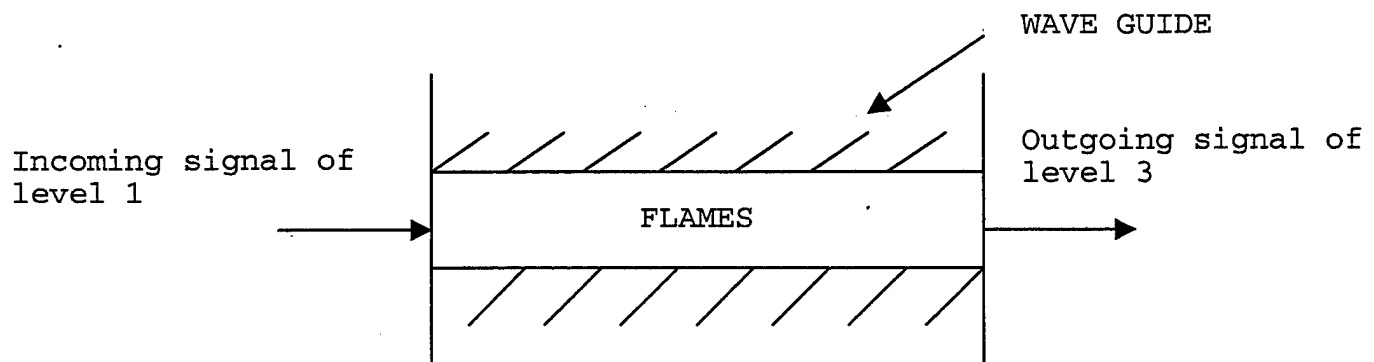


Figure 3.2: Waveguide Measurement Setup.

from the received power (at the same frequency) without the flame (level 2), would give us the flame attenuation. Since we would have control over the width of the flame, we would

be able to accurately determine the flame attenuation per unit length (dB/m).

The advantage of this method is that we have control over the direction of energy propagation within the waveguide. The signal is confined within the waveguide and its energy is forced to move only forward or backward. No energy escapes due to scattering from the fire, so in essence what we measure is pure signal attenuation due to flame. In addition to this, using a directional coupler in the transmitting end of the waveguide would allow us to measure the reflections from the fire and by subtracting that from the transmitted signal, to figure out the exact amount of energy going through the flame.

The waveguide measurement method described above was proposed in conjunction with the SCFE. However, budget limitations did not allow the WFE to be conducted.

3. Single Path Propagation Measurements

The second approach for measuring the path loss of an RF signal transmitted through fire, is by using a pair of narrowband, narrowbeam, linearly polarized antennas for transmission and reception. Using high gain (directive) antennas allows measuring the direct, unobstructed signal propagation path loss. The narrow antenna beams involved

eliminate to a large extent the necessity of accounting for reflections of the signal from the surrounding objects.

This second approach was followed during the SCFE on board ex-USS SHADWELL. The concept of the "differential method" for the measurements was used in the same way as outlined for the WFE. Initially, without fire, the signal generator sent a signal (level 1) through the transmitting antenna. The signal (level 2) arrived at the receiving antenna and was measured for 401 frequencies between 2.4 and 2.485 GHz. Next, the measurements were repeated with fire between the two antennas as shown in Figure 3.3. A new signal (level 3) was measured at the receiving antenna for each of the 401 frequencies. The difference of the two

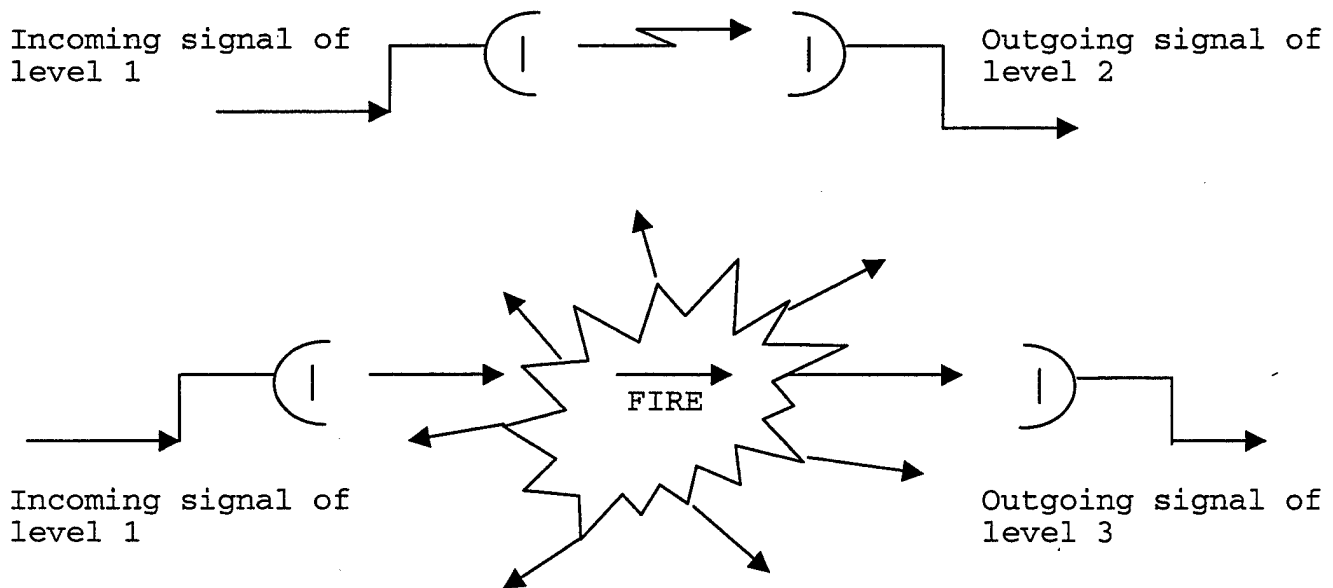


Figure 3.3: Single Path Propagation Measurement Setup.

received signals (levels 2 and 3) was used to calculate the path loss difference and from it the incremental path loss (attenuation). In this case, the RF energy is not confined and so a certain amount is unaccounted for due to scattering from the fire.

Therefore, we can identify two mechanisms of loss involved:

- loss caused by scattering
- loss due to attenuation by the fire

The combined effect of the two mechanisms is measured at the receiving antenna. Furthermore, this measurement method is more ambiguous than the waveguide measurement method, because of the changing fire width. An open fire is more dynamic than the controlled one in the waveguide, so we have first to determine an average fire width and then to extract the incremental path loss (dB/m).

4. Multipath Propagation (Fading) Measurements

The most realistic, but also the most complicated case, is the multipath propagation measurement method. In this case non-directional antennas are used for the measurements as shown in Figure 3.4. The transmitting antenna radiates in all directions, and the RF energy arrives to the receiving antenna in many different ways. Again, measurements with and

without fire are considered. If we were in free space without scatterers or reflectors, this situation would be the same as the one involving highly directive antennas, because the only signal path would be the line-of-sight path between the antennas.

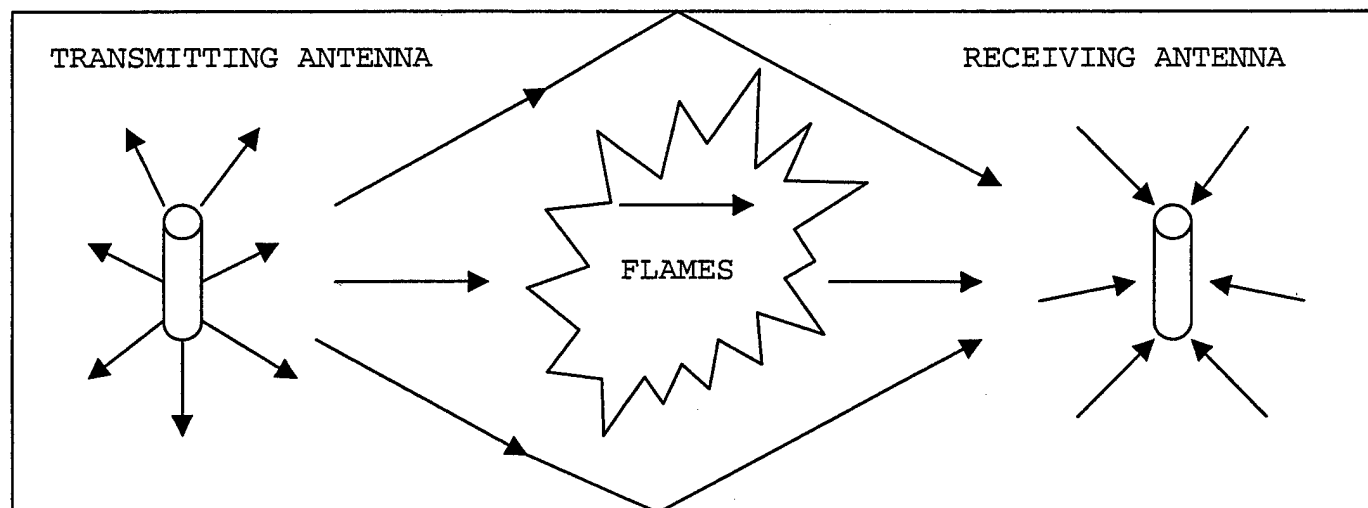


Figure 3.4: Multipath Propagation Measurement Setup.

However, a realistic shipboard communications application involves by and large omni-directional antennas (such that communication in any direction is possible) within a confined space with many scatterers (metallic objects, machinery) and reflectors (metallic floor, ceiling and surrounding walls). Depending on the layout of the compartment, the propagation of the RF energy may take place via a direct (line-of-sight) path between the antennas and

also by way of scattering from the wall surfaces and the objects in the compartment and by diffraction over or around them. Due to multiple reflections and diffractions from various objects, the electromagnetic waves travel along different paths of varying lengths. As a result, the incoming waves arrive from different directions with different amplitudes and time delays. They combine vectorially at the receiver antenna to give a signal that is a composite of a direct component and "diffuse" components. The resultant received signal may fluctuate rapidly, depending on the distribution of amplitudes and phases amongst the component waves, giving rise to fading.

To illustrate the significance of an induced phase shift to a signal, let us consider a signal with amplitude A (a random variable), and phase Φ (also a random variable), represented at one time instant by the phasor shown in Figure 3.5. Assuming that no other signal is present, we will always measure the constant (lying on a circle) amplitude A of the signal, regardless of the value of the phase Φ . However, in the case of two incoming signals, one from the direct path (signal A) and one from a reflection with a time delay (signal B), the measured results are different since we measure their vectorial combination (signal C, see Figure 3.6). Assuming that the two signals have comparable amplitudes, their relative phase shift can

cause constructive or destructive addition of the two signals. The amplitude of the resultant phasor can thus fluctuate from almost zero to double the direct signal amplitude, as shown in Figure 3.6.

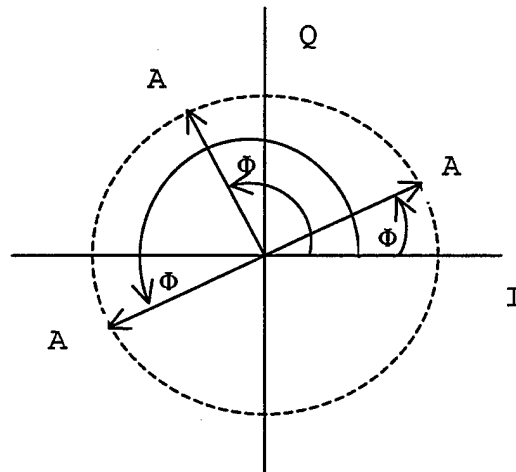


Figure 3.5: Phasor of Signal With Amplitude and a Variable Phase Φ .

We know that the phase shift for a time harmonic electromagnetic wave is related to the time delay Δt as:

$$\Delta\Phi = \omega \cdot \Delta t \quad (3.11)$$

For a high angular frequency ω , therefore, a small change in Δt can result in a significant phase shift. A time delay Δt also creates a different phase shift at different frequencies, causing a signal increase at some frequencies and signal cancellation at other frequencies, depending on

the phase differences ($\pi/2$, π , $3\pi/2$, 2π etc.). This situation results in frequency selective fading. The propagation between two antennas in a multipath situation may thus be modeled as a time-varying, linear two-port with an uneven time-averaged frequency response.

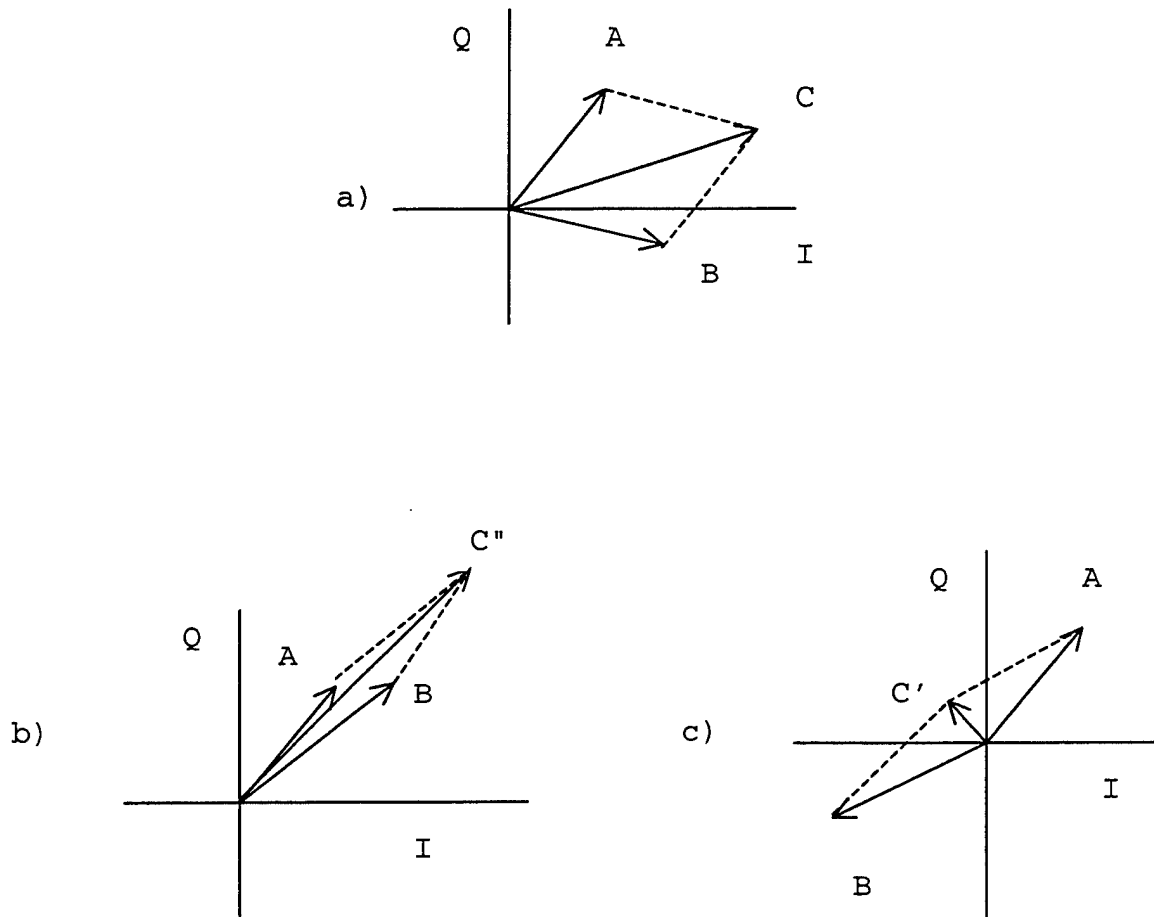


Figure 3.6: (a) Phasors for Two Signals A, B With Their Phasor Addition C, (b) Constructive Phasor Addition C'', and (c) Destructive Phasor Addition C'.

Now, when fire is introduced between the antennas it adds an additional phase shift, because of the change of the velocity of wave propagation through fire compared to the free space that fire occupies. This additional phase shift can cause the peaks and the nulls in the frequency response to shift.

This measurement method allows us to measure the fire attenuation only indirectly. The fluctuations of the wave's phase shifts, cause constructive and destructive interference at different frequencies, at different times. In other words, we have a time-averaged probability density function of the signal strength for each frequency of interest. The average value of this distribution (averaged over both time and frequency) will give us the attenuation (path loss) for the frequency range of interest. This result should be similar to the results obtained by the other two methods (waveguide, direct path). It must be noted that the "fading" environment determines the resulting probability density function. If, for example, we change the compartment the probability density function will change, but the attenuation measured due to fire, which is the statistical average of the distribution, should remain the same.

Depending on the number and type of propagation paths, the distribution of the signal strength can follow either the Rician or the Rayleigh distribution [Ref.4]. The

difference is the existence or the absence of a direct (dominant) signal. When we have a direct, line-of-sight, propagation path and multiple reflections and diffractions from the surrounding walls and objects, then we probably have a dominant signal of significant strength and multiple contributions from the other weaker returns. In this case, as shown in Figure 3.7, the phase shifts result in small displacements of the resultant phasor about the dominant signal. The signal

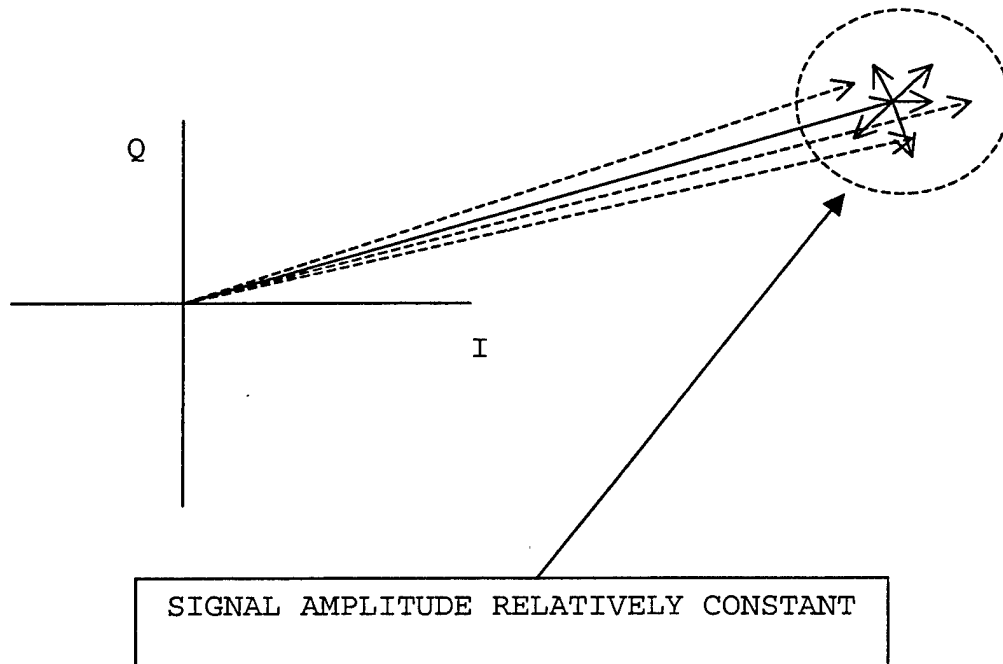


Figure 3.7: Phasor for a Sum of a Dominant (Direct) Signal and a Number of Smaller Reflected Signals.

amplitude in such a case is well modeled by the Rician distribution shown in Figure 3.8. In the literature, the Rician distribution is often described in terms of the parameter K (in dB) defined as:

$$K = 10 \log \frac{r_s^2}{2\sigma^2} \quad (3.12)$$

where r_s is the signal's dominant component and σ^2 is the mean power received. The parameter K can be interpreted as the ratio of the power in the dominant signal to that in the multipath (reflections) components. The Rician distribution reduces to the Rayleigh distribution in the special case of $r_s=0$. [Ref.4]

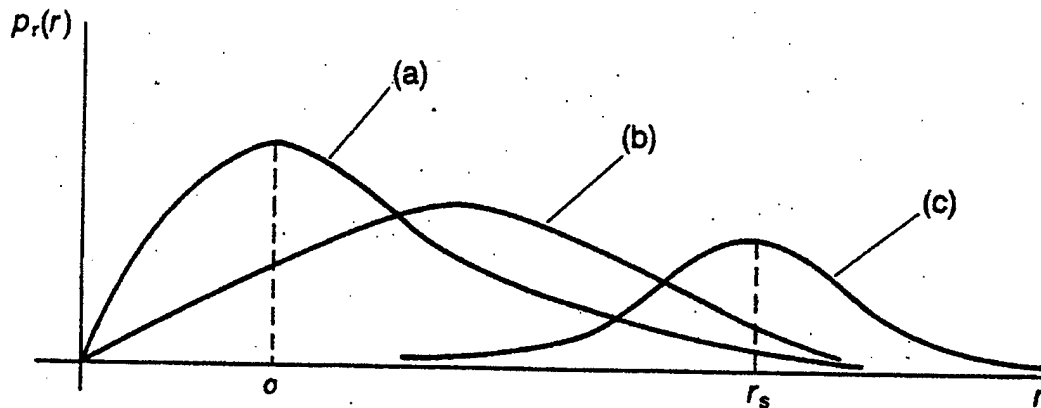


Figure 3.8: Rician Probability Distribution Function; (a) $K \rightarrow 0$, (b) $K=1$, (c) $K \gg 1$. From Ref.[4].

If the line of sight is blocked, the dominant signal is absent and we have only the reflections, which are of

similar amplitude. In this case, as shown in Figure 3.9, phase shifts result in larger movements of the resultant phasor created by the combination of the incoming signals.

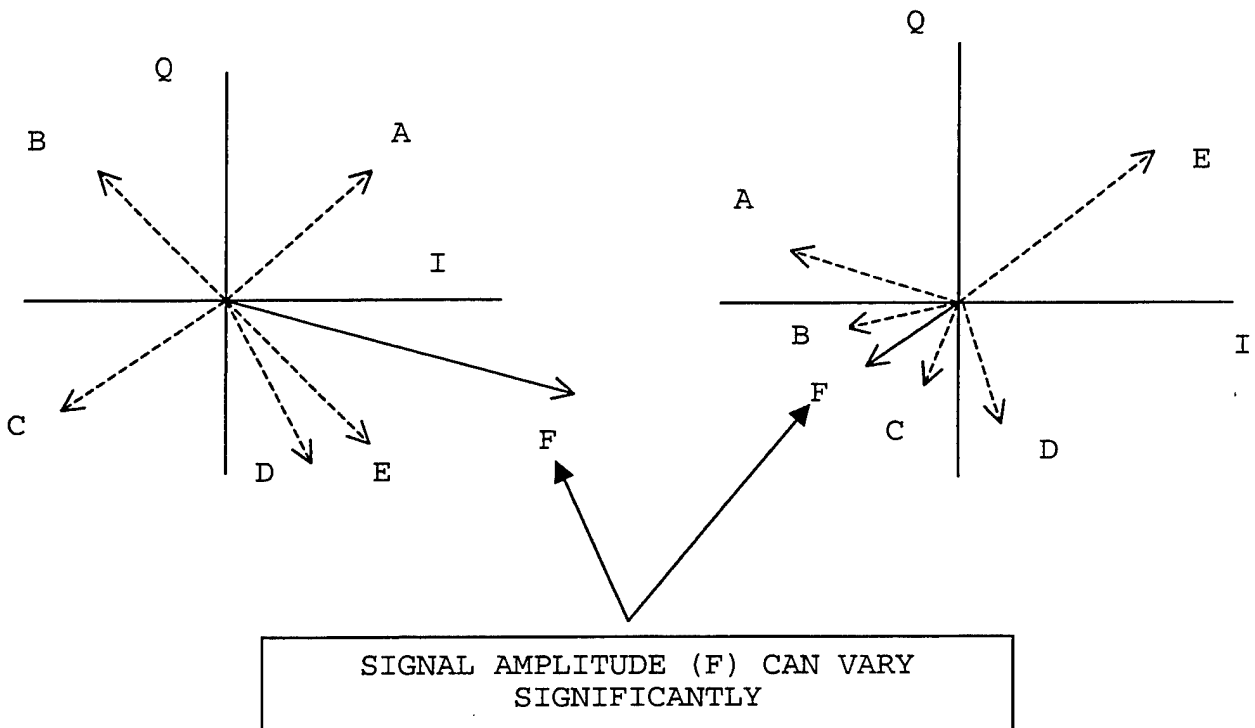


Figure 3.9: Phasor for a Sum of a Number of Reflected Signals (No Dominant Signal).

The signal amplitude in such a case is well modeled by the Rayleigh distribution shown in Figure 3.10.

It must be noted here that a direct, line-of-sight, propagation path does not necessarily mean that we have one dominant signal and Rician signal distribution. The existence of good reflectors around the transmitting and/or receiving antennas can create many incoming signals (due to reflections) with high amplitude comparable to the direct

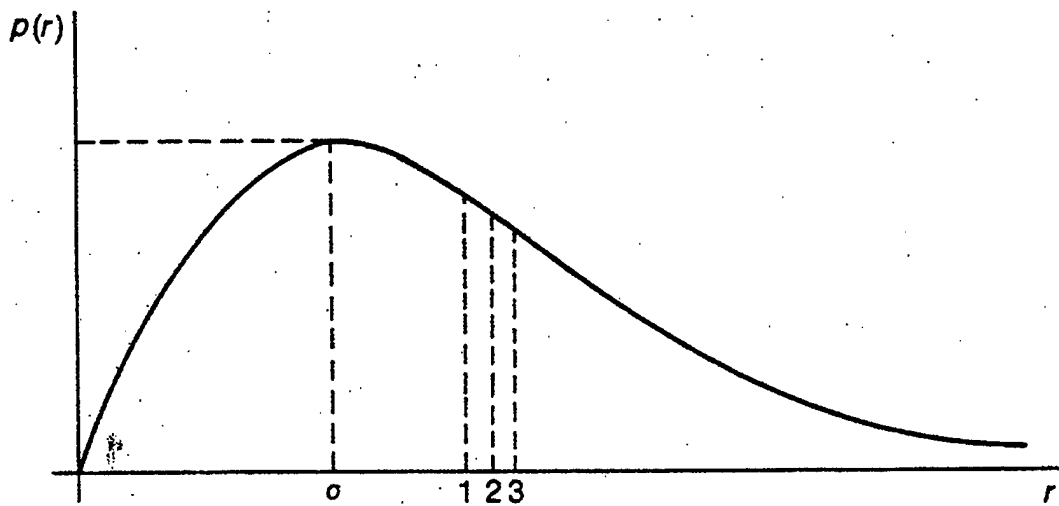


Figure 3.10: Rayleigh Probability Distribution Function; 1=Median (50%) Value, 1.1774σ , 2=Mean Value, 1.2533σ , 3=RMS Value, 1.41σ . From Ref.[4]

(line-of-sight) signal. In such a case the signal strength at the receiver may be also modeled as a Rayleigh distributed random variable.

IV. PHYSICS OF BASIC PROPAGATION MECHANISMS

Propagation of RF energy within confined spaces is strongly influenced by the local features. Reflection, diffraction, scattering and absorption are the basic propagation mechanisms which impacted propagation of the RF energy during the experiments conducted onboard ex-USS SHADWELL. These mechanisms are briefly explained in this section because they are the basis for understanding possible causes of the propagation loss.

Quantifying the individual contributions of these various mechanisms would have required us to measure quantities such as particle size and density (for scattering and absorption calculation for example), for which the ex-USS SHADWELL was not instrumented. Therefore, the following is a short review of the basic mechanisms to understand the possible contributions to the overall attenuation, but without attempting to determine the exact contribution of each mechanism. The exception to this is the case of the attenuation caused by plasma which is discussed in Chapter V. The plasma exception is taken because the plasma's attenuation abruptly changes as the operating frequency crosses the so called "plasma frequency".

A. REFLECTION

Reflection occurs when an electromagnetic wave propagating in one medium impinges upon another medium/object, which has different electrical properties and very large dimensions compared to the wavelength of the propagating wave. If the plane wave is incident on a perfect dielectric, part of the energy is transmitted into the second medium and part of the energy is reflected back into the first medium, and there is no loss of energy in absorption. If the plane wave is incident on a perfect conductor, then all incident energy is reflected back into the first medium without loss of energy. For the case of the measurements onboard ex-USS SHADWELL walls, floor, ceiling and various metal objects existing within the measurements compartment served as reflectors. Due to the above environment, we present in the following section the reflection of electromagnetic waves at a conducting surface.

1. Electromagnetic Waves in Conductors

In the case of conductors (metal in our case), the free current density J_f is not zero, as it is for the case of propagation through vacuum or loss-free dielectrics materials. With this, Maxwell's Equations for linear media assume the form [Ref.8]:

$$\nabla \cdot \mathbf{E} = 0 \tag{4.1}$$

$$\nabla \cdot \mathbf{B} = 0 \quad (4.2)$$

$$\nabla \times \mathbf{E} = -\frac{\partial \mathbf{B}}{\partial t} \quad (4.3)$$

$$\nabla \times \mathbf{B} = \mu\epsilon \frac{\partial \mathbf{E}}{\partial t} + \mu\sigma \mathbf{E} \quad (4.4)$$

where:

\mathbf{E} = Electric field intensity vector (Volts/meter)

\mathbf{B} = Magnetic flux density

μ = Permeability of a material

ϵ = Permittivity of a material

σ = Conductivity of a material

If we apply the curl to Equations 4.3, 4.4 we obtain the wave Equations for \mathbf{E} and \mathbf{B} :

$$\nabla^2 \mathbf{E} = \mu\epsilon \frac{\partial^2 \mathbf{E}}{\partial t^2} + \mu\sigma \frac{\partial \mathbf{E}}{\partial t} \quad (4.5)$$

$$\nabla^2 \mathbf{B} = \mu\epsilon \frac{\partial^2 \mathbf{B}}{\partial t^2} + \mu\sigma \frac{\partial \mathbf{B}}{\partial t} \quad (4.6)$$

Solutions to these wave equations (assuming a plane wave solution propagating in x-direction, with E_0 and B_0 the

amplitudes of the electric and magnetic field respectively)
are:

$$E(x,t) = E_o e^{i(\kappa x - \omega t)} \quad (4.7)$$

$$B(x,t) = B_o e^{i(\kappa x - \omega t)} \quad (4.8)$$

with the complex wave number as follows:

$$\kappa^2 = \mu \epsilon \omega^2 + i \mu \sigma \omega \quad (4.9)$$

If we take the square root of Equation 4.9 we have:

$$\kappa = \kappa_+ + i \kappa_- \quad (4.10)$$

$$\kappa_{\pm} = \omega \sqrt{\frac{\epsilon \mu}{2}} \left[\sqrt{1 + \left(\frac{\sigma}{\epsilon \omega} \right)^2} \pm 1 \right]^{\frac{1}{2}} \quad (4.11)$$

The imaginary part of the wave number κ results in an attenuation of the wave (decreasing amplitude with increasing x) [Ref.8]:

$$E(x,t) = E_o e^{-\kappa_- x} e^{i(\kappa_+ x - \omega t)} \quad (4.12)$$

$$B(x,t) = B_o e^{-\kappa_- x} e^{i(\kappa_+ x - \omega t)} \quad (4.13)$$

A measure of the depth that an electromagnetic wave penetrates a conductor is the skin depth. The skin depth is defined as the distance within which the amplitude of the wave is reduced 2.71 times:

$$d = \left(\frac{1}{\kappa_-} \right) \quad (4.14)$$

The real part of the wave number κ determines the wavelength λ , the propagation speed v , and the index of refraction n in the usual way:

$$\lambda = \frac{2\pi}{\kappa_+}, \quad v = \frac{\omega}{\kappa_+}, \quad n = \frac{c\kappa_+}{\omega} \quad (4.15)$$

In the case of a "good" conductor where $\sigma \gg \omega\epsilon$, κ_+ and κ_- are almost equal, and the skin depth decreases with increasing frequency:

$$\kappa_+ \cong \kappa_- \cong \sqrt{\frac{\omega\sigma\mu}{2}}, \quad d \cong \frac{\lambda}{2\pi} \quad (4.16)$$

In this regime the skin depth is smaller than the wavelength and the wave is attenuated away before it completes a single cycle. For the case of steel floor, walls

and ceiling of the measurement compartment in ex-USS SHADWELL the skin depth (penetration of electromagnetic wave) can be computed using Equations 4.14 and 4.16. For steel, the conductivity is $\sigma = 4.5 - 7.7 \times 10^6$ S/m and the permeability is $\mu = \mu_0 = 4\pi \times 10^{-7}$ H/m [Ref.9]. Using frequency $f = 2.4$ GHz and applying the values to Equations 4.14 and 4.16 we determine the skin depth of only $d = 3.7 - 4.84$ μm . As a result, we expect almost all of the electromagnetic energy to be reflected off the walls, as we are going to show in the next section.

2. Reflection for Normal Incidence to a Conducting Surface

To analyze reflection of an electromagnetic wave at normal incidence at an interface between two media we need the boundary conditions that exist on the interface. The general boundary conditions for electrodynamics, for linear media, in terms of E and B are:

$$\epsilon_1 E_{1\perp} - \epsilon_2 E_{2\perp} = \sigma_f \quad (4.17)$$

$$B_{1\perp} = B_{2\perp} \quad (4.18)$$

$$E_{1\parallel} = E_{2\parallel} \quad (4.19)$$

$$\frac{1}{\mu_1} B_{1\parallel} - \frac{1}{\mu_2} B_{2\parallel} = K_f \times \tilde{n} \quad (4.20)$$

where σ_f is the free space surface charge and K_f the free surface current at the boundary. The unit vector \tilde{n} is perpendicular to the surface of the interface, pointing from medium (2) to medium (1). In addition to these, in Equation 4.20, for the right-hand side not to be zero, the surface current density would have to be infinite (skin depth $\rightarrow 0$). However, this cannot happen except for the case of perfect conductor. Therefore, the right-hand side of Equation 4.20 has to be zero for all physical conducting surfaces.

Let us suppose now that we have a non-conducting linear medium 1 (air) and a conducting medium 2 (steel) and their interface coinciding with the yz -plane as shown in Figure 4.1. A monochromatic plane wave travelling in medium 1, is incident on the boundary resulting in a reflected wave propagating back to medium 1 and a transmitted wave which is attenuated as it penetrates into the conductor. The respective E and B vectors for the three waves are:

$$E_I(x,t) = E_{o_I} e^{i(\kappa_1 x - \omega t)} \tilde{j} \quad B_I(x,t) = \frac{1}{v_1} E_{o_I} e^{i(\kappa_1 x - \omega t)} \tilde{k} \quad (4.21)$$

$$E_R(x,t) = E_{o_R} e^{i(-\kappa_1 x - \omega t)} \tilde{j} \quad B_R(x,t) = -\frac{1}{v_1} E_{o_R} e^{i(-\kappa_1 x - \omega t)} \tilde{k} \quad (4.22)$$

$$E_T(x,t) = E_{o_T} e^{i(\kappa_2 x - \omega t)} \tilde{j} \quad B_T(x,t) = \frac{\kappa_2}{\omega} E_{o_T} e^{i(\kappa_2 x - \omega t)} \tilde{k} \quad (4.23)$$

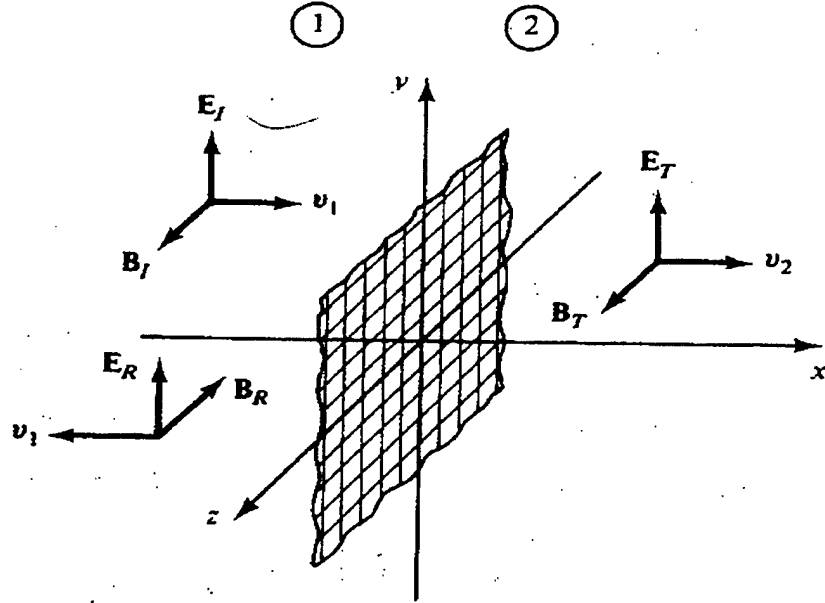


Figure 4.1: Propagation of an Electromagnetic Wave from a Non-Conducting (1) to a Conducting (2) Medium. From Ref.[8]

At the boundary ($x = 0$), the combined wave in medium 1 must join the wave in medium 2, while the boundary conditions have to be satisfied. Since E perpendicular on both sides is equal to 0, boundary condition 4.17 gives us $\sigma_f = 0$. B perpendicular is also zero, so boundary condition 4.18 is also satisfied. From boundary condition 4.19 we have:

$$E_{o_i} + E_{o_R} = E_{o_T} \quad (4.24)$$

and from boundary condition 4.20 we have:

$$\frac{1}{\mu_1 v_1} (E_{o_i} - E_{o_r}) - \frac{1}{\mu_2} \frac{\kappa_2}{\omega} E_{o_t} = 0 \quad (4.25)$$

If we set:

$$\beta = \frac{\mu_1 v_1 \kappa_2}{\mu_2 \omega} \quad (4.26)$$

then Equation 4.25 becomes:

$$E_{o_i} - E_{o_r} = \beta E_{o_t} \quad (4.27)$$

From Equations 4.24 and 4.27 it follows that:

$$E_{o_r} = \left(\frac{1-\beta}{1+\beta} \right) E_{o_i}, \quad E_{o_t} = \left(\frac{2}{1+\beta} \right) E_{o_i} \quad (4.28)$$

The electric field intensity of the reflected and transmitted waves may be related to the incident wave in the medium of origin through the Fresnel reflection coefficient R . The reflection coefficient is defined as:

$$R = \frac{|E_{o_r}|^2}{|E_{o_i}|^2} = \left(\frac{1-\beta}{1+\beta} \right)^2 \quad (4.29)$$

For the case of the perfect conductor we have:

$$\sigma \rightarrow \infty, \Rightarrow \beta \rightarrow \infty \Rightarrow E_{o_r} = -E_{o_i} \Rightarrow R=1 \quad (4.30)$$

In this case the wave is totally reflected, with a 180° phase shift [Ref.8]. For a good (but not perfect) conductor, where $\sigma \gg \omega\epsilon_2$, $|\beta|$ is very large and after expansion in powers of $1/\beta$ we have:

$$\frac{1-\beta}{1+\beta} = -\frac{\left(1-\frac{1}{\beta}\right)}{\left(1+\frac{1}{\beta}\right)} \cong -\left(1-\frac{1}{\beta}\right)^2 \cong \frac{2}{\beta} - 1 \Rightarrow R \cong \left|1-\frac{2}{\beta}\right|^2 \cong 1 - 2\frac{(\beta+\beta^*)}{|\beta|^2}$$

or by substituting Equations 4.26, 4.10 and 4.16 we have the reflection coefficient for the case of a good conductor [Ref.8]:

$$R \cong 1 - \sqrt{8 \frac{\mu_2}{\mu_1} \left(\frac{\omega\epsilon_1}{\sigma} \right)} \quad (4.31)$$

For the case of the measurements onboard ex-USS SHADWELL, if we substitute in Equation 4.31 the values for transition from air to steel $\mu_1 = \mu_2 = \mu_0 = 4\pi \times 10^{-7}$ H/m (we assume $\mu_2 = \mu_0$ which is the least favorable case for us) $\epsilon_1 = \epsilon_2 = \epsilon_0 = 8.85 \times 10^{-12}$ F/m, $\sigma = 4.5 - 7.7 \times 10^6$ S/m for frequency $f = 2.4$ GHz, the reflection coefficient is 0.9995 - 0.9996. In other

words, 99.95% to 99.96% of the energy is reflected off the steel walls as expected from the previous analysis.

B. DIFFRACTION OVER OBSTACLES

Diffraction occurs when the propagation path between the transmitter and the receiver is obstructed by a surface that has sharp irregularities (edges). The secondary waves resulting from the obstructing surface are present throughout the space and even behind the obstacle, giving rise to a "bending" of waves around the obstacle. Although the received field strength decreases rapidly as a receiver moves deeper into the obstructed (shadowed) region, the diffraction field still exists and often has sufficient strength to produce a useful signal. At high frequencies, diffraction, like reflection, depends on the geometry of the object, as well as the amplitude, phase, and polarization of the incident wave at the point of diffraction. In addition to the free-space "spreading" loss, the metal structures and objects, which existed in the compartment where measurements took place, could have produced additional losses caused by destructive interference of the direct and diffracted electromagnetic waves.

The phenomenon of diffraction can be explained by Huygens' principle. Huygens' principle, which can be deduced from Maxwell's Equations, states that every point on a propagating wave front acts as the new source of spherical

secondary wavelets (with the same frequency as that of the primary wave) and that a new wave front can be constructed from the envelope of these secondary waves. This is illustrated in Figure 4.2 for a plane wave front that has reached the position AA'. As an illustration of the principle, Figure 4.2 shows how wavelets originating from three representative points on AA' reach the wave front BB'. [Ref.4, 10]

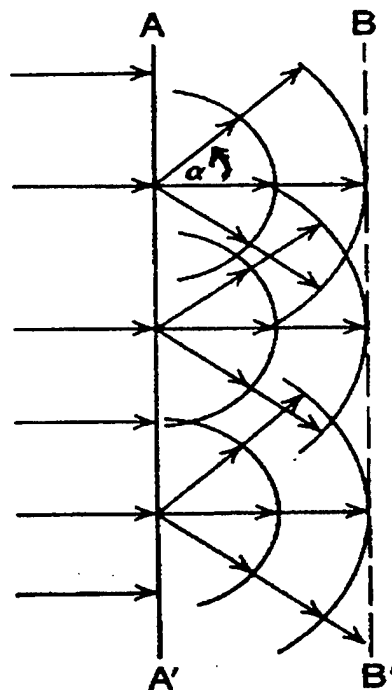


Figure 4.2: Huygens' Principle Applied to Propagation of Plane Waves. From Ref.[4]

Suppose now that the wave front encounters an obstacle. As shown in Figure 4.3 beyond the obstacle (which is assumed

to be impenetrable or perfectly absorbing) only a wave front CC' exists. Simple ray theory would suggest that no electromagnetic field exists in the shadow region below the dotted line BC , but Huygens' principle states that wavelets originating from all points on BB' , like P for

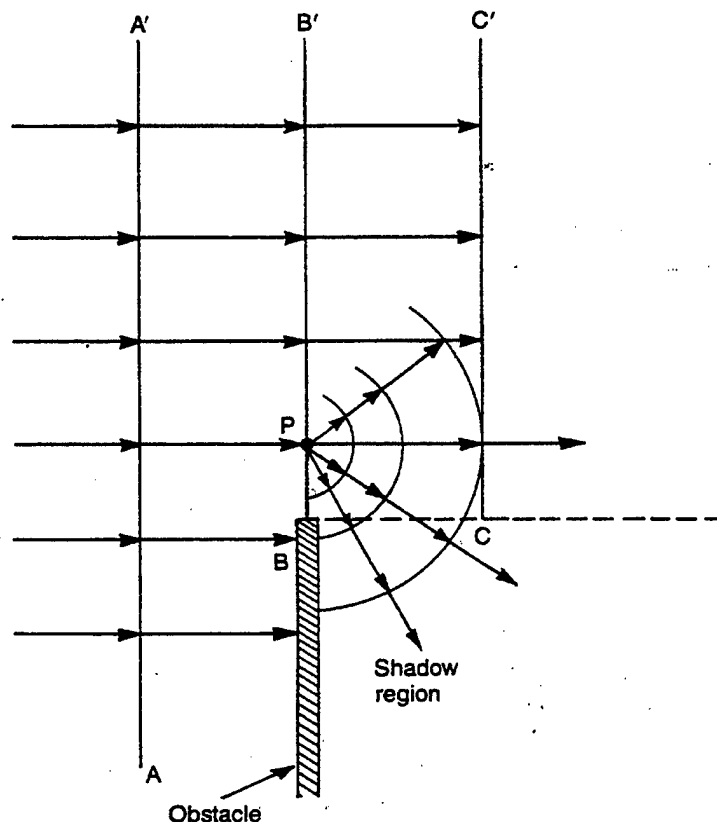


Figure 4.3: Diffraction at the Edge of an Obstacle.

From Ref. [4]

example, propagate into the shadow region. The field strength of the diffracted wave in the shadowed region is

the vector sum of the electric field components of all the secondary wavelets in the space around the obstacle.

C. SCATTERING AND ABSORPTION FROM PARTICLES

In passing through regions containing precipitation, whether in liquid or solid form, microwave radiation will be attenuated through two mechanisms [Ref.6]:

- Energy will be absorbed and converted into heat
- Energy will be scattered "out of the beam"

In this section, we outline how these two mechanisms may have contributed to the total attenuation of the propagated RF energy, during the SCFE measurements, because of the different particles suspended in the air (water droplets, smoke particles (soot), etc.).

1. Energy Absorption

Radio waves propagating through water mist and haze are attenuated. The precipitation droplets comprise a lossy dielectric and they absorb energy from the wave and convert it to heat. Each water droplet acts as a small "blob" of absorbing material. The theory for attenuation by water droplets is based on the calculation of the absorption cross

section σ_a of a single water droplet. This calculation [Ref.11] shows that the absorption cross section is proportional to:

$$\sigma_a \propto \lambda^2 \left(\frac{2\pi a}{\lambda} \right)^3 \quad (4.32)$$

where a is the radius of the droplet and λ the wavelength of the incident wave. The value of the absorption coefficient depends strongly on the composition, number density and size distribution of the aerosol particles suspended in the air.

At the wavelength of our interest ($\lambda = 12$ cm) the dielectric absorption increases rapidly as the drop size increases, and its contribution to total attenuation is comparable to that from scattering. Also, if the particle size and concentration are sufficiently large (water mist created by the extinguishing system in our case), a thin film of water may form (on solid surfaces) which may absorb a considerable fraction of the energy incident upon it.

2. Energy Scattering

Scattering is the process by which the energy in an electromagnetic wave is intercepted and re-radiated into 4π steradian solid angle. It results from the interaction of the wave field with the electron oscillators in the

scattering medium. If the energy of an electromagnetic wave does not match the energy of one of the atom's energy state transitions, the atom will scatter the energy. The atoms (or the molecules) of the scattering medium are excited by the incoming wave field, behaving as forced harmonic oscillators which reradiate at the frequency of the incident wave. However, there is a phase difference (phase lag) of the secondary wave relative to the primary wave, dependent on the difference between the incident wave frequency and the oscillator resonance frequency. The spatial distribution of the scattered radiation is strongly dependent on the ratio of the particle size and the incident wavelength. For particles very small compared to wavelength, the scattering is approximately isotropic. As the ratio of particle size to wavelength increases, the scattering is basically concentrated into the forward hemisphere. [Ref.12]

The scattering characteristics of an object are also strongly dependent on the frequency of the incident wave. Depending on the size of the scattering object (length L) and the wavelength $k = 2\pi / \lambda$ of the incident electromagnetic wave, three frequency regions are important [Ref.13]:

Low-frequency region, where $kL \ll 1$

Resonance region, where $kL \rightarrow 1$

High-frequency region, where $kL \gg 1$

We are going to focus on the first one, where the size of the scattering particles is very small relative to the incident wavelength. This region is called the Rayleigh region.

The radius of water droplets and smoke particles ranges from a fraction of a millimeter up to several millimeters, so Rayleigh scattering theory is valid for the wavelength of our interest ($\lambda = 12$ cm). Since the size of the particles is small compared to the incident wavelength, the phase variation of the incident plane wave across the extent of the scattering particle is essentially small, and the induced current on the body is approximately constant in amplitude and phase. As a result, at these frequencies the particular shape of the scattering object is not important and we can make the assumption of spherical particles (even if they are not always such) with an equivalent radius.

The theory for electromagnetic scattering by particles is based on the calculation of the scattering cross section σ_s of a single particle. This calculation (Rayleigh scattering theory) is straightforward for the case of a spherical particle having a radius no larger than $\lambda/10$, and predicts that the scattering cross section is proportional to [Ref.11]:

$$\sigma_s \propto \lambda^2 \left(\frac{2\pi a}{\lambda} \right)^6 \quad (4.33)$$

where α is the radius of the droplet and λ the wavelength of the incident wave. The value of the scattering coefficient depends strongly on the composition, number density and size distribution of the particles suspended in the air [Ref.14].

Gustav Mie gave the rigorous solution [Ref.14] of the scattering problem for homogeneous spherical particles of any size in 1908. Mie scattering includes Rayleigh scattering as the limit of small particle regime.

V. PHYSICS OF ELECTROMAGNETIC WAVES PROPAGATION THROUGH FIRE

An important issue during the SCFE was the effect of fire on the propagation of electromagnetic waves. The crucial question was whether a chemical (fuel) fire at sea level pressure was hot enough to substantially ionize the air and create plasma. If this were the case then we would observe significant signal attenuation or even interruption of communication between the transmitting and receiving antennas due to the signal reflection on the plasma boundary.

This Chapter describes the fundamentals of electromagnetic propagation through plasma. Parameters important in plasma creation are examined and the question, whether plasma created by the fuel fires during the SCFE affected the RF energy propagation, is addressed.

A. BASIC PLASMA CONCEPTS

A plasma is a gas of charges, which are coupled to one another via their self-consistent electric and magnetic fields. It is called the fourth state of matter and makes up more than 99% of the visible universe by some estimates. Due to this reason, the propagation of electromagnetic waves in plasmas occurs in a number of problems and different

branches of science (radio astronomy, optical astronomy, nuclear physics etc.). [Ref.15]

1. Electron Debye Length

We will start the examination of plasma behavior by introducing one of the important plasma parameters, the electron Debye length λ_{De} . The Debye length is the distance at which the field of an individual charge is shielded out by the response of the surrounding charges, and is given in m by [Ref.16]:

$$\lambda_{De} = \sqrt{\frac{\epsilon_0 K_B T}{ne^2}} \quad (51)$$

where:

n = charge density m^{-3}

T = absolute temperature K

$e = 1.6022 \times 10^{-19}$ C, the electron charge

$K_B = 1.3807 \times 10^{-23}$ J/K, Boltzmann constant

$\epsilon_0 = 8.85 \times 10^{-12}$ C²/Nm², permittivity of free space

When $K_B T = \theta_{ev}$ is expressed in units of eV and n in units of cm^{-3} then the electron Debye length λ_{De} in cm is given by:

$$\lambda_{De} = 750 \sqrt{\frac{\theta_{ev}}{n}} \quad (5.2)$$

When the number of electrons in a sphere with radius λ_{De} becomes very large, collisions between the particles of the plasma can be ignored [Ref.16]. The number of electrons in the Debye sphere is N_D :

$$N_D = \frac{4}{3} \pi n_e \lambda_{De}^3 \quad (5.3)$$

where n_e is the electron density. [Ref.16]

2. Plasma Frequency

A characteristic feature of plasma is its ability to support waves or collective modes of interaction. In the simplest case, these waves correspond to charge density fluctuations at a characteristic frequency determined by the electrons and/or the ions. In plasma there are two kinds of these waves: a high frequency wave called an electron plasma wave and a low frequency wave called an ion acoustic wave.

To examine high frequency charge density fluctuations associated with the motion of the electrons, we treat the massive ions as immobile and we introduce the Vlasov equation which, augmented with Maxwell's equations, gives a

complete description of collisionless plasma behavior. The Vlasov equation, given by:

$$\frac{\partial f_j}{\partial t} + v \frac{\partial f_j}{\partial x} + \frac{q_j}{m_j} \left(E + \frac{v \times B}{c} \right) \frac{\partial f_j}{\partial v} = 0 \quad (5.4)$$

applies to each charge "species" in the plasma. The distribution function $f_j(x, v, t)$ characterizes particles of species j in phase space (x, v) as a function of time. The Vlasov equation says that $f_j(x(t), v(t), t)$ is a constant in time: $df/dt=0$. By taking different velocity moments of the Vlasov equation, we can derive equations for the evolution in space and time, of the density, mean velocity, and pressure of each species. Two of these equations are the continuity and force equations for the density n_j and mean velocity u_j of particles with charge q_j , pressure p_j and mass m_j :

$$\frac{\partial n_j}{\partial t} + \frac{\partial}{\partial x} (n_j u_j) = 0 \quad (5.5)$$

$$n_j \left(\frac{\partial u_j}{\partial t} + u_j \frac{\partial u_j}{\partial x} \right) = \frac{n_j q_j}{m_j} \left(E + \frac{u_j \times B}{c} \right) - \frac{1}{m_j} \frac{\partial p_j}{\partial x} \quad (5.6)$$

For plasma composed of electrons and one species of ions, Equations 5.5 and 5.6 constitute the two-fluid model (the electrons as one fluid, the ions as the other). [Ref.16]

Considering only the electron density wave with wave-vector k in one-dimension (in the x -direction), and assuming that the wave has a phase velocity much greater than the electron thermal velocity v_{th} , $\omega/k \gg v_{th}$ we have the electron fluid equations:

$$\frac{\partial n_e}{\partial t} + \frac{\partial}{\partial x}(n_e u_e) = 0 \quad (\text{continuity equation}) \quad (5.7)$$

$$\frac{\partial}{\partial t}(n_e u_e) + \frac{\partial}{\partial x}(n_e u_e^2) = -\frac{n_e e E}{m_e} - \frac{1}{m_e} \frac{\partial p_e}{\partial x} \quad (\text{force equation}) \quad (5.8)$$

$$\frac{p_e}{n_e^3} = \text{constant} \quad (5.9)$$

Using these equations and the Poisson's equation to relate the electric field to the electron's density, the wave equation describing small amplitude fluctuations in electron density can be derived:

$$\left(\frac{\partial^2}{\partial t^2} - 3v_{th}^2 \frac{\partial^2}{\partial x^2} + \omega_p^2 \right) n_e = 0 \quad (5.10)$$

where ω_p is the electron plasma frequency, for a plasma with electron density n_e , given by:

$$\omega_p = \sqrt{\frac{e^2 n_e}{\epsilon_0 m_e}} \quad (5.11)$$

If the density is expressed in cm^{-3} then [Ref.16]:

$$\omega_p = 5.65 \times 10^4 \sqrt{n_e} \quad (5.12)$$

If we assume a plane-wave solution ($n_e \sim e^{i(kx - \omega t)}$) and substitute it into 5.10 then the dispersion relation for electron plasma oscillations will be:

$$\omega^2 = \omega_p^2 + 3k^2 v_{th}^2 \quad (5.13)$$

At long wavelengths, the frequency of these waves is essentially ω_p . [Ref.16]

3. Electromagnetic Wave Propagation in Plasmas

After examining the characteristic charge density oscillations, which are supported by plasma, in this section

we consider how plasma modifies the propagation of electromagnetic waves. We will try to investigate the linearized plasma response to a high frequency field of the form:

$$E = E(x)e^{-i\omega t} \quad (5.14)$$

To achieve this, we will first focus on the collisionless plasma behavior and assume that there are no large imposed (or self-generated) magnetic fields. The ions will be treated as stationary since the frequencies we are interested in are of the order of plasma frequency ω_p or higher. From the force Equation 5.8 for the electron fluid (linearized) if we neglect the term involving derivative (with respect to space) of the electron average velocity squared as a square of a small quantity, we get [Ref.16]:

$$\frac{\partial u_e}{\partial t} = -\frac{e}{m_e} E(x)e^{-i\omega t} \quad (5.15)$$

The current density is:

$$J = -n_e(x)eu_e \quad (5.16)$$

If we take the derivative of the above equation we have:

$$\frac{\partial J}{\partial t} = -n_e(x)e \frac{\partial u_e}{\partial t} \quad (5.17)$$

If we substitute equations 5.11 and 5.15 we get:

$$\frac{\partial J}{\partial t} = \omega_p^2 \epsilon_o E \quad (5.18)$$

and

$$J = \frac{i\omega_p^2 \epsilon_o E}{\omega} = \sigma E \quad (5.19)$$

As the result the conductivity of the plasma is:

$$\sigma = \frac{i\omega_p^2 \epsilon_o}{\omega} \quad (5.20)$$

We can now develop wave equations for the E and B fields through the Faraday's and Ampere's laws:

$$\nabla \times E = \frac{i\omega}{c} B \quad (5.21)$$

$$\nabla \times B = \frac{1}{\epsilon_o c} \sigma E - \frac{i\omega}{c} E \quad (5.22)$$

If we substitute σ (Equation 5.20) into Equation 5.22 we get:

$$\nabla \times B = -\frac{i\omega}{c} \epsilon E \quad (5.23)$$

where:

$$\epsilon = 1 - \frac{\omega_p^2}{\omega^2} \quad (5.24)$$

defines the permittivity of plasma. Applying the curl to 5.21 and substituting 5.23 we obtain the wave equation for E:

$$\nabla^2 E + \frac{\omega^2}{c^2} \epsilon E = 0 \quad (5.25)$$

In the same way the wave equation for B is:

$$\nabla^2 B + \frac{\omega^2}{c^2} \epsilon B = 0 \quad (5.26)$$

Assuming a spatial dependence e^{ikx} the above gives the dispersion relation for electromagnetic waves in plasma:

$$\frac{\omega^2}{c^2} \epsilon = k^2 \quad (5.27)$$

or by substituting the expression for ϵ :

$$\omega^2 = \omega_p^2 + k^2 c^2 \quad (5.28)$$

From Equation 5.28 we see that if $\omega < \omega_p$ the wave number k becomes imaginary and we do not have propagating waves. For frequencies in excess of ω_p , the wave number is real, and waves propagate without attenuation at a wave speed:

$$v = \frac{\omega}{k} = c \left(1 - \frac{\omega_p^2}{\omega^2} \right)^{-\frac{1}{2}} \quad (5.29)$$

and the index of refraction n_{refr} for plasma is:

$$n_{refr} = \sqrt{1 - \left(\frac{\omega_p}{\omega} \right)^2} \quad (5.30)$$

As a result, the plasma frequency ω_p is the minimum frequency for electromagnetic wave propagation in plasma. Since the characteristic response time for electrons is

$1/\omega_p$, the electrons shield out the field of an electromagnetic wave when $\omega < \omega_p$. Hence the condition $\omega_p = \omega$ defines the maximum plasma density which an electromagnetic of frequency ω wave can penetrate. This critical density is:

$$n_{cr} = \frac{m_e \epsilon_0 \omega^2}{e^2} = \frac{1.1 \times 10^{21}}{\lambda_\mu^2} \text{ cm}^{-3} \quad (5.31)$$

where λ_μ is the free-space wavelength of the light in units of micrometers (10^{-6} m). [Ref.16]

4. Electromagnetic Wave Propagation in Collisional Plasma

So far in our analysis we have focused on the collisionless behavior of plasma. In this section we will present the modifications to plasma characteristics due to collisional effects. We have already mentioned that collisional effects due to discrete particle encounters can be neglected in plasma analysis, as the number of particles in Debye sphere becomes very large. However, even then some collisions occur.

To analyze the collisional plasma behavior, we first have to include a collision term in the Vlasov equation, which now becomes [Ref.16]:

$$\frac{\partial f_j}{\partial t} + \mathbf{v} \cdot \frac{\partial f_j}{\partial \mathbf{x}} + \frac{q_j}{m_j} \left(E + \frac{\mathbf{v} \times \mathbf{B}}{c} \right) \cdot \frac{\partial f_j}{\partial \mathbf{v}} = \sum_l \left(\frac{\partial f_{jl}}{\partial t} \right) \quad (5.32)$$

where the time derivative of f_{j1} represents the rate of change of f_j due to collisions with the 1th charge species. Following the same analysis as before (by taking the velocity moments of Vlasov equation) the linearized force equation for the electron fluid can be derived:

$$\frac{\partial u_e}{\partial t} = -\frac{e}{m_e} E(x) e^{-i\omega t} - \nu_{ei} u_e \quad (5.33)$$

where ν_{ei} is the collision frequency which describes electron scattering by the ions.

The collision frequency depends on the average of the electron velocity distribution. With $\theta_{ev} = K_B T$ in units of eV and n_e in units of cm^{-3} the collision frequency is given by:

$$\nu_{ei} = 3 \times 10^{-6} \frac{n_e Z}{\theta_{ev}^{\frac{3}{2}}} \ln(\Lambda) \quad (5.34)$$

where Z is the atomic number and Λ is the ratio of the minimum and maximum impact parameter [Ref.16]. The maximum impact parameter is approximately the electron Debye length

and the minimum impact parameter is the larger of the distance of closest approach (mv_e^2/Ze^2) or the DeBroglie wavelength of the electron ($h/2\pi mv_e$, where h is the Planck's constant). Using the distance of closest approach, Λ is given by:

$$\Lambda = \frac{12\pi N_D}{Z} \quad (5.35)$$

A detailed discussion of the derivation of electron-ion collision frequency is given in Chapter 5 of Ref.16.

Solving the linearized force Equation 5.33 for the electron fluid, after sufficient time it gives:

$$u_e = \frac{ieE}{m_e(\omega + i\nu_{ei})} \quad (5.36)$$

The plasma current density and the conductivity are then:

$$J = -n_e e u_e = \frac{i\varepsilon_0 \omega_p^2}{\omega + i\nu_{ei}} E = \sigma E \quad (5.37)$$

$$\sigma = \frac{i\omega_p^2 \varepsilon_0}{\omega + i\nu_{ei}} \quad (5.38)$$

Considering again Faraday's and Ampere's laws we have the modified, due to collisional behavior, complex dielectric permittivity of the plasma given by:

$$\varepsilon = 1 - \frac{\omega_p^2}{\omega \cdot (\omega + i\nu_{ei})} \quad (5.39)$$

In the same way as before, applying the curl to Faraday's and Ampere's Equations gives the wave equations, from which the dispersion relation for electromagnetic waves in collisional plasma can be derived as:

$$\omega^2 = k^2 c^2 + \omega_p^2 \left(1 - \frac{i\nu_{ei}}{\omega} \right) \quad (5.40)$$

assuming that $\nu_{ei}/\omega \ll 1$. In this case the electromagnetic waves are damped. Expressing $\omega = \omega_{real} - i\nu_{dmp}/2$, where ν_{dmp} is the energy damping rate and assuming that $\nu_{dmp} \ll \omega_{real}$, we obtain:

$$\omega_{real} = \sqrt{\omega_p^2 + k^2 c^2} \quad (5.41)$$

and

$$\nu_{dmp} = \frac{\omega_p^2}{\omega_{real}^2} \nu_{ei} = \frac{n_e}{n_{cr}} \nu_{ei} \quad (5.42)$$

The collisional damping through Equation 5.42 gives us the following physical interpretation: the rate of energy loss from the electromagnetic wave must balance the rate at which the oscillatory energy of the electrons is randomized by electron-ion scattering [Ref.16]. A diagram of attenuation of electromagnetic waves as a function of collision frequency and electromagnetic wave frequency can be found in Ref.17.

B. FLAMES AND PLASMA

Having examined the fundamental parameters of plasmas and the effects of a plasma on electromagnetic wave propagation, in this section we relate ionization in fires with plasma properties. We will also apply the theoretical analysis of plasma behavior of the previous section to the SCFE, in order to resolve whether plasma conditions existed and how the propagation of the RF energy was affected.

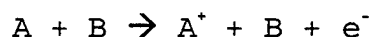
1. Ionization Due to Flames

Ion concentrations found in the reaction zones of unseeded premixed hydrocarbon/air and hydrocarbon/oxygen flames at pressures between 2 and 760 mm/Hg lie in the range 10^9 - 10^{12} ions/cm³, concentration being highest when acetylene is the fuel. However, depending on the fuel type much lower ion concentrations have been observed. For example, carbon monoxide, hydrogen and carbon disulfide have

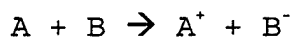
been found to produce only minute concentrations of ions when burned in air oxygen. [Ref.17]

Ion production usually requires considerable energy and the ionization potentials for most atoms and molecules are of magnitude 4-20 eV. There are many processes that result in ionization, the most important being:

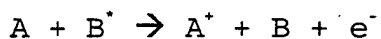
Ionization by collision:



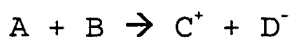
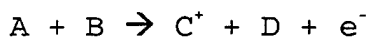
Ionization by electron transfer:



Ionization by transfer of excitation energy:



Chemi-ionization:



The asterisk indicates an excited internal energy state. An increase in temperature will result in an increase in ionization energy, which subsequently results in an increase in the fraction of the original molecules that are

ionized. The conclusion is that charged particles exist within a fire, but the question is when the transition from a flame to appreciable ionized plasma occurs. [Ref.17]

According to measurements, ion concentration peaks in the reaction zone of the flame. Figure 5.1 shows how ion concentration profile, as measured by electric probes, fits into the structure of a flat flame.

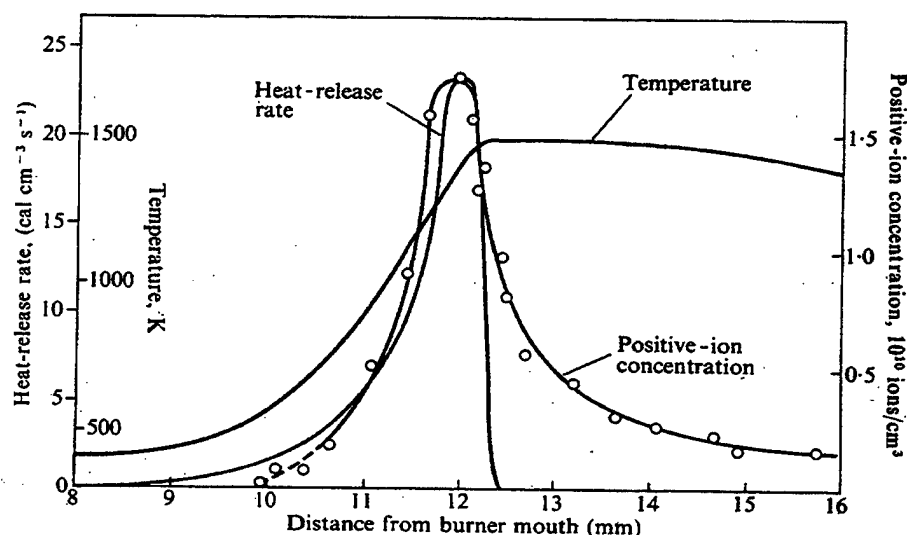


Figure 5.1: Positive Ion Concentration, Heat Release Rate and Temperature Versus Distance from Burner Mouth. Dashed Line Indicates the Uncertain Region in Ion-Concentration Measurements. From Ref.[17]

The concentrations and rates of generation of ions reach maxima close to the final temperature. In the case of normal hydrocarbon flames of low final temperatures, the

ionization peaks, which are thought to be caused by chemi-ionization, give by far the highest concentrations of free charges in the vicinity of the reaction zone. In addition to these, heptane and diesel fuels induce ionization near the flame.

2. Dilute Plasma Created During SCFE and its Effect on Propagation of RF Energy

During many experiments in the field of combustion in the past, appreciable attenuation in atmospheric pressure flames was obtained for frequencies of 100 GHz or lower, which includes our band of interest (Ref.17). Therefore, although no reflection of RF energy by the flames occurred during the NRL measurements at Chesapeake Bay, the possibility existed that attenuation due to plasma effects during the SCFE was significant. The calculation that follows indicates that the hydrocarbon (diesel, heptane) fuel fires during the SCFE, were not hot enough to create substantially ionized plasma that would attenuate the propagated RF energy.

The electron concentrations found naturally in flames are on the order of $10^9 - 10^{12}$ ions/cm³ [Ref.17]. Figures 5.2 and 5.3 place average electron concentrations for flames (average temperature 1000 K) in the region of $10^7 - 10^9$ ions/cm³. [Ref.18,19] For the measurements in SCFE two different fuels were used: diesel and heptane. The highest

temperatures of the flames (where ionization concentration is maximum) recorded for both fuels were below 900 K. Due to the fact that no instrumentation was used for measurements of ionization of the flames, for our analysis we will assume

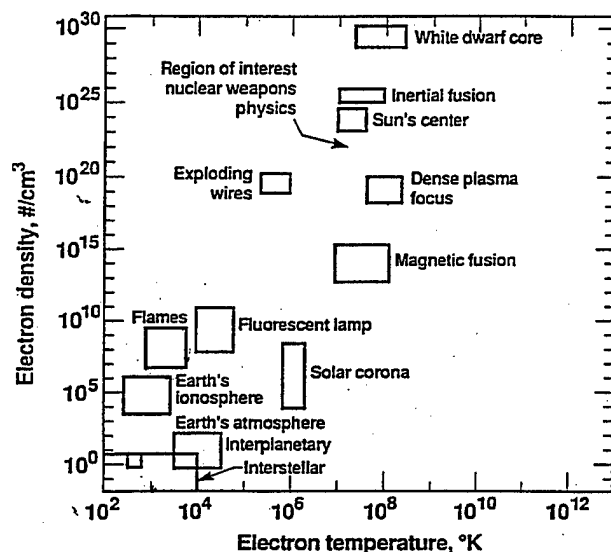


Figure 5.2: Electron Density Versus Electron Temperature for Different Plasmas in the Universe. From Ref.[18]

that the ionization of the flames was in the region of 10^9 ions/cm³, considering the highest prevailing temperatures (~900 K).

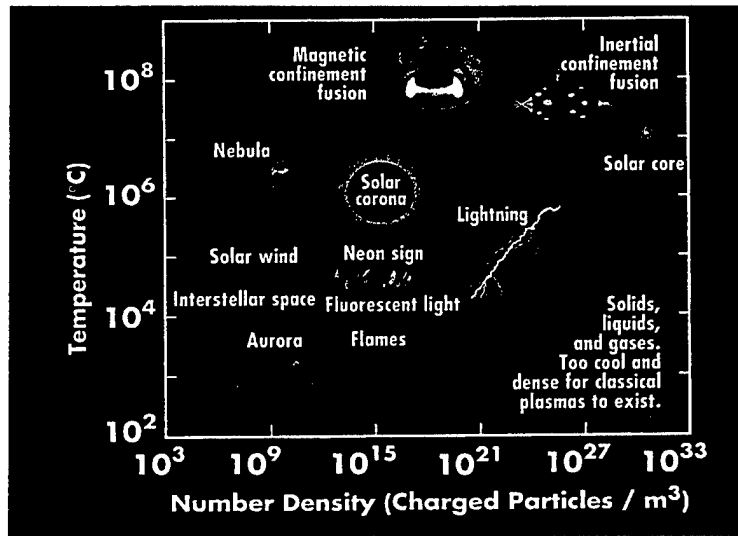


Figure 5.3: Electron Density Versus Electron Temperature for Different Plasmas in the Universe. From Ref.[19]

Initially we calculate the plasma frequency and the electron Debye length for $n_e = 10^9 \text{ cm}^{-3}$. Using Equation 5.12 the plasma frequency is $\omega_p = 1.79 \times 10^9 \text{ rad}$ or $f_p = \omega_p / 2\pi = 285 \text{ MHz}$. Using Equation 5.1 and for temperature $T = 900 \text{ K}$, the electron Debye length is $\lambda_{De} = 6.55 \times 10^{-5} \text{ m}$.

Considering the above results, for the case of collisionless plasma behavior, we can safely estimate that attenuation due to plasma did not occur during SCFE due to the fact that the frequency band used for the measurements (2.4 - 2.485 GHz) was well above the plasma frequency. As a result, the propagating RF energy penetrated the dilute plasma created by fire and the attenuation caused, if any was insignificant.

Assuming collisional plasma behavior, we must calculate the collision frequency of the plasma. Using Equation 5.3 we first calculate the number of electrons in the Debye sphere for electron Debye length $\lambda_{De} = 6.55 \times 10^{-3}$ cm as $N_D = 1177$ electrons. The temperature of $T = 900$ K translates to $\theta_{ev} = 0.0776$ eV. Next, from Equation 5.35 we determine $\Lambda = 44371.8$. Substituting these values of θ_{ev} and Λ in Equation 5.34 allows us to calculate the collision frequency of plasma as $\nu_{ei} = 1.485$ MHz. The critical density for the frequency of 2.4 GHz ($\lambda_\mu = 125 \times 10^3$ μm) that we used, calculated by Equation 5.31, is $n_{cr} = 7.04 \times 10^{10}$ cm^{-3} . Using now Equation 5.42 with $n_e = 10^9$ cm^{-3} , $n_{cr} = 7.04 \times 10^{10}$ cm^{-3} , and $\nu_{ei} = 1.485$ MHz we calculate the energy damping rate $\nu_{dmp} = 21.1$ KHz. This energy damping rate gives us an absorption length ($\lambda_{abs} = c/\nu_{dmp}$) of $\lambda_{abs} = 14.2$ km, much greater than the width of the plasma in SCFE and the wavelength ($\lambda = 0.125$ m) used for the measurements. Due to this fact, we can also safely estimate (for the case of collisional plasma behavior) that the propagated RF energy penetrated the dilute plasma without significant attenuation.

Therefore, the answer to the question of whether the fires during the SCFE measurements were hot enough to create significantly ionized plasma is negative. The plasma created by the flames was dilute and the contribution to the total

attenuation of the propagated RF energy insignificant. If our assumption for the concentration of ions in the plasma ($n_e = 10^9$ ions/cm³) was incorrect and the flames had concentrations 10^{11} ions/cm³ or greater, then the plasma frequency would be greater than the frequency used for the measurements. In such a case, when the flames reach their maximum temperature, the ion concentration would be maximum and the plasma would block (reflect) the propagated RF energy. If this were the case, during the measurements with the high directivity antennas, we would have measured large signal attenuation between the transmitting and receiving antenna. However, this never happened.

VI. INSTRUMENTATION USED FOR SCFE

In this Chapter we will discuss the SCFE measurements setup. The software program that was developed in LabVIEW to automate the measurements, and the hardware used are presented.

A. HARDWARE USED AND MEASUREMENT SETUP

As mentioned in previous Chapters, the objective of the SCFE was to measure the attenuation through actual ship compartment fire in the 2.4 - 2.485 GHz ISM band. The bistatic measurement system used for the measurements of SCFE consisted of the following:

- PC with plug-in GPIB board
- HP 8756A Scalar Network Analyzer (SNA)
- HP 8350B Sweep Oscillator with HP 83525B RF plug-in
- HP 8566B Spectrum Analyzer (100 Hz - 2.5 GHz/2 - 22 GHz)
- HP 778D Dual Directional Coupler
- Varian TWTA Power Amplifier (30 dB Gain)
- TTE ISM 304 Chebyshev Compline Bandpass Filter
- Winncom WR2400-24 Parabolic Grid Antennas
- Cushcraft S2307AMP10SMF DirectLink Patch Antennas

The measurements were performed using the SNA to measure the magnitude of the insertion loss (S_{21}) between the transmitting and receiving antennas; i.e., in every case (run) of the experiment the SNA was measuring the difference between the reference (transmitted) and the received signal powers, and the computer which controlled the measurements stored the data for further processing. Both narrow band, narrow beam, linearly polarized antennas and narrow band, non-directional patch antennas were used for the measurements. Figures 6.1 and 6.2 show the experiment set up with the narrow band, narrow beam antennas and the non-directional patch antennas, respectively.

The HP 8756A Scalar Network Analyzer was used in combination with the HP 778D Dual Directional Coupler so as to achieve normalization of the received signal to the Sweep Oscillator power level. In this way, errors caused by instability ("drift") of the Sweep Oscillator power level were eliminated. The SNA was configured to measure the magnitude of the "insertion loss" S_{21} , the ratio of powers of the transmitted (reference, channel R) and the incident (received, channel B) signals versus frequency, which was the goal of the experiment. However, the SNA was simultaneously measuring the "return loss" S_{11} , the ratio of powers of the transmitted (reference, channel R) and the reflected (channel B) signals versus frequency, for the sake

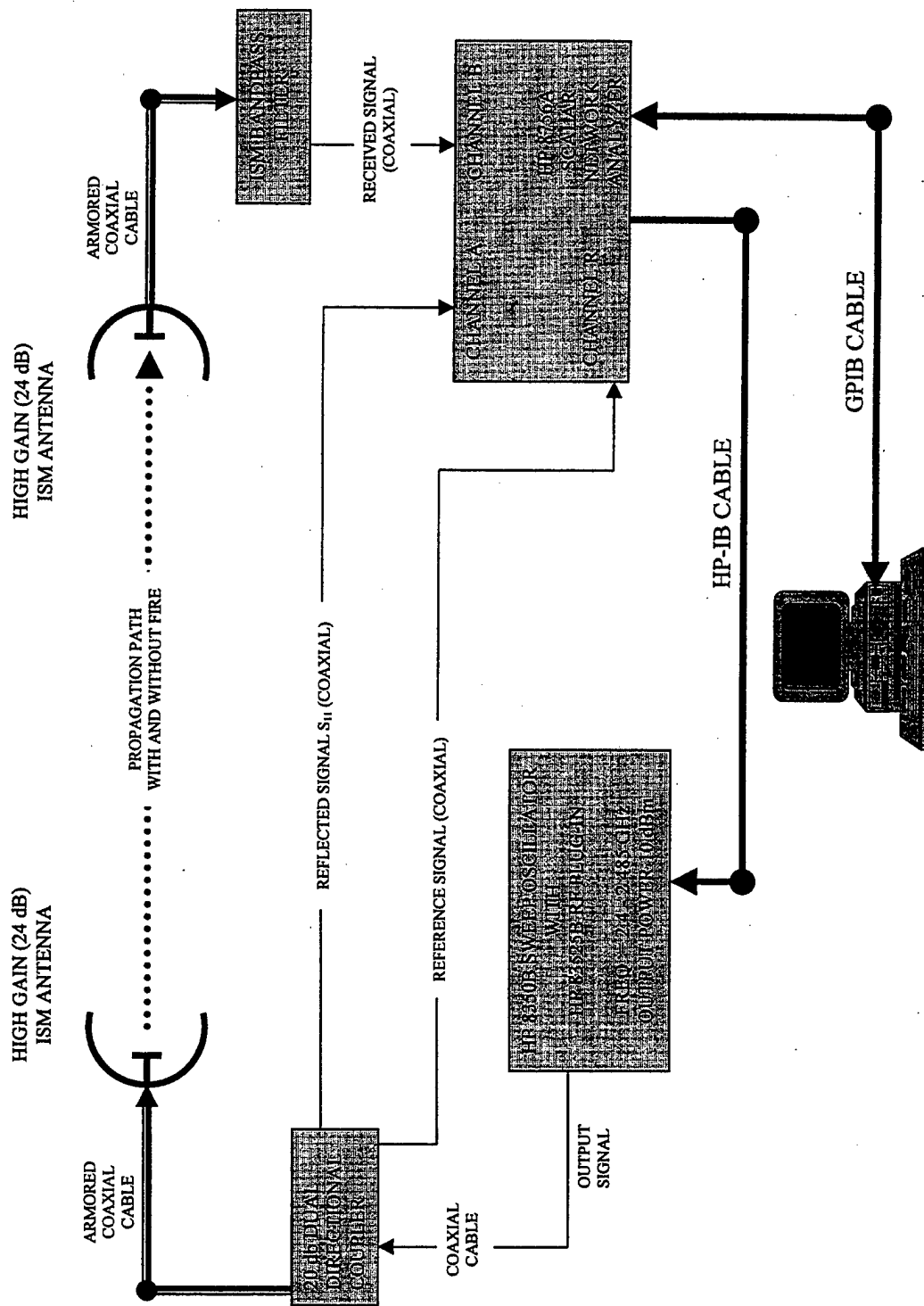


Figure 6.1: Measurement Setup Using High Gain Antennas.

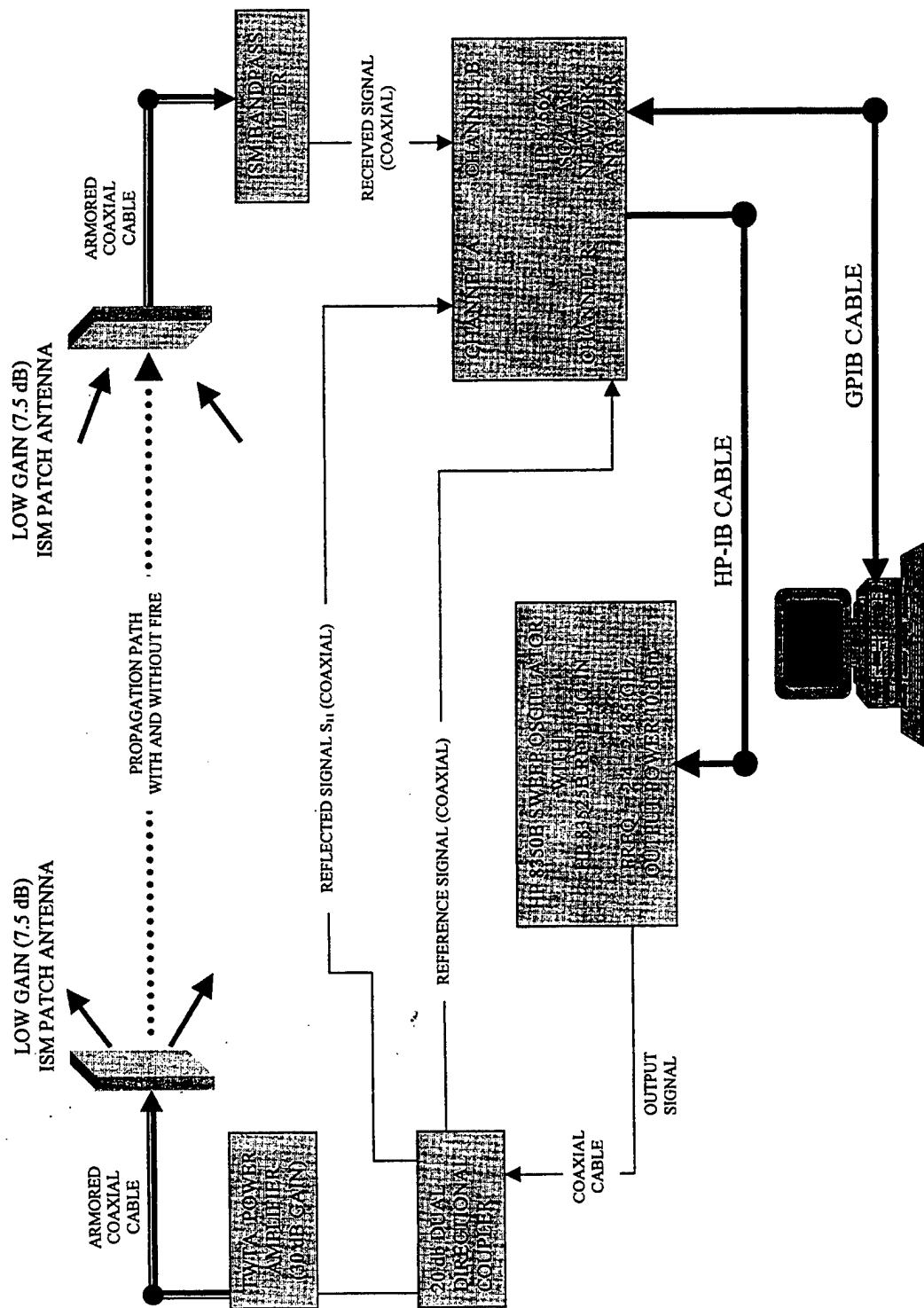


Figure 6.2: Measurement Setup Using Low Gain Antennas.

of completeness. The SNA measured 401 data points corresponding to 401 frequencies evenly distributed between 2.4 GHz and 2.485 GHz (frequency step of ~ 0.21 MHz).

The HP 8350A Sweep Oscillator with the HP 83525B RF plug-in was configured to "sweep" a 10 dBm signal every 0.8 sec over 2.4 GHz to 2.485 GHz frequency range. The signal passing through the Dual Directional Coupler was fed to the transmitting antenna through a heat-resistant, "armored" coaxial cable. The reference signal and the reflected signal, reduced both by 20 dB by the directional coupler were applied to channels R and A of the SNA respectively.

The signal received by the receiving antenna was fed to an ISM bandpass filter through an "armored" coaxial cable. The bandpass filter was centered at 2.442 GHz with 1 dB bandwidth of 85 MHz. The 50 dB rejection bands of the filter were from 0 to 2.365 GHz and from 2.523 to 5 GHz. The output of the ISM bandpass filter was applied to channel B of the SNA.

As mentioned before, two kinds of antennas were used for the SCFE. The Winncom parabolic grid directional antennas were linearly polarized with a gain of 24 dBi. Their frequency bandwidth was 2.4 - 2.485 GHz and they had 3-dB beamwidth of 7.5° . The Cushcraft DirectLink series patch antennas, were also linearly polarized and had a gain of 7.5 dBi. Their frequency bandwidth was 2.3 - 2.5 GHz and

they had 3 dB beamwidth of 50° and 65° for the E and H planes respectively. The antennas and their specification data are shown in Appendix A.

Before starting the actual SCFE measurements we used a HP8566B Spectrum Analyzer as a narrowband receiver to detect and measure any possible interfering signals (with the sweep oscillator turned off) in the 2.4 GHz to 2.485 GHz ISM band. The set up of this configuration is shown in Figure 6.3. No interfering signals of significant strength were detected in the course of the experiment.

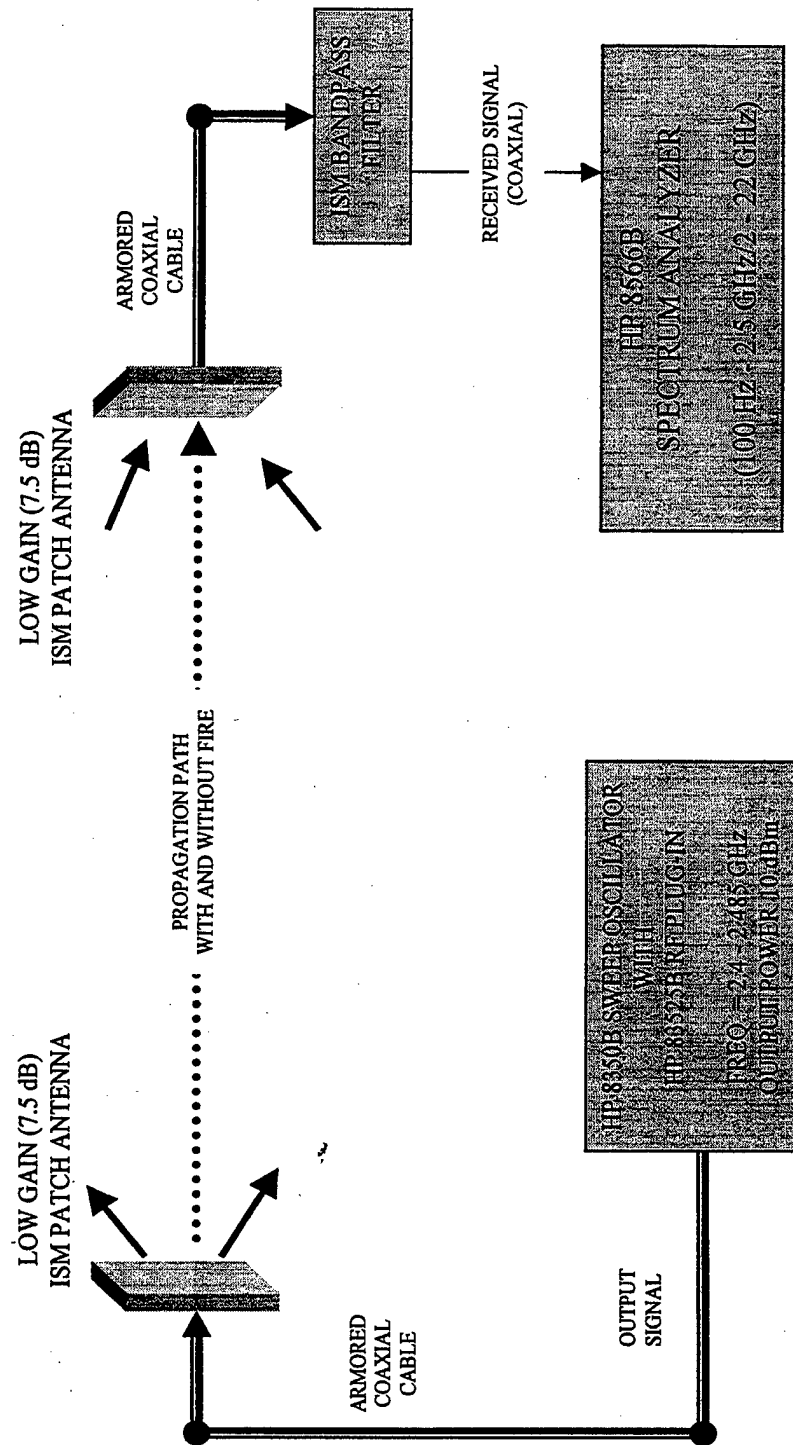


Figure 6.3: Measurement Setup Using Spectrum Analyzer.

B. DATA ACQUISITION/CONTROL SOFTWARE DESIGN

As mentioned above during the SCFE the scalar network analyzer was used to measure the magnitude of the insertion loss (S_{21}) between the transmitting and the receiving antennas. In order to control the instruments (SNA HP 8756A, Sweep Oscillator HP 8350A) and acquire the measured data from the SNA, a software program had to be developed. This program was developed in LabVIEW (Laboratory Virtual Instrument Engineering Workbench) and was run on a PC with a GPIB (General-Purpose Interface Bus) board installed.

1. General Purpose Interface Bus (GPIB)

The General Purpose Interface Bus (GPIB), also called IEEE 488, is a link, or interface system, through which interconnected electronic devices communicate. This is done by installing a plug-in GPIB board in the computer and then connecting the respective instruments directly to this board with a GPIB cable. The GPIB cable is a shielded 24-conductor cable, which has both a plug and a receptacle connector at each end, as shown in Figure 6.4. There are two ways of linking GPIB devices; linear or star configurations, shown in Figure 6.5 [Ref.20].

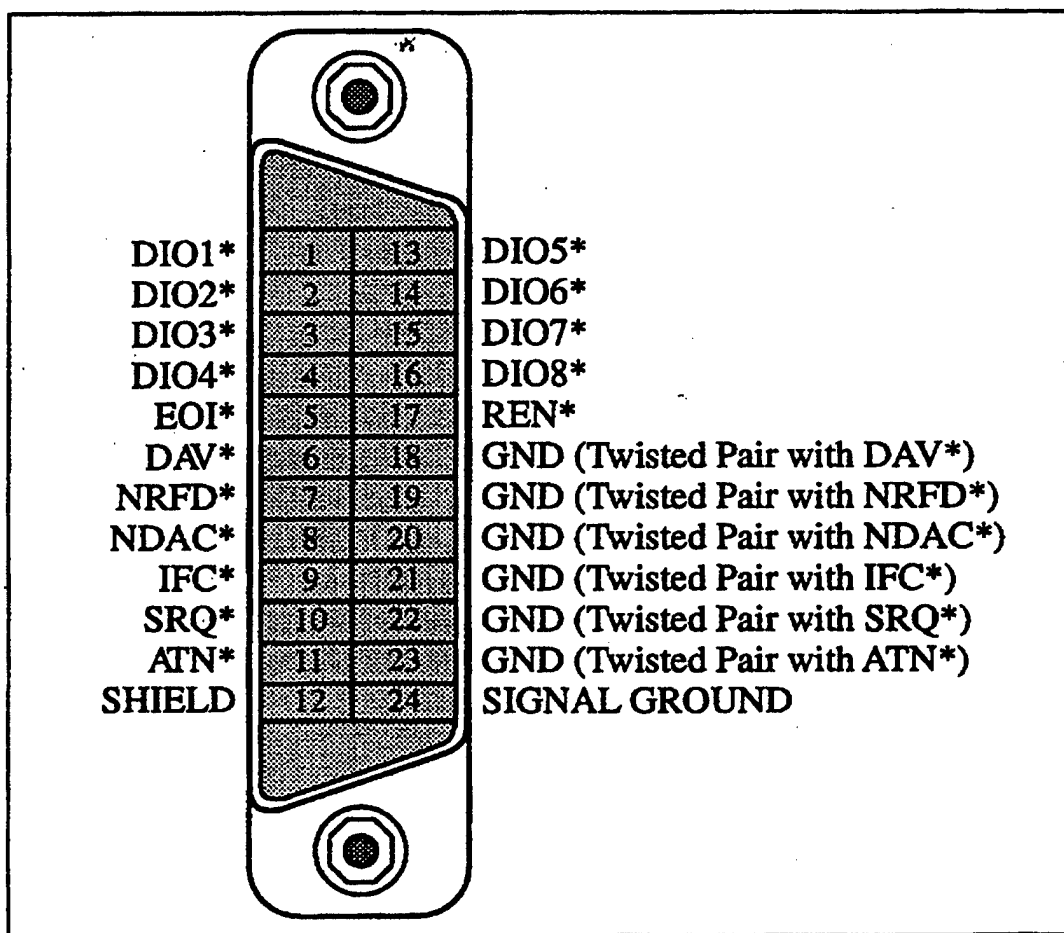


Figure 6.4: GPIB Connector Showing Signal Assignment.
From Ref.[20]

During SCFE linear linking configuration was used to connect the PC, the SNA, and the Sweep Oscillator. The SNA and the Sweep Oscillator were connected with HP-IB cable, which is the HP equivalent of the GPIB cable.

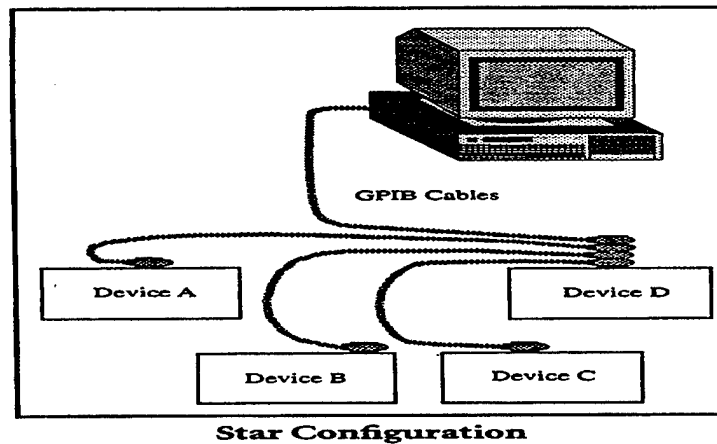
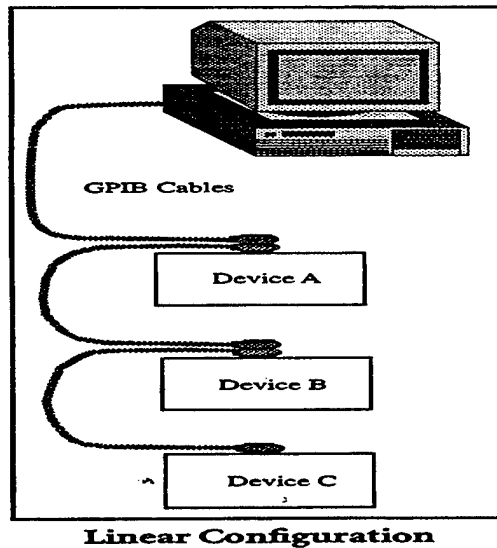


Figure 6.5: Linking GPIB Devices Together - Linear Configuration and Star Configuration. From Ref.[20].

The GPIB carries device-dependent messages and interface messages. GPIB devices can be Talkers, Listeners, and Controllers. The SNA in our case was a Talker and a Listener as well. The Controller manages the flow of information on the GPIB by sending commands to all devices.

With the GPIB interface board and its software, the computer played all three roles:

- Controller - to manage the GPIB
- Talker - to send data
- Listener - to receive data

In order to have control of the communication between the PC and the SNA, a program needed to be developed in LabVIEW.

2. LabView Program for Controlling the SNA and Acquiring the Measured Data

The software compiler used to develop the data acquisition and control software for this experiment was National Instruments "LabVIEW". A program was developed to control the SNA through the PC, and to display the data being measured, with a simultaneous storage of the data on the PC's hard disk for future processing.

LabVIEW is a powerful and flexible instrumentation and analysis software system. It departs from the sequential nature of the traditional programming languages and features a graphical programming environment and all the tools needed for data acquisition, analysis, and presentation. With this graphical programming language, called "G", we can program using block diagram approach. After we create the block diagram program, LabVIEW compiles it into machine code.

LabVIEW programs are called Virtual Instruments (VIs). A VI consists of a front panel and a block diagram. The front panel specifies the inputs and outputs and features the user interface for interactive operation. The LabVIEW compiler contains many library components to assist in programming; "for-next" loops, "while" loops, multiplication and min/max subroutines, string functions and more. "Behind" the front panel is the block diagram, which is the actual executable program. The components of a block diagram, icons, represent lower-level "instruments" and program control structures. We "wire" the icons together to create the software flow desired in the block diagram.

LabVIEW integrates data acquisition, analysis, and presentation in one system. An instrument library with drivers for hundreds of popular instruments simplifies instrument control applications. Because LabVIEW is graphical in nature, it is inherently a data presentation package. Output appears in the form of charts, graphs, and user-defined graphics. LabVIEW was chosen for our experiment because of its compatibility and ease of use with GPIB hardware.

The flow chart shown in Figure 6.6 depicts the data acquisition/control algorithm used in our experiment. The actual LabVIEW software program is shown in Appendix B.

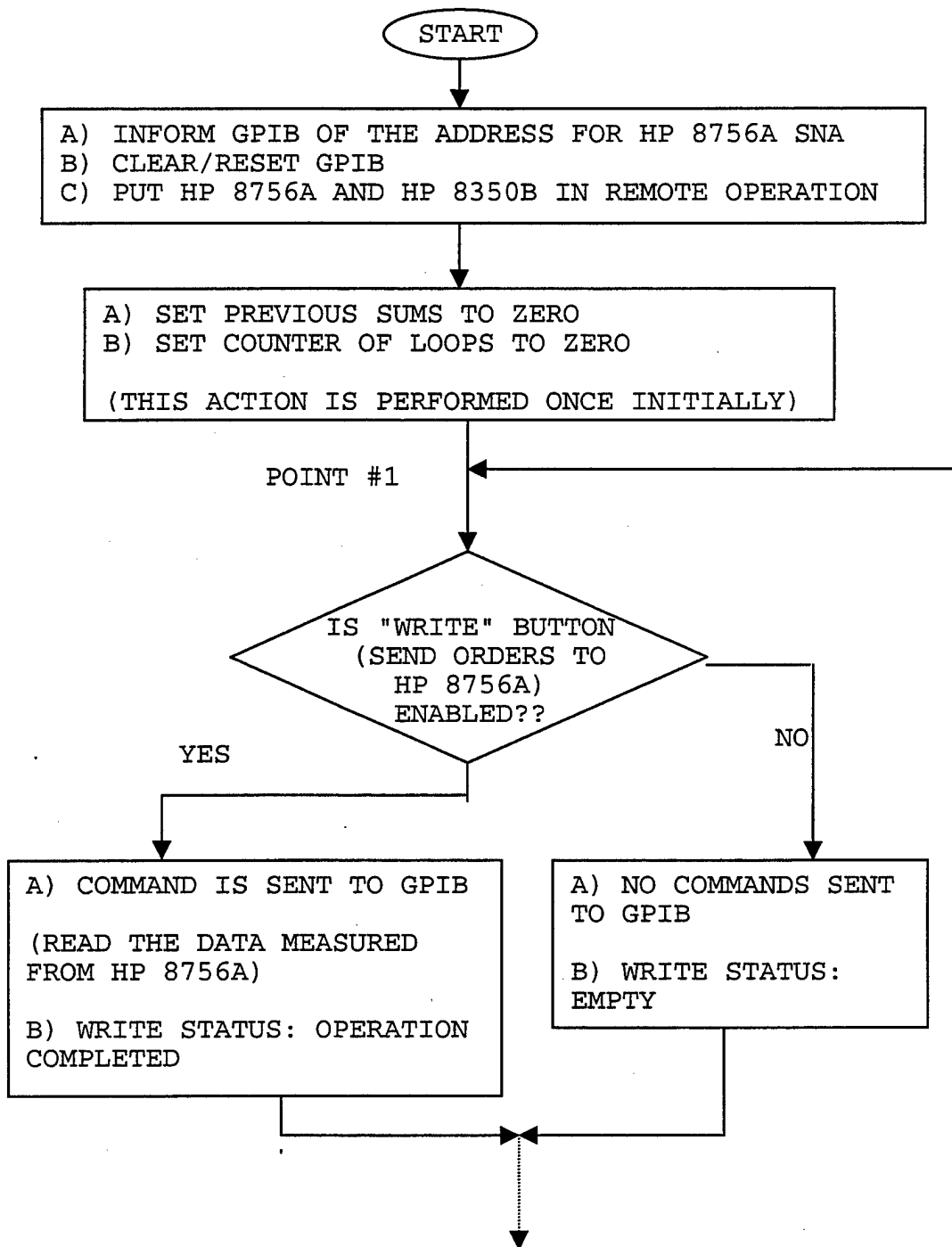


Figure 6.6 (A): Data Acquisition/Control Software Flow Chart.

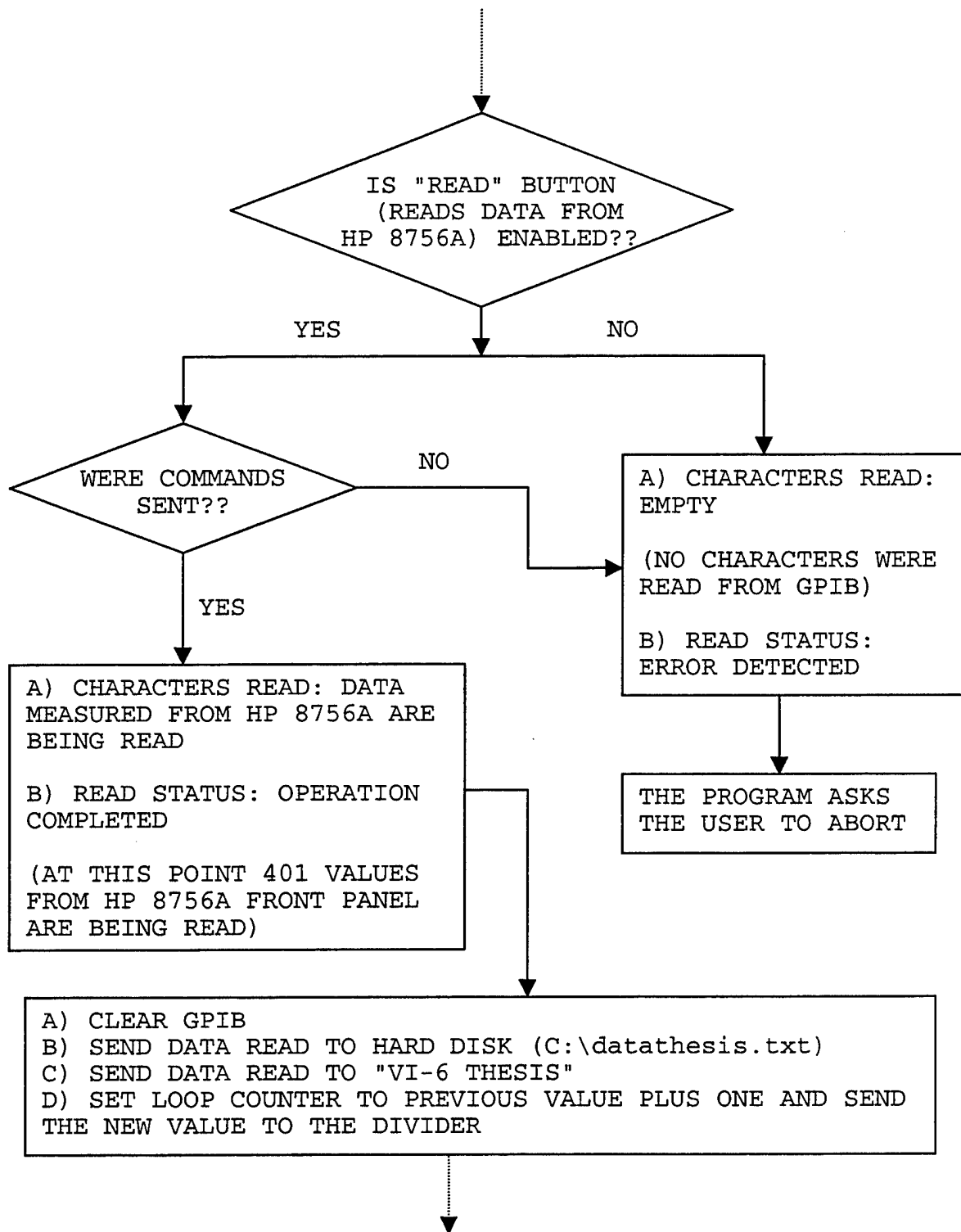


Figure 6.6 (B): Data Acquisition/Control Software Flow Chart.

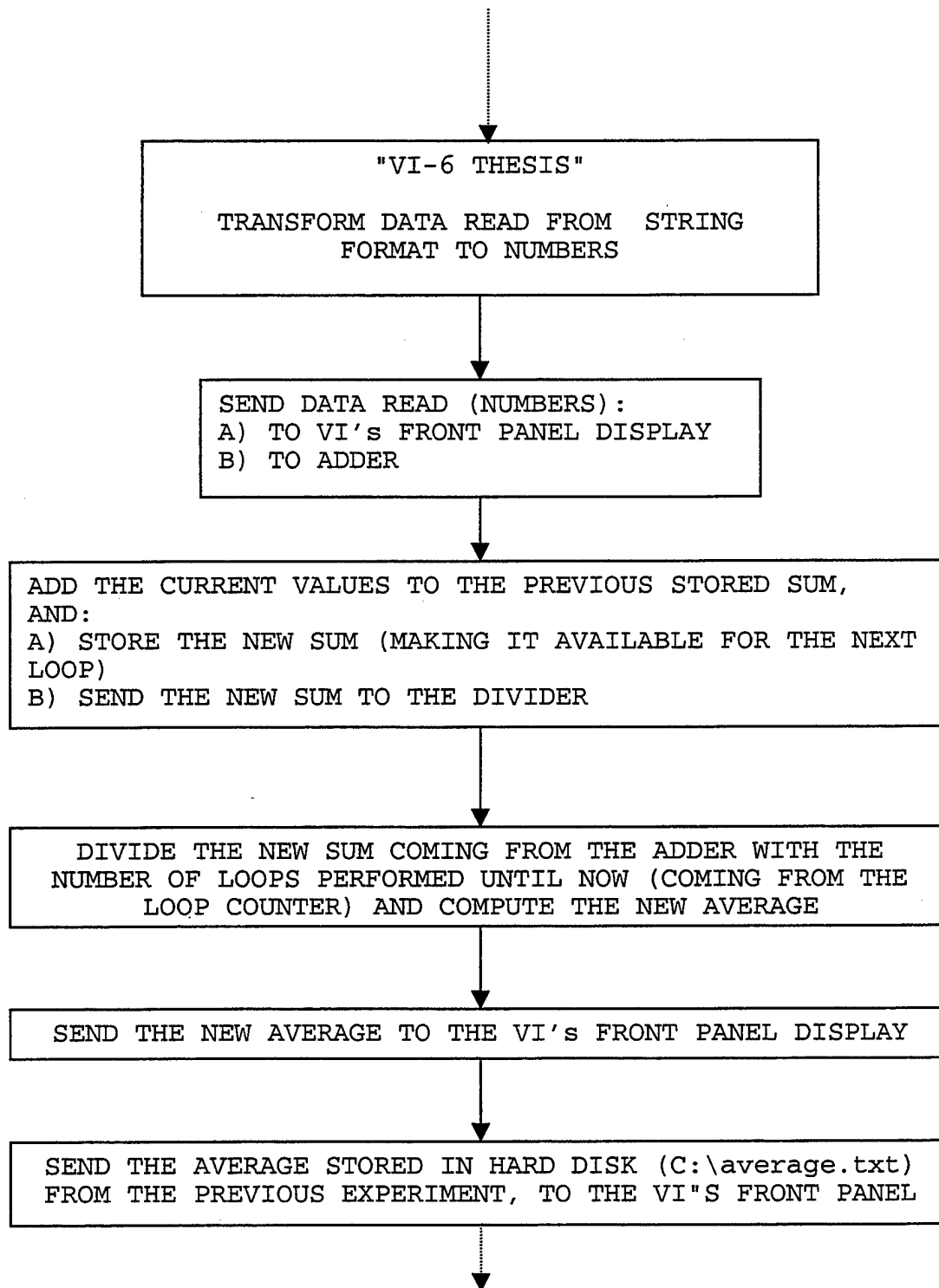


Figure 6.6 (C): Data Acquisition/Control Software Flow Chart.

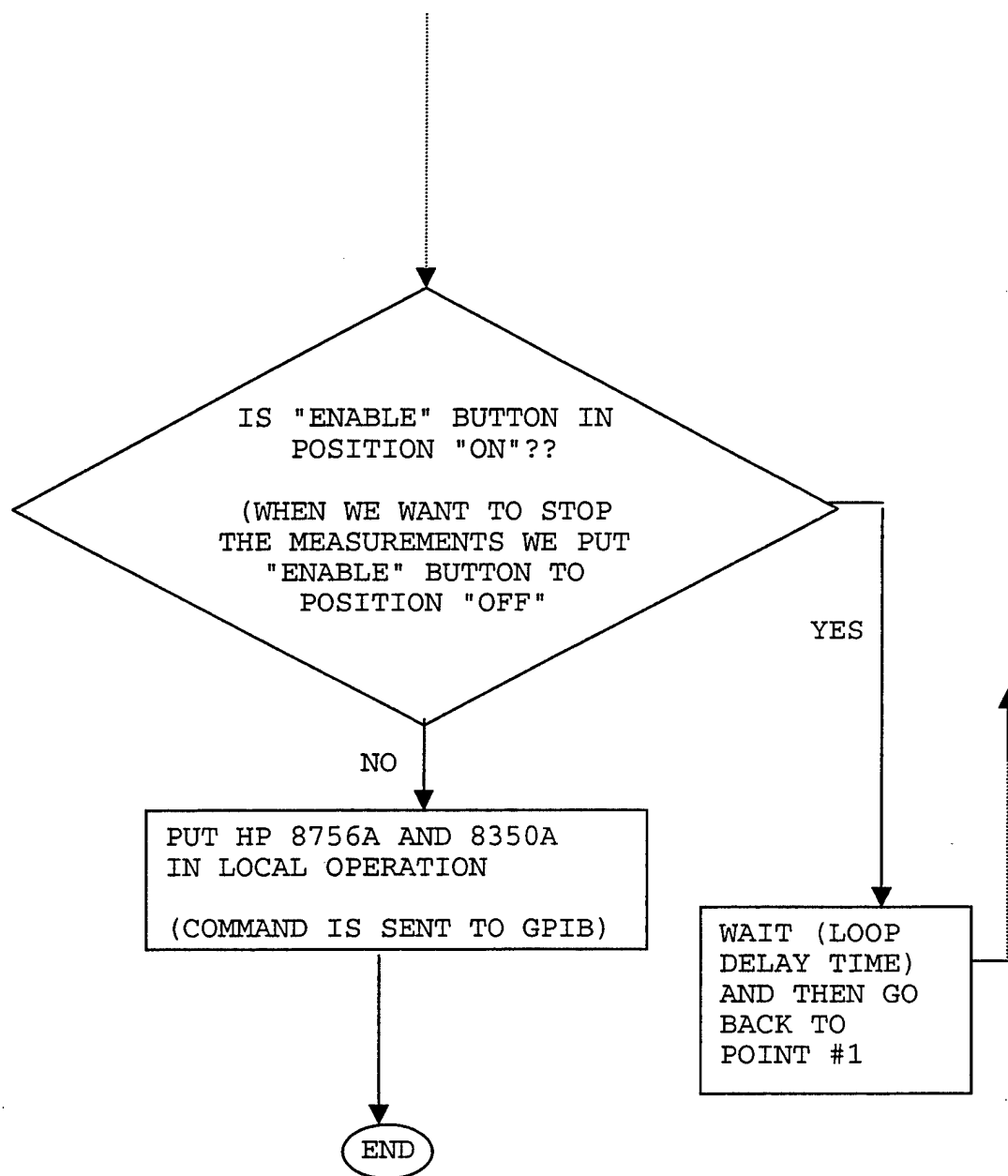


Figure 6.6 (D): Data Acquisition/Control Software Flow Chart.

VII. MEASUREMENT PROCEDURE

In this Chapter we will discuss the measurement procedure followed during the SCFE. The scenarios, including the different configurations of antennas, polarizations and fuel types used, in addition to the different compartment conditions (pre-fire, fire, mist, steam, ventilation) under which measurements were conducted are described.

The SCFE was performed onboard ex-USS SHADWELL, the Naval Research Laboratory's Advanced Fire Research Vessel in Mobile, Alabama. In Appendix C information about the ship and the measurement compartment is presented.

A. FUEL TYPE AND ANTENNA CONFIGURATIONS USED

The SCFE equipment setup and tests were conducted on Wednesday, May 12 of 1999, and the actual measurements took place on Thursday, May 13, and Friday, May 14 of 1999. On Thursday, May 13, all the measurements were conducted using diesel fuel, poured in a pan, as the "fire source". The diesel pan was approximately halfway between the transmitting and the receiving antenna. On Friday, May 14, the measurements were conducted using heptane as the "fire source". Heptane was sprayed from sprinklers scattered within the measurement compartment. These spray fires had

higher temperatures than the diesel fires, but much less smoke.

The attenuation in the 2.4 GHz to 2.485 GHz ISM band was measured using a pair of narrowband, narrow beam (high gain/directivity) linearly polarized antennas. The use of narrowband antennas helped us suppress out-of-band interference and the antenna directivity helped us suppress those paths that did not pass directly through fire. The attenuation was also measured using a pair of non-directional, low gain, patch antennas which are more representative of typical communications antennas for indoor use. For both types of antennas, two sets of measurements were conducted such that the attenuation through fire was measured for horizontal and vertical polarizations.

B. MEASUREMENT SCENARIOS

During SCFE measurements, data were taken at 401 frequencies from 2.4 to 2.485 GHz at the rate of 401 data points per 0.8 seconds. The transmitting and the receiving antennas were positioned, for all the runs, in the same place in the "simulated" machine space. The measurement equipment was set up in the "engineering station" compartment adjacent to the "machine" space where hydrocarbon fuel fires were set. The measurement and equipment compartments are shown in Appendix C.

1. Day One (Thursday, May 13) Measurements

As mentioned earlier, during this part of the experiment diesel pan fires were measured. Four runs (sets) of measurements were conducted during this first day. Each measurement run lasted approximately twenty minutes, and both high and low gain antennas were measured for both polarizations. Table 7.1 depicts these runs and the antennas and polarizations used in every run, in the order they were conducted.

Run #	Type of Antennas Used	Polarization
1	Parabolic Directional Antenna (High Gain)	Vertical
2	Parabolic Directional Antenna (High Gain)	Horizontal
3	Patch Antenna (Low Gain)	Vertical
4	Patch Antenna (Low Gain)	Horizontal

Table 7.1: SCFE Runs for the First Day of Measurements.

Every run started with a five-minute pre-fire "cold" measurement. This was done so as to have the reference data to compare with the fire data and extract the fire attenuation. After each cold run, measurements were taken with diesel fire lasting for about five minutes. Although ventilation was on during this phase, smoke was building up rapidly. Next, the ship's fire extinguishing system was turned on, and we had about two minutes of measurements with water mist. The water mist phase lasted only approximately

two minutes in order to minimize the water use and compartment flooding, as requested by the ex-USS SHADWELL management. During this phase the ventilation was off, and the measurement compartment was full of smoke, while steam was building up.

The measurements continued with compartment cooling which lasted approximately three minutes. During this phase the ventilation was on, the smoke was diluting, and the steam was liquefying. After the compartment had cooled, free of smoke and steam, post-fire measurements of approximately five minutes were taken to complete a "run". For each run, the pre-fire, fire, and post-fire data were stored in three different PC files for future processing.

2. Day Two (Friday, May 14) Measurements

On Friday, May 14, heptane spray fires were measured for the high gain antennas only, due to the limitation of time imposed by the NRL's personnel. Each heptane fire lasted approximately only one (1) minute. Longer duration would have damaged the ship's structure since heptane spray fires caused the metal in the compartment, in the vicinity of the flame to glow red-hot after only one minute. In order to acquire adequate data, the measurements were repeated four times without changing antennas and polarizations. In total, eight runs (sets) of measurements were conducted

during the second day. Table 7.2 depicts these runs and the antennas and polarizations used in every run, in the order they were conducted.

Run #	Type of Antennas Used	Polarization
1 through 4	Parabolic Directional Antenna (High Gain)	Horizontal
5 through 8	Parabolic Directional Antenna (High Gain)	Vertical

Table 7.2: SCFE Runs for the Second Day of Measurements.

On the second day we took pre-fire (cold) measurements, of five minutes duration each, two times: once with the antennas in Horizontally Polarized, and once with the antennas in vertical polarization. After these "cold" measurements, we conducted four identical fire/post-fire measurement runs for each polarization. Every run lasted approximately seven minutes and started with a one-minute heptane spray fire. During this phase, ventilation was on, and little smoke was building up. Next, the ship's fire extinguishing system was turned on, and we had about two minutes of measurements with water mist. During this phase the ventilation was off, there was some smoke in the measurement compartment, while steam was building up.

The measurements continued with approximately two minutes of compartment cooling without ventilation. The

smoke in the measurement compartment was diluting, and the steam was liquefying. Every run finished with approximately two minutes of compartment cooling with ventilation. During this last phase, the measurement compartment was almost free of smoke and steam. For each run, the pre-fire, fire, and post-fire data were again stored in three different PC files for future processing.

VIII.CODE DEVELOPMENT FOR DATA ANALYSIS

A. INITIAL REQUIREMENTS

During the two days of measurements approximately 10 million data samples were collected. These had to be manipulated in order to extract the statistical results. Due to the number of samples, the use of a computer was necessary. MATLAB programming language was chosen since it:

- is familiar to the user, and leads to a faster turnaround time
- offered extended capabilities for signal processing, with the use of the signal processing toolbox
- could be used on-site.

B. CODE DEVELOPED ON SITE

To achieve the best results the quality of the measurements taken had to be examined on the spot. In addition an early estimate of the effect of the fire was desirable. For this reason immediately after each set of measurements was taken, a basic statistical analysis was performed using a notebook PC with a jazz drive and MATLAB software. The analysis program was written on-site and it was used as the basis for the development of a more involved code after the measurements have been completed.

LabVIEW created large ASCII-delimited data files for the measurements. Reading such a file while running a MATLAB

code results in a very slow program. This dictated the need for a small MATLAB program that would read the ASCII delimited files and save them in a matrix form file (*.dat). This transformation was executed only once for each data file.

A fast way to examine the quality/consistency of the measurements was by evaluating the frequency average of the attenuation created by the fire or the fire extinguishing system as functions of time. The changes in average attenuation would indicate changes in the experiment conditions such as opening and closing of doors, change in the ventilation system, intrusion of a person in the signal propagation path; and so on.

The data analysis code was initially developed for the first set of measurements; the high gain vertically polarized antennas. For the remaining sets of measurements the length of the files and the points of the run phase changes (pre-fire, fire, water mist, steam buildup, post-fire or ventilation for the third day) had to be changed accordingly.

During the measurements three files were created for each antenna and polarization run. The first file contained the data collected during the pre-fire phase, the second file contained the data collected during the fire, water mist, and steam development, and the third file contained

the data taken after the evacuation (ventilation) of the compartment (for the diesel fire only). The MATLAB pre-processor code read the files and created a single matrix that included all the data. The data (insertion loss) were in dB units. The main signal analysis program first transformed the data to the linear form. Next the program calculated the gain created by the fire (and its byproducts). To accomplish this, the 5-minute pre-fire measurements of insertion loss were used as reference. The approximately 400 samples that were taken for each of the 501 frequencies in the 2.4-2.485 GHz range were averaged across time giving 501 averaged pre-fire values, one for each frequency. These 501 values were used as the denominators for each "time row" of the matrix of data for the fire and post-fire phases. Finally the gain after the ventilation/evacuation of the compartment was calculated to verify that the measured figures were close to the pre-fire ones. This was done to ensure the integrity of the measurements, since a large deviation would indicate that there was a change in the initial conditions due to:

- A possible cable/connector failure.
- Change in the compartment parameters, such as open doors, antenna position changes.
- Antenna failure due to the exposure to high temperatures, etc.

The new matrix containing the gain in linear form was then transposed. By taking the mean of the matrix the frequency average across time was obtained. These values were then transformed back into dB units and plotted versus time. Additionally the inverse values were plotted showing the attenuation created by the fire.

C. DEVELOPMENT OF THE STATISTICAL ANALYSIS CODE

The MATLAB statistical analysis code, whose listing is given in Appendix D, was developed such that it would have the following characteristics:

- Provide the needed statistical analysis results
- Have the ability to analyze all the sets of measurements
- Be user friendly such that anyone could analyze the data without any assistance

The structure of the code was influenced by the way the experiments were performed. During the diesel fire experiments there was only one set of measurements for each antenna for each of the two polarizations, while on the other hand, there were four sets of measurements for the heptane fire. The programs developed reflect this difference but nevertheless present the same type of statistical data for both diesel and heptane fires, allowing for

straightforward comparison. The code consists of the following task-oriented sections:

- Selection of the measurements set according to the type of fire, type of antennas and polarization
- Initialization phase
- Estimation of the attenuation
- Surface plots
- Frequency averaging
- Time averaged attenuation versus frequency
- Probability density functions
- Frequency response autocorrelation functions
- Estimation of frequency difference with least total attenuation
- Temperature plots
- Temperature/Attenuation correlation

1. Selection of the Measurements Set According to the Type of Fire, Type of Antennas and Polarization.

The first step is the selection of the fire type, antenna type, and polarization to be analyzed. The user is first asked to select either diesel or heptane fire. The selection is performed with a menu that has the two choices. After the selection, depending on the choice, the code proceeded to one of the two sub-programs: one for the diesel fire experiments and the other for the heptane fire experiments. The user is next asked to choose the type of

antennas and either the vertical or the Horizontally Polarized. The choices are different for each type of fire since different sets of measurements were performed.

2. Initialization Phase

After the user had selected the type of fire, antennas, and polarization the code read the corresponding data files and created MATLAB variables accordingly. For the diesel fire experiments a single column "matrix" is sufficient for the data. On the other hand for the heptane fire experiments a four column data matrix is needed because each experiment was repeated four times for heptane fires.

3. Estimation of the Path Loss / Attenuation

a) Diesel Fire

The data from each experiment is read from three data files into three matrices. The first matrix contains the path loss data (in dB) for the pre-fire phase, the second the path loss data for the fire, water mist, and steam build-up phase, and the third the path loss data after the ventilation of the compartment. From these, three new matrices with data in linear "units" are created. A single matrix containing all of the data in linear form was created. This matrix was used to calculate the attenuation. Next the gain for the fire is calculated. To accomplish

this, the 5-minute pre-fire measurements were used as a reference as described in section VII B. A single matrix is also created containing all the gain data in dB. In addition three matrices are created containing the gain in linear units, one for each phase (fire, water mist, and steam).

b) Heptane Fire

For the Heptane fire measurements we had four of each of the files and matrices referenced in VIII c(3)(a). Our approach was to take the average of the four matrices representing four repetitions of the same measurement. Since the length of each phase ("cold", fire, mist, steam, and ventilation) was somewhat different for the four "repetitions", to create our average matrix we took as the length of each phase the shortest of the four. In this way the elements of our averaged matrices were always the averages of the four elements that correspond to the same frequency and relative time in the phase of a particular run. From this point on the procedure for calculating different statistical quantities is the same for the diesel and heptane fires.

4. Surface Plots

To visualize the effects of the fire and to quickly examine the quality of our data, 3D plots were created for

the path loss and the attenuation, selecting the x-axis as time, y-axis as frequency, and z-axis as the path loss or attenuation. 3D plots allow us to determine the continuity and consistency of the data taken. They also show effectively any changes in the experiment conditions such as opening and closing of doors, change in the ventilation system, or intrusion of a person in the antenna beam. In the program the user is also given the choice of having planes parallel to the yz plane drawn to indicate the transition from one phase of the run to the next.

5. Estimation of Frequency Averages

The estimation of the attenuation was performed rather simply. The matrix containing the gain in linear form was transposed. Averaging each column of the new matrix produced the frequency-averaged gain as a function of time. The reciprocal of the resulting single row matrix was transformed in dB units. To obtain the estimation of the path loss required an additional step of converting the path loss data from linear form to dB.

The plots that also indicate the transition points from one phase to the next. In addition each phase had a different color suggesting the physical conditions of the experiment (blue for the "cold" phase, red for the fire etc).

6. Estimation of Time Averages

To estimate the time-average attenuation for each phase the mean of the matrices that contained the data for each individual phase was evaluated. The resulting values are divided by the time and frequency average "cold gain" and the fire "depth" and transformed into dB units. For the path loss the division with the average "cold" gain was omitted. The results are plotted, for each phase of both the heptane and the diesel fires.

7. Estimation of the Density and Distribution Functions

The next step was to estimate the probability density functions (pdf) and the cumulative distribution functions (cdf). To estimate the probability density function the histogram command is applied to the attenuation matrix, creating the probability density function estimates for each phase. Also, the probability density function estimate for the entire experiment is obtained by applying the histogram command to the matrix containing the data for all the phases of the experiment. Applying the cumulative sum command to the probability density function the cumulative distribution functions estimates are obtained. An error check is also performed to confirm that the highest cdf value is equal to 1.

8. Estimation of the Frequency Response Autocorrelation Functions

To estimate the frequency response autocorrelation function the linear gain data matrix was used. Four individual gain matrices were created each containing the data for a single phase. The next step was to take the Fast Fourier Transform (FFT) of the attenuation matrix. Averaging the magnitude of the FFT matrix and performing the Inverse Fast Fourier Transform (IFFT) an estimate of the frequency response autocorrelation function is obtained. The results were plotted individually for each phase and also for the entire experiment.

9. Estimation of Frequency Difference with Least Total Attenuation.

The frequency difference with the smallest combined time-average attenuation is calculated from the measured data. To decrease the computational time the time-averaged attenuation for all phases is first calculated. A "nested" loop is used, with the outer loop selecting frequencies and the inner loop selecting a frequency difference, taking into account that the higher the chosen frequency was, the lower the upper limit of the frequency difference should be, such that the two frequencies are always within data frequency range. The "scan" is performed across all frequencies and the sum of attenuations that correspond to the same

frequency difference is averaged. The averaged attenuation is plotted versus the frequency difference, indicating which frequency difference has the least average attenuation.

10. Temperature Plots

During the experiments temperature readings were recorded for all cases except for the measurements of the patch antennas. For the diesel fire the temperature data during the fire were plotted on the same graph versus time for a number of locations. For the heptane fire measurements, since each experiment was repeated four times, with fire duration of at least one-minute, the averages of the four temperature data sets were calculated and plotted as functions of time.

11. Correlation Between Temperature and Attenuation

The degree of correlation between the temperature increase and the frequency averaged attenuation increase is also of interest. Since the number of samples for the temperature and the attenuation taken over the same phase were not the same, an interpolation is performed to create arrays of the same size. For the temperatures, the mean temperature is subtracted from the temperature data matrix giving a matrix that contains only the temperature variations around the mean (the time varying component of the temperature). The same procedure is followed for the

frequency-averaged attenuation giving us the attenuation variation around the mean as a function of time. A "running average" is also performed to eliminate the rapid (noise-like) fluctuations of the attenuation.

A coefficient for each element of the time varying attenuation matrix is calculated by dividing the attenuation by the element of the time varying temperature matrix corresponding to the same time instant. Next, the time-averaged coefficient is calculated. Finally, each time-varying temperature data array was multiplied by the average coefficient to create arrays of "attenuation" calculated from the temperature data.

If the temperature and fire were perfectly correlated the rms error between the measured attenuation and the attenuation calculated from the fire temperature data would have been zero (the smaller the rms error, the better the correlation between the temperature and the attenuation). The time varying attenuation calculated from the temperature data and the measured attenuation are plotted on the same graph as functions of time.

IX. RESULTS FOR DIRECTIONAL ANTENNAS

In this chapter we present the (measured and processed) data for the four sets of measurements involving diesel and heptane fires and directional (high gain) antennas.

A. DIESEL FIRE

There are two sets of measurements for the diesel fire with the directional antennas:

- for vertical polarization and
- for Horizontally Polarized

1. Vertical Polarization

a) *Path Loss for Vertically Polarized, Directional Antennas*

First the measured path loss is presented as a surface plot with the x-axis as the time axis, the y-axis as the frequency axis and the z-axis for the path loss in dB. In Figure 9.1 the path loss plot is shown for the vertically polarized directional antennas. In this figure we have also shown the phase boundary planes. From the plot we see that initially we have an approximately five minutes of the pre-fire phase. For this phase the time has negative values going from -5 up to 0. At $t=0$ diesel fire and its measurements begin. The fire lasts for approximately five minutes (minutes 0-5) followed by a two minute water mist

phase (minutes 5-7) and five minute mist build-up phase (minutes 7-12). Finally we note approximately five minutes of the post-fire-phase.

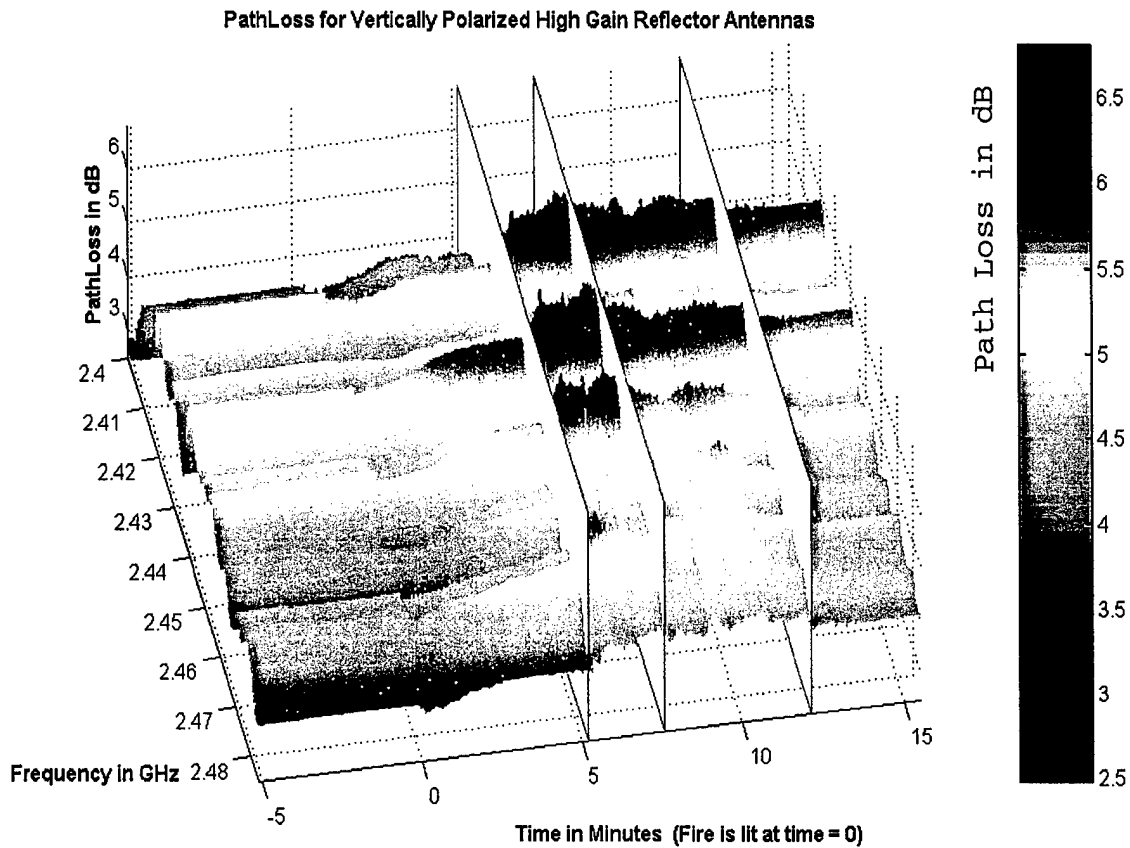


Figure 9.1: Path Loss for Vertically Polarized High Gain Antennas

In Figure 9.2 the same surface plot is shown without the phase boundaries. We note the continuity between the fire, water mist and steam build-up phases and a

discontinuity between the pre-fire phase and the fire phase ($t=0$) and between the steam build-up and the post-fire phase ($t=12$). These discontinuities are caused by the "interruptions" in the measurement process to allow for the personnel movement in the compartment to light the fire (at $t=0$) and inspect the completion of the particular experiment run (at $t=12$). Measurements taken during these activities would not be valid since the attenuation changed with people moving between the antennas.

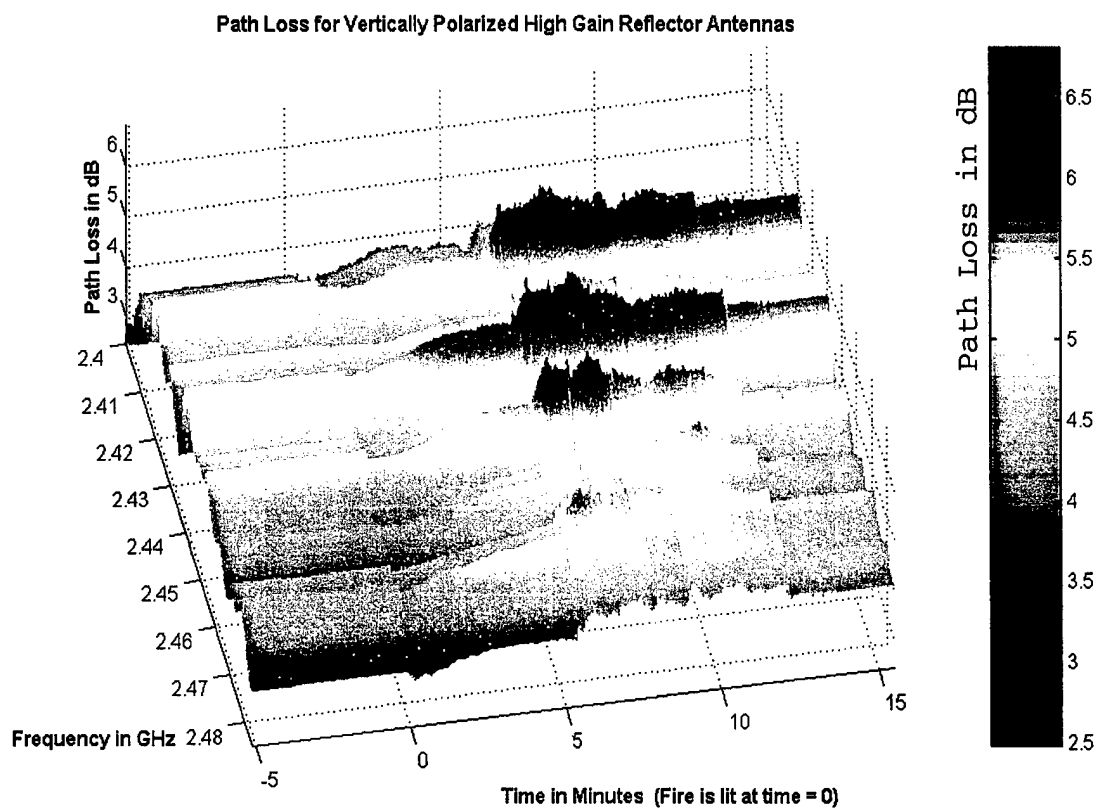


Figure 9.2: Path Loss for Vertically Polarized High Gain Antennas

In Figure 9.3 the "bird's eye" view of the path loss is presented. This allows us to visualize how the path loss changes with time and frequency. We note that for the five-minute pre-fire phase the path loss at each frequency has a constant value with time but is different for different frequencies. The path loss differences are mainly caused by the reflection/absorption characteristics of the portion of the compartment that is "visible" (within the main beam) to the two antennas.

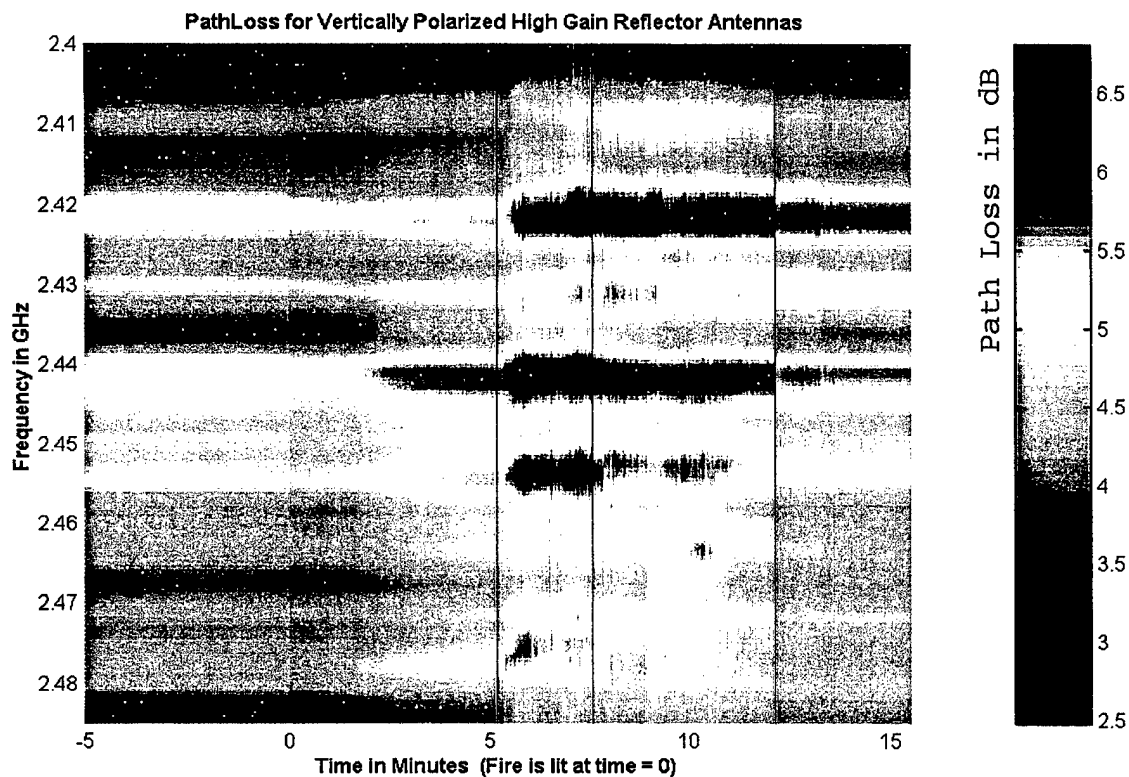


Figure 9.3: Path Loss for Vertically Polarized High Gain Antennas

After the fire has been lit the path loss increases gradually for all frequencies. The path loss reaches its peak during the water mist phase and then it starts falling again during the mist build-up phase. The highest measured value of the path loss was 6.5 dB. After the compartment ventilation the path loss values are significantly lower than the ones during the fire phase but higher than the values of the pre-fire phase because of the residual condensation in the compartment and on the antennas. Also, from Figure 9.3 we can see that the minima and maxima of the path loss do not shift appreciably along the frequency axis (the vertical direction) from one phase to the next. (This is a consequence of using directional antennas.)

**b) Attenuation for Vertically Polarized,
Directional Antennas**

We next present the attenuation surface plots. To create these plots we divided each path loss value by the time-averaged pre-fire phase path loss at the corresponding frequency. For this particular run there was a relatively large discontinuity between the pre-fire and fire phase ($t=0$) due to the door located behind one of the antennas that was open during the pre-fire phase and closed during

the fire phases (the door was used to get access to the compartment by the person starting the fire. To compensate for this path loss discontinuity we subtracted 0.2dB from the pre-fire values, thus eliminating the attenuation discontinuity at $t=0$. The result was then divided by the distance between the antennas to obtain the attenuation per unit length. The choice of the distance to obtain the attenuation per unit length (dB/m) requires some explanation. We selected the distance between the antennas (rather than the fire "depth") for the following reasons:

- The fire depth was ambiguous and changing with time
- The smoke and heat were distributed throughout the compartment and not confined to the "flame" region only
- The antennas were placed close to the fire source (as close as the compartment geometry and the maximum temperature that the antenna could sustain permitted)
- The distance between the antennas was 7.66 meters and the fire pool depth was 1 meter

In Figure 9.4 the attenuation surface plot for the vertically polarized directional antennas is shown with the phase boundary planes. For the pre-fire phase (time between

-5 and 0 minutes) the attenuation is approximately 0 dB/m, as we would expect since we used the time-averaged path loss for the pre-fire phase as the reference for each frequency. Therefore, during the pre-fire phase there are no "peaks and valleys" in the surface plot.

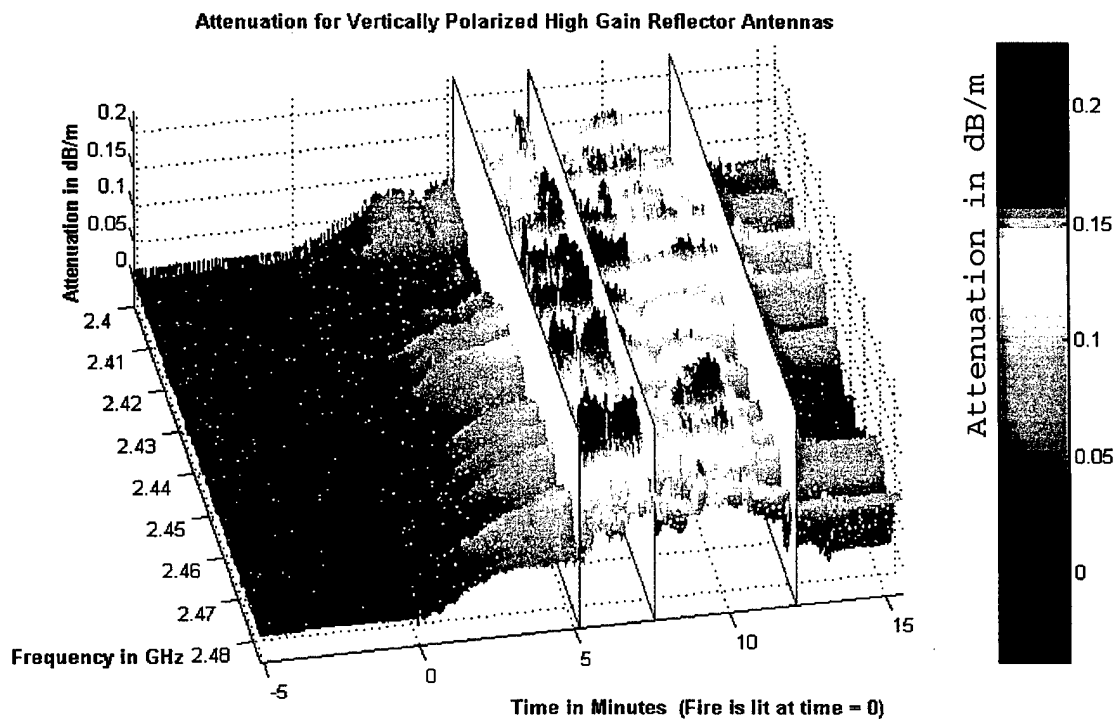


Figure 9.4: Attenuation for Vertically Polarized High Gain Antennas

In Figure 9.5 the same surface plot is shown but without the phase boundaries. We note a gradual increase in attenuation during the fire phase, as the heat and smoke build-up in the compartment. At about 5 minutes after the fire was lit (from minutes 5-7) there is an abrupt increase

in attenuation caused by the activation of the water mist fire-extinguishing system. After two minutes of fire extinguishing the compartment is saturated with steam and smoke (from minute 7 to 12) and the attenuation remains relatively high (but not as high as during the fire-extinguishing phase). Upon ventilation of the compartment the attenuation decreases (from minute 12 on) towards the values prior to the fire (for negative time).

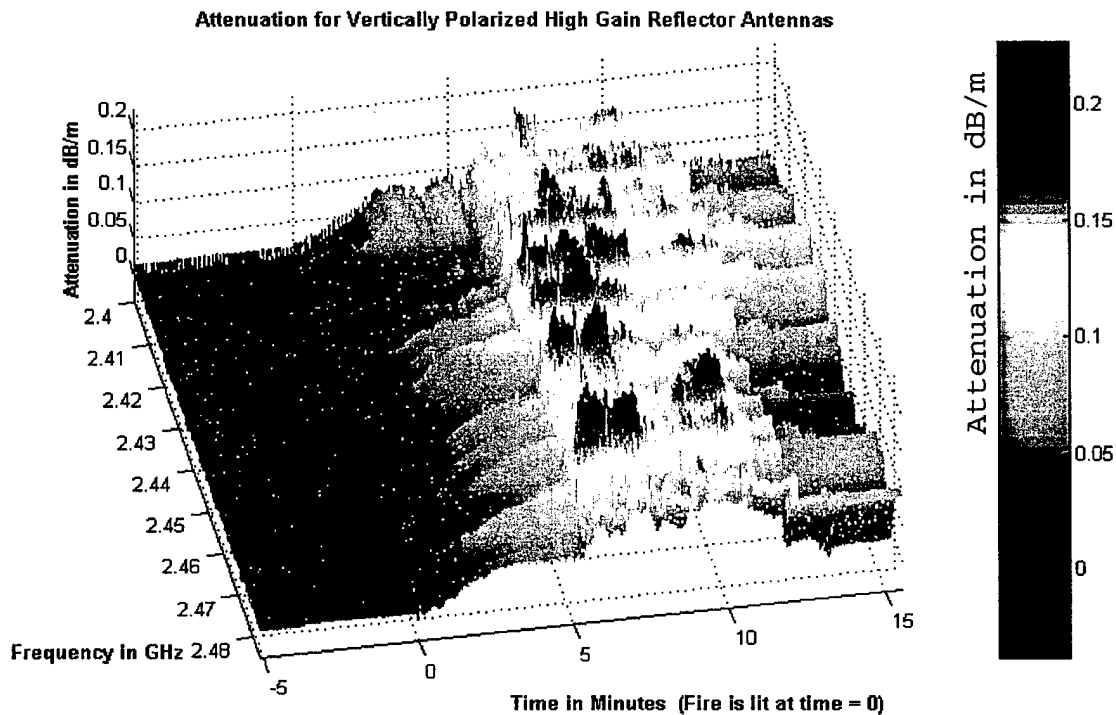


Figure 9.5: Attenuation for Vertically Polarized High Gain Antennas

In Figure 9.6 the same surface plot is shown, viewed directly from the z-axis (the "birds-eye" view) clearly showing the attenuation changes for different phases and for

different frequencies. The attenuation per meter reached its maximum value during the water mist fire-extinguishing phase and (for particular frequencies) it was on the order of 0.2 dB/m. The maximum attenuation for the fire phase was on the order of 0.09 dB/m.

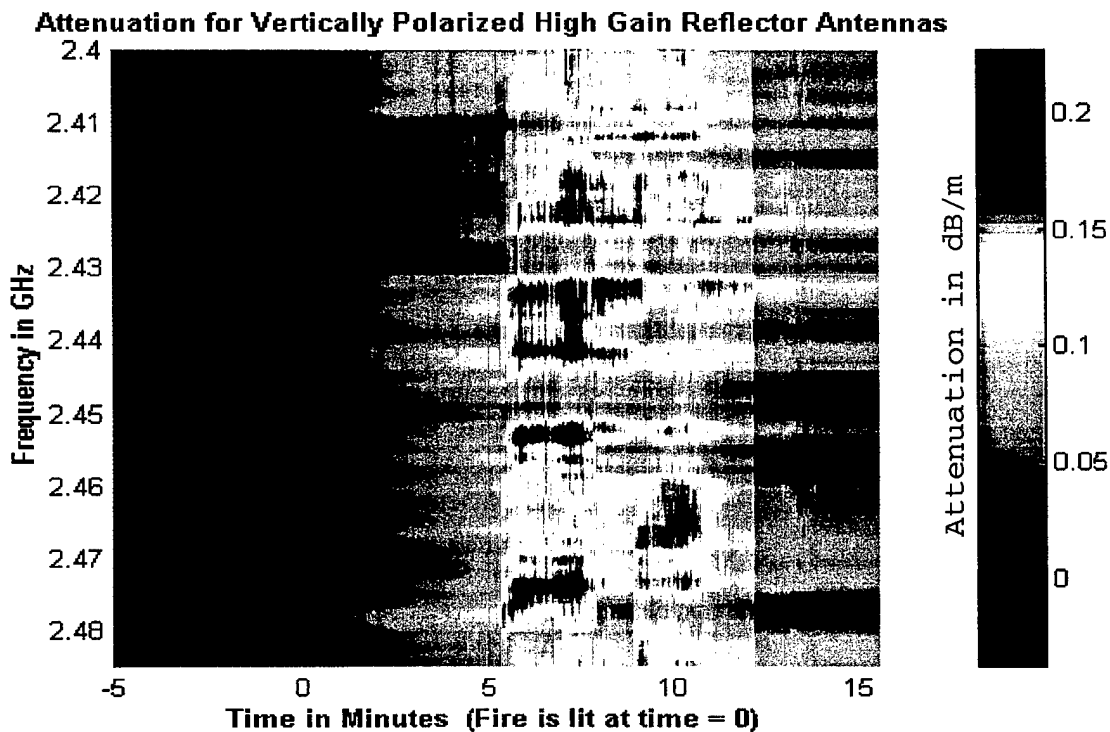


Figure 9.6: Attenuation for Vertically Polarized High Gain Antennas

c) Frequency-Averaged Path Loss for Vertically Polarized Directional Antennas

The first statistical analysis we performed was to determine the frequency-averaged path loss. As shown in Figure 9.7 the frequency-averaged path loss for the pre-fire phase is almost constant at around 4.3 dB. A discontinuity is also visible at $t=0$ between the pre-fire and the fire phase. As already mentioned this was due to the

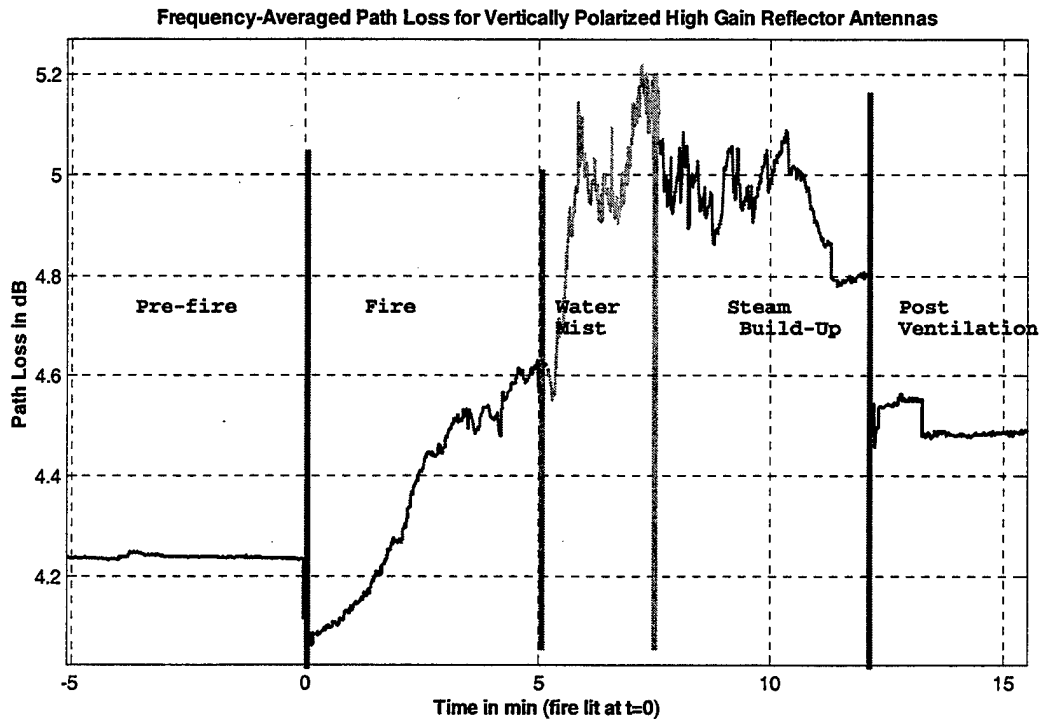


Figure 9.7: Frequency-Averaged Path Loss for Vertically Polarized High Gain Antennas

door located behind one of the antennas that was open during the pre-fire phase and closed during the fire phases (the

door was used to get access to the compartment by the person starting the fire). After the fire was lit the frequency-averaged path loss increased with time. The rate of increase was not constant and it depended on the fire intensity and the ventilation arrangement during this phase. After the water mist system was turned on the frequency-averaged path loss increased rapidly. During this phase the frequency-averaged path loss reached its peak value of ~ 5.2 dB. The averaged path loss started to decrease slowly during the steam build-up phase. Again there is a discontinuity between the steam build-up phase and post-fire phase. This is due to the fact that the post-fire phase measurements were taken approximately ten minutes after the steam build-up phase had ended, the steam was evacuated from the compartment, and the safety personnel inspected the compartment. The frequency-averaged path loss for the post-fire phase is almost constant at about 4.5 dB (slightly higher than for the pre-fire phase). Also during the post-fire phase we can see a change in the compartment (caused by opening or closing of the compartment doors) causing small but abrupt path-loss changes, on the order of 0.2 dB.

d) Frequency-Averaged Attenuation for Vertically Polarized Directional Antennas

Our next step was to determine the frequency-averaged attenuation in dB/m. The shape of the frequency-averaged attenuation as a function of time is the same as for the path loss, except of the elimination of the discontinuity at $t=0$, as shown in Figure 9.8. The only difference between the frequency-averaged attenuation and the frequency-averaged path loss is the division by a constant distance. The maximum frequency-averaged attenuation is approximately 0.15 dB/m. During the fire phase the frequency-averaged attenuation did not exceed 0.07 dB/m.

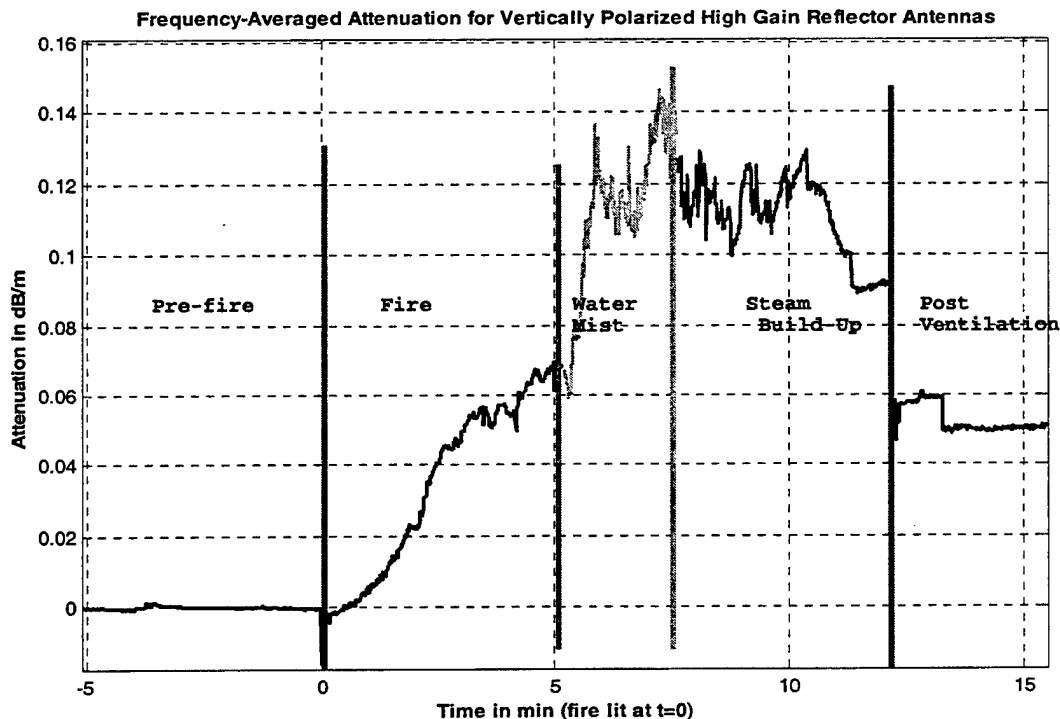


Figure 9.8: Frequency-Averaged Attenuation for Vertically Polarized High Gain Antennas

After the water mist fire extinguishing system was turned on there was a small drop in attenuation (0.01 dB/m) because the smoke and fire were nearly instantaneously suppressed. However as the steam started building up the attenuation increased, reaching its maximum value after about 1.5 minutes, before starting to decrease slowly as the temperature and the steam density gradually decreased.

e) *Temperature vs. Time for Vertically Polarized Directional Antennas*

The temperature taken at five different locations in the compartment is shown in Figure 9.9 as a function of time. The highest temperature curve is the flame temperature at the fuel pan level. (This temperature curve is actually the average of three sets of temperature data taken at three different locations at the fuel pan level.) We note that the temperature rapidly rises to about 600° C and remains around that value for the fire duration. The small fluctuations occur due to changes in the fire conditions such as ventilation rate, smoke density, etc. The next highest temperature curve is for the data taken at an elevation of 11 feet and at the horizontal distance of 3 feet from the fuel pan. The maximum temperature is approximately 200° C. The third highest curve is for the data taken at the height of 7ft and for the horizontal distance from the fuel pan of 3 feet. The maximum temperature at this height is 120° C.

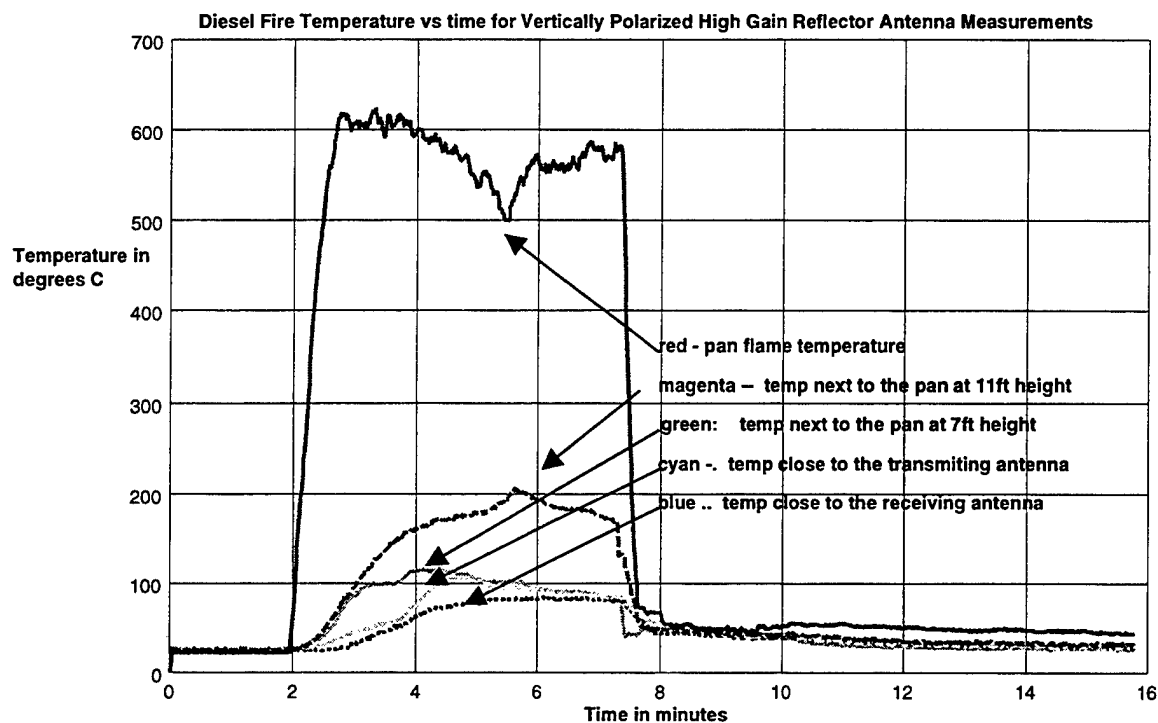


Figure 9.9: Diesel Fire Temperature versus Time for Vertically Polarized High Gain Antennas

The two lowest curves are for the temperature next to the two antennas. We note that the temperature next to the transmitting antenna reached a maximum of approximately 110° C and that the temperature next to the receiving antenna reached the maximum of approximately 90° C. The antennas withstood these temperatures (for fires of short duration) without damage.

**f) Scaled Attenuation and Temperature vs. Time
for Vertically Polarized Directional Antennas**

Our next objective was to determine if there was a relation between the temperature increase close to the antennas and the attenuation increase. To accomplish this we subtracted the mean values from the attenuation and the temperature data. Next we determined an average coefficient which, when multiplied with the time-varying temperature data, would yield the best "curve fit" for the time-varying attenuation. A very close relationship between the temperature increase and the attenuation increase is evident in Figure 9.10.

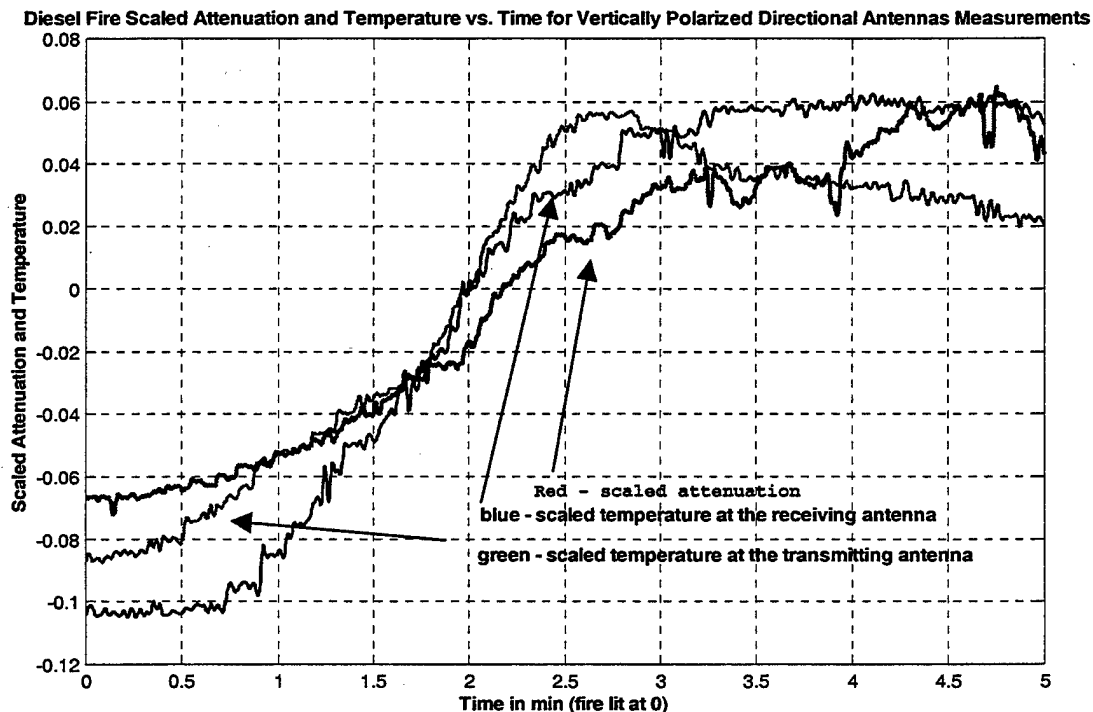


Figure 9.10: Diesel Fire Scaled Attenuation and Temperature versus Time for Vertically Polarized High Gain Antennas

g) Diesel Fire Time-Averaged Path Loss for Vertically Polarized Directional Antennas

Our next step was to calculate the time-averaged path loss for the fire phase. As shown in Figure 9.11 the time-averaged path loss ranged between about 2.7 and 5.5dB, a variation (with frequency) of close to 3dB. The plot also shows the minimum and maximum values of path loss for each frequency component. The maximum path loss occurs at 2.442 GHz and the minimum path loss occurs at 2.403 GHz.

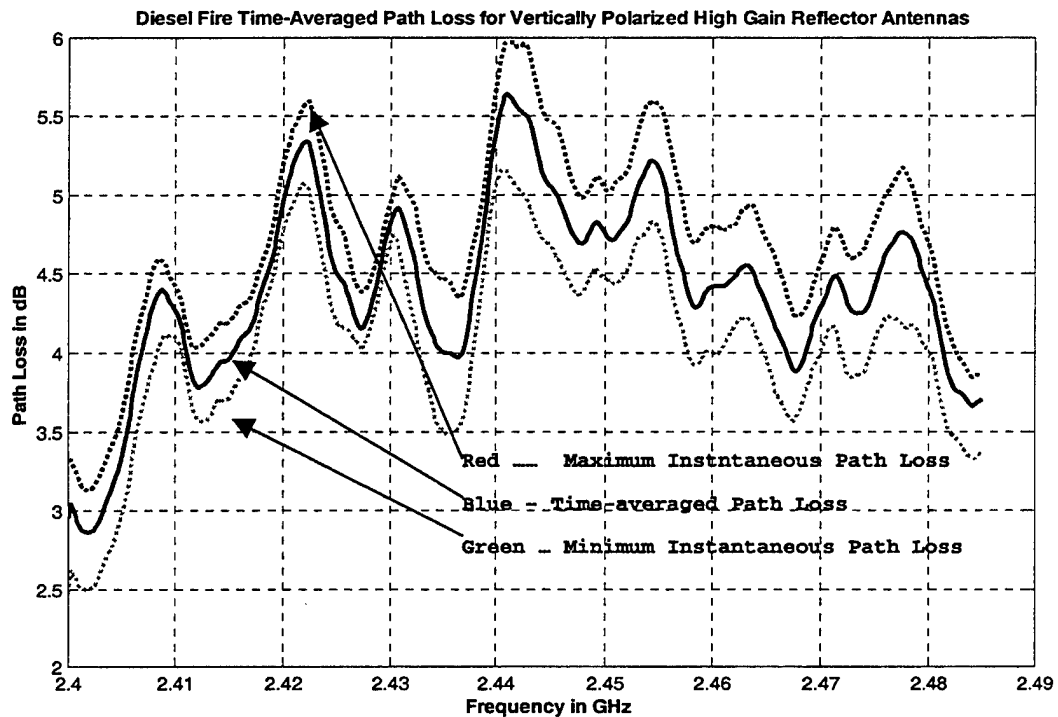


Figure 9.11: Diesel Fire Time-Averaged Path Loss for Vertically Polarized High Gain Antennas

The maximum and minimum path loss curves follow the time-averaged attenuation curve, that is the zero slope points for all three curves are located at the same frequencies.

In Figure 9.12 the time-averaged path loss for the fire and the pre-fire phases are shown in order to assess the effects of fire. Again the minima and maxima of the path loss are located at the same frequencies. This indicates that there is no change in the propagation characteristics of the compartment due to the fire except that there is an increase between 0 and 0.5 dB (depending on the frequency) of the time-averaged path loss, caused by the fire.

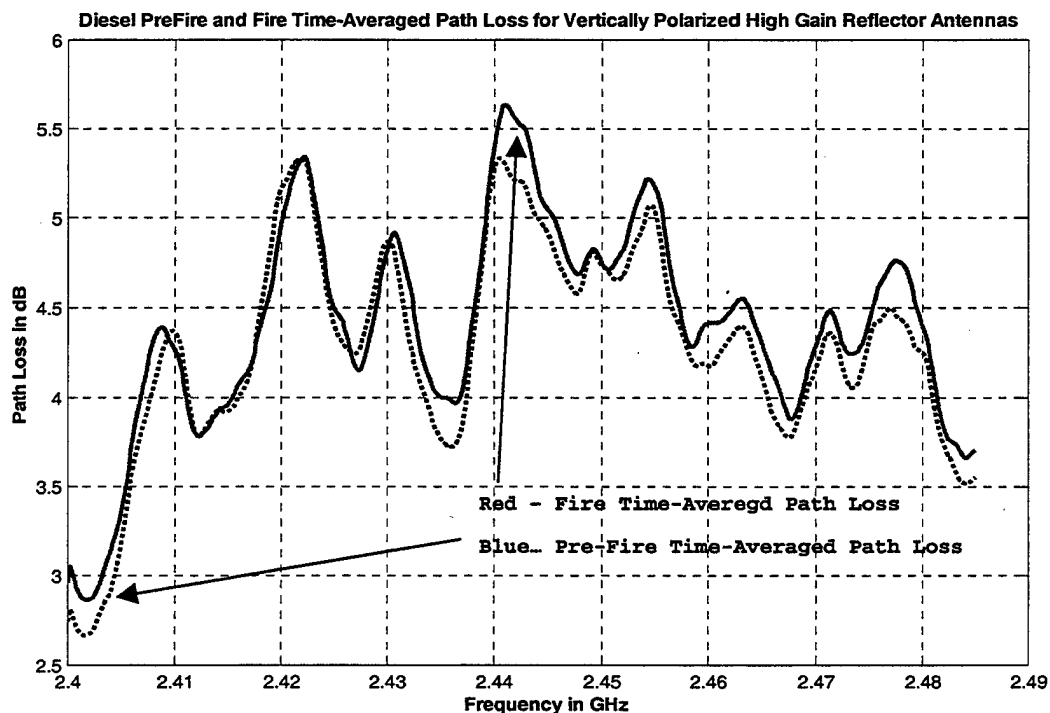


Figure 9.12: Diesel Pre-Fire and Fire Time-Averaged Path Loss for Vertically Polarized High Gain Antennas

h) Diesel Fire Attenuation for Vertically Polarized Directional Antennas

The time-averaged attenuation per meter for the fire phase is shown in Figure 9.13. The maximum attenuation again occurs at 2.442 GHz. The maximum time-averaged attenuation is about 0.065 dB/m. The minimum attenuation for most frequency components is below the 0 dB axis indicating a small gain of less than about 0.02 dB/m.

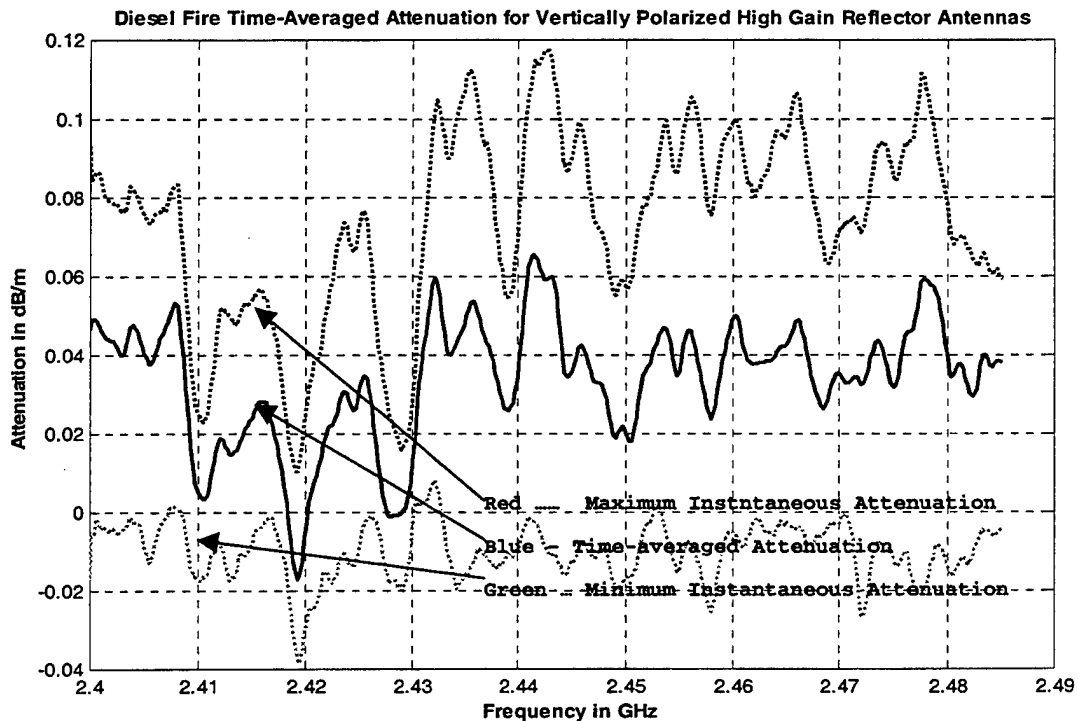


Figure 9.13: Diesel Fire Time-Averaged Attenuation for Vertically Polarized High Gain Antennas

i) Water Mist Phase Time-Averaged Path Loss for Vertically Polarized Directional Antennas

Our next step was to calculate the time-averaged path loss during the water mist phase. As shown in Figure 9.14 the time-averaged path loss ranged between 3.4 and 6.3 dB, again a variation of close to 3dB. The maximum time-averaged path loss of 6.6 dB occurs at 2.442 GHz and the

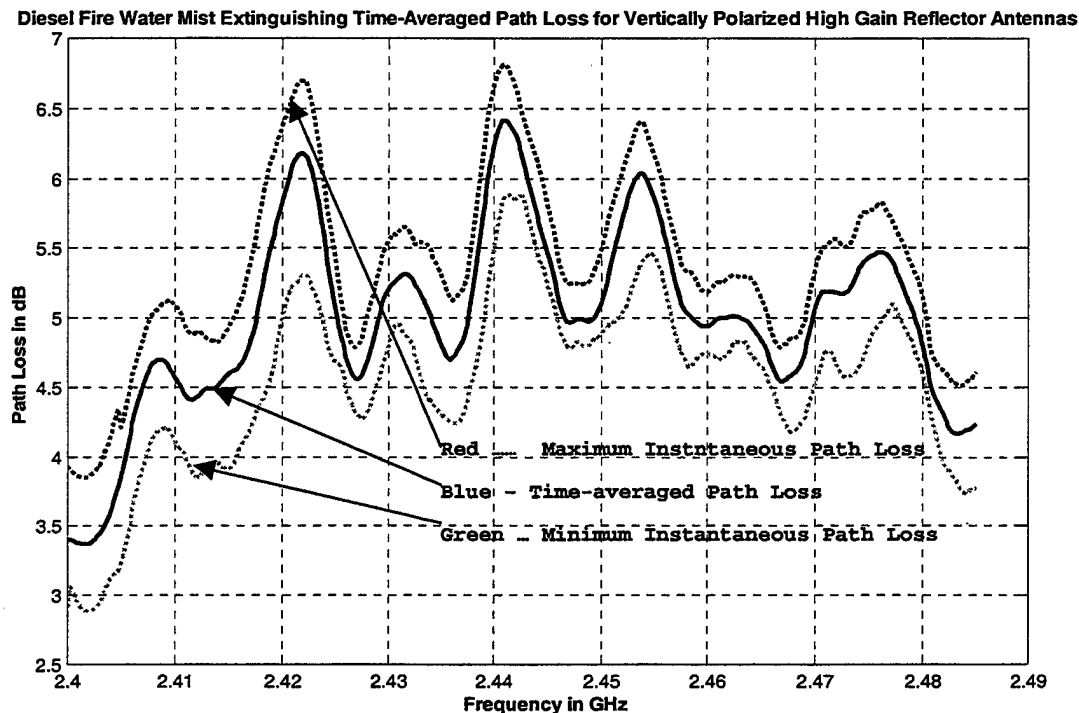


Figure 9.14: Diesel Fire Water Mist Extinguishing Time-Averaged Path Loss for Vertically Polarized High Gain Antennas

minimum path loss of 2.7 dB occurs at 2.403 GHz, the same frequencies as for the fire phase. Also, the zero slope points for all three curves (min, max and average path loss) occur at the same frequencies.

The time-averaged path loss curves for the water mist and the pre-fire phases are shown in Figure 9.15. Again the zero slope points are located at the same frequencies. This indicates that there is no change in the compartment

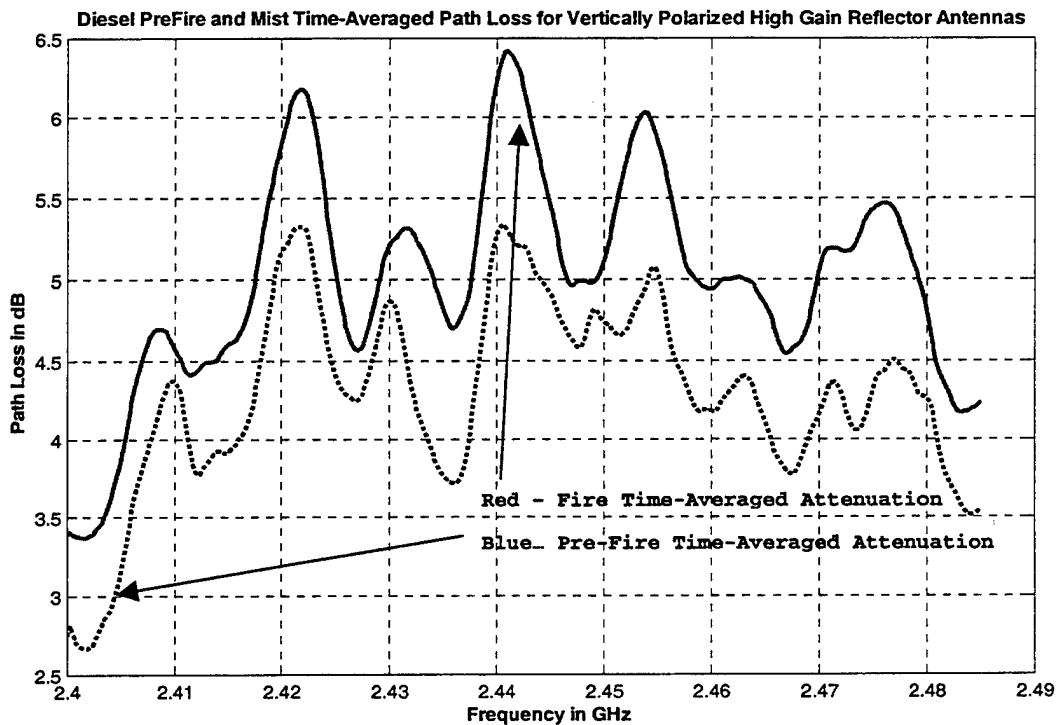


Figure 9.15: Diesel PreFire and Mist Time-Averaged Path Loss for Vertically Polarized High Gain Antennas

propagation characteristics between the two phases, the only difference being that for the water mist phase there is an increase of 0.5 to 1dB for the time-averaged path loss.

j) Water Mist Time-Averaged Attenuation for Vertically Polarized Directional Antennas

The time-averaged attenuation per meter for the water mist phase is shown in Figure 9.16. The time-averaged attenuation ranges between 0.07 and 0.18 dB/m. The maximum instantaneous attenuation of 0.22 dB/m occurs at 2.433 GHz.

Diesel Fire Water Mist Extinguishing Time-Averaged Attenuation for Vertically Polarized High Gain Reflector Antennas

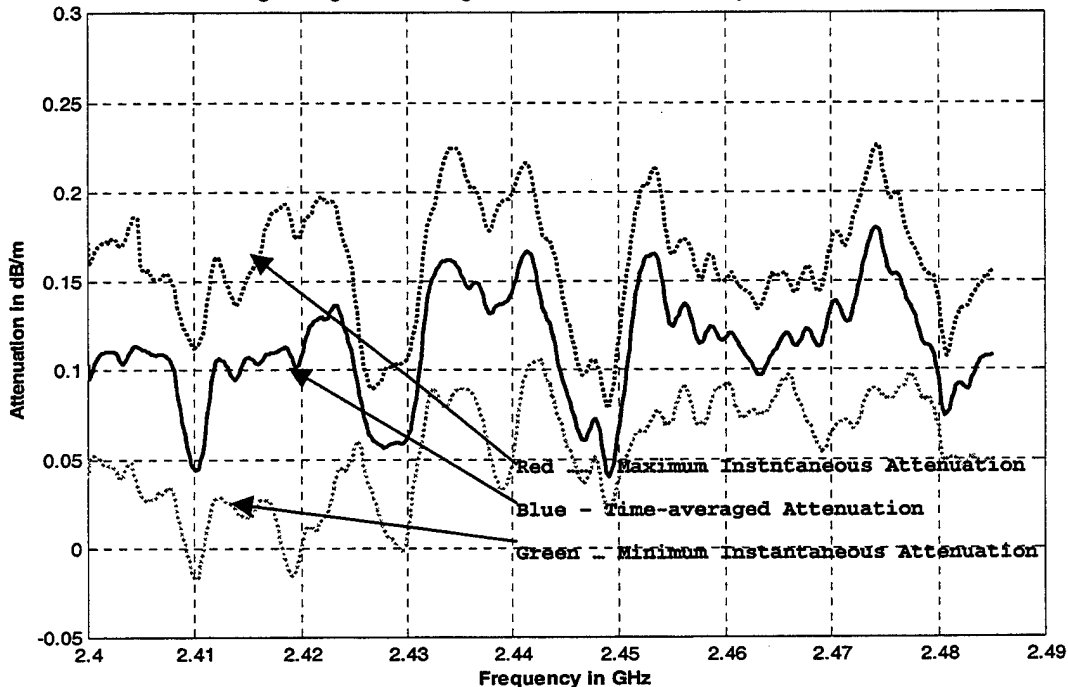


Figure 9.16: Diesel Fire Water Mist Extinguishing Time-Averaged Attenuation for Vertically Polarized High Gain Antennas

k) Steam Build-Up Phase Time-Averaged Path Loss for Vertically Polarized Directional Antennas

Next we calculated the time-averaged path loss for the steam build-up phase. As shown in Figure 9.17 the time-averaged path loss ranged between 3.2 and 6.2 dB, again a 3dB variation. Also shown on the same plot are the minimum

and maximum values of the path loss for each frequency. The maximum path loss of 6.5 dB occurs at 2.442 GHz and the minimum path loss of 3.2 dB occurs at 2.403 GHz, the same frequencies as for the fire phase. Again the zero slope points for all three curves are located at the same

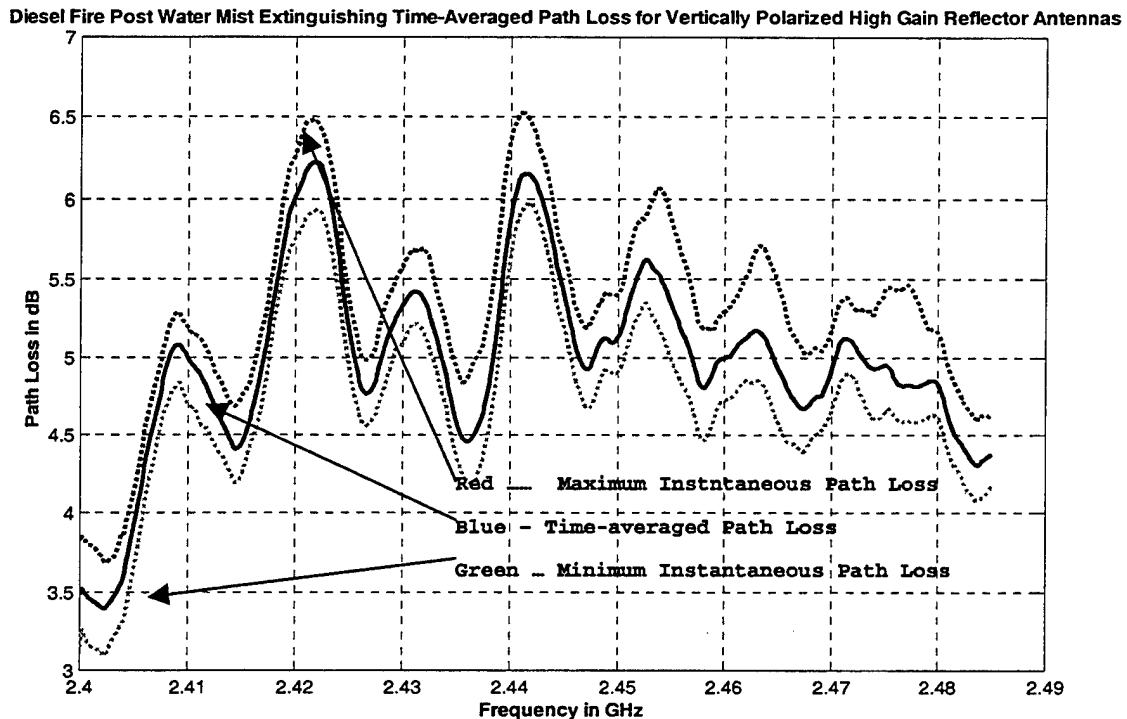


Figure 9.17 Diesel Fire Post Water Mist Extinguishing Time-Averaged Path Loss for Vertically Polarized High Gain Antennas

frequencies, indicating that the "frequency response" for the path between the antennas does not change depending on whether there is fire or water mist in the compartment except for the path loss increase or decrease ("scaling").

In Figure 9.18 the time-averaged path loss curves for the water mist and the pre-fire phases are shown. Again

the zero slope points (maxima and minima) are located at the same frequencies. This indicates that there is no change in the compartment propagation characteristics except for the additional path loss of between 0.8 and 1.3 dB due to the steam and residual smoke in the compartment.

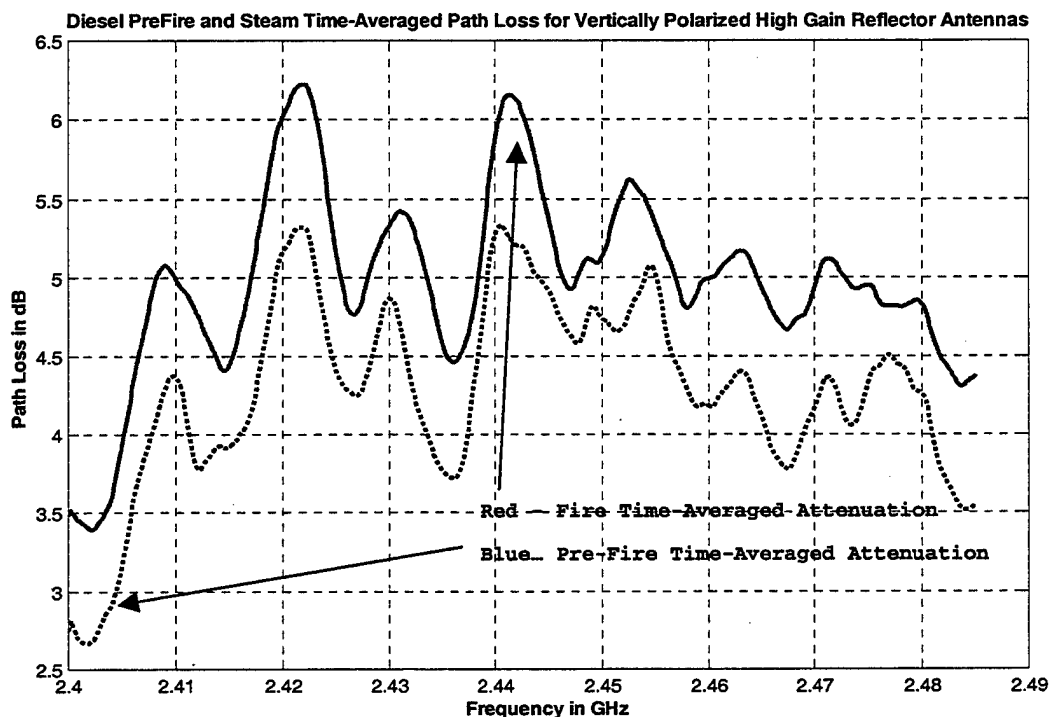


Figure 9.18: Diesel Pre-Fire and Steam Time-Averaged Path Loss for Vertically Polarized High Gain Antennas

1) Steam Build-Up Time-Averaged Attenuation for Vertically Polarized Directional Antennas

In Figure 9.19, the time-averaged attenuation per meter during the steam build-up phase shows that the maximum attenuation occurs at 2.442 GHz. The values of the time-averaged attenuation per meter vary between 0.06 and 0.16

dB/m, slightly lower than the values measured for the water mist phase.

Diesel Fire Post Water Mist Extinguishing Time-Averaged Attenuation for Vertically Polarized High Gain Reflector Antennas

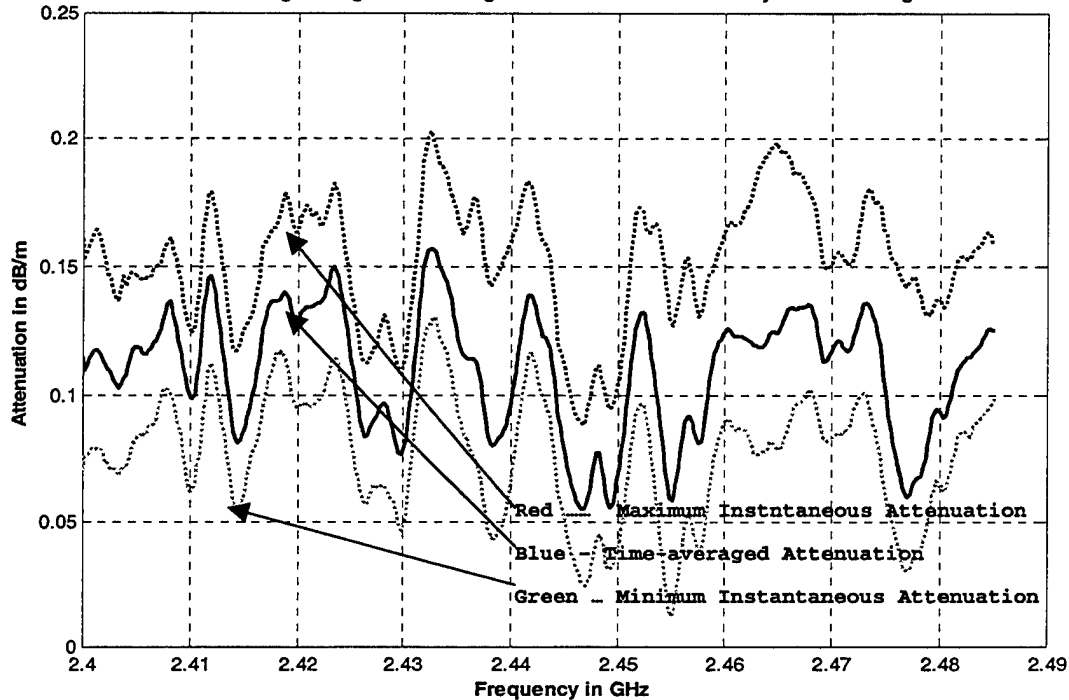


Figure 9.19: Diesel Fire Post Water Mist Extinguishing Time-Averaged Attenuation for Vertically Polarized High Gain Antennas

m) Attenuation Probability Density Functions for Vertically Polarized Directional Antennas

The attenuation probability density functions (pdf's) for each frequency scan for the vertically polarized directional antennas are shown in Figure 9.20a. The plot shows that the pdf vary with time and that the attenuation caused by fire and the follow on phases is non stationary. Initially, when the fire was lit at $t=0$ the attenuation has about 0 dB mean and a small standard deviation. As the fire

develops the pdf shifts towards higher attenuation values and the standard deviation of the pdf increases. At $t=5$ min, when the water mist extinguishing system is turned on, the pdf shifts abruptly towards even higher attenuation values and the standard deviation increases further. At $t=7$ min, when the water mist extinguishing system is turned off, the

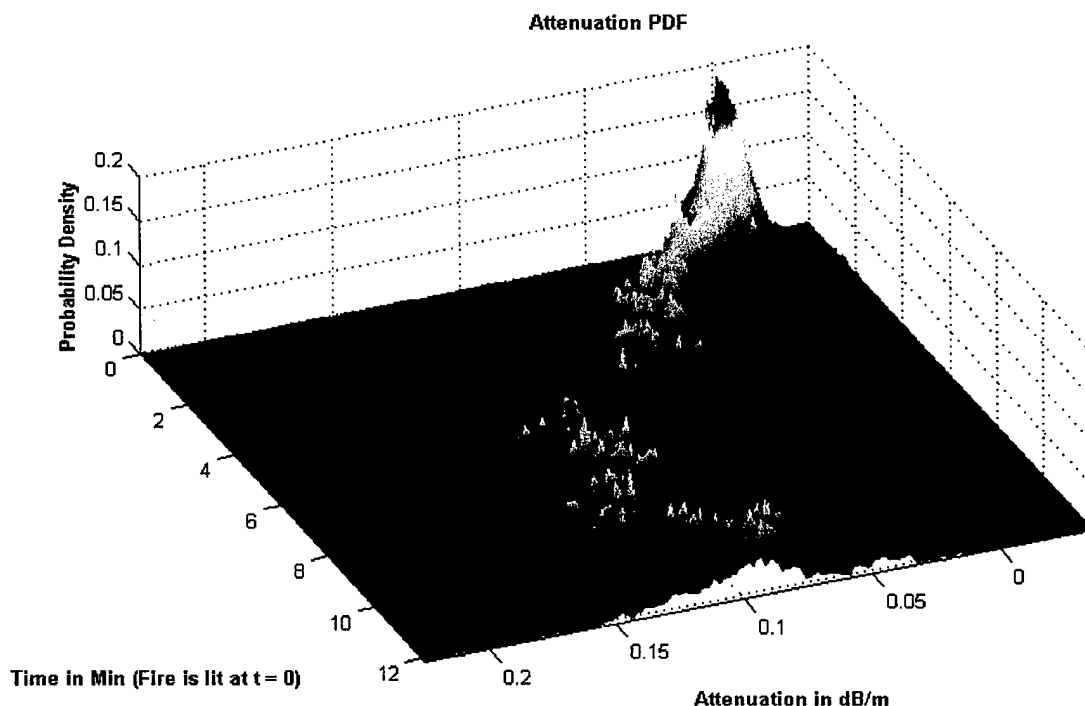


Figure 9.20a: Attenuation Probability Density Function Mesh Plot

pdf starts shifting back towards lower attenuation values, but the standard deviation remains high. Because of the non-stationarity of the pdf's the time-averaged pdf's are presented. For the fire phase, the averaging is done over

the last minute of the fire phase, corresponding to the "fully developed" fire/smoke while for the other phases pdf's for the entire phases are time-averaged.

The attenuation probability density functions for the three phases (fire, water mist and steam build-up) for the vertically polarized directional antennas during the diesel fire experiments are shown in Figure 9.20b. Also shown is the "average" attenuation probability density function for all phases. The pdf's for the three phases resemble **Gaussian** distributions (plotted with the dotted

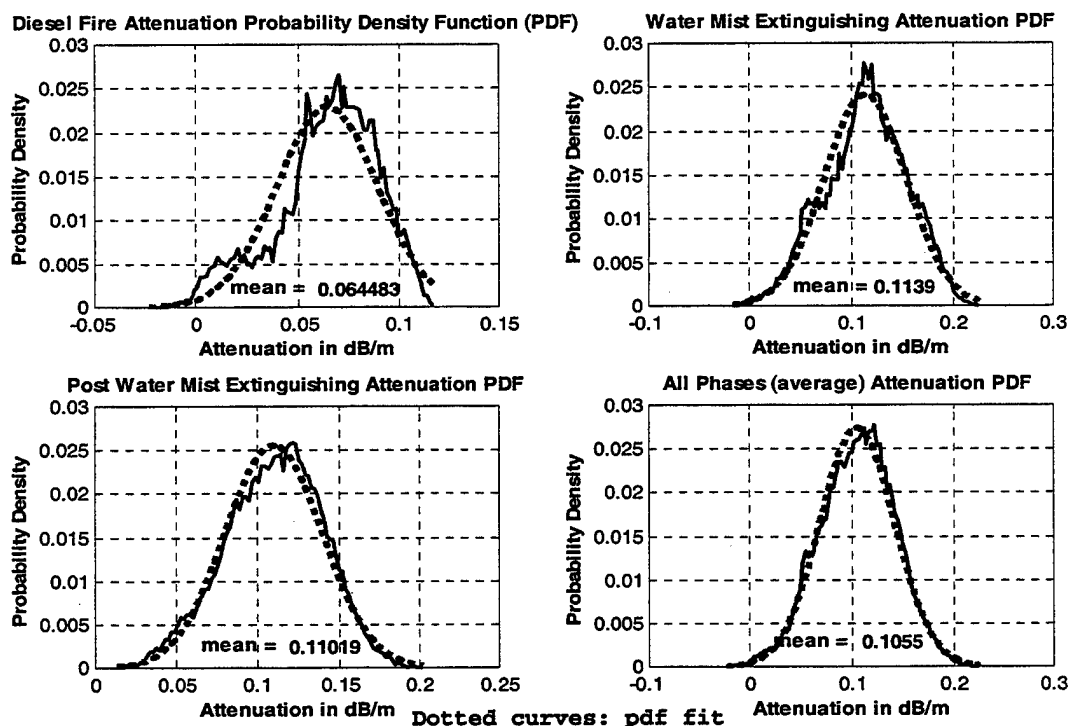


Figure 9.20b: Attenuation Probability Density Functions

line). For the fully developed fire (the last minute of the fire phase) the mean attenuation was 0.064 dB/m . For the water mist phase the mean attenuation was 0.113 dB/m . For the steam build-up phase the mean attenuation was 0.110 dB/m. Finally the all-phases pdf has the average attenuation of 0.105 dB/m.

The cumulative distribution functions for the attenuation for the three phases individually and the overall cumulative distribution function are shown in Figure 9.21. From the fire phase cdf we can determine that there is a 0.95 probability that the attenuation will be lower than 0.1 dB/m. Similarly for the water mist phase there is a 0.95

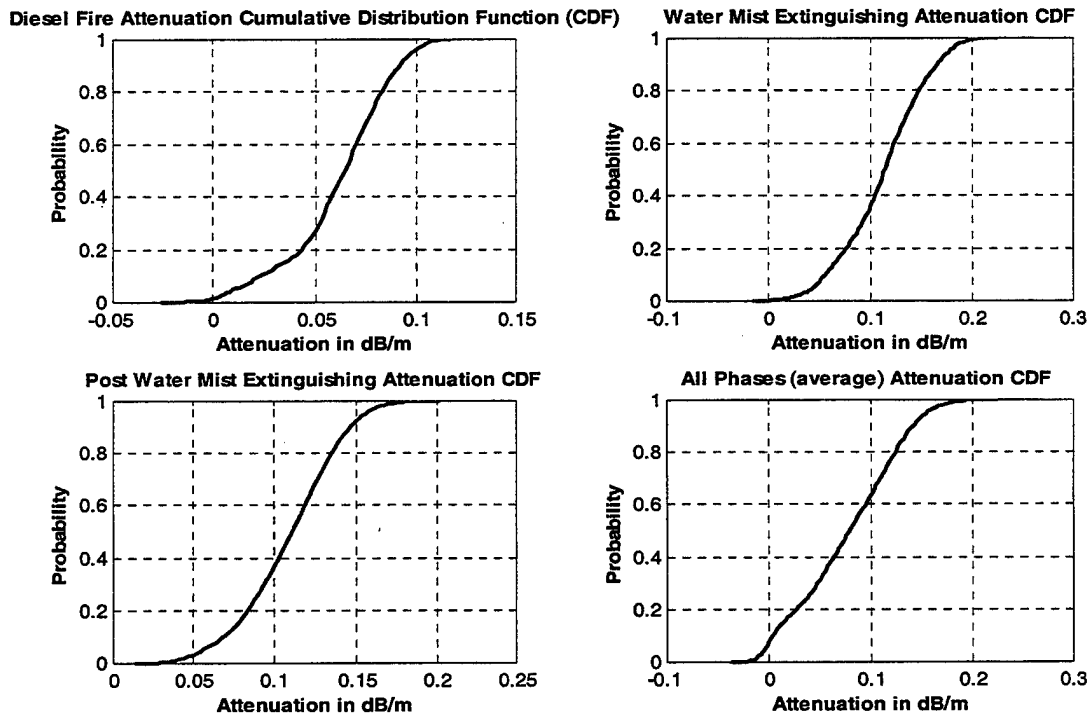


Figure IX-21: Attenuation Cumulative Distribution Functions

probability that the attenuation will be less than 0.18 dB/m. For the steam build-up phase the 0.95 point occurs for the attenuation of 0.15 dB/m. This shows that the attenuation of the water mist-extinguishing phase causes larger attenuation than the fire itself. For all the phases there is 95% probability that the attenuation is going to be less than 0.16 dB/m.

n) Autocorrelation Functions

Our next step was to determine the attenuation correlation between different frequencies for the different phases of the experiment. Initially we estimated the freque-

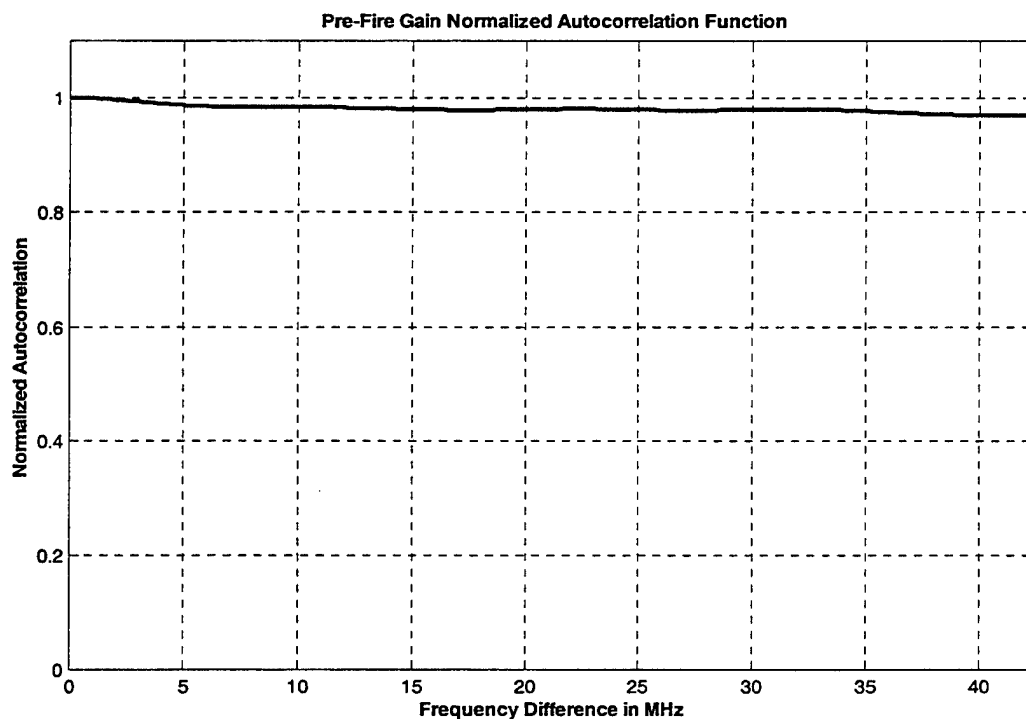


Figure 9.22: Pre Fire Gain Normalized Autocorellation Function

ncy response autocorrelation function for the pre-fire phase. In Figure 9.22 the plot of the autocorrelation function indicates a high degree of correlation between attenuation at different frequencies. This dependency suggests that the attenuation does not vary much with frequency.

Continuing on to the fire phase the autocorellation function plot in Figure 9.23 is similar to the pre-fire plot. The high values of correlation also follow from the results obtained from the comparison of the pre-fire and diesel fire time-averaged path loss plots.

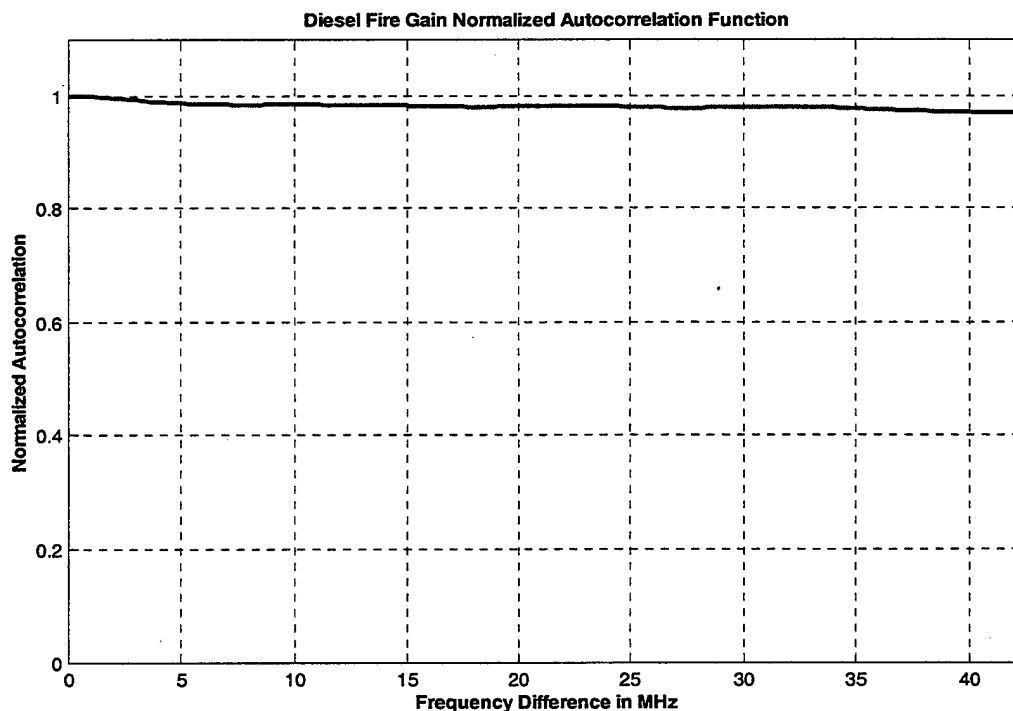


Figure 9.23: Fire Gain Normalized Autocorellation Function

As shown in Figure 9.12, path loss for all frequency components increased in a similar way and all the minima and maxima remained at the same frequencies. Figures IX-24 and IX-25 show the autocorellation function plots for the water mist and steam build-up phases. These plots are similar to the plots for the pre-fire and diesel fire phases.

The attenuation's relative invariance with frequency is the consequence of using directional antennas

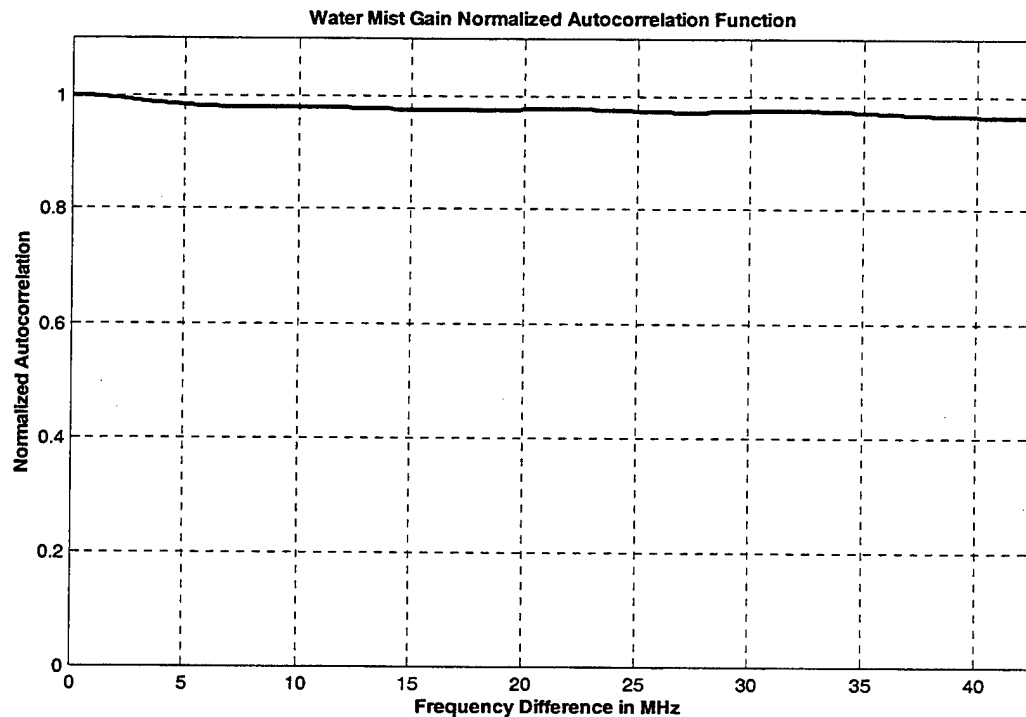


Figure IX-24: Water Mist Gain Normalized Autocorellation Function

for the experiment. There is little effect of the compartment, since the antenna beam is very narrow, a

single, line-of-sight path dominates the propagation, and the attenuation due to fire, smoke, and water mist does not vary significantly over the narrow 2.4 GHz ISM frequency band.

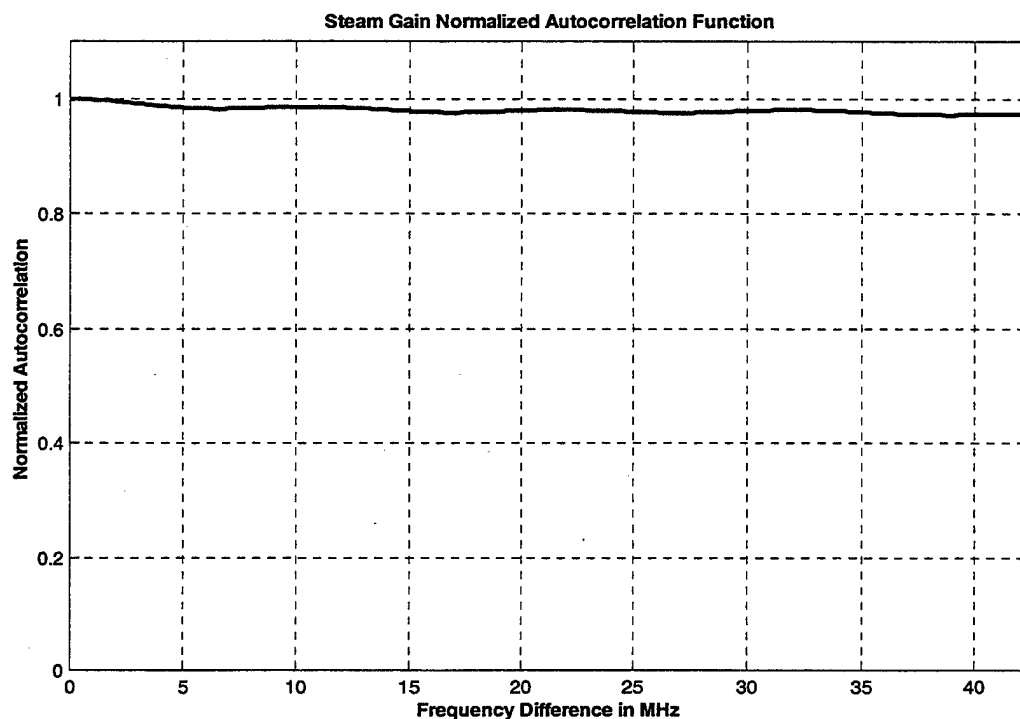


Figure 9.25: Steam Build-Up Gain Normalized Autocorellation Function

o) Estimation of the best frequency difference

The last step was to estimate the frequency difference that, on average, would provide the least combined (sum of) attenuation. This information would be useful if a dual-frequency (diversity) transmission system was used. As seen in Figure 9.26 for the vertically polarized antennas this frequency difference is about 25

MHz, but the changes in combined attenuation are very small. The values close to the full ISM bandwidth (85 MHz) are unreliable because of the diminishing number of frequencies averaged.

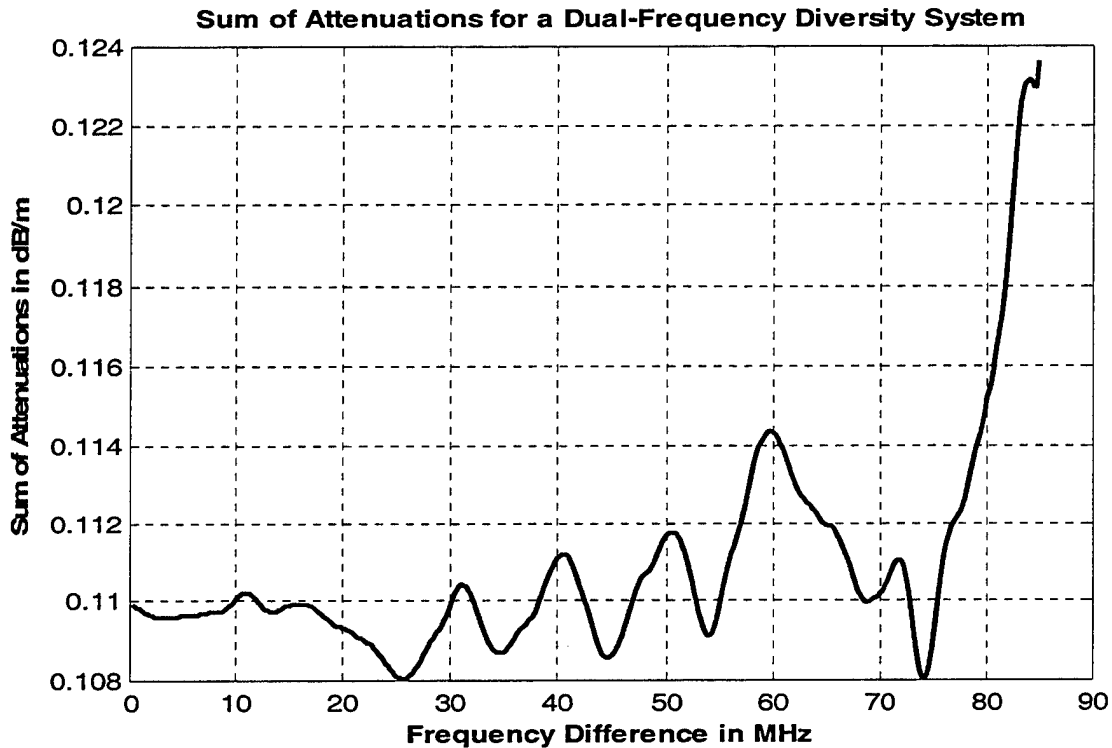


Figure 9.26: Sum of Attenuation for a Dual-Frequency Diversity System

2. Horizontal Polarization

a) *Path loss for Horizontally Polarized Directional Antennas*

First the measured path loss is presented as a surface plot with the x-axis as the time axis, the y-axis as the frequency axis and the z-axis as the path loss (in dB)

axis. In Figure 9.27 the path loss plot is shown for the horizontally polarized directional antennas. In this figure we have also shown the phase boundary planes. From the plot we see that initially we have an approximately five-minute

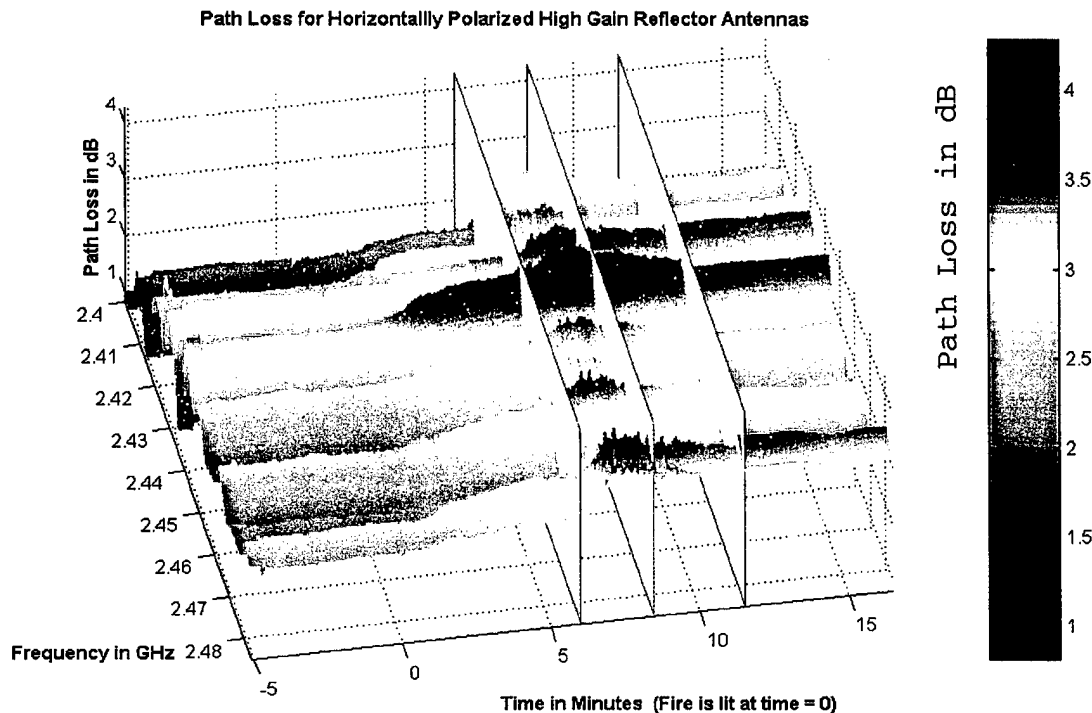


Figure IX-27: Path Loss for Horizontally Polarized High Gain Antennas pre-fire phase. For this phase the time has negative values going from -5 up to 0. At $t=0$ diesel fire and its measurements begin. The fire lasts for approximately six minutes (minutes 0-6) followed by a two minute water mist phase (minutes 6-8) and four minute mist build-up phase (minutes 8-12). Finally we note approximately five minutes of post-fire phase.

In Figure 9.28 the same surface plot is shown without the phase boundaries. We note the continuity between the pre-fire, fire, water mist and steam build-up phases,

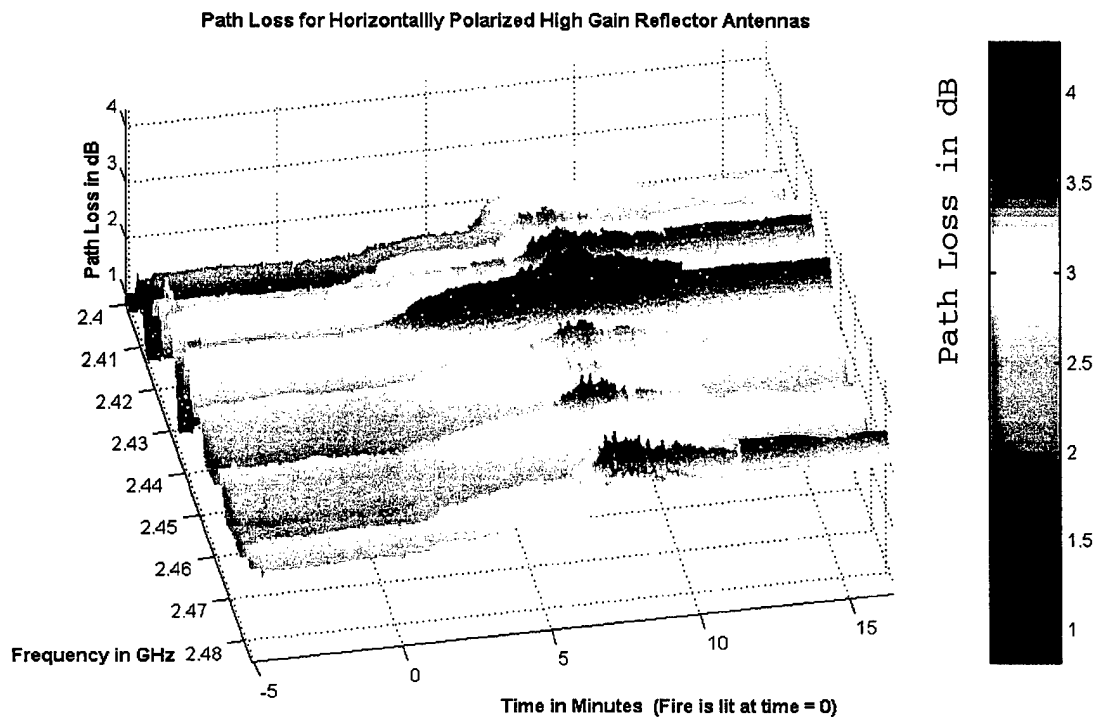


Figure 9.28: Path Loss for Horizontally Polarized High Gain Antennas

and a discontinuity between the steam build-up and the post-fire phase ($t=12$). The discontinuities are caused by the "interruptions" in the measurement process to allow for the personnel movement in the compartment to either light the fire (at $t=0$) or to inspect the completion of the particular experiment run (at $t=12$). Measurements taken during these activities would not be valid since the attenuation changed with people moving between the antennas.

In Figure 9.29 the "bird's eye" view of the path loss is presented. This allows us to visualize how the path loss changes with time and frequency. We note that for the five-minute pre-fire phase the path loss at each frequency has a constant value with time but is different for

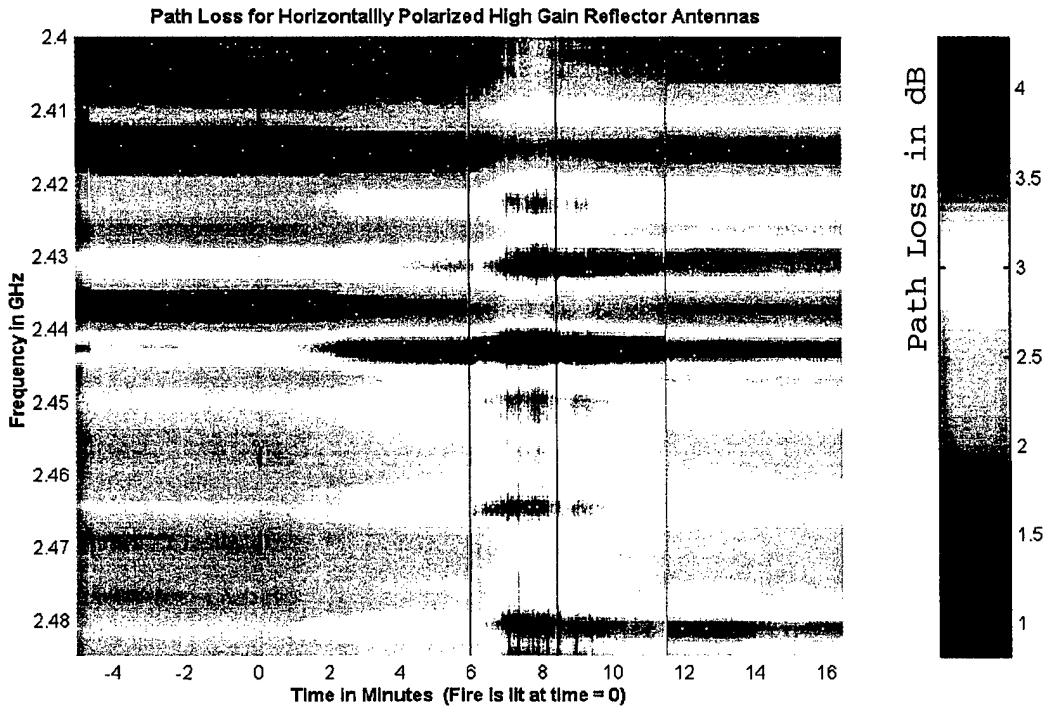


Figure 9.29: Path Loss for Horizontally Polarized High Gain Antennas

different frequencies. The path loss differences are mainly caused by the reflection/absorption characteristics of the portion of the compartment that is "visible" (within the main beam) to the two antennas.

After the fire has been lit the path loss increases gradually for all frequencies. The path loss

reaches its peak during the water mist phase and then it starts falling again during the mist build-up phase. The highest measured value of the path loss was 4.5 dB. After the compartment ventilation the path loss values are significantly lower than the ones during the fire phase but higher than the values of the pre-fire phase because of the residual condensation in the compartment and on the antennas. Also, from Figure 9.29 we can see that the minima and maxima of the path loss do not shift appreciably along the frequency axis (in the vertical direction) from one phase to the next. (This is a consequence of using directional antennas.)

b) Attenuation for Horizontally Polarized Directional Antennas

We next present the attenuation surface plots. To create these plots we divided each path loss value by the time-averaged pre-fire phase path loss at the corresponding frequency. The result was then divided by the distance between the antennas to obtain the attenuation per unit length. The choice of the distance to obtain the attenuation per unit length (dB/m) requires some explanation. We selected the distance between the antennas (rather than the fire "depth") for the following reasons:

- The fire depth was ambiguous and changing with time

- The smoke and heat were distributed throughout the compartment and not confined to the "flame" region only
- The antennas were placed close to the fire source (as close as the compartment geometry and the maximum temperature that the antenna could sustain permitted)
- The distance between the antennas was 7.66 meters and the fuel pool width was 1 meter

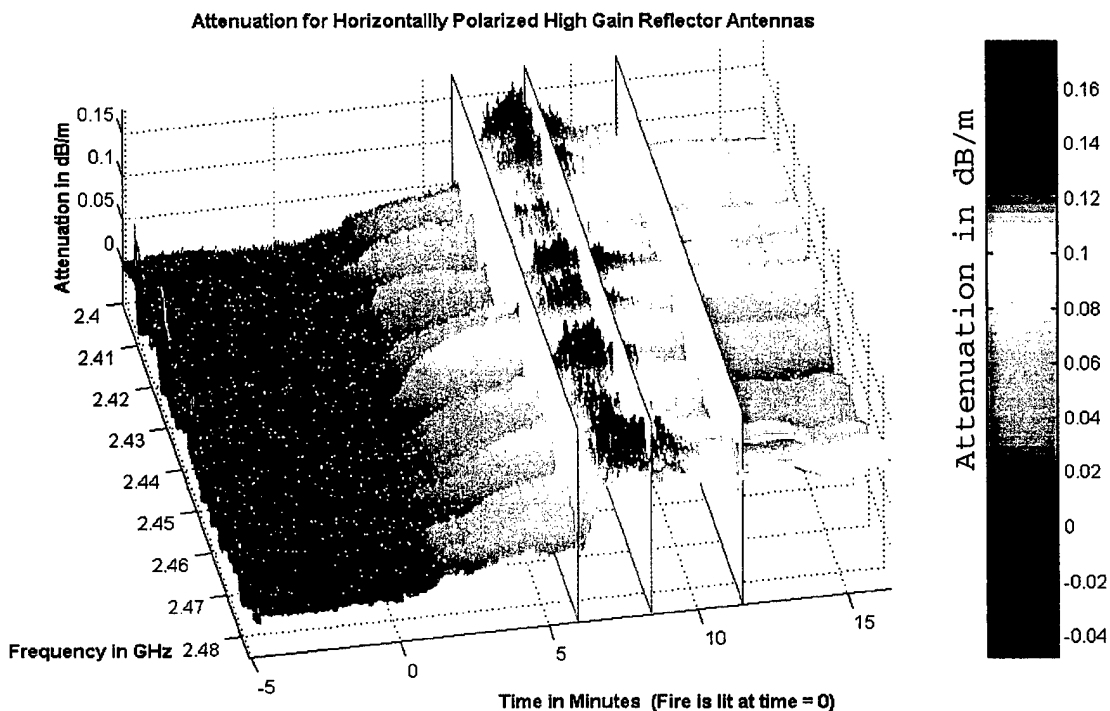


Figure 9.30: Attenuation for Horizontally Polarized High Gain Antennas

In Figure 9.30 the attenuation surface plot for the horizontally polarized directional antennas is shown with the phase boundary planes. For the pre-fire phase (time between -5 and 0 minutes) the attenuation is approximately 0 dB/m, as expected, since the time-averaged path loss for the pre-fire phase was used as the reference for each frequency. Therefore, during the pre-fire phase there are no "peaks and valleys" in the surface plot.

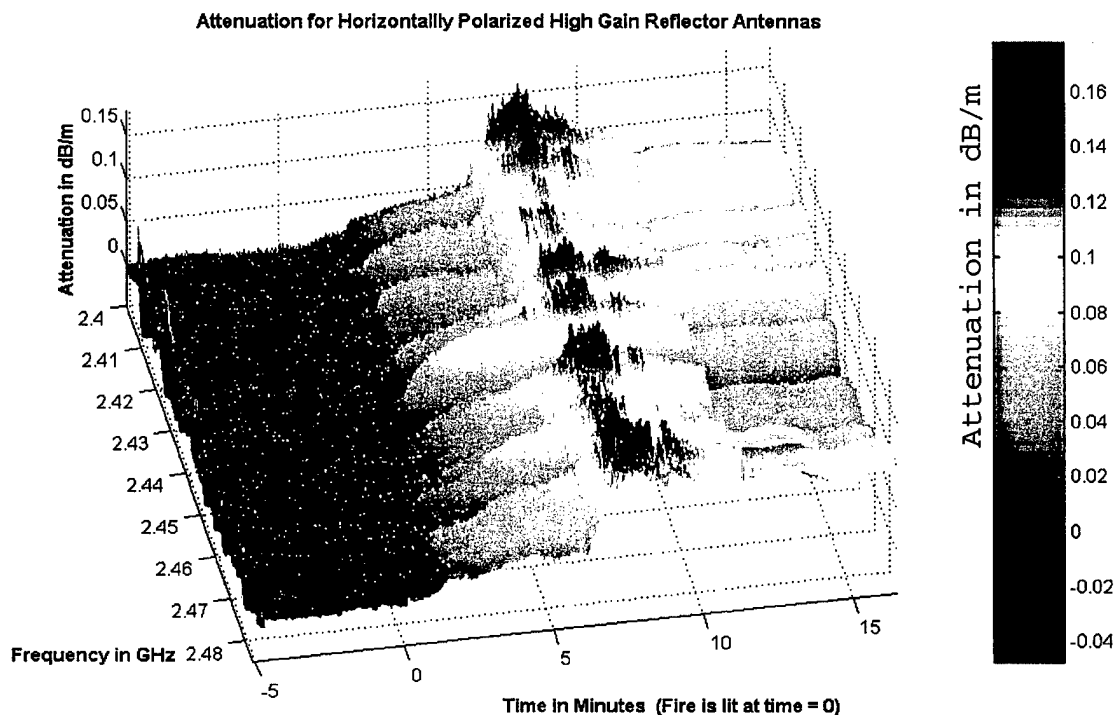


Figure 9.31: Attenuation for Horizontally Polarized High Gain Antennas

In Figure 9.31 we show the same surface plot but without the phase boundaries. We note a gradual increase in attenuation during the fire phase, as the heat and smoke build-up in the compartment. At about 6 minutes after the fire was lit (from minutes 6-8), there is an abrupt increase in attenuation caused by the activation of the water mist fire-extinguishing system. After two minutes of fire extinguishing the compartment is saturated with steam and

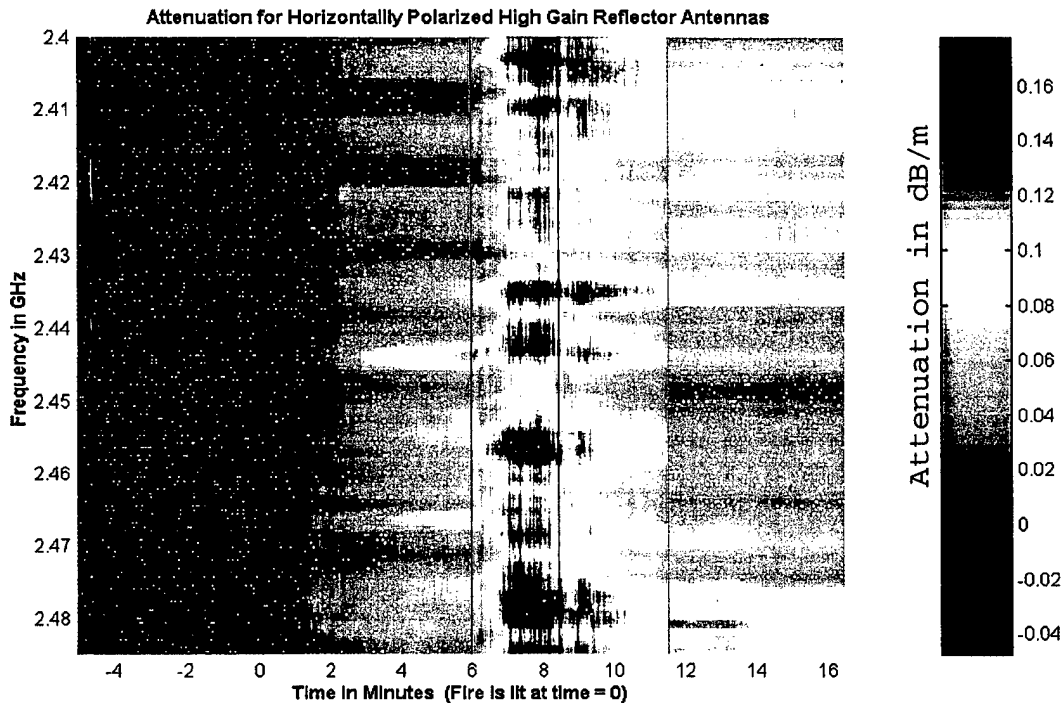


Figure 9.32: Attenuation for Horizontally Polarized High Gain Antennas

smoke (from minute 8 to 12) and the attenuation remains relatively high (but not as high as during the fire-

extinguishing phase). Upon ventilation of the compartment the attenuation decreases (from minute 12 on) towards the values prior to the fire (for negative time). In Figure 9.32 the same surface plot is shown, viewed directly from the z-axis (the "birds-eye" view) clearly showing the attenuation changes for different phases and for different frequencies. The attenuation per meter reached its maximum value during the water mist fire extinguishing phase and (for particular frequencies) it was on the order of 0.18 dB/m. The maximum attenuation for the fire phase was on the order of 0.12 dB/m.

c) Frequency-Averaged Path Loss for Horizontally Polarized Directional Antennas

The first statistical analysis we performed was to determine the frequency-averaged path loss. As shown in Figure 9.33 the frequency-averaged path loss for the pre-fire phase is almost constant at around 2.1 dB. When the fire was lit the frequency-averaged path loss increased with time. The rate of increase was not constant with time and it depended on the fire intensity and the ventilation arrangement during this phase. After the water mist system was turned on the frequency-averaged path loss increased rapidly. During this phase the frequency-averaged path loss reached its peak value of ~3.3 dB. The averaged path loss started to decrease slowly during the steam build-up phase.

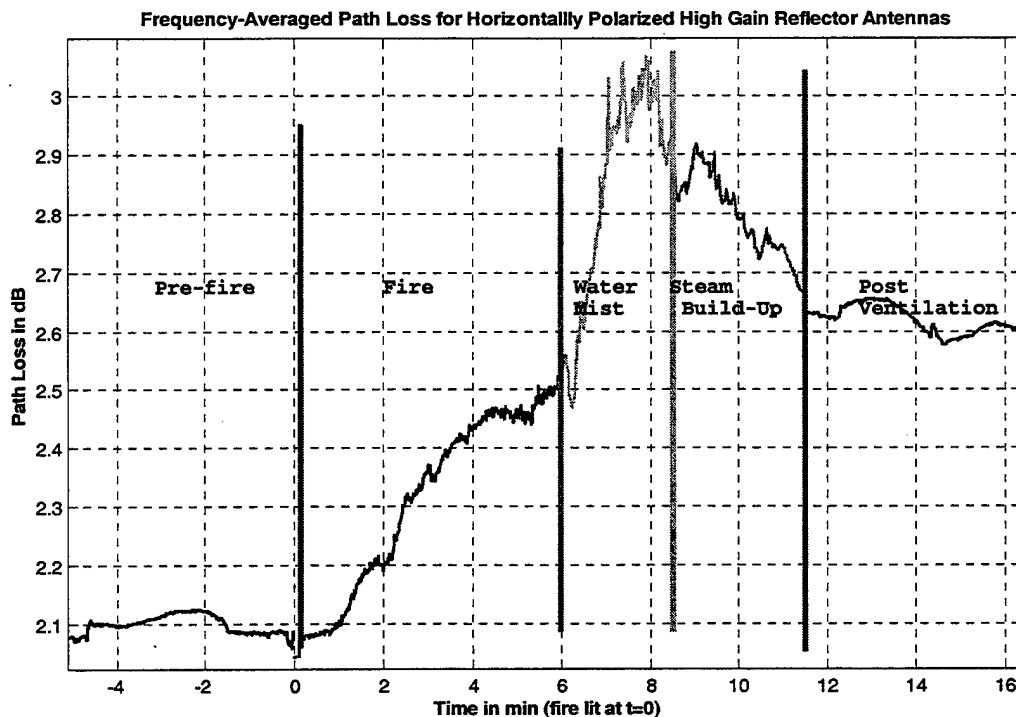


Figure 9.33: Frequency-Averaged Path Loss for Horizontally Polarized High Gain Antennas

Again there is a discontinuity between the steam build-up and the post-fire phase. This happens because the post-fire phase measurements were taken approximately ten minutes after the steam build-up phase had ended, and the steam was evacuated from the compartment. We can see that the averaged path loss is almost constant at about 2.65 dB.

d) Frequency-Averaged Attenuation for Horizontally Polarized Directional Antennas

Our next step was to determine the frequency-averaged attenuation in dB/m. The shape of the frequency-averaged attenuation as a function of time is exactly the

same as for the path loss, as shown in Figure 9.34. The only difference between the frequency-averaged attenuation

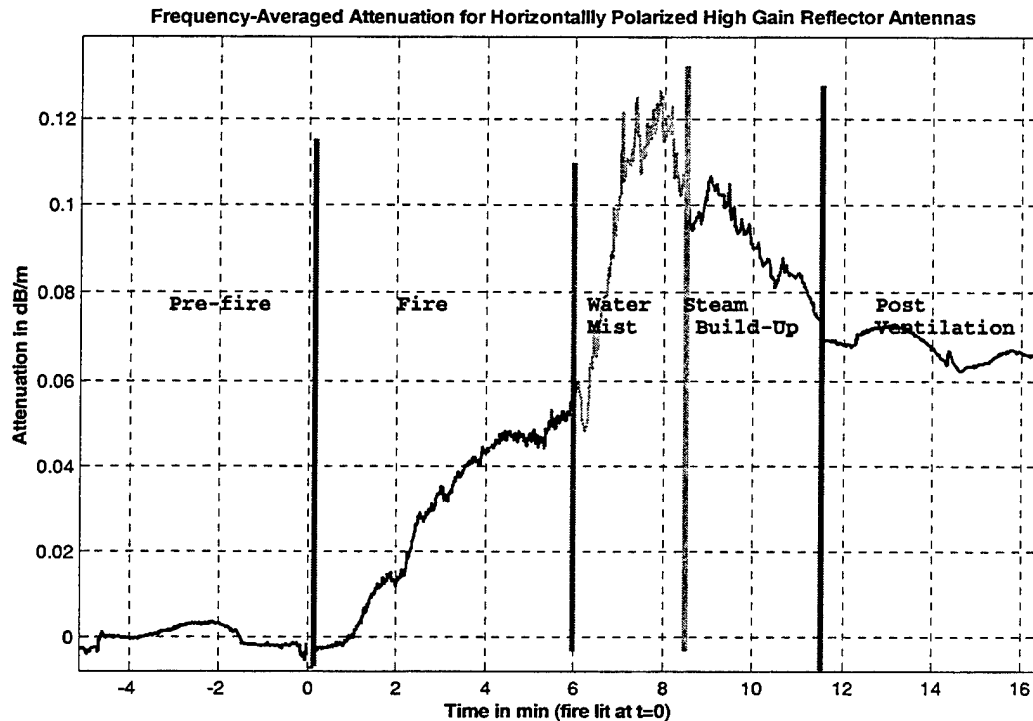


Figure 9.34: Frequency-Averaged Attenuation for Horizontally Polarized High Gain Antennas

and the frequency-averaged path loss is the division by a constant distance. The maximum averaged attenuation is approximately 0.13 dB/m. During the fire phase the attenuation did not exceed 0.06 dB/m. After the water mist fire extinguishing system was turned on there was a small drop in attenuation (0.01 dB/m) because the smoke and fire were nearly instantaneously suppressed. However as the steam started building up the attenuation increased reaching its maximum value after about 1.5 minutes before starting to

decrease slowly as the temperature and the steam density gradually decreased.

**e) *Temperature vs. Time for Horizontally
Polarized Directional Antennas***

The temperature taken at five different locations in the compartment is shown in Figure 9.35 as a function of time. The highest temperature curve in the plot is the flame temperature at the fuel pan level. (This temperature curve is actually the average of three sets of temperature data taken at three different locations at the fuel pan level.) We note that the temperature rapidly rises to about 600° C and remains around that value for the fire duration. The small fluctuations occur due to changes in the fire conditions such as ventilation rate, smoke density, etc. The next highest temperature curve is for the data taken at an elevation of 11 feet and at the horizontal distance of 3 feet from the pan. The maximum temperature is approximately 200° C. The third highest curve is for the data taken at the height of 7 ft and for the 3-ft horizontal distance from the fuel pan. The maximum temperature at this height is 110° C. The two lowest curves are for the temperature next to the two antennas. We note that the temperature next to the transmitting antenna reached a maximum of approximately 80° C and the temperature next to the receiving antenna reached

a maximum of approximately 70° C. The antennas withstood these temperatures (for fires of short duration) without damage.

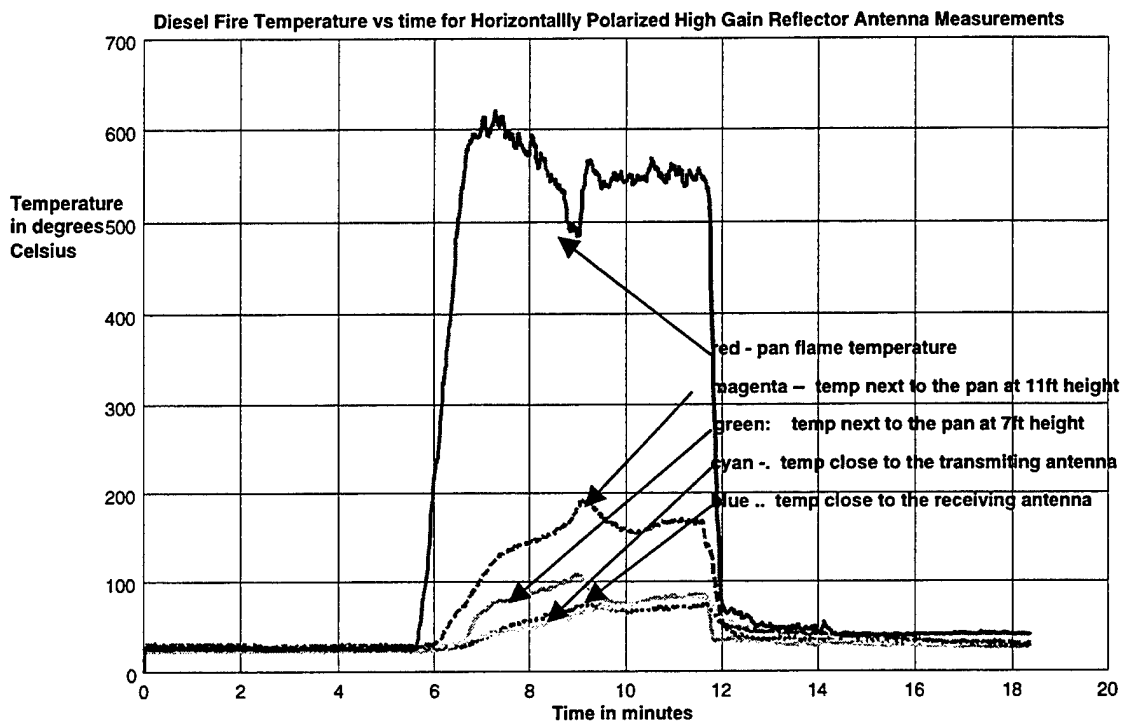


Figure 9.35: Diesel Fire Temperature versus Time for Horizontally Polarized High Gain Antennas

f) Scaled Attenuation and Temperature vs. Time for Horizontally Polarized Directional Antennas

Our next objective was to determine if there was a relation between the temperature increase close to the antennas and the attenuation increase. To accomplish this we subtracted the mean values from the attenuation and the temperature data. Next we determined an average coefficient

Diesel Fire Scaled Attenuation and Temperature for Horizontally Polarized High Gain Reflector Antenna Measurements

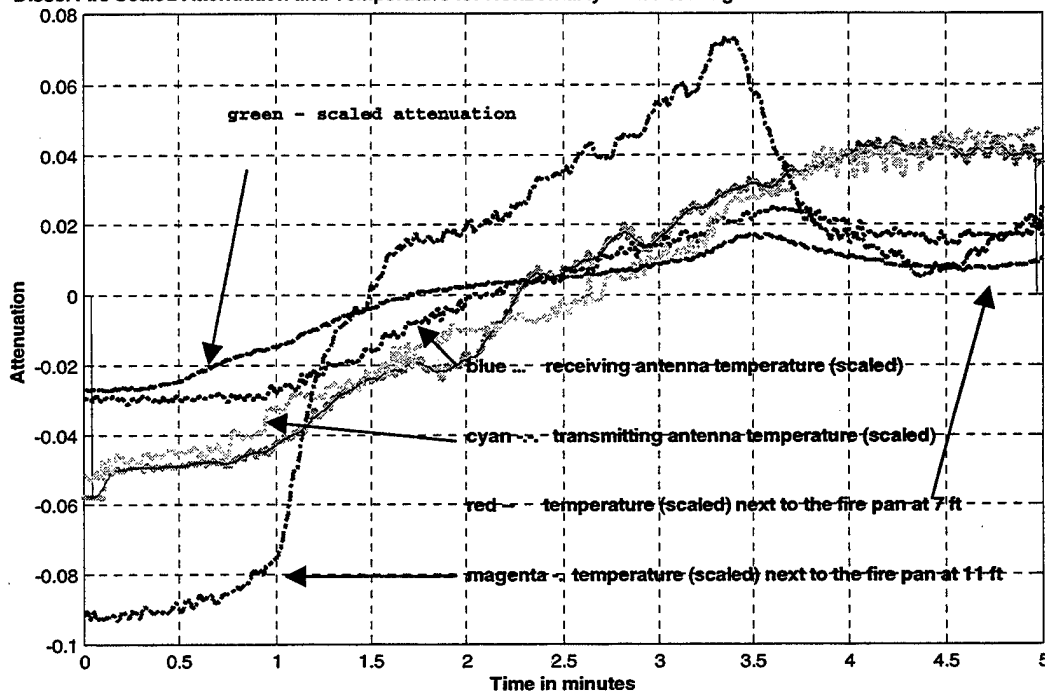


Figure 9.36: Diesel Fire Scaled Attenuation and Temperature versus Time for Horizontally Polarized High Gain Antennas

which, when multiplied with the time-varying temperature would yield the best "curve fit" for the time-varying attenuation. A close relationship between the temperature increase and the attenuation increase is evident in Figure 9.36.

g) Diesel Fire Time-Averaged Path Loss for Horizontally Polarized Directional Antennas

Our next step was to calculate the time-averaged path loss for the fire phase. As shown in Figure 9.37 the

time-averaged path loss ranged between 1.3 and 3.6 dB, a frequency variation (with frequency) of close to 2.5 dB.

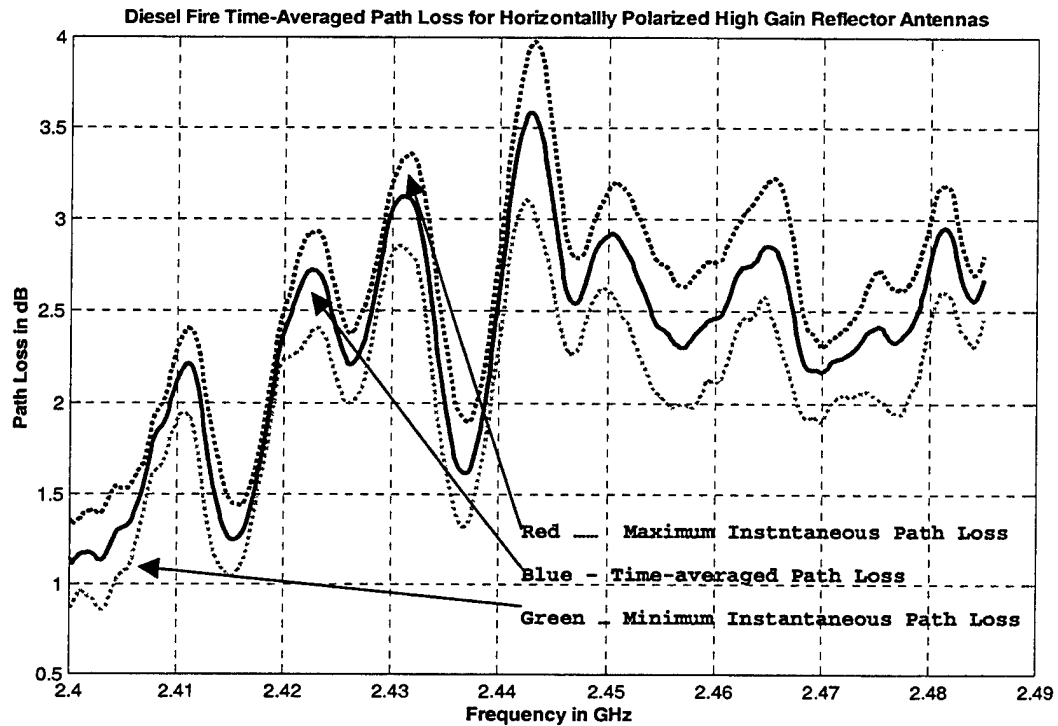


Figure 9.37: Diesel Fire Time-Averaged Path Loss for Horizontally Polarized High Gain Antennas

The plot also shows the minimum and maximum values of path loss for each component. The maximum path loss occurs at 2.442 GHz and the minimum path loss occurs at 2.403 GHz. The maximum and minimum path loss curves follow the time-averaged path-loss curve, that is the zero slope points for all three curves are located at the same frequencies. The maximum and minimum points occur approximately at the same frequencies they occurred for the

vertical polarization indicating that the compartment has similar characteristics for both polarizations.

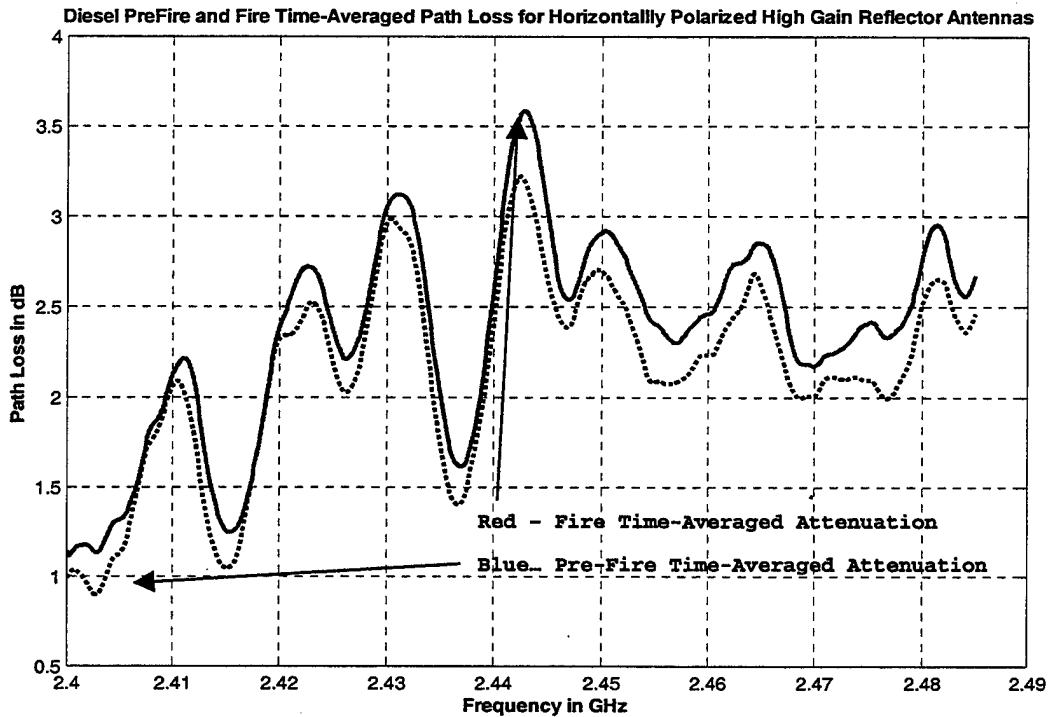


Figure 9.38: Diesel Pre-Fire and Fire Time-Averaged Path Loss for Horizontally Polarized High Gain Antennas

In Figure 9.38 the time-averaged path loss for the fire and the pre-fire phases are shown together in order to assess the effects of fire. Again the minima and maxima of the path loss are located at the same frequencies. This indicates that there is no change in the propagation characteristics of the compartment due to the fire except that there is an increase between 0 and 0.4 dB (depending on the frequency) of the time-averaged path loss.

h) Diesel Fire Time-Averaged Attenuation for Horizontally Polarized Directional Antennas

The time-averaged attenuation per meter during the fire phase is shown in Figure 9.39. The maximum attenuation

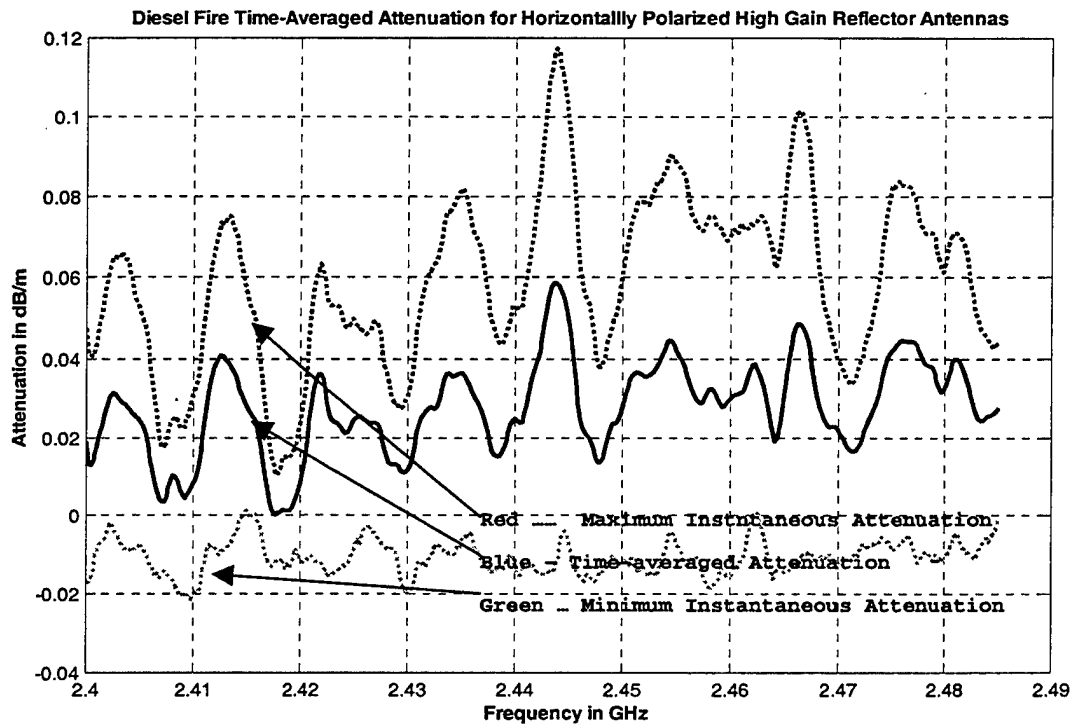


Figure 9.39: Diesel Fire Time-Averaged Attenuation for Horizontally Polarized High Gain Antennas

occurs again at 2.442 GHz. The maximum time-averaged attenuation is about 0.055 dB/m. The minimum attenuation for each frequency component is below the 0 dB axis indicating a small gain (of about 0.01 dB/m).

i) Water Mist Phase Time-Averaged Path Loss for Horizontally Polarized Directional Antennas

Our next step was to calculate the time-averaged path loss during the water mist phase. As shown in Figure 9.40 the time-averaged path loss ranged between 1.7 and 4.2dB, again a variation of close to 2.5dB. The maximum time-averaged path loss of 4.25dB occurs at 2.442 GHz and the minimum time-averaged path loss of 1.7dB occurs at 2.403 GHz, the same frequencies as for the fire phases. Also the zero slope points for all three curves (min, max and average path loss) occur at the same frequencies.

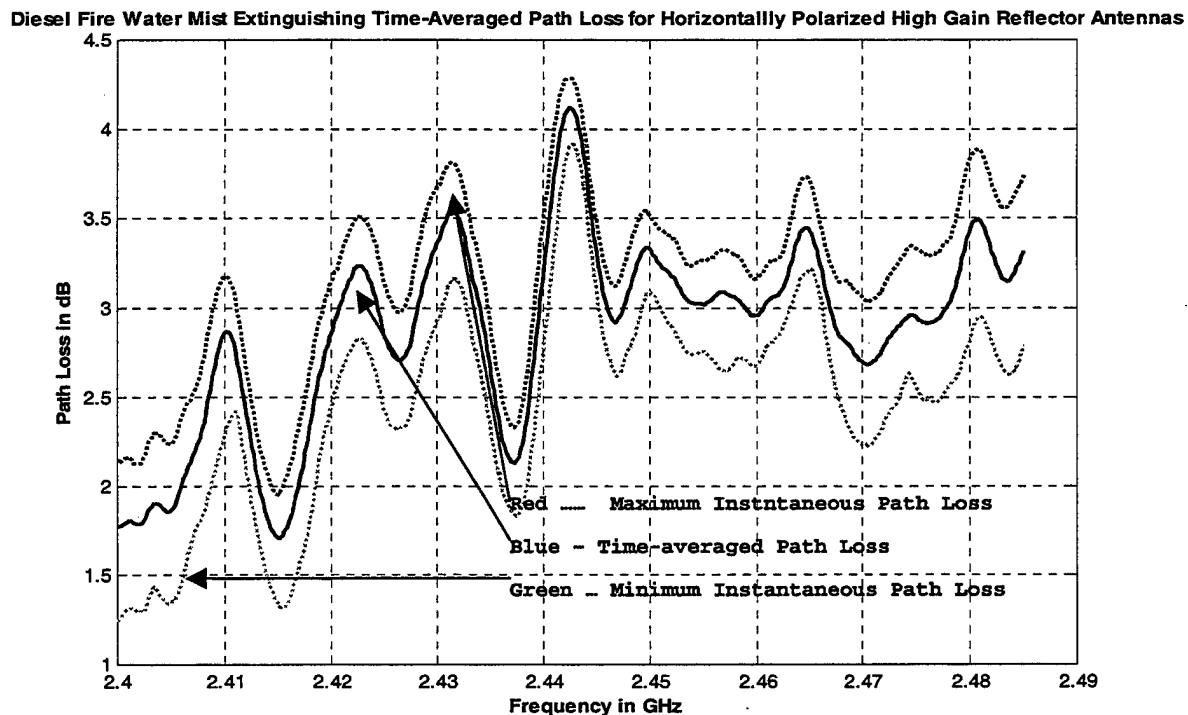


Figure 9.40: Diesel Fire Water Mist Extinguishing Time-Averaged Path Loss for Horizontally Polarized High Gain Antennas

The time-averaged attenuation curves for the water mist and the pre-fire phases are shown in Figure 9.41. Again the zero slope points are located at the same frequencies. This indicates that there is no change in the compartment propagation characteristics between the two phases, the only difference being that for the water mist phase there is an increase of 0.5 to 1dB for the time-averaged path loss.

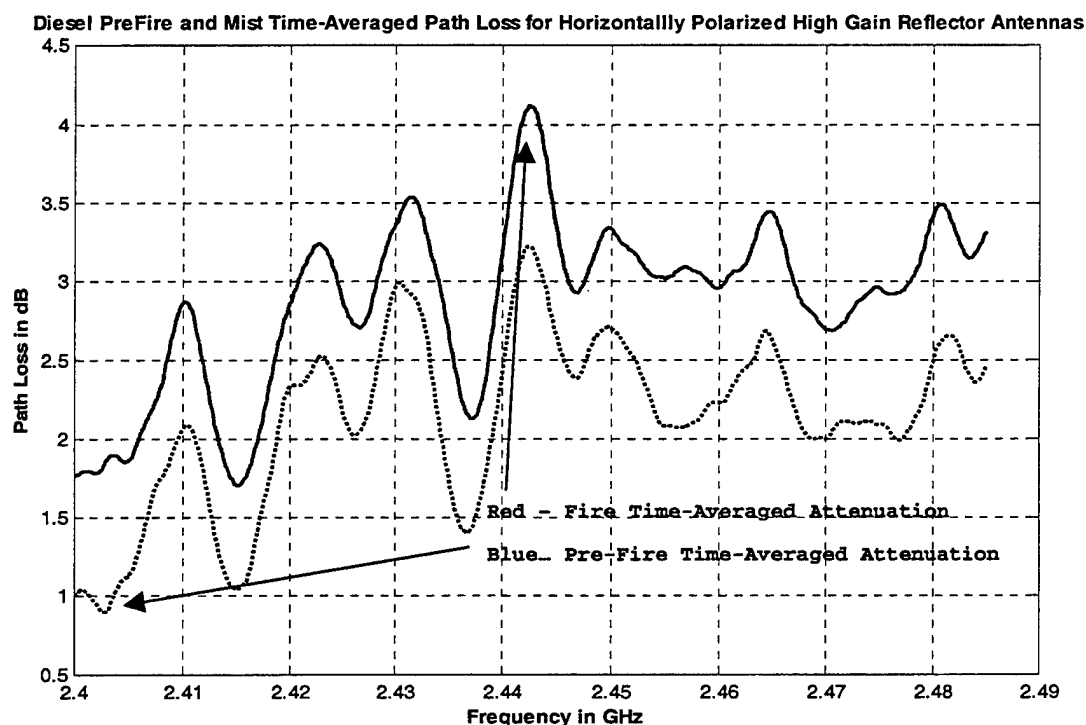


Figure 9.41: Diesel Pre-Fire and Water Mist Time-Averaged Path Loss for Horizontally Polarized High Gain Antennas

j) Water Mist Time-Averaged Attenuation for Horizontally Polarized Directional Antennas

The time-averaged attenuation per meter for the water mist phase is shown in Figure 9.42. The time-averaged

attenuation ranges between 0.05 and 0.13 dB/m. The maximum instantaneous attenuation of 0.18 dB/m occurs at 2.48 GHz.

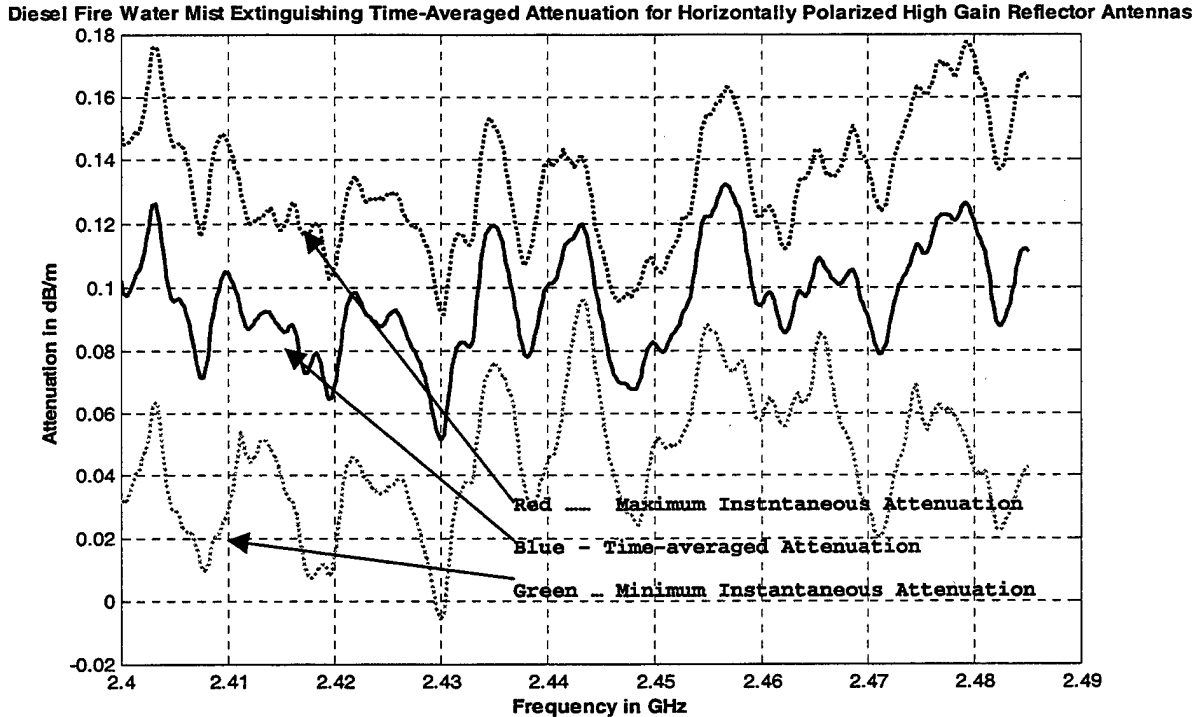


Figure 9.42: Diesel Fire Water Mist Extinguishing Time-Averaged Attenuation for Horizontally Polarized High Gain Antennas

k) Steam Build Up Phase Time-Averaged Path Loss for Horizontally Polarized Directional Antennas

Next we calculated the time-averaged path loss for the steam build-up phase. As shown in Figure 9.43 the time-averaged path loss ranged between 1.7 and 3.9 dB, a 3 dB variation. Also shown on the same plot are the minimum and maximum values of the path loss for each frequency. The maximum path loss of 4.2 dB occurs at 2.442 GHz and the

minimum path loss of 1.3 dB occurs at 2.401 GHz, almost the same frequencies as for the fire phase. Again the zero slope points for all three curves are located at the same frequencies, indicating that the "frequency response" for the path between the antennas does not change depending on whether there is fire or water mist in the compartment except for the path loss increase or decrease ("scaling").

Diesel Fire Post Water Mist Extinguishing Time-Averaged Path Loss for Horizontally Polarized High Gain Reflector Antennas

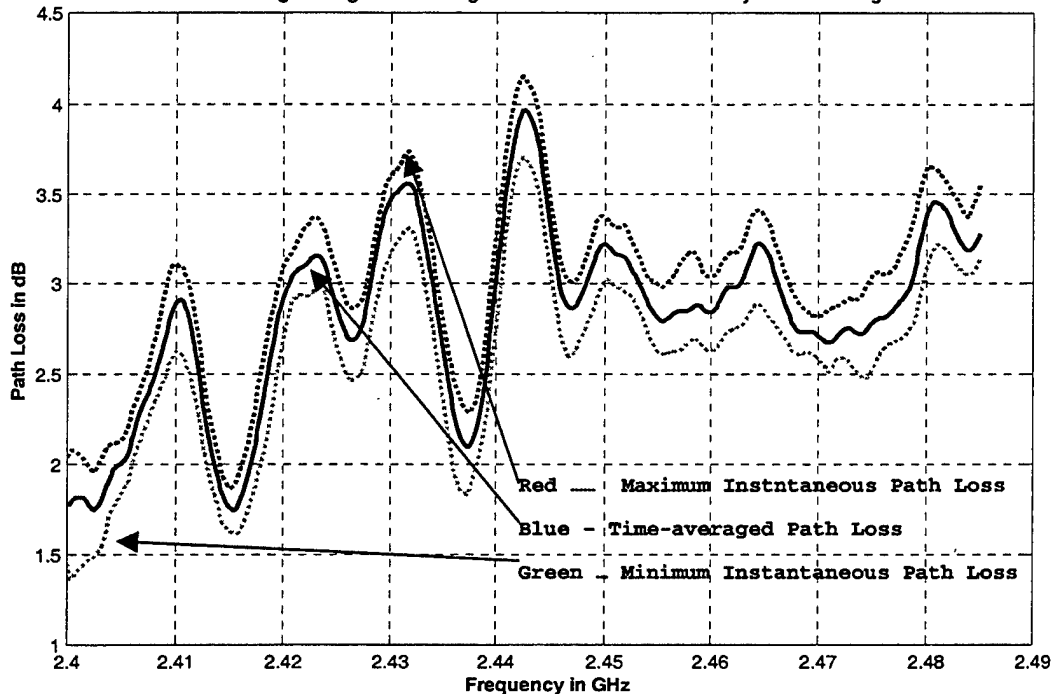


Figure 9.43 Diesel Fire Steam Build-Up Time-Averaged Path Loss for Horizontally Polarized High Gain Antennas

In Figure 9.44 the time-averaged path loss curves for the steam and the pre-fire phases are shown. Again the zero slope points (maxima and minima) are located at the same frequencies. This indicates that there is no change in

the compartment propagation characteristics except for the additional path loss of between 0.5 and 0.8 dB due to the residual steam and smoke in the compartment.

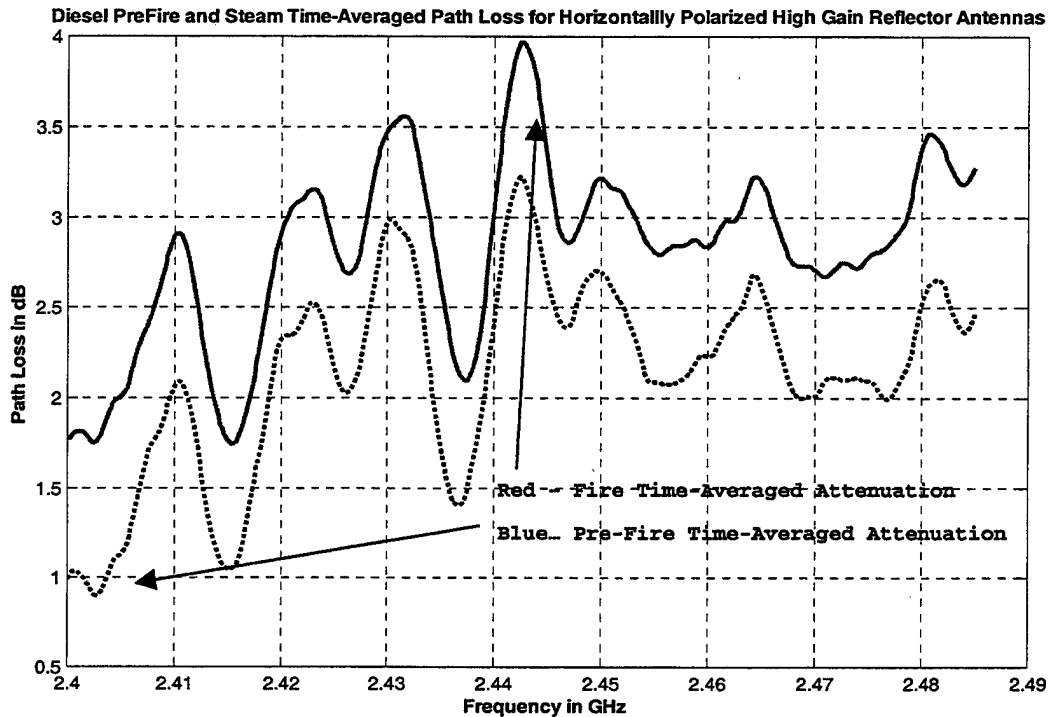


Figure 9.44: Diesel Pre-Fire and Steam Build-Up Time-Averaged Path Loss for Horizontally Polarized High Gain Antennas

1) ***Steam Build-Up Time-Averaged Attenuation for Horizontally Polarized Directional Antennas***

In Figure 9.45 the time-averaged attenuation per meter during the steam build-up phase shows that the maximum attenuation occurs at 2.435 GHz. The values of the time-averaged attenuation vary between 0.05 and 0.11 dB/m, slightly lower than the values measured for the water mist phase.

Diesel Fire Post Water Mist Extinguishing Time-Averaged Attenuation for Horizontally Polarized High Gain Reflector Antennas

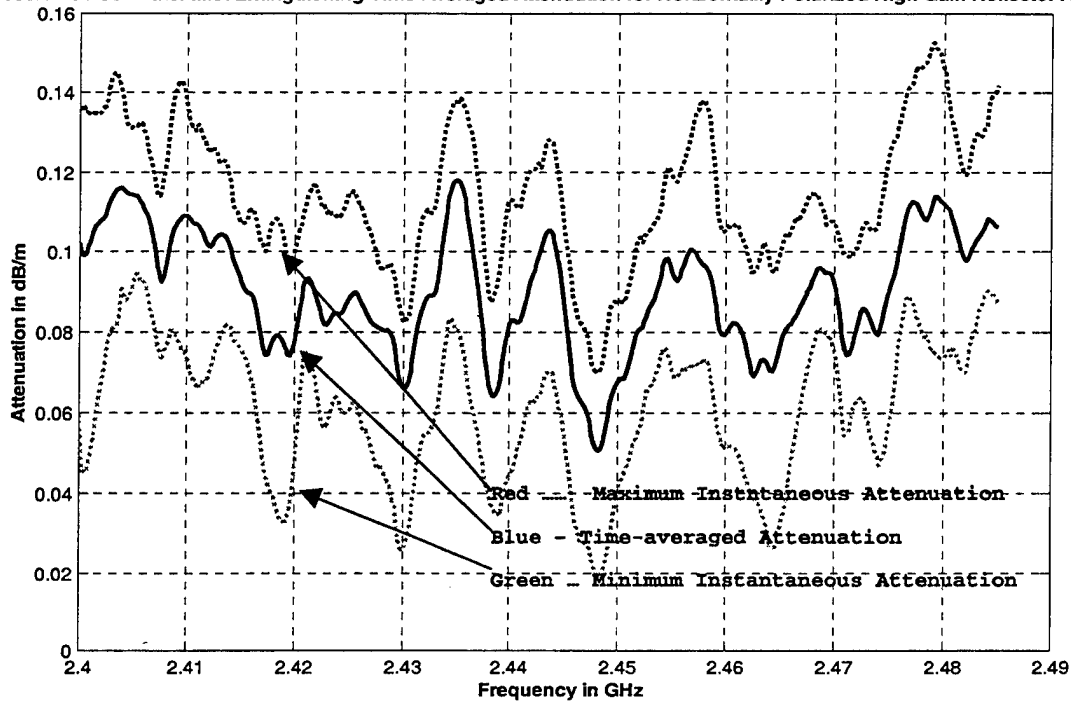


Figure 9.45 Diesel Fire Steam Build-Up Time-Averaged Path Loss for Horizontally Polarized High Gain Antennas

m) Attenuation Probability Density Functions for Horizontally Polarized Directional Antennas

The attenuation probability density functions (pdf) for each frequency scan for the horizontally polarized directional antennas are shown in Figure 9.46a. The plot shows that the pdf vary with time and that the attenuation caused by fire and the follow on phases is non stationary. Initially, when the fire was lit at $t=0$ the attenuation has about 0 dB mean and a small standard deviation. As the fire develops the pdf shifts towards higher attenuation values and the standard deviation of the pdf increases. At $t=5$,

when the water mist extinguishing system is turned on, the pdf shifts abruptly towards even higher attenuation values and the standard deviation increases further. At $t=7$, when the water mist extinguishing system is turned off, the pdf

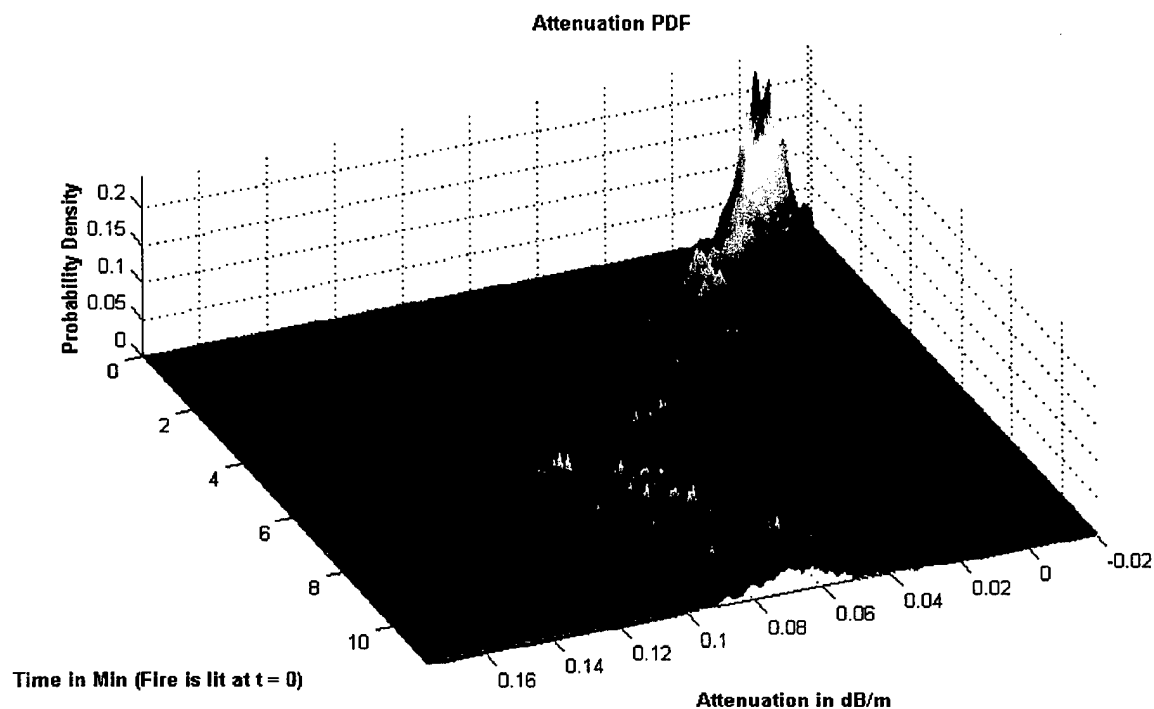


Figure 9.46a: Attenuation Probability Density Function Surface Plot

starts shifting back towards lower attenuation values, but the standard deviation remains high. Because of the non-stationarity of the pdf's the time-averaged pdf's are presented. For the fire phase, the averaging is done over the last minute of the fire phase, corresponding to the

"fully developed" fire/smoke while for the other phases pdf's for the entire phases are time-averaged.

The attenuation probability density functions for the three phases (fire, water mist and steam build-up) for the horizontally polarized directional antennas during the diesel fire experiments are shown in Figure 9.46b. Also shown is the "average" attenuation probability density function for all phases.

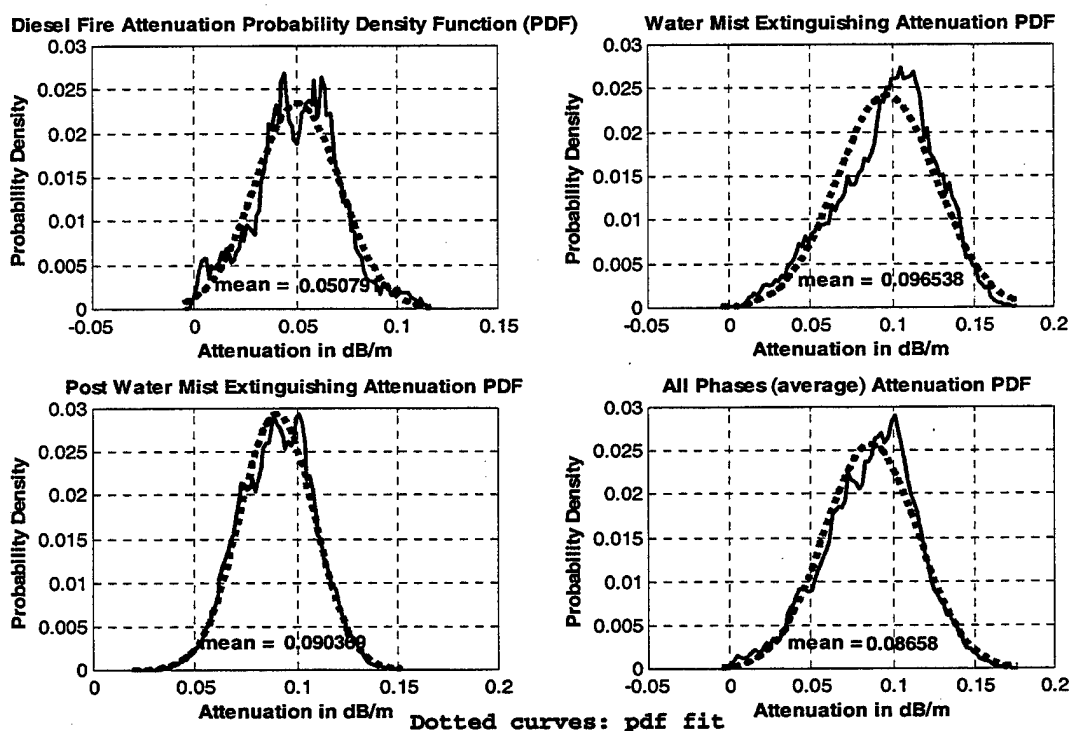


Figure 9.46b: Attenuation Probability Density Functions

The pdf's for the three phases resemble **Gaussian** distributions. For the fully developed fire (last minute of the fire phase) the mean attenuation was 0.050 dB/m . For

the water mist phase the mean attenuation was 0.096 dB/m. For the steam build-up phase the mean attenuation was 0.090 dB/m. Finally the all-phases pdf has the average attenuation of 0.086 dB/m.

The cumulative distribution functions for the attenuation for the three phases individually and the over-

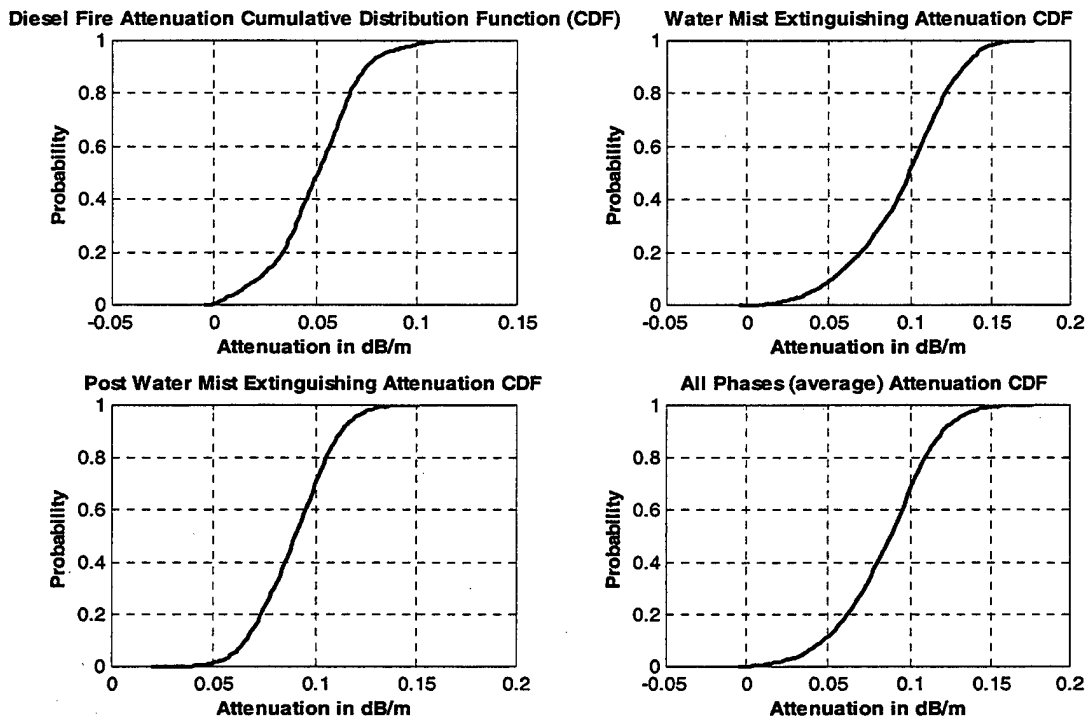


Figure 9.47: Attenuation Cumulative Distribution Functions

all cumulative distribution functions are shown in Figure 9.47. From the fire phase cdf we can determine that there is a 0.95 probability that the attenuation will be lower than 0.09 dB/m. Similarly for the water mist phase there is a 0.95 probability that the attenuation will be less than 0.14

dB/m. For the steam build-up phase the 0.95 probability holds for the attenuation less than 0.12 dB/m. This shows that the attenuation of the water mist extinguish phase causes larger attenuation than the fire itself. For all the phases there is 95% probability that the attenuation is going to be less than 0.13 dB/m.

n) Autocorrelation Functions

Our next step was to determine the attenuation correlation between different frequencies for the different phases of the experiment. Initially we estimated the frequency response autocorrelation function for the pre-fire phase. In Figure 9.48 the plot of the autocorrelation function indicates a high degree of correlation between attenuation at different frequencies. This dependency suggests that the attenuation does not vary much with frequency.

Continuing on to the fire phase the autocorrelation function plot in Figure 9.49 is similar to the pre-fire plot. The high values of correlation also follow from the results obtained from the comparison of the pre-fire and diesel fire time-averaged path loss plots. (As shown in figure IX-38 path loss for all frequency components increased in a similar way and all the minima and maxima remained at the same frequencies.) Figures IX-50 and IX-51 show the autocorrelation function plots for the water

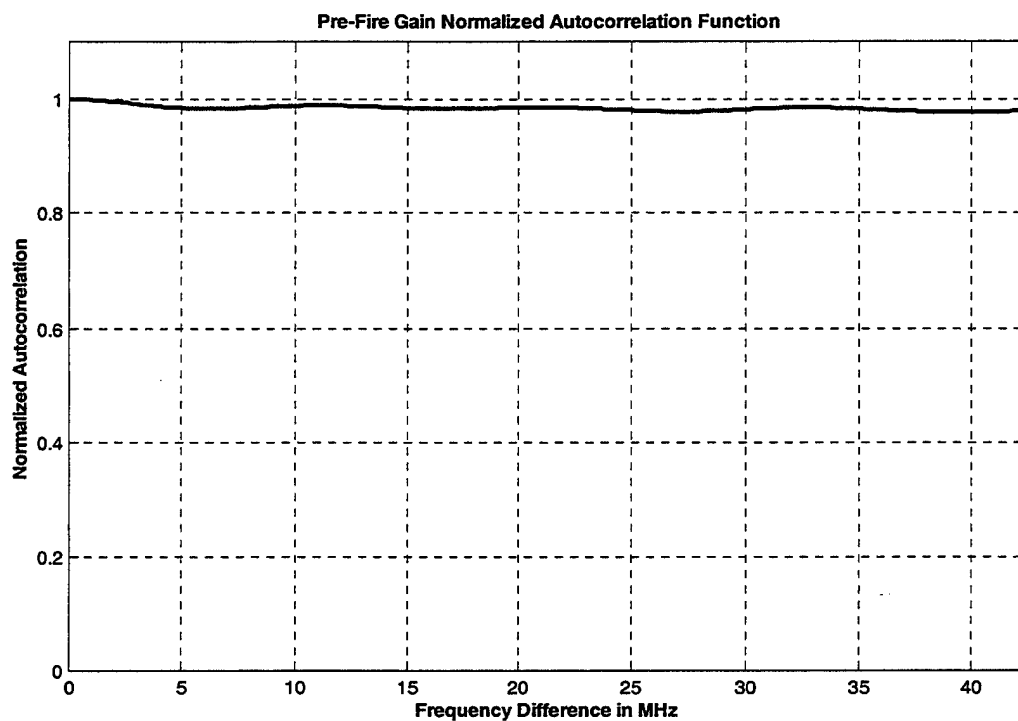


Figure 9.48: Pre Fire Gain Normalized Autocorellation Function

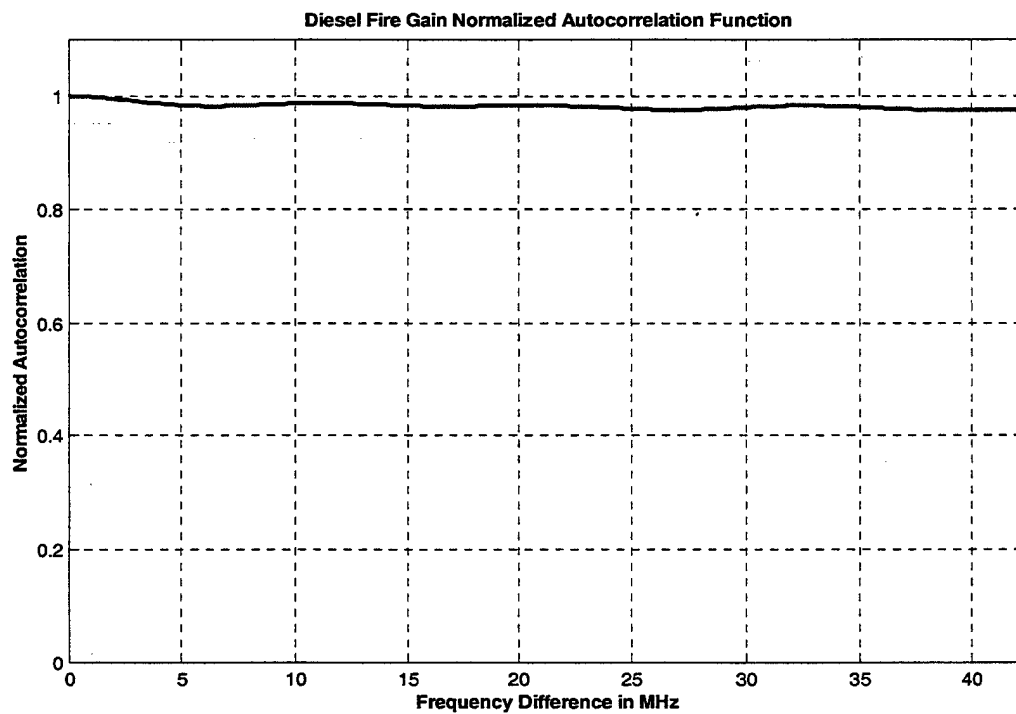


Figure 9.49: Fire Gain Normalized Autocorellation Function

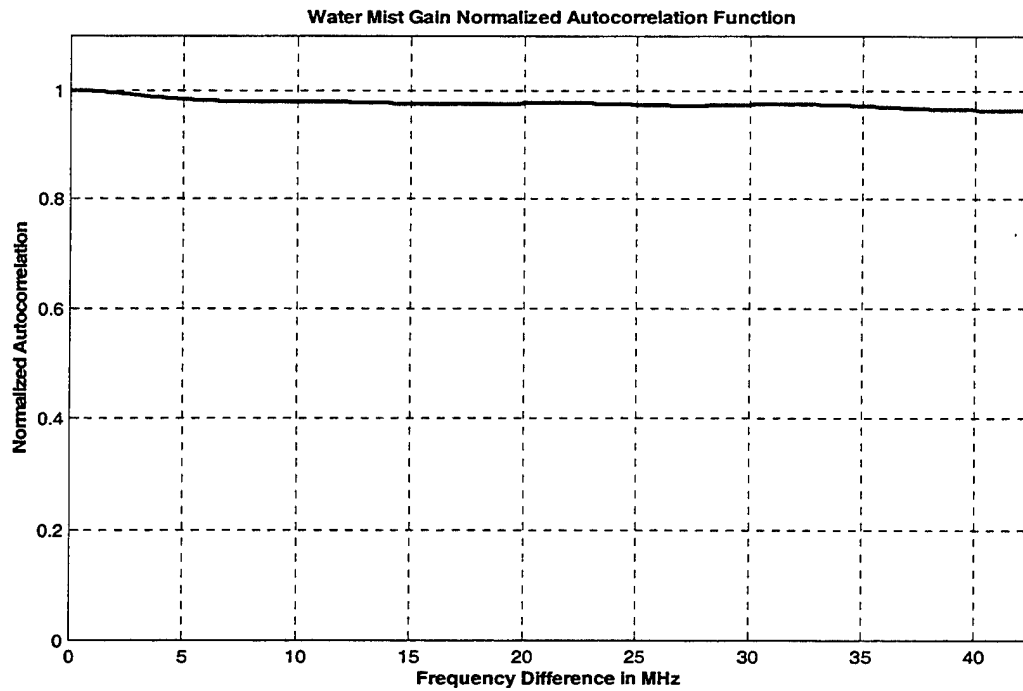


Figure 9.50: Water Mist Gain Normalized Autocorrelation Function

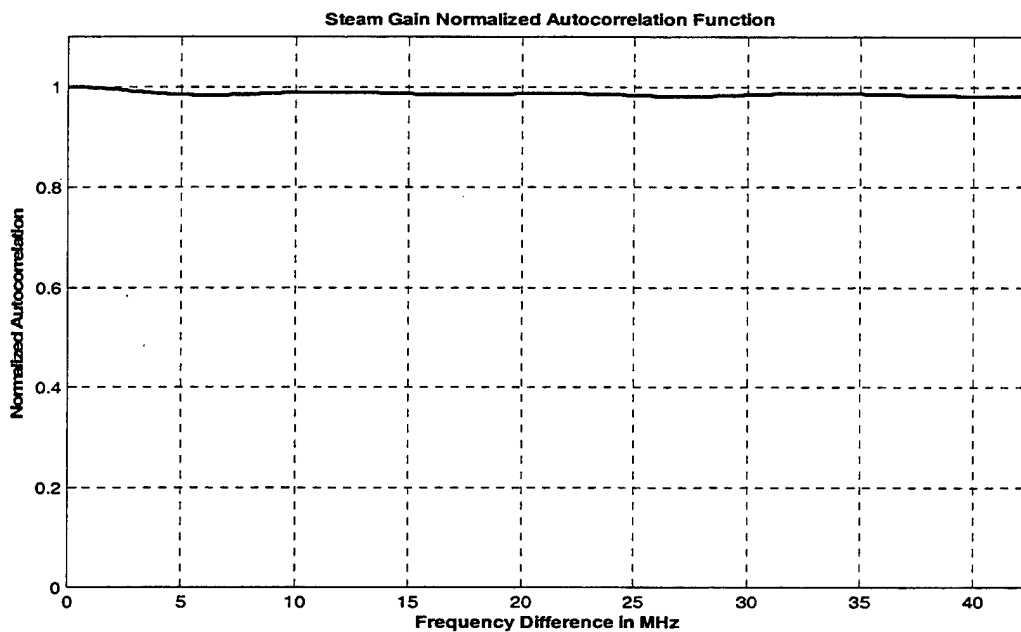


Figure 9.51: Steam Build-Up Gain Normalized Autocorrelation Function

mist and steam build-up phases. These plots are similar to the plots for the pre-fire and diesel fire phases.

The attenuation's relative invariance with frequency is the consequence of using directional antennas (the antenna beam is very narrow and a single, line-of-sight path dominates the propagation). Furthermore the attenuation due to fire, smoke, and water mist does not vary significantly over the narrow 2.4 GHz ISM frequency band.

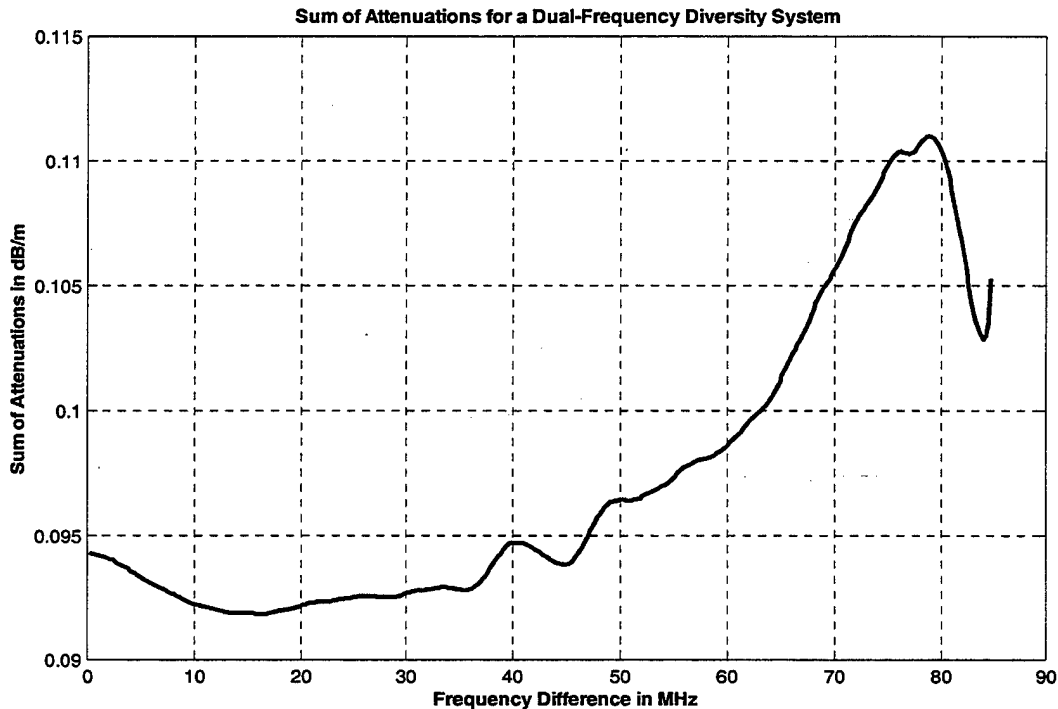


Figure 9.52: Sum of Attenuation for a Dual-Frequency Diversity System

o) Estimation of the best frequency difference

The last step was to estimate the frequency difference that, on average, would provide the least combined (sum of) attenuation. This information would be useful if a dual-frequency (diversity) transmission system was used. As seen in Figure 9.52 for the horizontally polarized antennas this frequency difference is about 13 MHz, but the changes in combined attenuation are very small. The values close to the full ISM bandwidth (85 MHz) are unreliable because of the diminishing number of frequencies averaged.

B. HEPTANE FIRE

There are two sets of measurements for the heptane fire with directional antennas:

- for vertical polarization and
- for Horizontally Polarized

The data presented and used for the statistical analysis are averages of the data collected during the four consecutive heptane fire cycles for each polarization. In this way we compensated for the reduced duration of each fire (1 minute instead of 4) such that approximately the same number of "fire" samples can be collected as for the diesel fire experiments.

1. Vertical Polarization

a) Path loss for Vertically Polarized, Directional Antennas

First the measured path loss is presented as a surface plot with the x-axis as the time axis, the y-axis as the frequency axis and the z-axis as the path loss (in dB) axis. In Figure 9.53 the path loss plot is shown for the vertically polarized directional antennas. In this figure we have also shown the phase boundary planes. From the plot we see that initially we have an approximately five minute pre-fire phase. For this phase the time has negative values

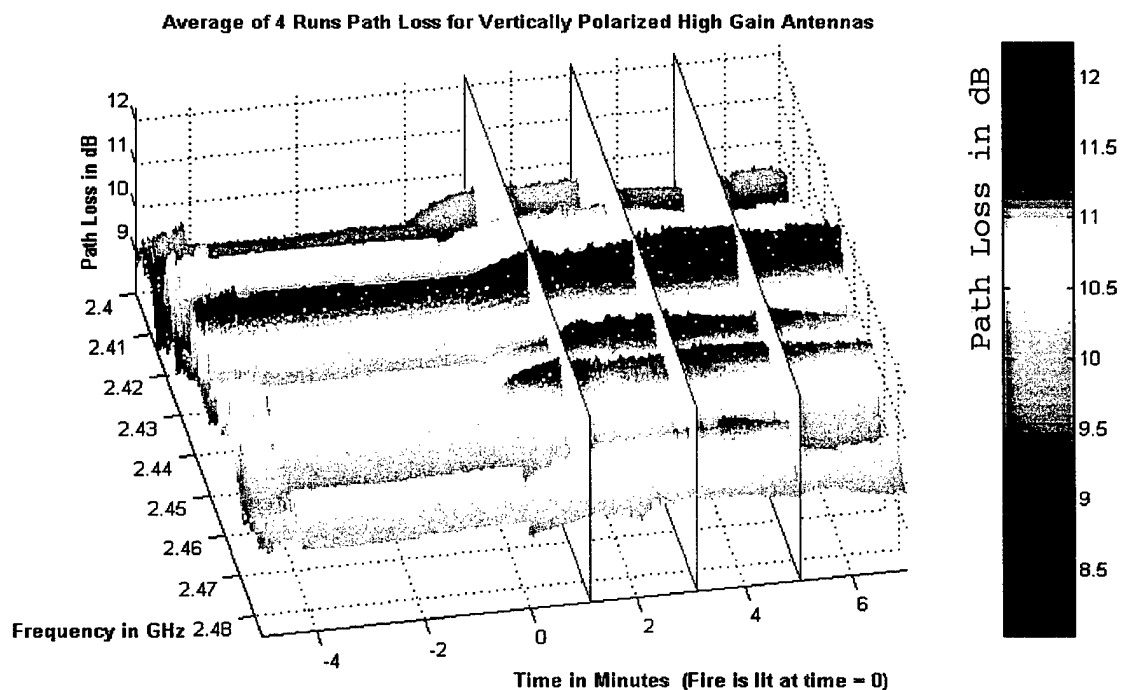


Figure 9.53: Path Loss for Vertically Polarized High Gain Antennas

going from -5 up to 0. At $t=0$ heptane fire and its measurements begin. The fire lasts for approximately one minute (minutes 0-1) followed by a two minute water mist phase (minutes 1-3), a two minute mist build-up phase (minutes 3-5), and finally the two minute ventilation phase (minutes 5-7).

In Figure 9.54 the same surface plot is shown without the phase boundaries. We note the continuity between the fire, water mist, steam build-up and ventilation phases,

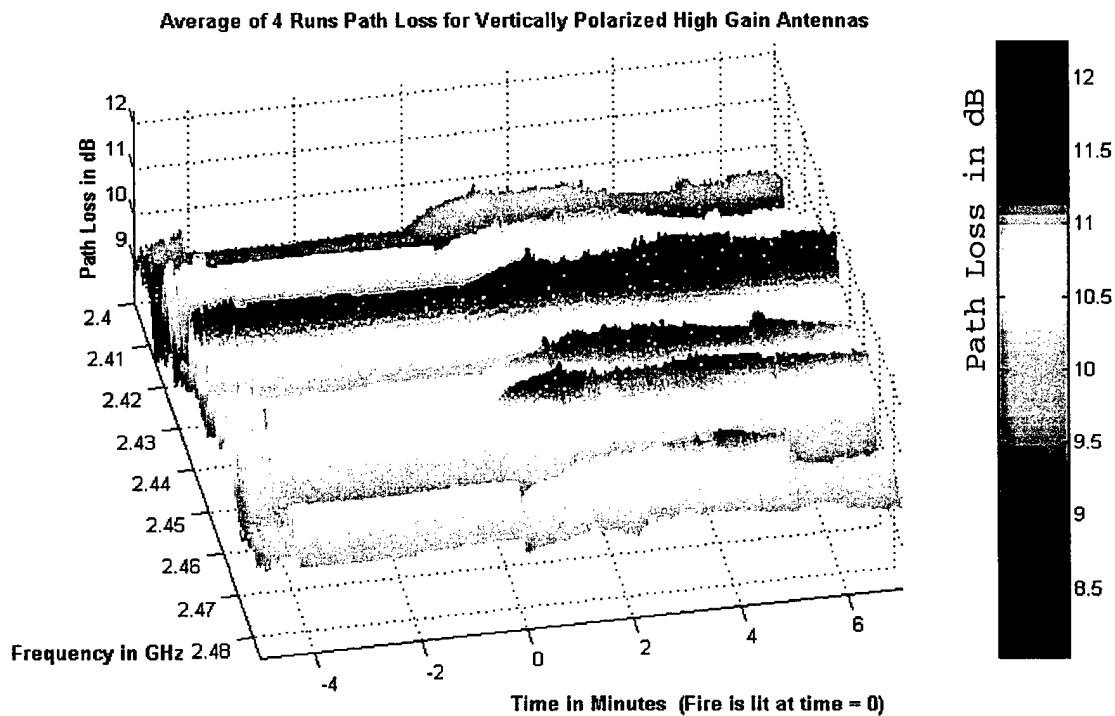


Figure 9.54: Path Loss for Vertically Polarized High Gain Antennas

and a discontinuity between the pre-fire and fire phase ($t=0$). This discontinuity is caused by the interruption in the measurement process to allow for the personnel movement in the compartment to light the fire ($t=0$). Measurements taken during this phase would not be valid since the attenuation changed with people moving between the antennas.

In Figure 9.55 the "bird's eye" view of the path loss is presented. This allows us to visualize how the path

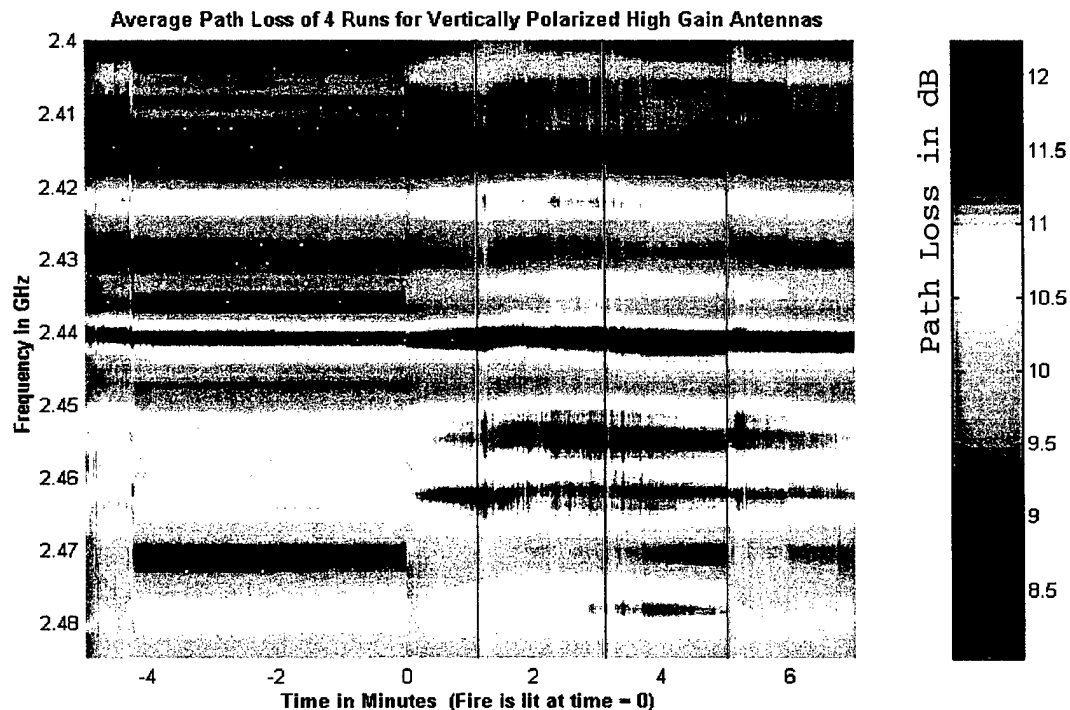


Figure 9.55: Path Loss for Vertically Polarized High Gain Antennas

loss changes with time and frequency. We note that for the five-minute pre-fire phase the path loss at each frequency has a constant value with time but is different for different frequencies. The path loss differences are mainly

caused by the reflection/absorption characteristics of the portion of the compartment that is "visible" (within the main beams) to the two antennas.

After the fire has been lit the path loss increases rapidly for all frequencies. The path loss reaches its peak during the water mist phase and then it starts falling again during the mist build-up phase. The highest measured value of the path loss was 12.2 dB. During the compartment ventilation the path loss values are significantly lower than the ones during the fire phase but higher than the values of the pre-fire phase because of the residual condensation in the compartment and on the antennas. Also, from Figure 9.55 we can see that the minima and maxima of the path loss do not shift appreciably along the frequency axis (in the vertical direction) from one phase to the next. (This is a consequence of using directional antennas.)

**b) Attenuation for Vertically Polarized,
Directional Antennas**

We next present the attenuation surface plots. To create these plots we divided each path loss value by the time-averaged pre-fire phase path loss at the corresponding frequency. The result was then divided by the distance between the antennas to obtain the attenuation per unit length. The choice of the distance to obtain the attenuation

per unit length (dB/m) requires some explanation. We selected the distance between the antennas (rather than the fire "depth") for the following reasons:

- The fire depth was ambiguous for the pressurized heptane spray sources that were used to create the fire
- The heat and smoke were distributed throughout the compartment
- The antennas were placed close to the fire sources (heptane pressure spray nozzles)
- The distance between the antennas was 7.66 meters

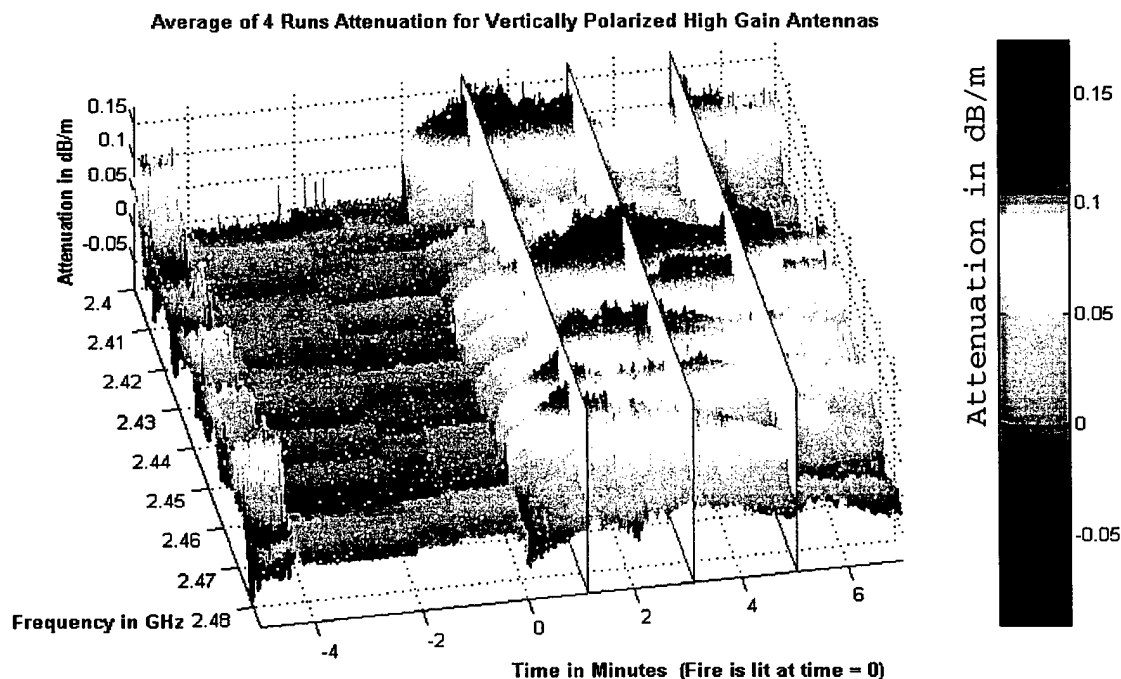


Figure 9.56: Attenuation for Vertically Polarized High Gain Antennas

In Figure 9.56 the attenuation surface plot for the vertically polarized directional antennas is shown with the phase boundary planes. For the pre-fire phase (time between -5 and 0 minutes) the attenuation is approximately 0 dB/m, as expected, since the time-averaged path loss for the pre-fire phase was used as the reference for each frequency. Therefore, during the pre-fire phase there are almost no "peaks and valleys" in the surface plot.

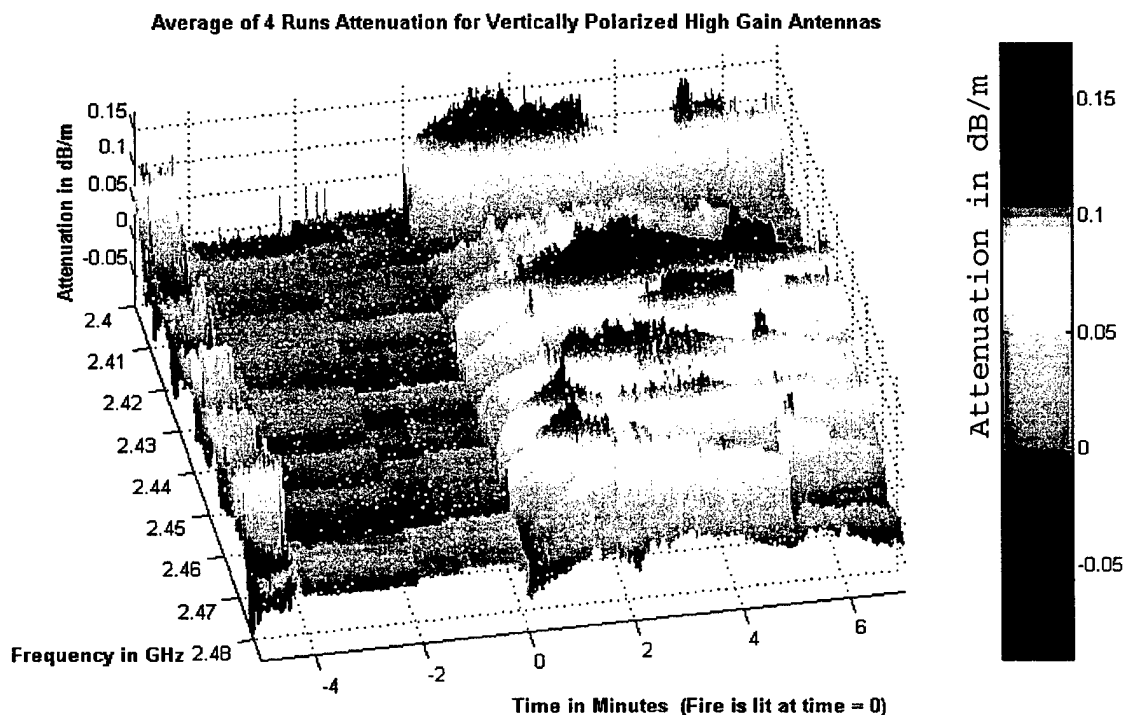


Figure 9.57: Attenuation for Vertically Polarized High Gain Antennas

In Figure 9.57 the same surface plot is shown but without the phase boundaries. In contrast to the diesel fire we note a fast increase in attenuation during the spray fire phase, because the heat and smoke build-up very quickly in the compartment. At about 1 minute after the fire was lit (from minutes 1-3), the water mist fire-extinguishing system is activated causing further increase in attenuation. After two minutes of fire extinguishing the compartment is saturated with steam and smoke (from minute 3 to 5) and the attenuation remains relatively high (but not as high as for the fire-extinguishing phase). During the ventilation of the compartment the attenuation decreases (from minute 5 on) towards the values prior to the fire (for negative time).

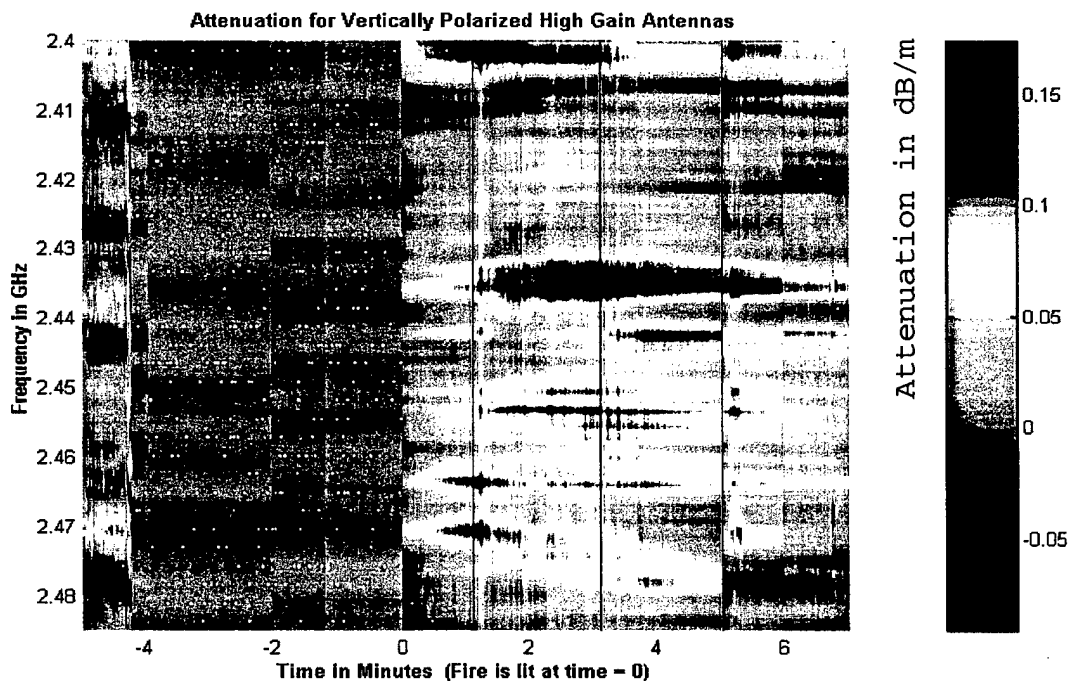


Figure 9.58: Attenuation for Vertically Polarized High Gain Antennas

In Figure 9.58 the same surface plot is shown, viewed directly from the z-axis (the "birds-eye" view) clearly showing the attenuation changes for different phases and for different frequencies.

The attenuation per meter reached its maximum value during the water mist fire extinguishing phase and (for particular frequencies) it was on the order of 0.17 dB/m. The maximum attenuation for the fire phase was on the order of 0.13 dB/m

c) Frequency-Averaged Path Loss for Vertically Polarized Directional Antennas

The first statistical analysis we performed was to determine the frequency-averaged path loss. As shown in Figure 9.59 the frequency-averaged path loss for the pre-fire phase is almost constant at around 9.8dB. A small discontinuity during the pre-fire phase ($t=-1.2$) is also visible. The most likely explanation for this is that it was due to the door located behind one of the antennas that was open initially during the pre-fire at one of the four fire runs and then closed (the door was used to get access to the compartment by the person starting the fire). After the fire was lit the frequency-averaged path loss increased with time. The rate of increase was very high because of the high intensity of the heptane "spray" fire. After the water mist system was turned on the frequency-average path loss increased rapidly.

During this phase the frequency-averaged path loss reached its peak value of $\sim 10.3\text{dB}$. The steam created from the burning spray fire caused the initial spike. The fire was actually put out by cutting the fuel feed. Upon extinguishing the fire the steam production rate reduced drastically, quickly reducing the path loss. The averaged path loss started to decrease slowly during the steam build-up and ventilation phases.

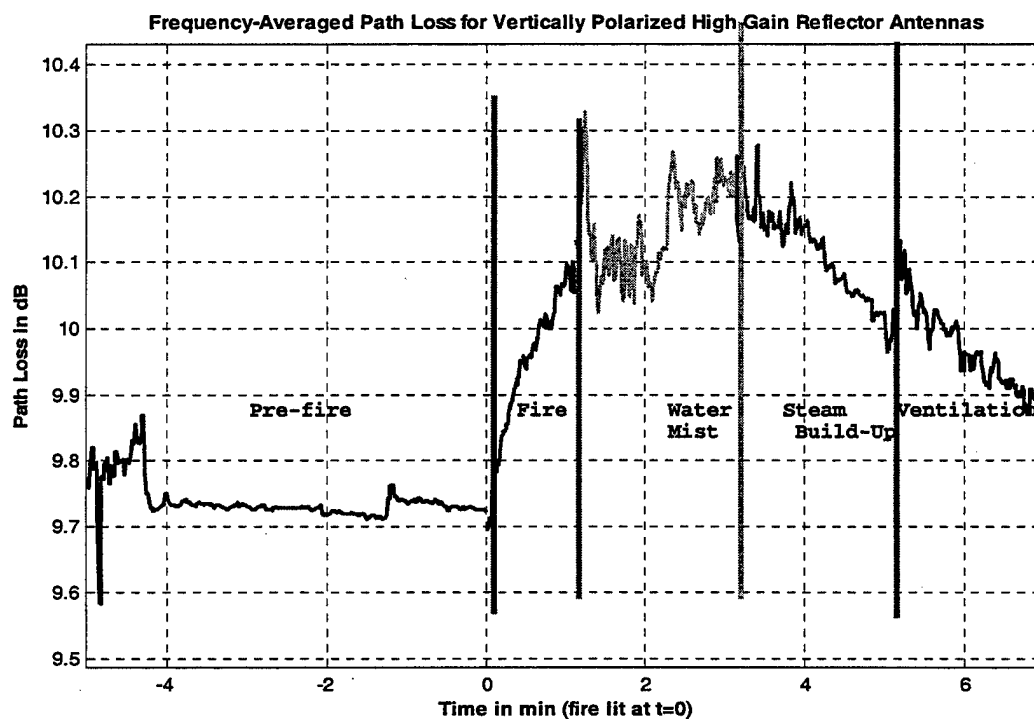


Figure 9.59: Frequency-Averaged Path Loss for Vertically Polarized High Gain Antennas

d) Frequency-Averaged Attenuation for Vertically Polarized Directional Antennas

Our next step was to determine the frequency-averaged attenuation in dB/m. The shape of the frequency-averaged attenuation as a function of time is exactly the same as the path loss, as shown in Figure 9.60. The only difference between the frequency-averaged attenuation and the frequency-averaged path loss is the division by a constant distance. The maximum frequency-averaged attenuation is approximately 0.075 dB/m. During the fire phase the frequency-averaged attenuation did not exceed 0.045 dB/m.

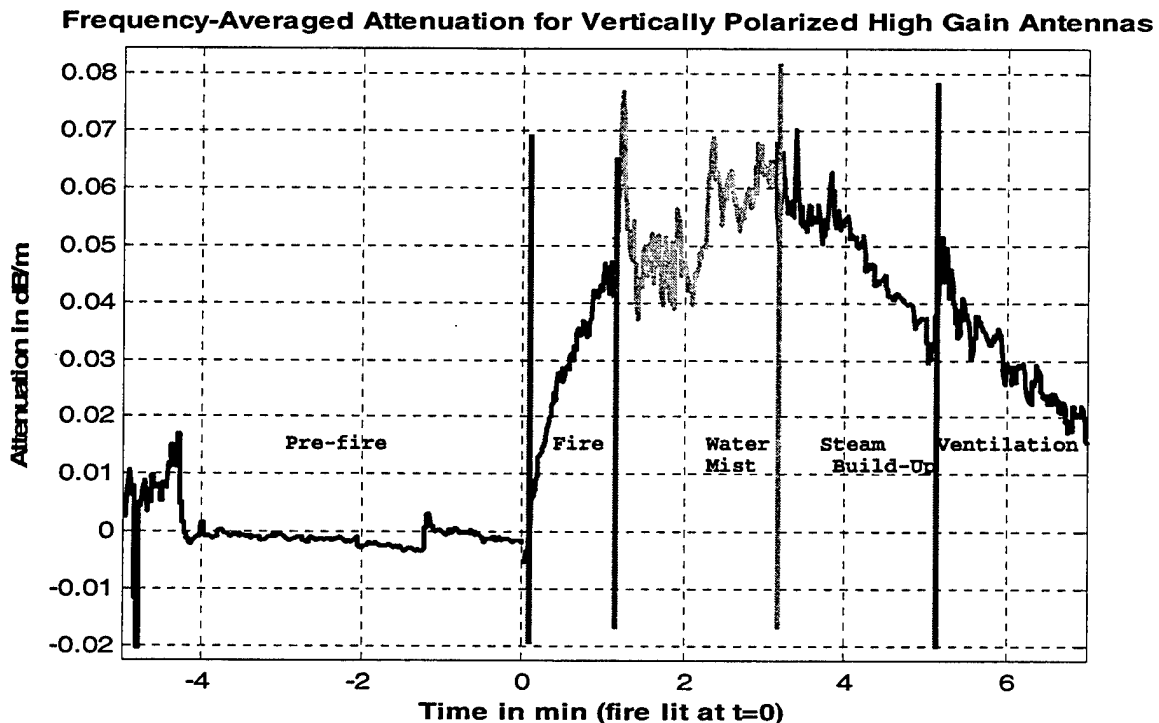


Figure 9.60: Frequency-Averaged Attenuation for Vertically Polarized High Gain Antennas

e) *Temperature vs. Time for Vertically Polarized Directional Antennas*

The average temperature taken, during the first minute of fire, at four different locations in the compartment is shown in Figure 9.61 as a function of time. The highest temperature is for the data taken at an elevation of 11 feet and at the horizontal distance of 3 feet from the pan. The maximum temperature is approximately 240° C. The second highest curve (counting from the highest temperature curve) is for the data taken at the height of 7ft and for the horizontal distance from the fuel pan of 3 feet. The maximum temperature at this height is 45° C. The two lowest curves are for the temperature next to the two antennas. We note that the temperature next to the transmitting antenna reached a maximum of approximately 45° C and that the temperature at the receiving antenna reached a maximum of approximately 40°C. The antennas withstood these temperatures (for fires of short duration) without damage. Note that there were no flame temperature measurements because we had a heptane "spray" fire and we there was no burning fuel surface whose temperature could be measured.

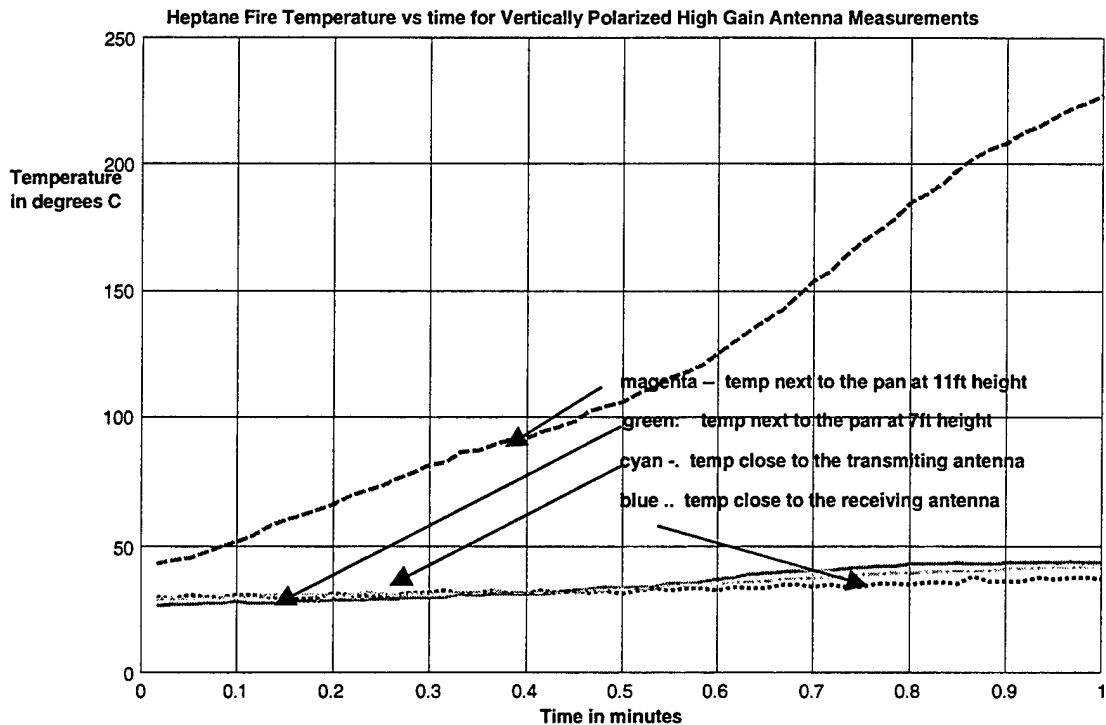


Figure 9.61: Heptane Fire Temperature versus Time for Vertically Polarized High Gain Antennas

f) Scaled Attenuation and Temperature vs. Time for Vertically Polarized Directional Antennas

Our next objective was to determine if there was a relation between the temperature increase close to the antennas and the attenuation increase. To accomplish this we subtracted the mean values from the attenuation and the temperature data. Next we determined an average coefficient which, when multiplied with the time-varying temperature data, would yield the best "curve fit" for the time-varying attenuation. A very close relation between the temperature

increase and the attenuation increase is evident in Figure 9.62.

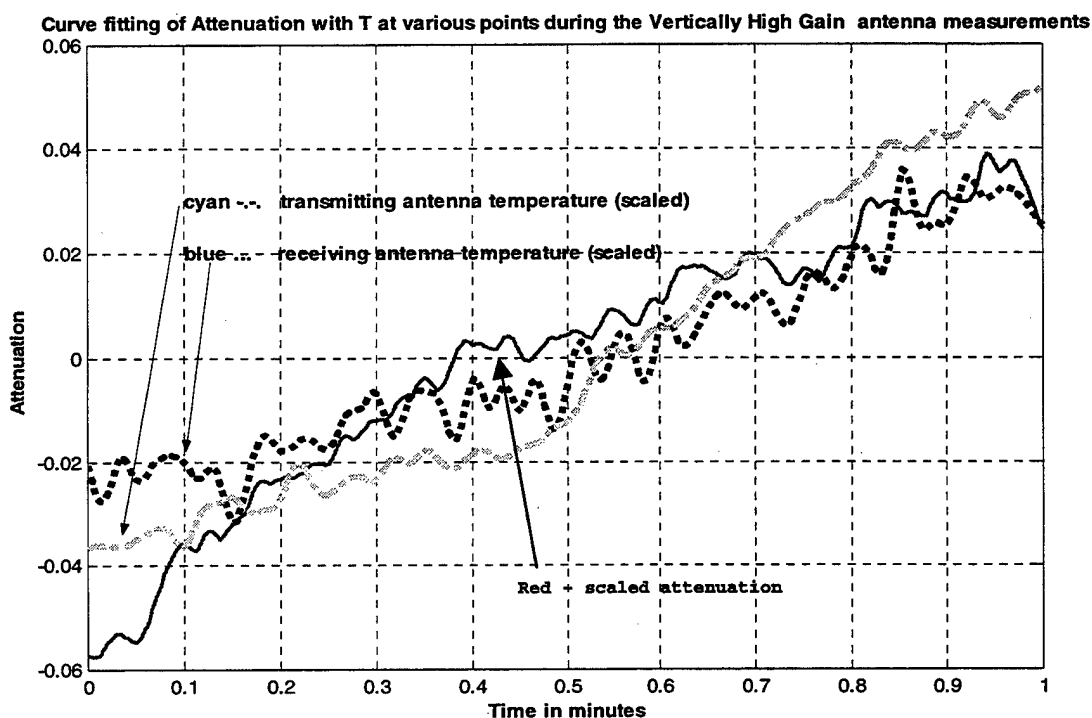


Figure 9.62: Heptane Fire Scaled Attenuation and Temperature versus time for Vertically Polarized High Gain Antennas

g) Heptane Fire Time-Averaged Path Loss for Vertically Polarized Directional Antennas

Our next step was to calculate the time-averaged path loss during the fire phase. As shown in Figure 9.63 the time-averaged path loss ranged between 8.5 and 11.7 dB, a variation (with frequency) of close to 3 dB. The plot also shows the minimum and maximum values of path loss for each frequency component. The maximum path loss of 11.9dB occurs at 2.442 GHz and the minimum path loss of 8.3dB occurs at

2.415 GHz. The maximum path loss is at the same frequency as for the diesel fire experiments.

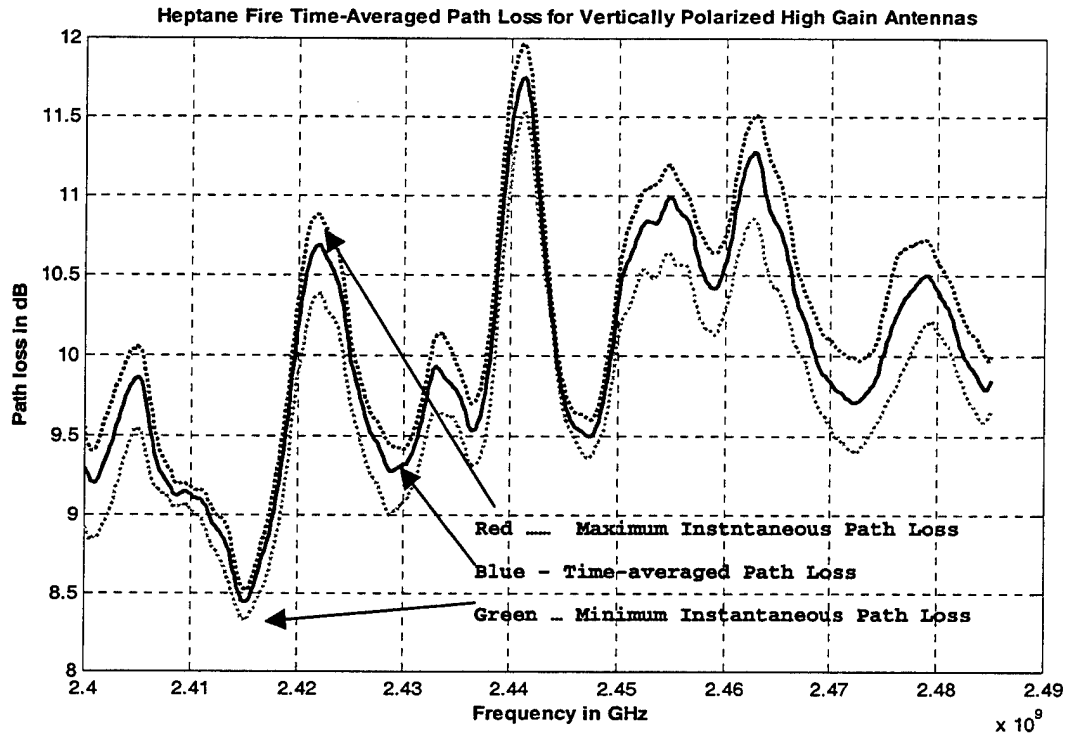


Figure 9.63: Heptane Fire Time-Averaged Path Loss for Vertically Polarized High Gain Antennas

The maximum and minimum path loss curves follow the time-averaged attenuation curve, that is the zero slope points for all three curves are located at the same frequencies.

In Figure 9.64 the time-averaged path loss curve for the fire and the pre-fire phases are shown in order to assess the effects of fire. Again the minima and maxima of the path loss are located at the same frequencies. This indicates that there is no change in the propagation

characteristics of the compartment due to the fire except that there is an increase between 0 and 1 dB (depending on the frequency) of the time-averaged path loss, caused by the fire.

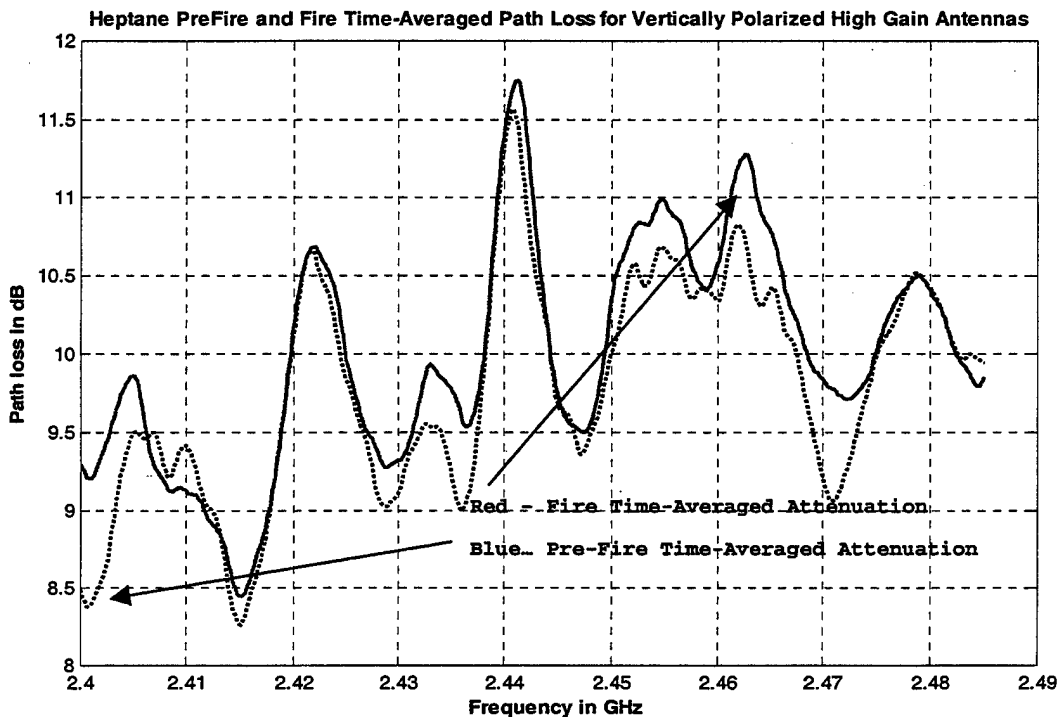


Figure 9.64: Heptane Pre-Fire and Fire Time-Averaged Path Loss for Vertically Polarized High Gain Antennas

h) Heptane Fire Time-Averaged Attenuation for Vertically Polarized Directional Antennas

The time-averaged attenuation per meter during the fire phase is shown in Figure 9.65. The maximum attenuation is at 2.4 GHz. The maximum time-averaged attenuation is 0.11 dB/m. The minimum attenuation for each frequency component

is below the 0dB axis indicating a small gain of about -0.02 dB/m. This is the consequence of the small path loss drop, caused by the closing of the compartment doors at the start of the fire phase.

Heptane Fire Time-Averaged Attenuation for Vertically Polarized High Gain Antennas

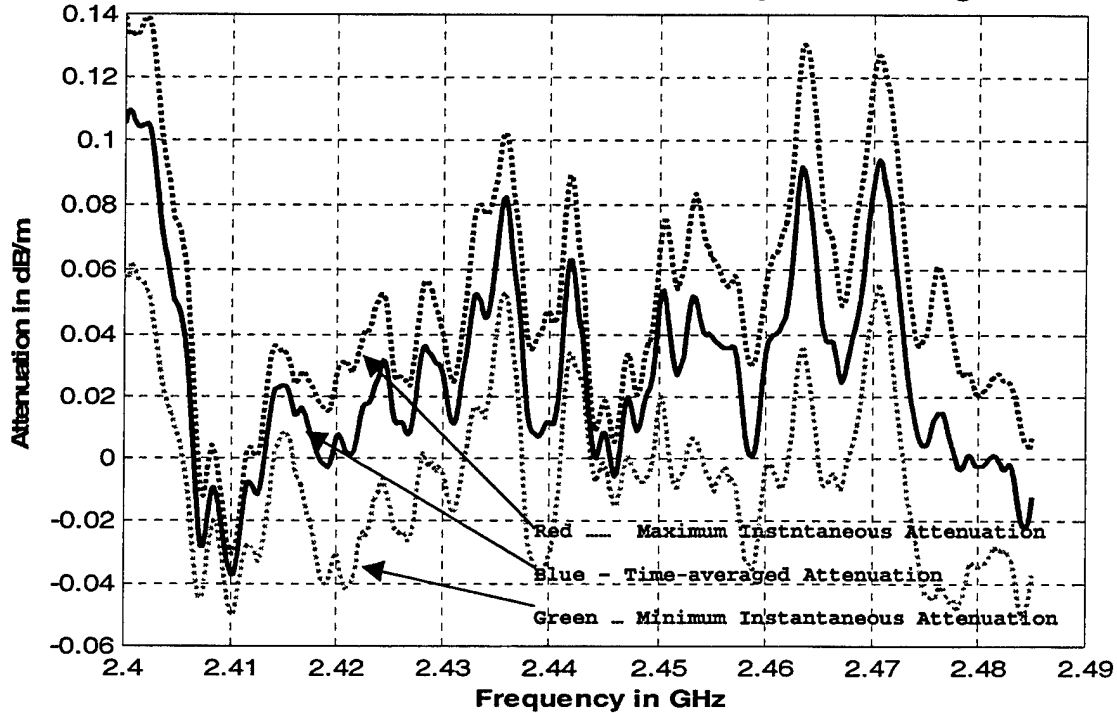


Figure 9.65: Heptane Fire Time-Averaged Attenuation for Vertically Polarized High Gain Antennas

i) Water Mist Phase Time-Averaged Path Loss for Vertically Polarized Directional Antennas

Our next step was to calculate the time-averaged path loss during the water mist phase. As shown in Figure 9.66 the time-averaged path loss ranged between 8.7 and 11.5dB, again a variation of close to 3dB. The maximum time-averaged path loss of 11.8dB occurs at 2.442 GHz and the

minimum path loss of 8.7dB occurs at 2.415 GHz, the same frequencies as for the fire phase. Also the zero slope points for all three curves (min, max and average path loss) occur at the same frequencies.

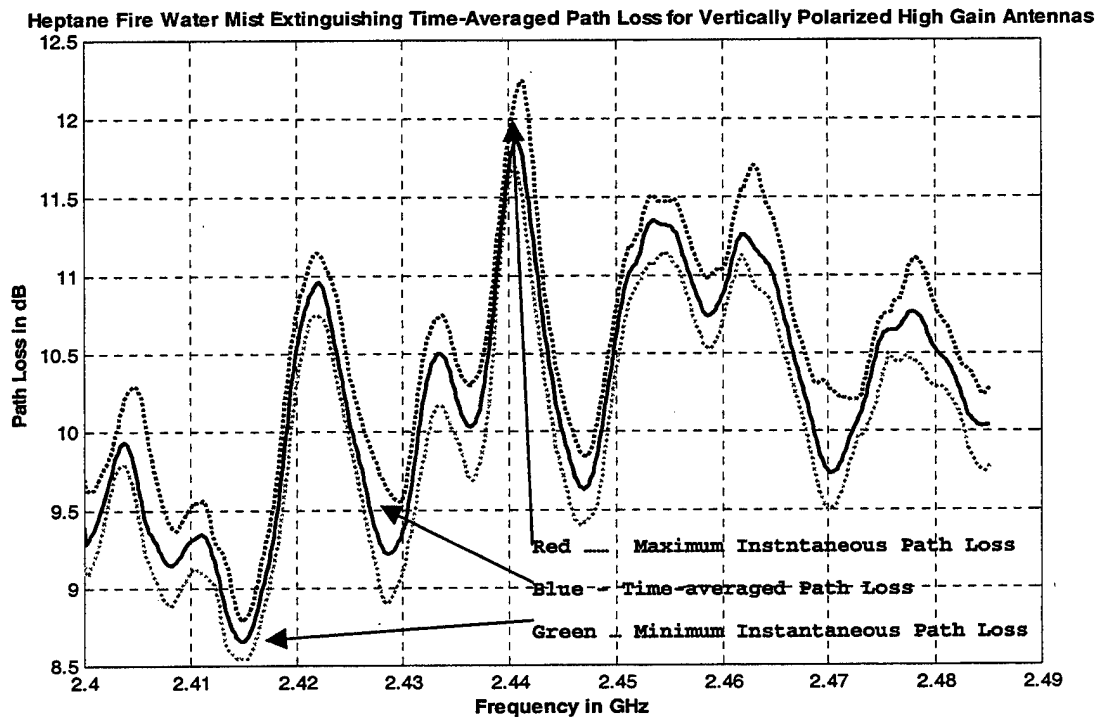


Figure 9.66: Heptane Fire Water Mist Extinguishing Time-Averaged Path Loss for Vertically Polarized High Gain Antennas

The time-averaged path loss curves for the water mist and the pre-fire phases are shown in Figure 9.67. Again the zero slope points are located at the same frequencies. This indicates that there is no change in the compartment propagation characteristics between the two phases. During the water mist phase there is an increase of 0.5 to 1dB for the time-averaged path loss.

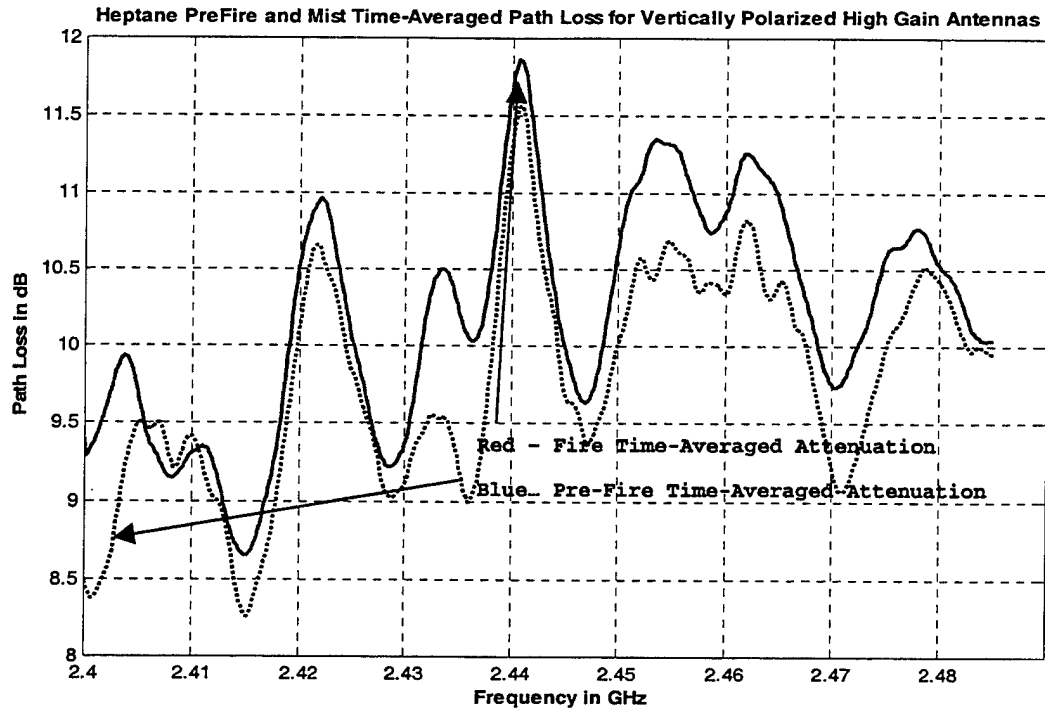


Figure 9.67: Heptane Pre-Fire and Mist Time-Averaged Path Loss for Vertically Polarized High Gain Antennas

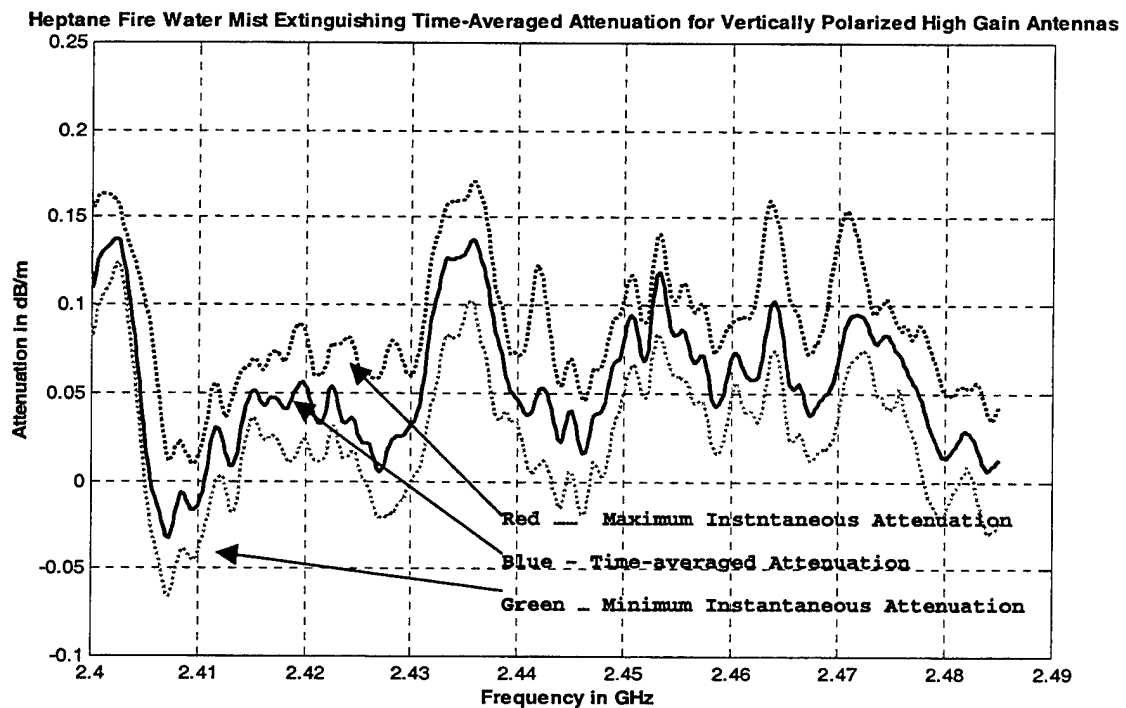


Figure 9.68: Heptane Fire Water Mist Extinguishing Time-Averaged Attenuation for Vertically Polarized High Gain Antennas

j) Water Mist Time-Averaged Attenuation for Vertically Polarized Directional Antennas

The time-averaged attenuation per meter for the water mist phase is shown in Figure 9.68. The time-averaged attenuation ranges between -0.02 and 0.14 dB/m. The maximum instantaneous attenuation of 0.17 dB/m occurs at 2.402 GHz.

Heptane Fire Post Water Mist Extinguishing Time-Averaged Path Loss for Vertically Polarized High Gain Antennas

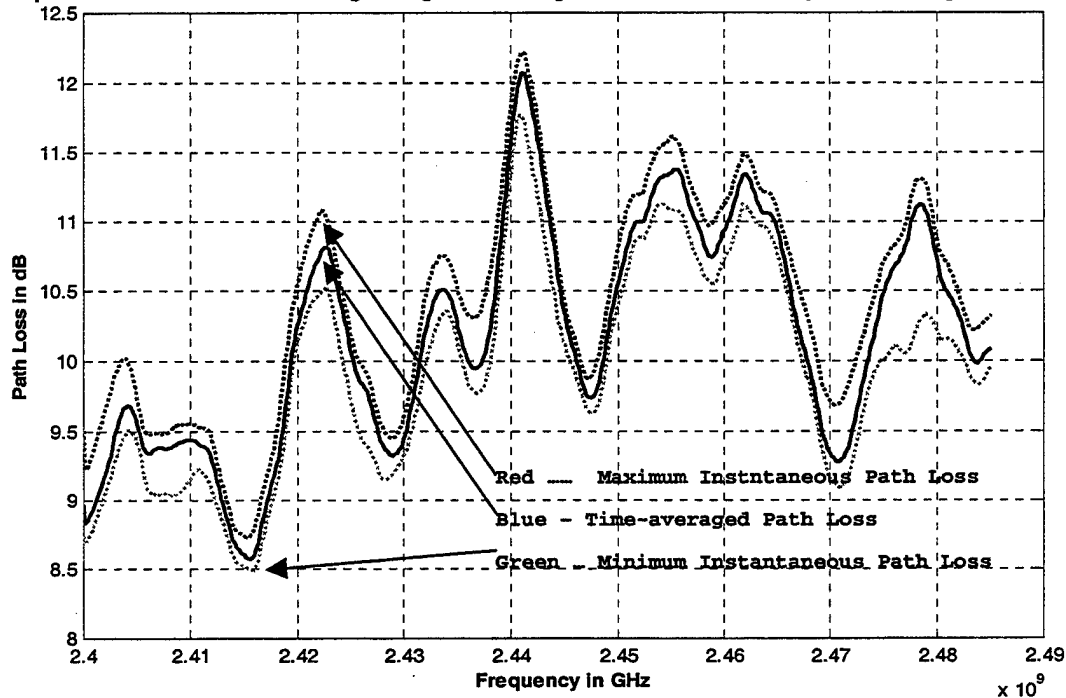


Figure 9.69: Heptane Fire Steam Build-Up Time-Averaged Path Loss for Vertically Polarized High Gain Antennas

k) Steam Build Up Phase Time-Averaged Path Loss for Vertically Polarized Directional Antennas

Next we calculated the time-averaged path loss for the steam build-up phase. As shown in Figure 9.69 the time-averaged path loss ranged between 8.6 and 12.1dB, a 3.5dB variation. Also shown on the same plot are the minimum and

maximum values of the path loss for each frequency. The maximum path loss of 12.2 occurs at 2.442 GHz and the minimum path loss of 8.5dB occurs at 2.415 GHz, the same frequencies as for the fire phase. Again the zero slope points for all three curves are located at the same frequencies, indicating that the "frequency response" for the path between the antennas does not change depending on whether there is fire or water mist in the compartment except for the path loss increase or decrease ("scaling").

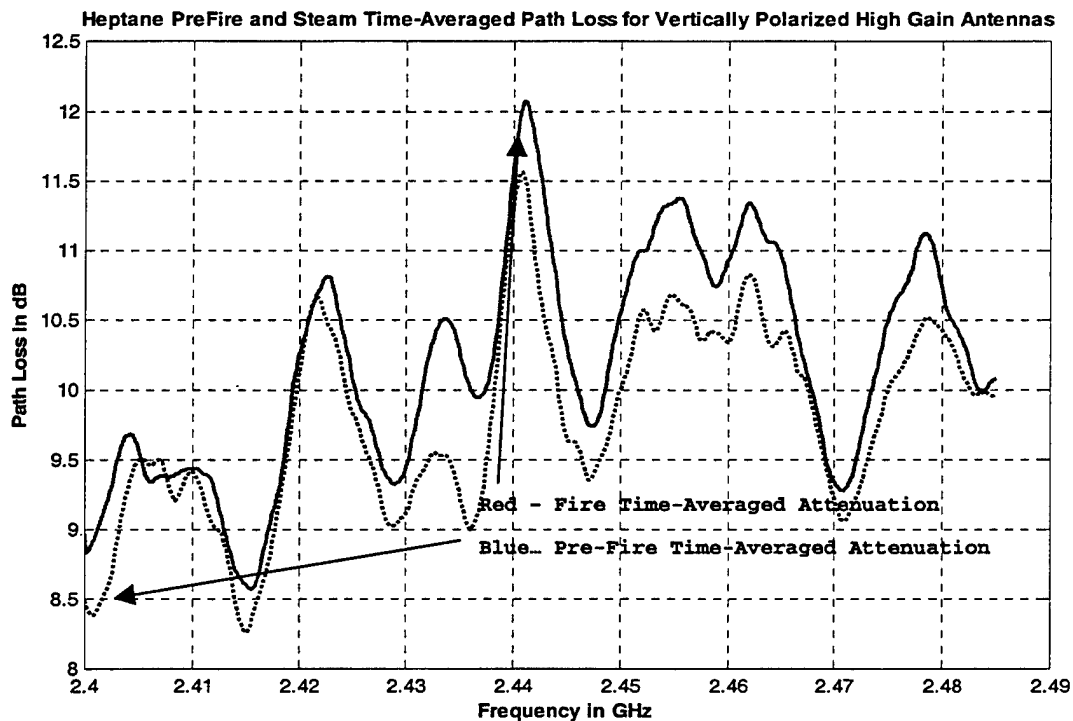


Figure 9.70: Heptane Pre-Fire and Steam Build-Up Time-Averaged Path Loss for Vertically Polarized High Gain Antennas

In Figure 9.70 the time-averaged path loss curves for the steam build-up and the pre-fire phases are shown. Again the zero slope points (maxima and minima) are located at the same frequencies. This indicates that there is no change in the compartment propagation characteristics except for the additional path loss of between 0.2 and 1.0 dB due to the residual steam and smoke in the compartment.

Heptane Fire Post Water Mist Extinguishing Time-Averaged Attenuation for Vertically Polarized High Gain Antennas

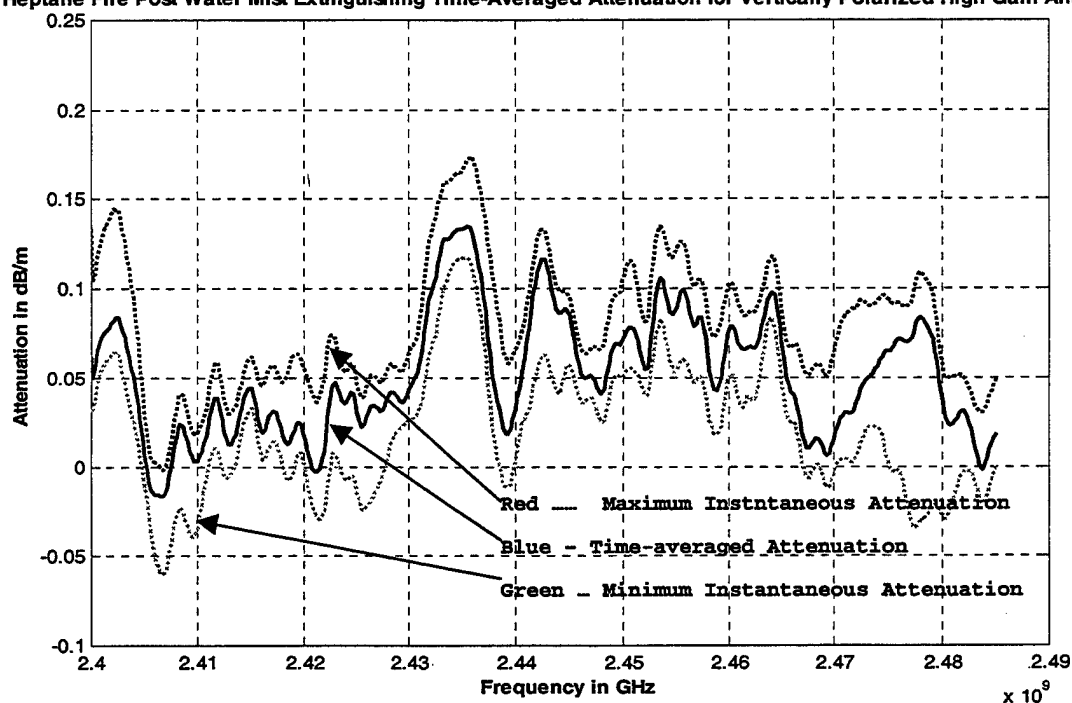


Figure 9.71: Heptane Fire Steam Build-Up Time-Averaged Attenuation for Vertically Polarized High Gain Antennas

1) Steam Build-Up Time-Averaged Attenuation for Vertically Polarized Directional Antennas

In Figure 9.71 the time-averaged attenuation per meter during the steam build-up phase shows that the maximum

attenuation of 0.17 dB/m occurs at 2.435 GHz. The value of the time-averaged attenuation per meter vary between -0.01 and 0.13 dB/m, slightly lower than the values measured for the mist build-up phase.

m) Ventilation Phase Time-Averaged Path Loss for Vertically Polarized Directional Antennas

The time-averaged path loss for the ventilation phase is shown in Figure 9.72. The time-averaged path loss ranged between 8.5 and 11.8 dB. Also shown on the same plot are the minimum and maximum values of the attenuation for each frequency. The maximum path loss of 12 dB occurs at 2.442 GHz and the minimum path loss of 8.3dB occurs at 2.403 GHz, the same frequencies as for the fire phase. Again the zero slope points for all three curves are located at the same frequencies.

In Figure 9.73 the time-averaged path loss curve for the ventilation and the pre-fire phases are shown. Again the zero slope points (maxima and minima) are located at the same frequencies. This indicates that there is no change in the compartment propagation characteristics except for the additional path loss of between 0 and 0.8 dB due to the residual steam and smoke in the compartment.

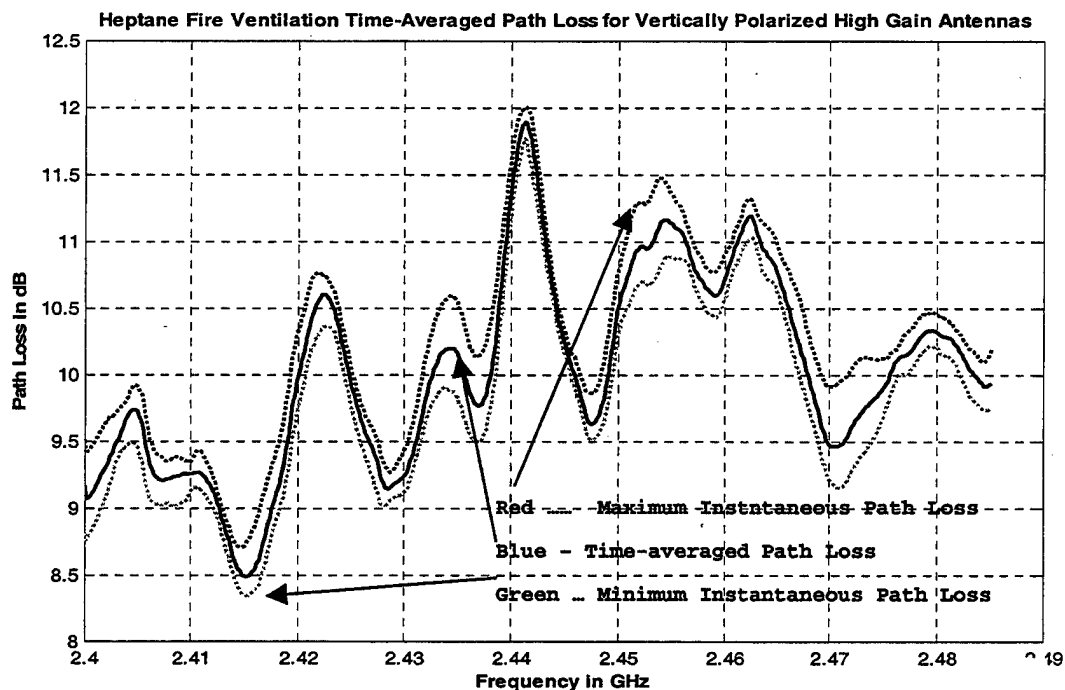


Figure 9.72: Diesel Fire Ventilation Time-Averaged Path Loss for Vertically Polarized High Gain Antennas

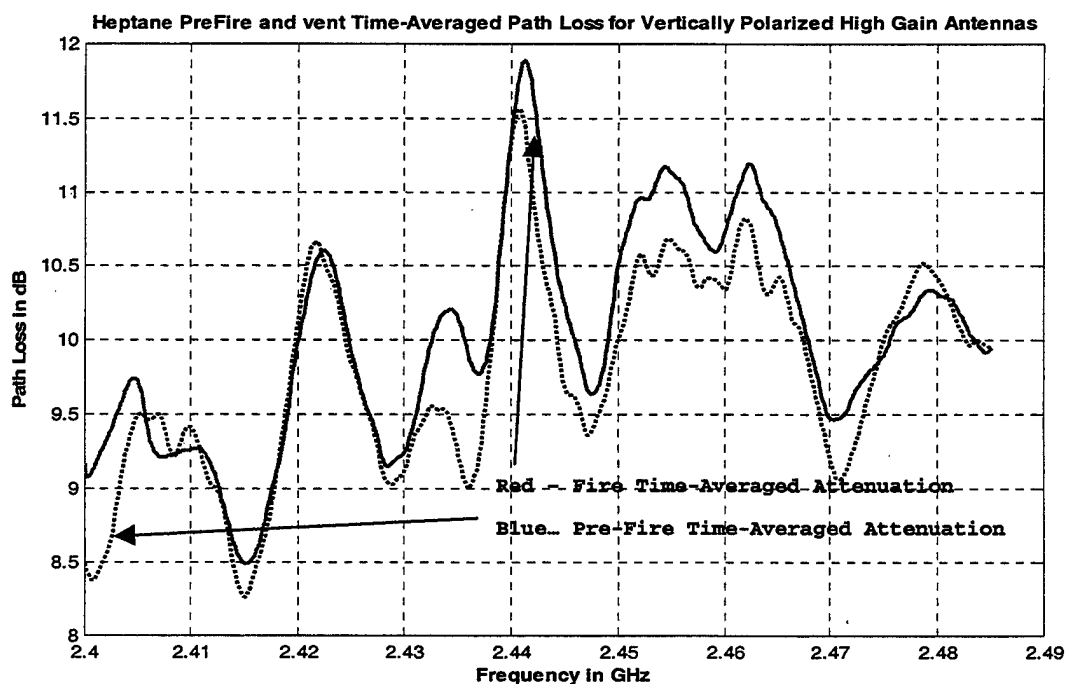


Figure 9.73: Diesel Pre-Fire and Ventilation Time-Averaged Path Loss for Vertically Polarized High Gain Antennas

n) Ventilation Phase Attenuation for Vertically Polarized Directional Antennas

In Figure 9.74 the time-averaged attenuation per meter during the ventilation phase shows that the maximum attenuation occurs at 2.415 GHz. The values of the time-averaged attenuation per meter vary between -0.04 and 0.12 dB/m, slightly lower than the values measured for the steam build-up phase.

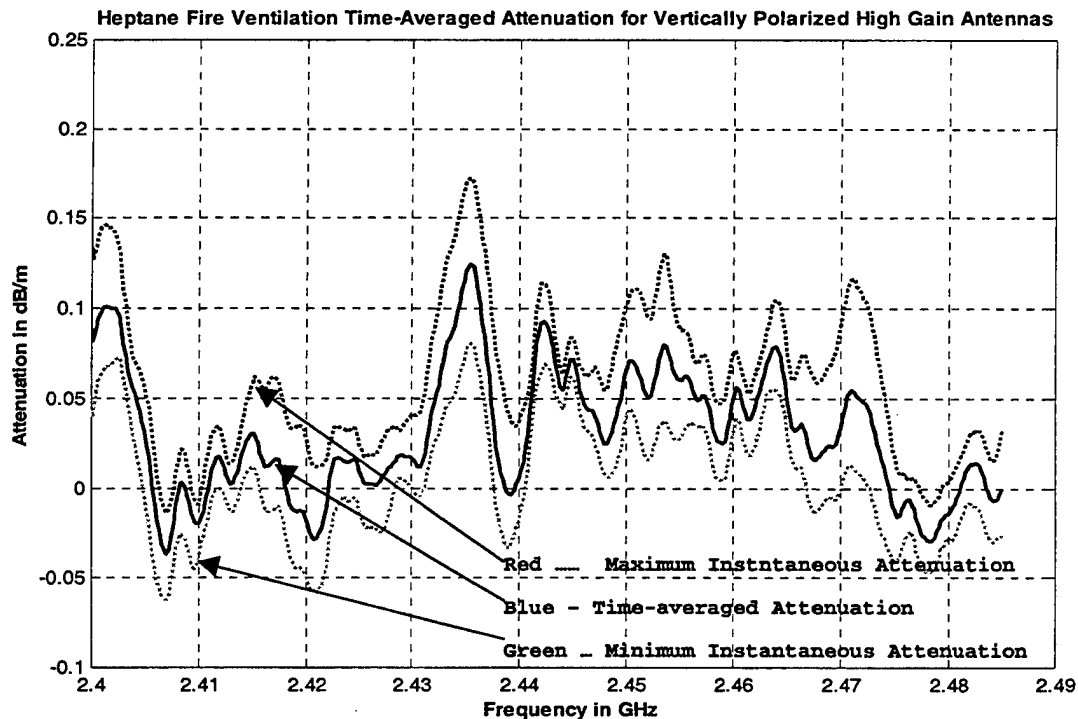


Figure 9.74: Diesel Fire Ventilation Time-Averaged Attenuation for Vertically Polarized High Gain Antennas

o) Attenuation Probability Density Functions for Vertically Polarized Directional Antennas

The attenuation probability density functions (pdf) for each frequency scan for the vertically polarized directional antennas are shown in Figure 9.75a. The plot shows that the pdf vary with time and that the attenuation caused by fire and the follow on phases is non stationary.

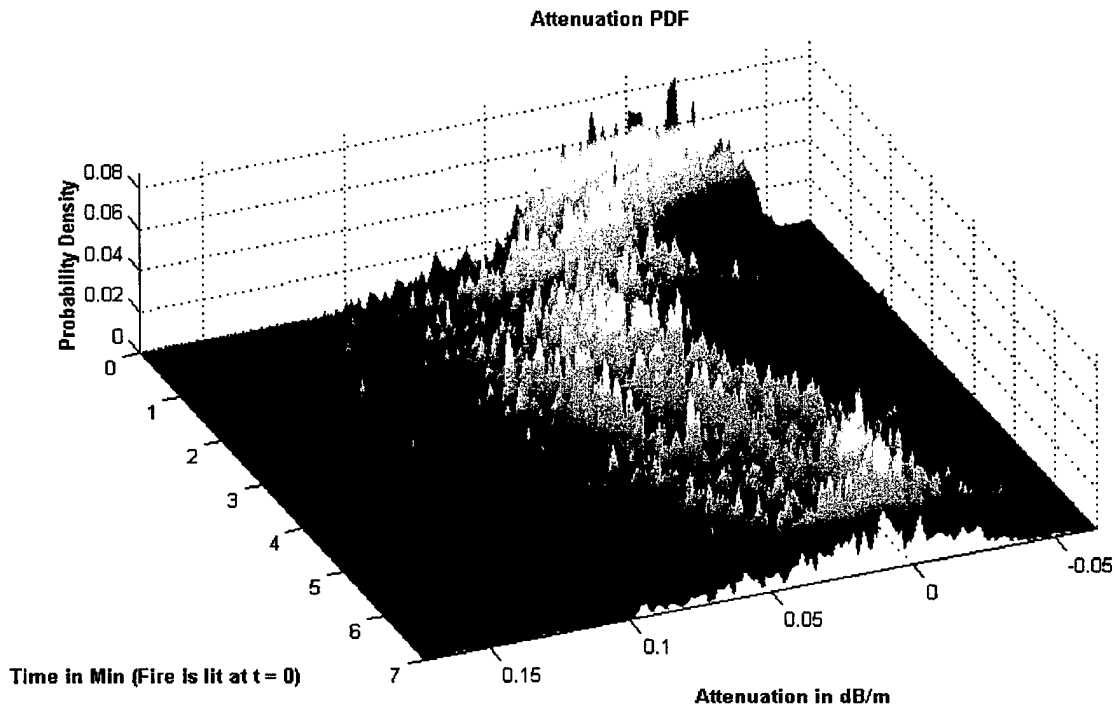


Figure 9.75a: Attenuation Probability Density Functions

Initially, when the fire was lit at $t=0$ the attenuation has about 0 dB mean and a large standard deviation. As the fire develops the pdf shifts towards higher attenuation values and the standard deviation of the

pdf increases. At $t=1$, when the water mist extinguishing system is turned on, the pdf shifts abruptly towards even higher attenuation values and the standard deviation increases further. At $t=3$, when the water mist extinguishing system is turned off, the pdf starts shifting back towards lower attenuation values, but the standard deviation remains high. Because of the non-stationarity of the pdf's the time-averaged pdf's are presented. For the fire phase, the averaging is done over the last minute of the fire phase, corresponding to the "fully developed" fire/smoke while for the other phases pdf's for the entire phases are time-averaged.

The attenuation probability density functions for the four phases (fire, water mist, steam build-up, and ventilation) for the vertically polarized directional antennas during the heptane fire experiments are shown in figures IX-75. Also, the "average" attenuation probability density function for all phases is shown in Figure 9.76. The pdf's for the four phases resemble Gaussian distributions. For the fully developed fire (last minute of the fire phase) the mean attenuation was 0.030 dB/m. For the water mist phase the mean attenuation was 0.054 dB/m. For the steam build-up phase the mean attenuation was 0.051 dB/m. For the ventilation phase the mean attenuation was 0.030 dB/m.

Finally the all-phases pdf has the average attenuation of 0.043 dB/m.

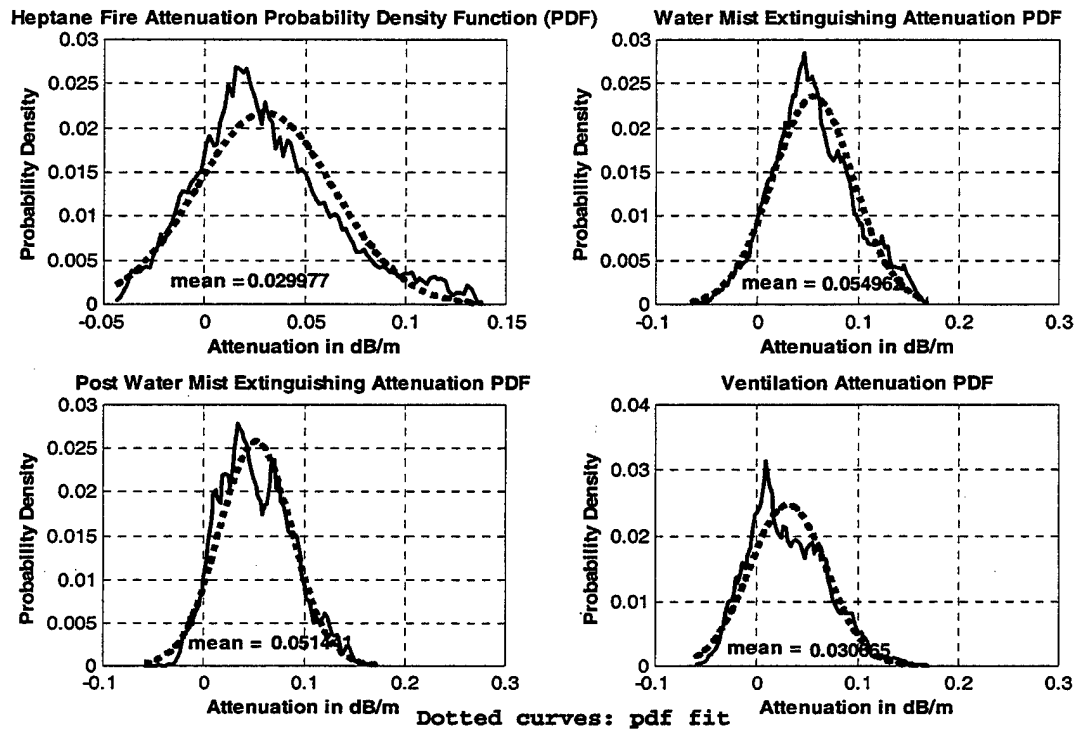


Figure 9.75b: Attenuation Probability Density Functions

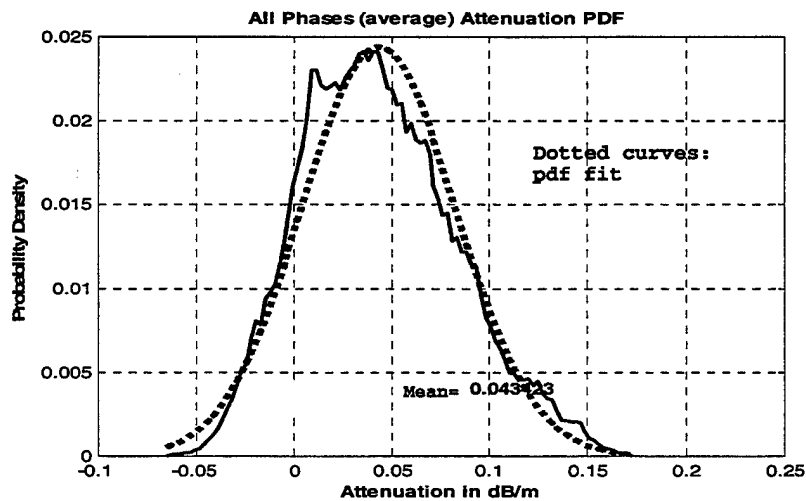


Figure 9.76: Attenuation Average Probability Density Functions

The cumulative distribution functions for the attenuation for the four phases individually and the overall cumulative distribution function are shown in figures IX-77 and IX-78. From the fire phase cdf we can determine that there is a 0.95 probability that the attenuation will be lower than 0.1 dB/m. Similarly for the water mist phase there is a 0.95 probability that the attenuation will be less than 0.13 dB/m. For the steam build-up phase the 0.95

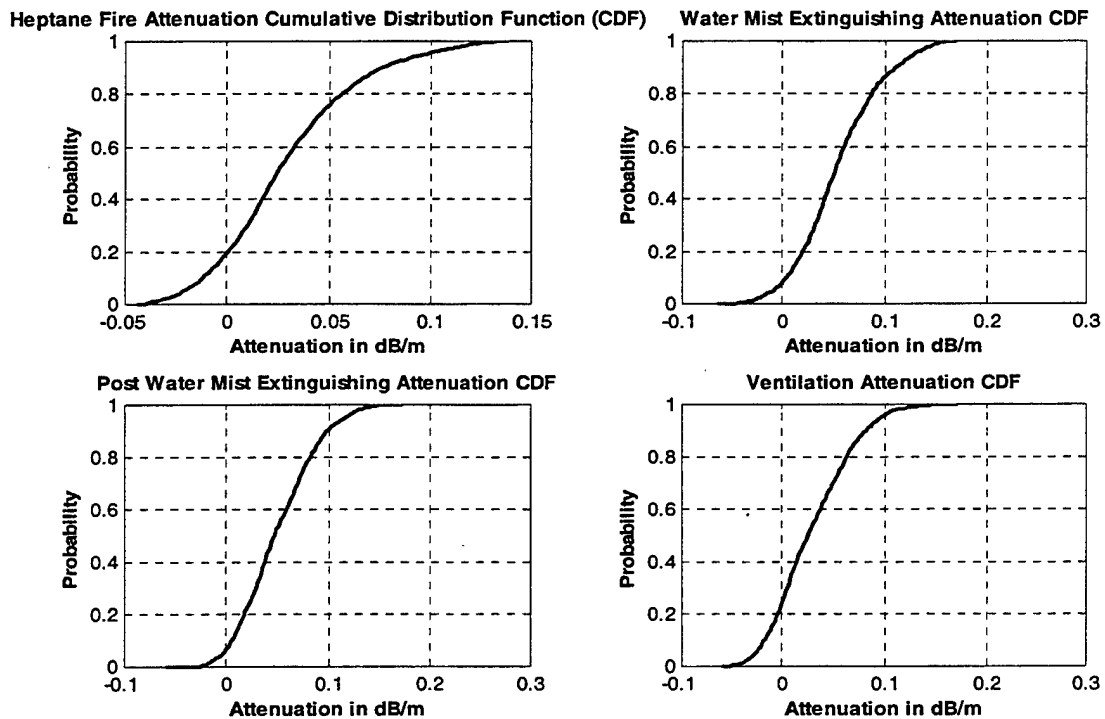


Figure 9.77: Attenuation Cumulative Distribution Functions

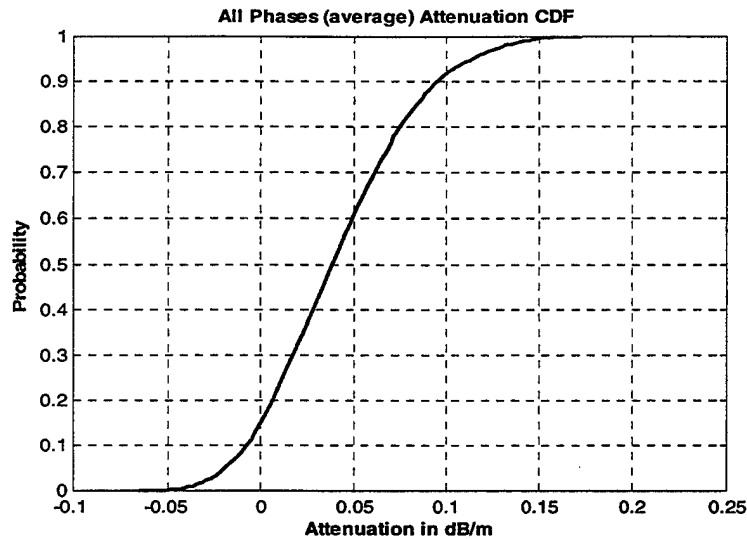


Figure 9.78: Attenuation Average Cumulative Distribution Function

attenuation less than 0.12 dB/m, and for the ventilation phase for attenuation less than 0.11 dB/m. This shows that the attenuation for the water mist extinguishing phase causes larger attenuation than the fire itself. For all the phases there is 0.95 probability that the attenuation is going to be less than 0.12 dB/m.

p) Autocorrelation Functions

Our next step was to determine the correlation between different frequencies for the different phases of the experiment. Initially we estimated the autocorrelation for the pre-fire phase. In Figure 9.79 the plot of the autocorrelation function indicates a high degree of correlation between attenuation at different frequencies.

This dependency suggests that the attenuation does not vary much with frequency.

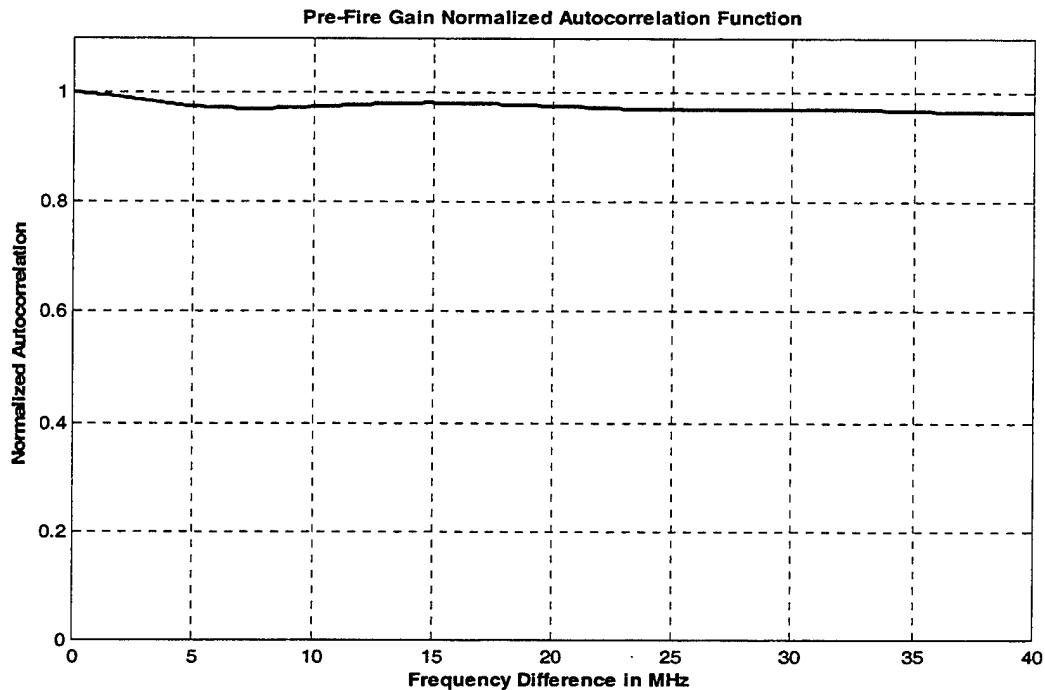


Figure IX-79: Pre Fire Gain Normalized Autocorellation Function

For the fire phase the autocorellation function shown in Figure 9.80 is similar to the pre-fire autocorellation function indicating that all of the frequency components attenuate in the same manner. The high values of correlation also follow from the results obtained from the comparison of the pre-fire and heptane fire time-averaged attenuation plots. As shown in Figure 9.64 the path loss for all frequency components increased in a similar way and all the minima and maxima remained at the same frequencies. Figures IX-81, IX-82 and IX-83 show the autocorellation functions for the water mist, steam build-

up, and ventilation phases. These plots are similar to the plots for the pre-fire and heptane fire phases.

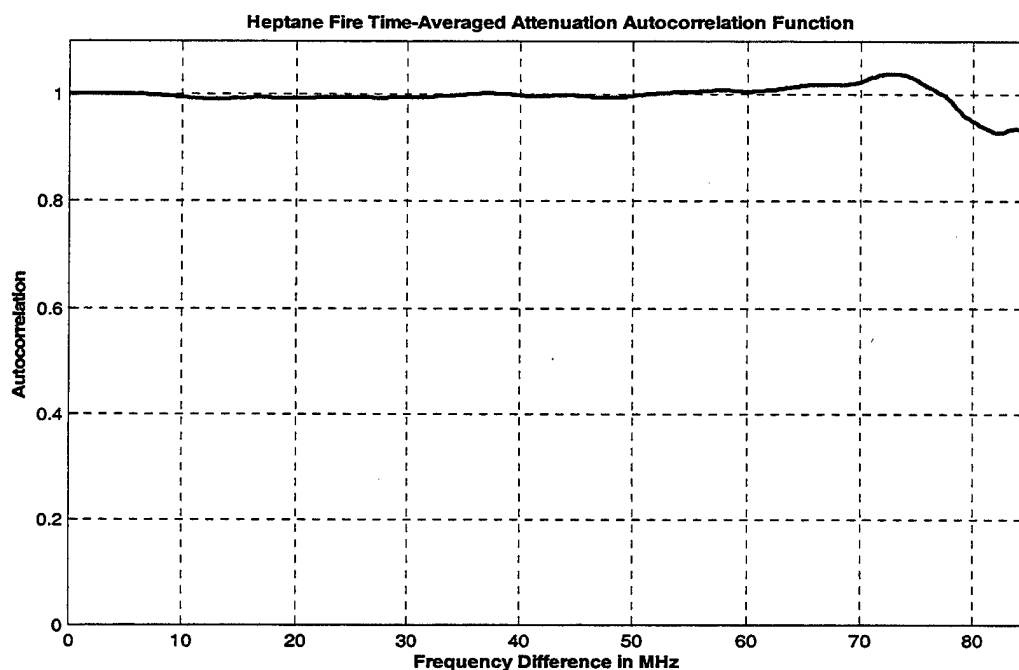


Figure IX-80: Fire Gain Normalized Autocorrelation Function

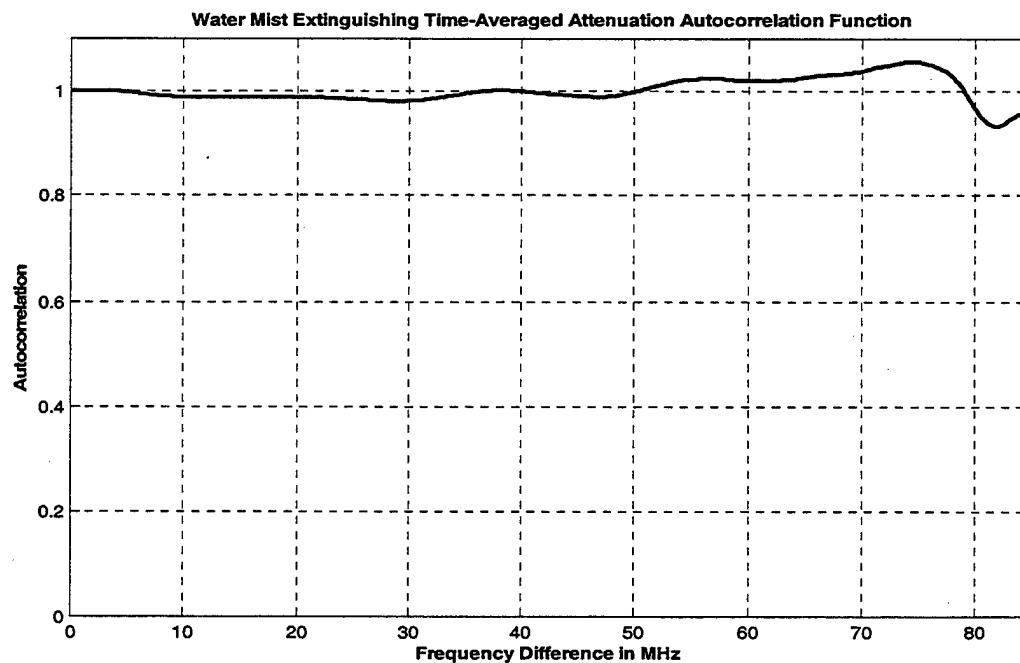


Figure IX-81: Water Mist Gain Normalized Autocorrelation Function

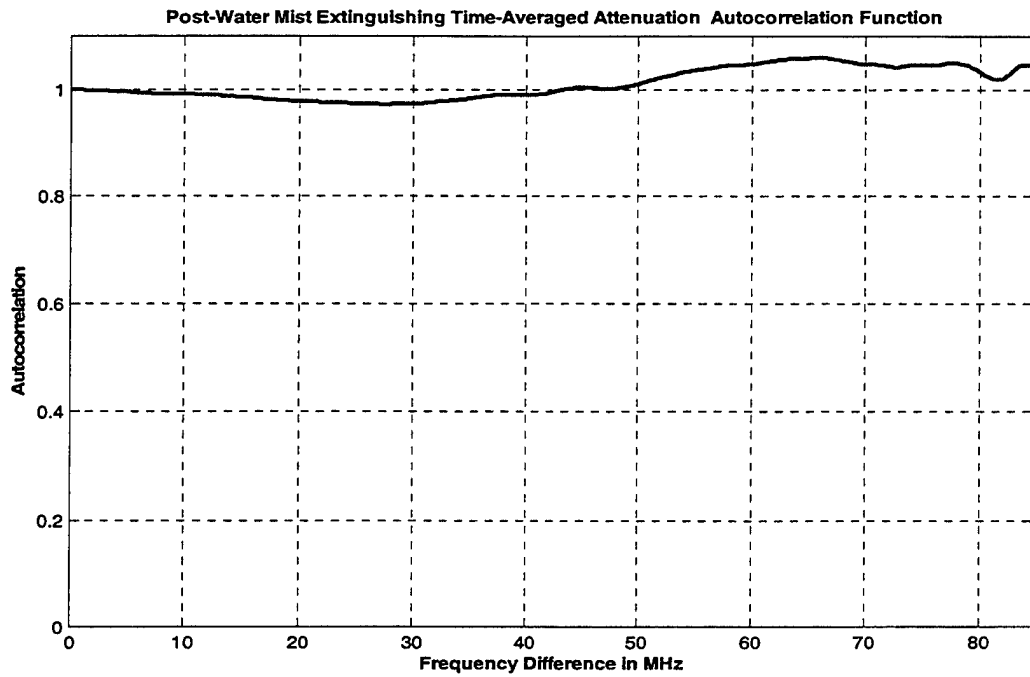


Figure 9.82: Steam Build-Up Gain Normalized Autocorrelation Function

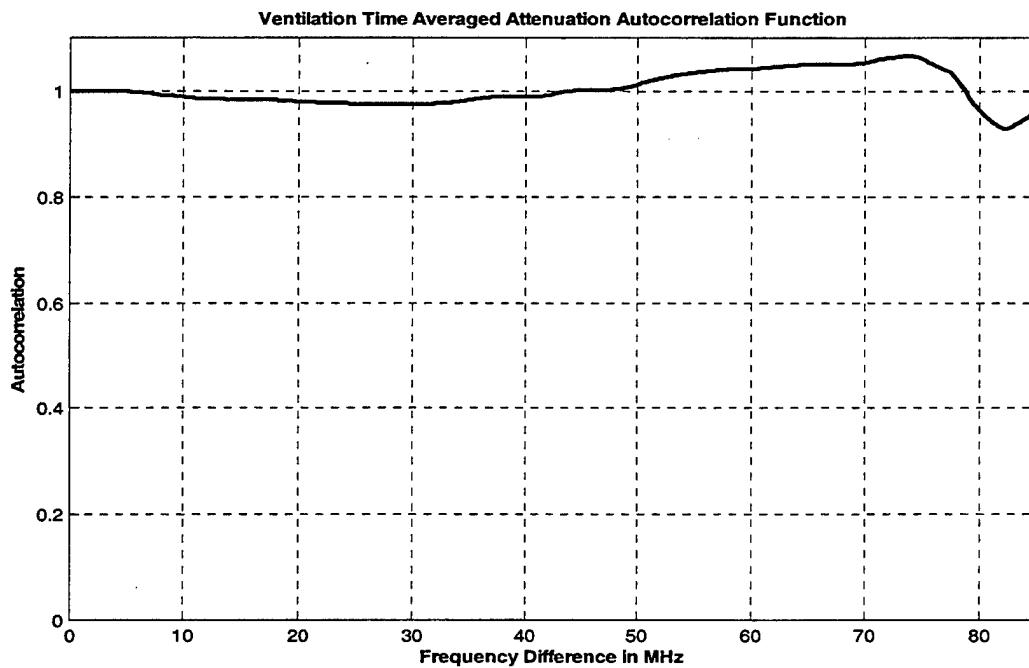


Figure 9.83: Ventilation Gain Normalized Autocorrelation Function

The attenuation's relative invariance with frequency is the consequence of using directional antennas. There is little effect of the compartment, since the antenna beam is very narrow and a single, line-of-sight path dominates the propagation, and the attenuation due to fire, smoke, and water mist does not vary significantly over the narrow 2.4 GHz ISM frequency band.

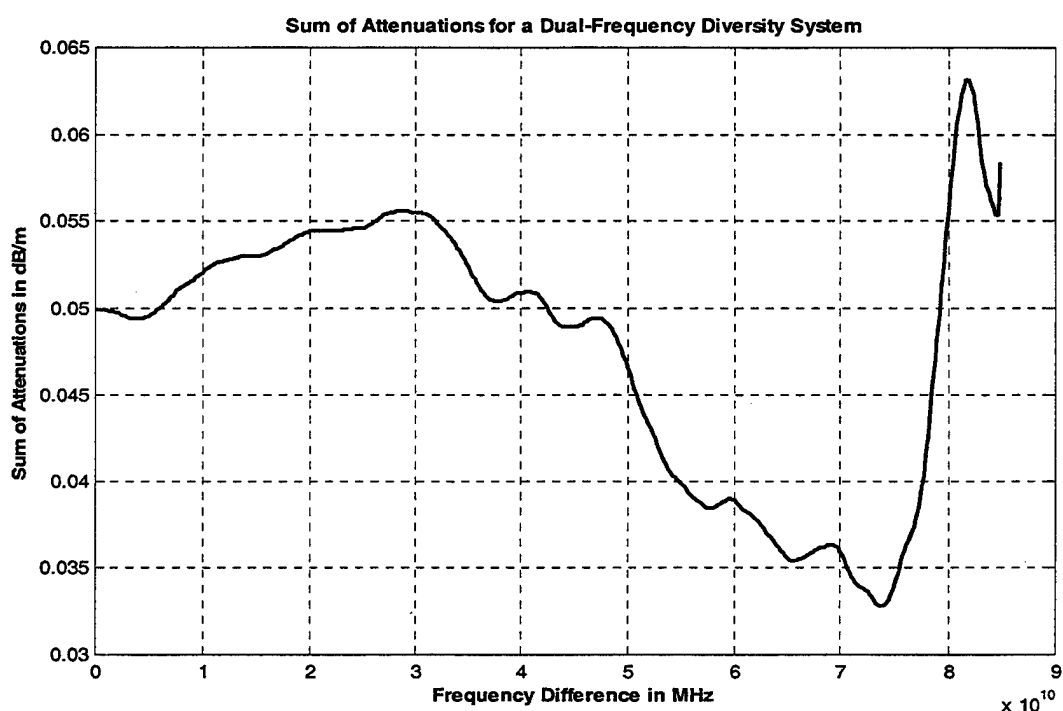


Figure 9.84: Sum of Attenuation for a Dual-Frequency Diversity System

q) Estimation of the best frequency difference

The last step was to estimate the frequency difference that, on average, would provide the least combined (sum of) attenuation. This would be useful if a

dual-frequency (diversity) transmission system was used. As seen in Figure 9.84 for the vertically polarized antennas this frequency difference is about 74 MHz. Note that the values very close to the full ISM bandwidth (85 MHz) are unreliable because of the diminishing number of frequencies averaged.

2. Horizontal Polarization

a) *Path loss for Horizontally Polarized Directional Antennas*

First the measured path loss is presented as a surface plot with the x-axis as the time axis, the y-axis as

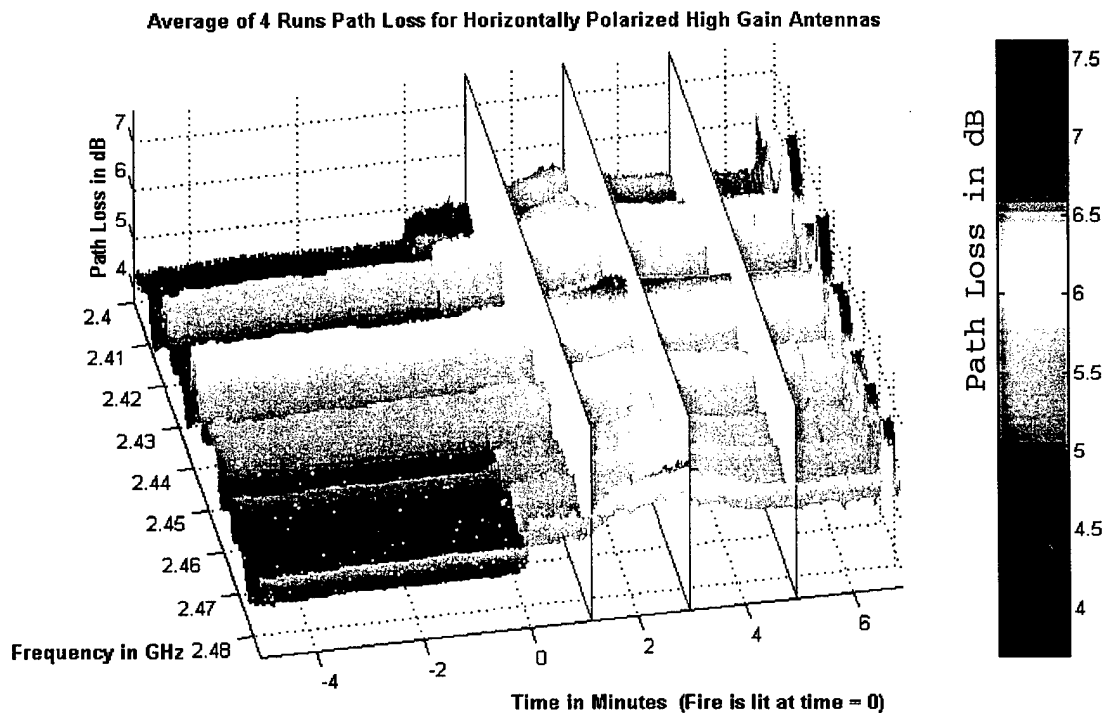


Figure 9.85: Path Loss for Horizontally Polarized High Gain Antennas

the frequency axis and the z-axis as the path loss (in dB) axis. In Figure 9.85 the path loss plot is shown for the horizontally polarized directional antennas. In this figure we have also shown the phase boundary planes. From the plot we see that initially we have an approximately five minute pre-fire phase. For this phase the time has negative values from -5 up to 0. At $t=0$ heptane fire and its measurements begin. The fire lasts for approximately one minute (minutes 0-1) followed by a two minute water mist phase (minutes 1-3), a two minute steam build-up phase (minutes 3-5), and finally a two minute ventilation phase (minutes 5-7).

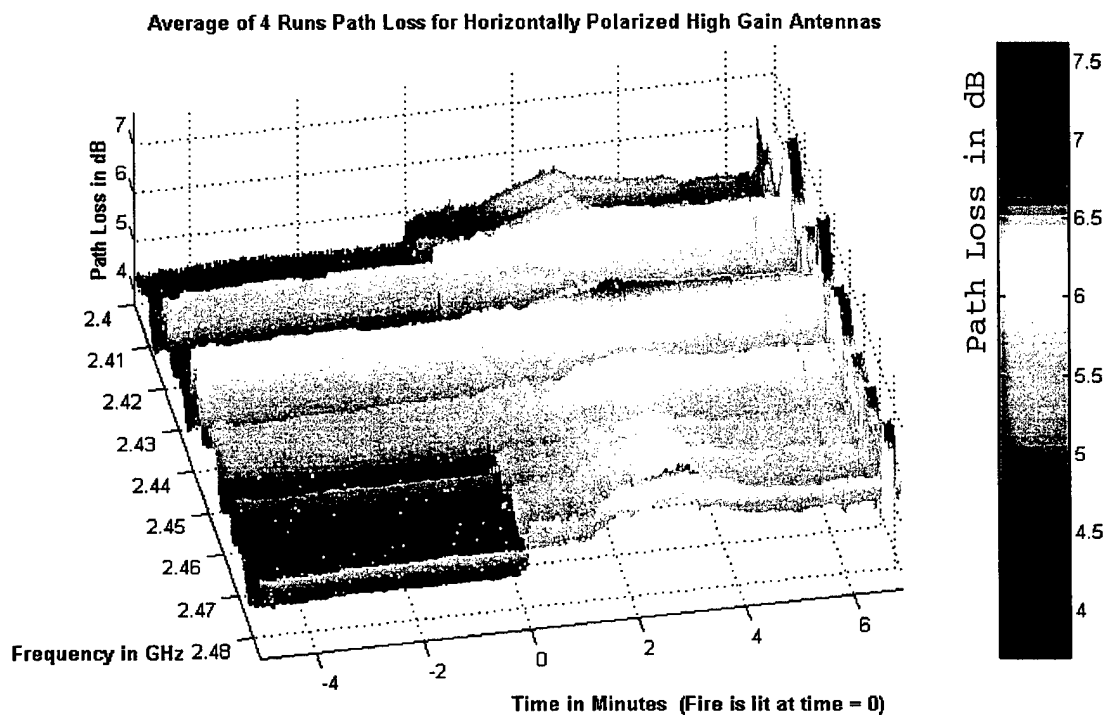


Figure 9.86: Path Loss for Horizontally Polarized High Gain Antennas

In Figure 9.86 the same surface plot without the phase boundaries is shown. We note the continuity between the fire, water mist, steam build-up and ventilation phases. There is a discontinuity between the pre-fire phase and the fire phase. This discontinuity is caused by the "interruption" in the measurement process to allow for the personnel movement in the compartment to light the spray fire ($t=0$). Measurements taken during this phase would not be valid since the attenuation changed with people moving between the antennas.

Average Path Loss of 4 Runs for Horizontally Polarized High Gain Antennas

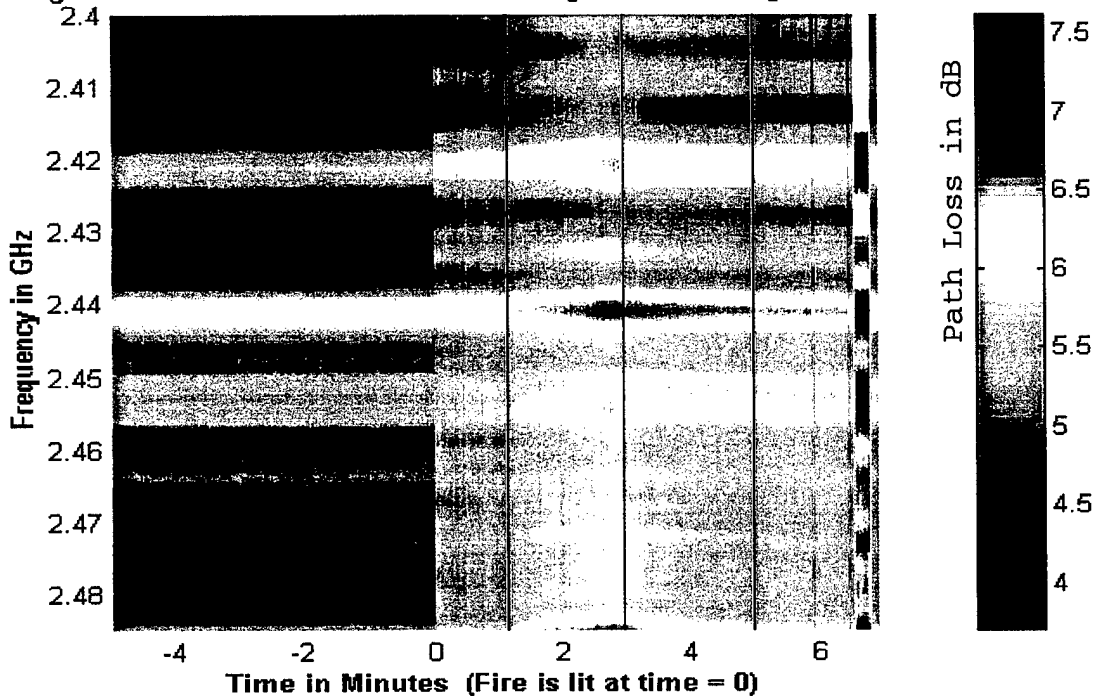


Figure 9.87: Path Loss for Horizontally Polarized High Gain Antennas

In Figure 9.87 the "bird's eye" view of the path loss is presented. This allows us to visualize the path loss changes with time and frequency. We note that for the five-minute pre-fire phase the path loss at each frequency has a value constant with time but different for different frequencies. The path loss differences are mainly caused by the reflections/absorption characteristics of portion of the compartment that is "visible" (within the main beams) to the two antennas.

After the fire has been lit the path loss increases almost instantly for all frequencies. This happened because of the high intensity of the spray fire from the moment the fire is lit. The path loss reaches its peak during the water mist phase and then it starts falling again during the steam build-up phase. The highest measured value of the path loss during the water mist phase was 6.5dB. During the ventilation phase the path loss values are significantly lower than the ones during the fire phase but higher than the values for the pre-fire phase because of the residual condensation in the compartment and on the antennas. Note that the highest measured value of about 7.5 dB, occurred because one of the fire fighting team members intruded accidentally into the antenna beam.

b) Attenuation for Horizontally Polarized Directional Antennas

We next present the attenuation surface plots. To create these plots we divided each path loss value by the time-averaged pre-fire phase path loss at the corresponding frequency. The result was then divided by the distance between the antennas to obtain the attenuation per unit length. The choice of the distance to obtain the attenuation per unit length (dB/m) requires some explanation. We selected the distance between the antennas (rather than the fire "depth") for the following reasons:

- The fire depth was ambiguous for the pressurized heptane spray sources that were used to create the fire
- The heat and smoke were distributed throughout the compartment
- The antennas were placed close to the fire sources (heptane pressure spray nozzles)
- The distance between the antennas was 7.66 meters

In Figure 9.88 the surface plot for the attenuation per meter for the horizontally polarized directional antennas is shown with the phase boundary planes

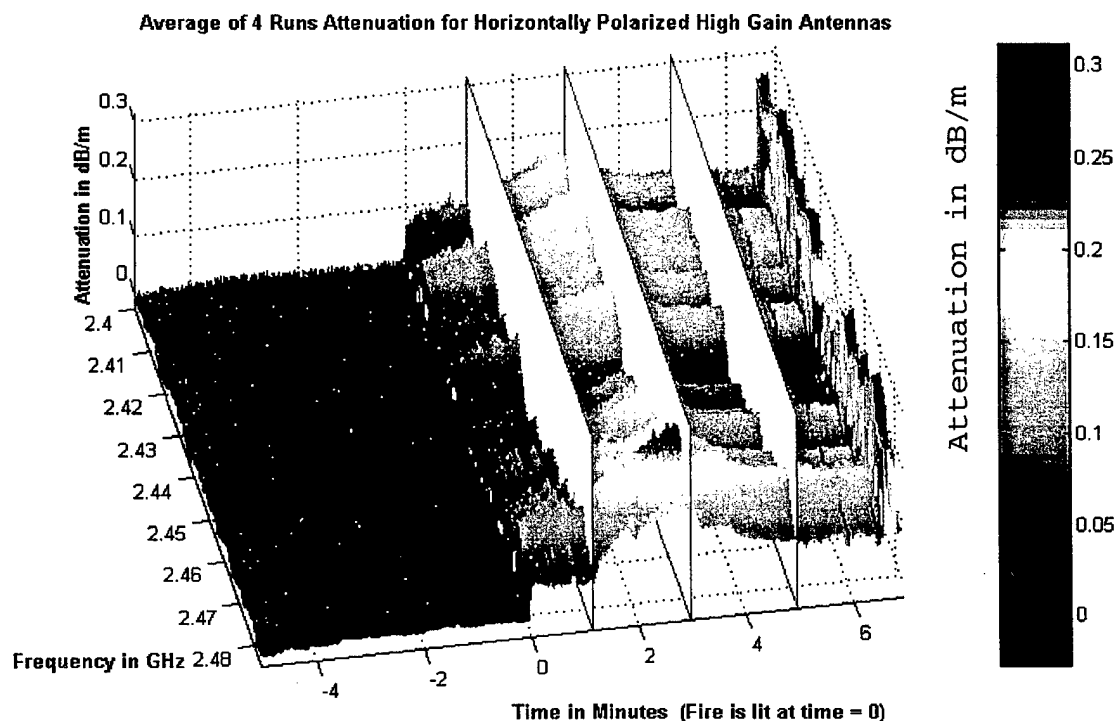


Figure 9.88: Attenuation for Horizontally Polarized High Gain Antennas

For the pre-fire phase (time between -5 and 0 minutes) the attenuation is approximately 0 dB/m as we would expect since we used the time-averaged path loss for the pre-fire phase as the reference for each frequency. Therefore during the pre-fire phase there are almost no "peaks and valleys" in the surface plot.

In Figure 9.89 the same surface plot is shown but without the phase boundaries. We note a stepped increase in attenuation when the fire was lit. At about one minute after

the fire was lit, there is a steep increase in attenuation, caused by the activation of the water mist fire-extingui-

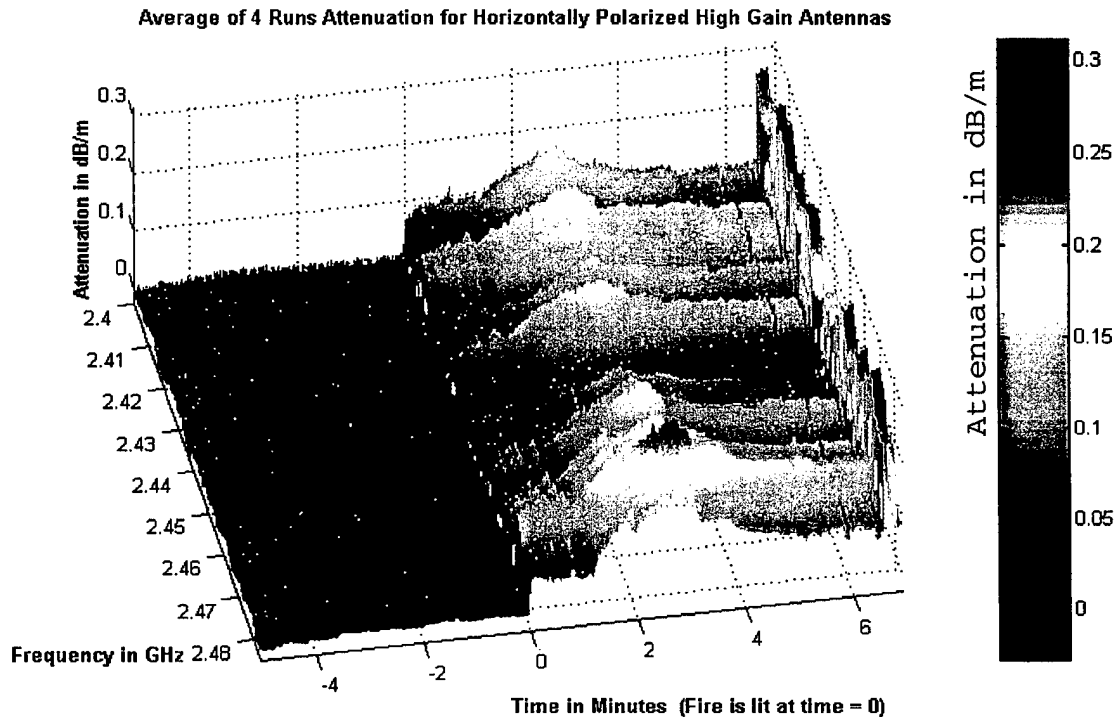


Figure 9.89: Attenuation for Horizontally Polarized High Gain Antennas

shing system. After two minutes of fire extinguishing the compartment is saturated with steam and smoke (from minute 3 to 5) and the attenuation remains relatively high (but not as high as during the fire-extinguishing phase). During the ventilation of the compartment the attenuation decreases (from minute 5 on) towards the values prior to the fire (for negative time).

In Figure 9.90 the same surface plot is shown, viewed directly from the z-axis (the "birds-eye" view) clearly showing the attenuation changes for different phases and for different frequencies.

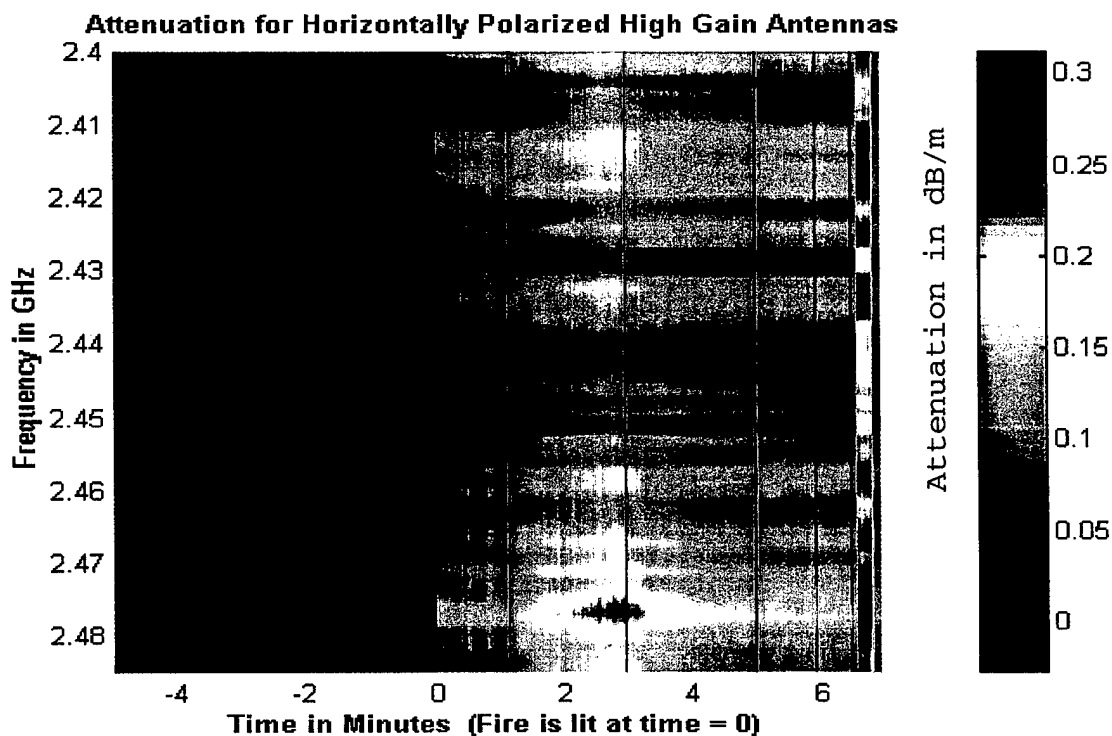


Figure 9.90: Attenuation for Horizontally Polarized High Gain Antennas

The attenuation per meter reached its maximum value during the water mist fire-extinguishing phase and for particular frequencies it was on the order of 0.28 dB/m.

c) Frequency-Averaged Path Loss for Horizontally Polarized Directional Antennas

The first statistical analysis we performed was to determine the frequency-averaged path loss. As shown in Figure 9.91 the frequency-averaged path loss for the pre-fire phase is almost constant at around 4.8 dB.

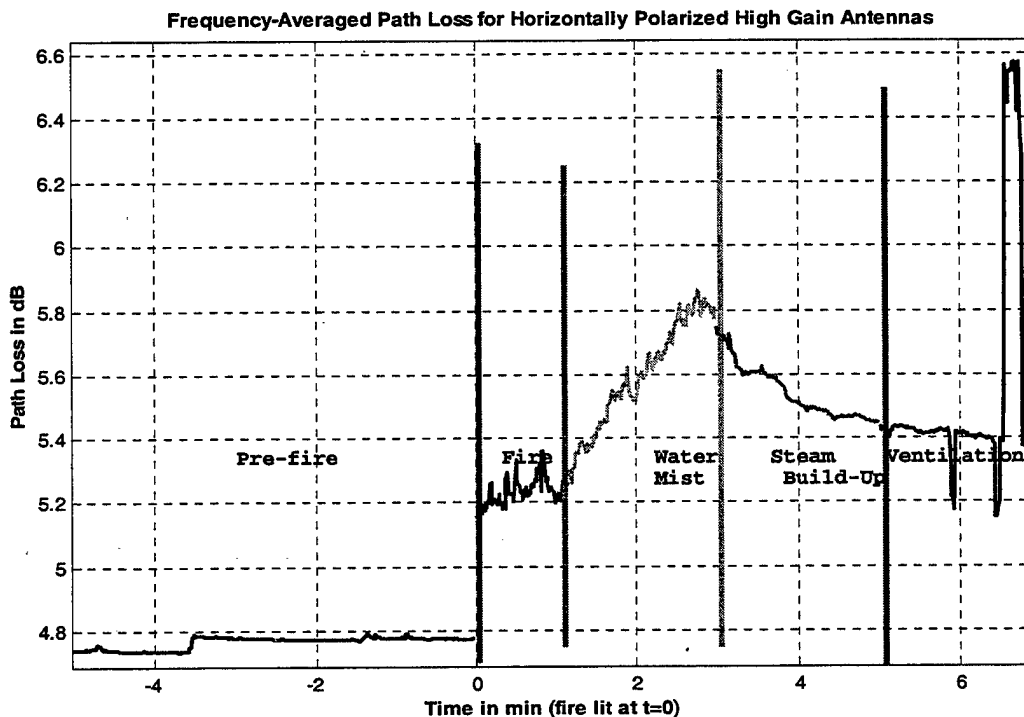


Figure 9.91: Frequency-Averaged Path Loss for Horizontally Polarized Directional Antennas

When the fire was lit the frequency-averaged path loss jumped to a value around 5.3 dB, as explained in IX-B-2-a. After the water mist system was turned on the frequency-averaged path loss increased rapidly. During this phase the frequency-averaged path loss reached its peak

value of 5.9 dB. The averaged path loss started to decrease slowly during the steam build-up and ventilation phase. During the last phase, at $t \sim 6.5$ a path loss increase to 6.5 dB can be observed, caused from the intrusion of the beam by a member of the support team.

**d) *Frequency-Averaged Attenuation for
Horizontally Polarized Directional Antennas***

Our next step was to determine the frequency-averaged attenuation in dB/m. The shape of the frequency-averaged attenuation as a function of time is exactly the same as the path loss, as shown in Figure 9.92. The only difference between the frequency-averaged attenuation and the frequency-averaged path loss is the division by a constant distance. The maximum attenuation is approximately 0.14 dB/m. During the fire phase the attenuation did not exceed 0.07 dB/m. After the water mist extinguishing system was turned on and the steam started building up the attenuation per meter increased reaching its maximum value at about 1.5 minutes after the start of this phase, before starting to decrease slowly as the temperature and the steam density gradually decreased. Again at $t \sim 6.5$ the attenuation increase is observed, due to the intrusion of the antenna beam.

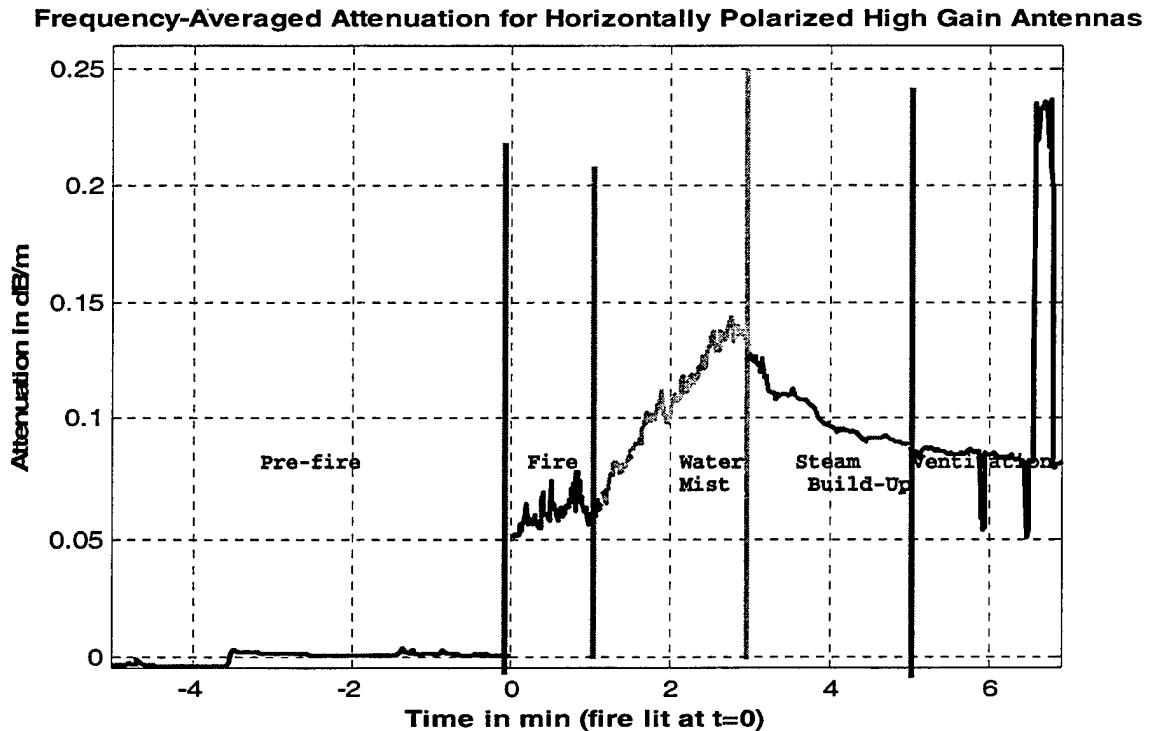


Figure 9.92: Frequency-Averaged Attenuation for Horizontally Polarized Directional Antennas

e) Temperature vs. Time for Horizontally Polarized Directional Antennas

The temperature taken at five different locations in the compartment is shown in Figure 9.93. The highest curve is for the temperature at the elevation of 11 feet and at the horizontal distance of 3 feet from the fuel pan (Diesel fuel pan was used to start the heptane "spray" fire.). The maximum temperature is approximately 325° C. The second highest curve is for the data taken at the elevation of 7ft and the horizontal distance from the fuel pan of 3 feet. The maximum temperature at this height is approximately 90° C.

The two lowest curves are for the temperature next to the two antennas. We note that the temperature next to the transmitting antenna reached a maximum of approximately 50° C and the temperature next to the receiving antenna reached a maximum of approximately 40° C. The antennas withstood these temperatures (for fires of short duration) without damage.

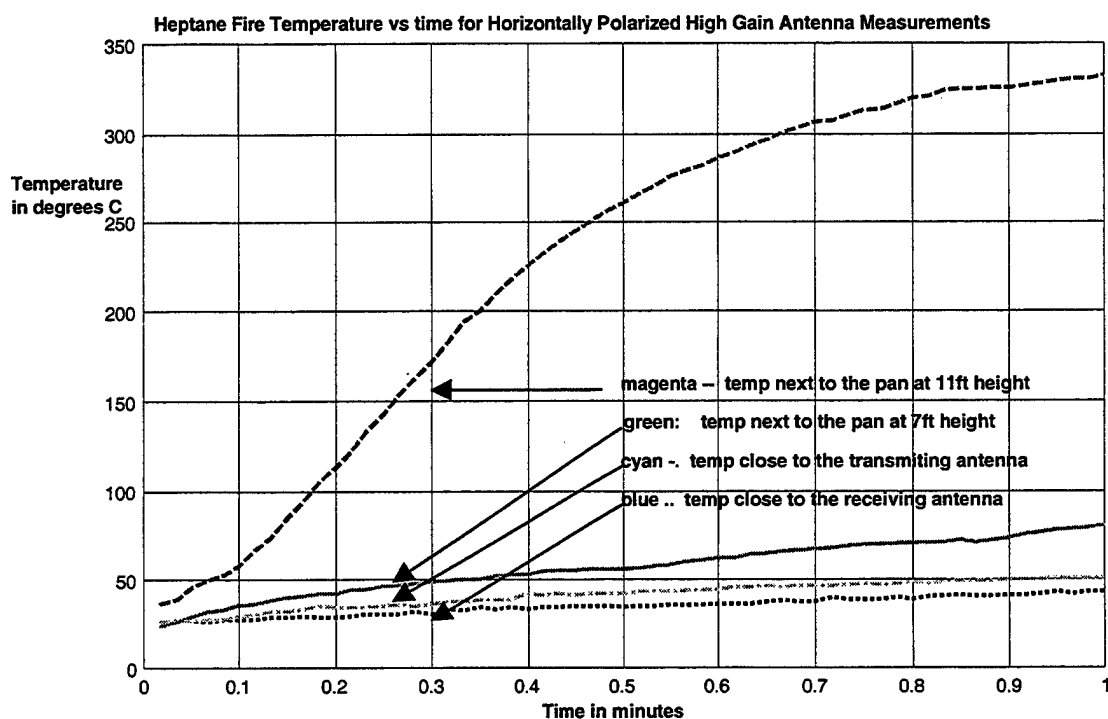


Figure 9.93: Heptane Fire Average Temperature versus Time for Horizontally Polarized Directional Antennas

**f) Scaled Attenuation and Temperature vs. Time
for Horizontally Polarized Directional
Antennas**

Our next objective was to determine if there was a relation between the temperature increase close to the antennas and the attenuation increase. To accomplish this we subtracted the mean values from the attenuation and the temperature data. Next we determined an average coefficient which, when multiplied with the time-varying temperature would yield the best "curve fit" for the time-varying attenuation. The attenuation and the temperature are related but not as closely as for the diesel fire.

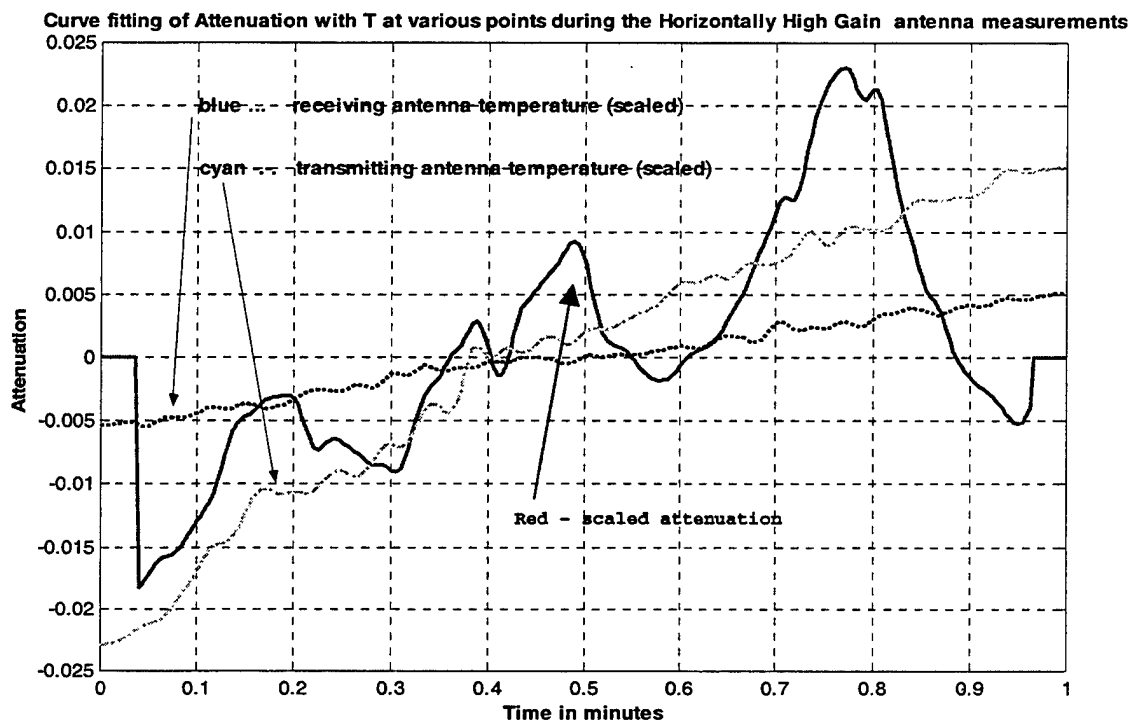


Figure 9.94: Heptane Fire Scaled Attenuation and Temperature vs. Time for Horizontally Polarized Directional Antennas

g) Heptane Fire Time-Averaged Path Loss for Horizontally Polarized Directional Antennas

Our next step was to calculate the time-averaged path loss during the fire phase. As shown in Figure 9.95 the time-averaged path loss ranged between 4.7 and 6.3 dB, a variation with frequency of close to 2.5 dB. The plot also shows the minimum and maximum values of path loss for each frequency component. The maximum path loss of 6.4 dB occurs at 2.442 GHz and the minimum path loss of 4.4 dB occurs at 2.413 GHz.

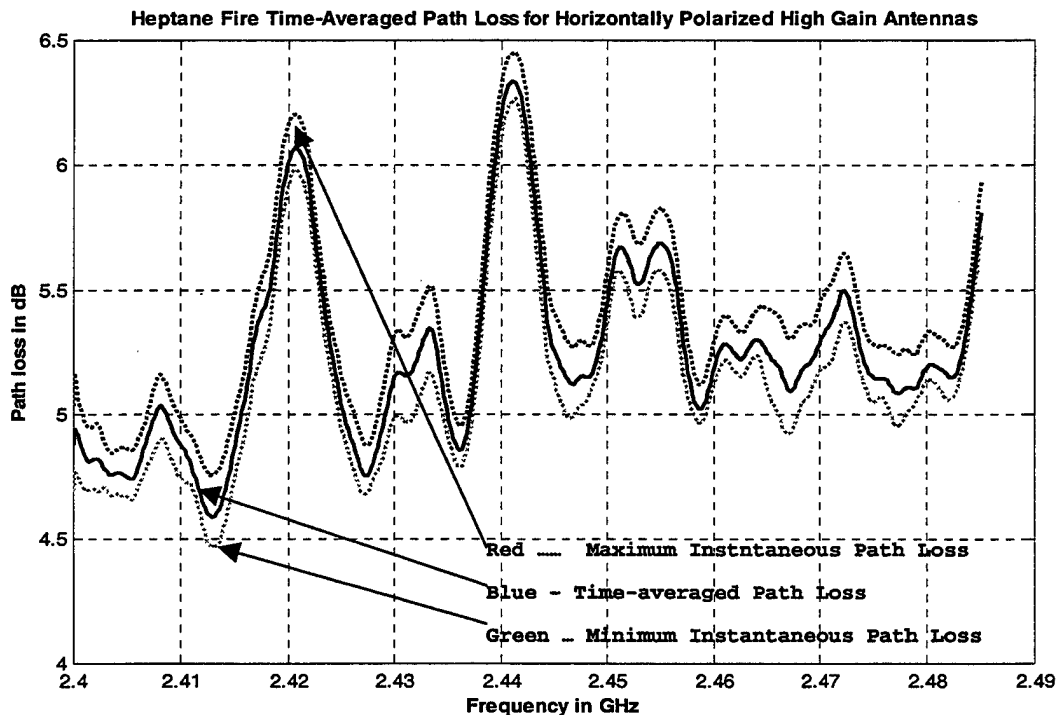


Figure 9.95: Heptane Fire Time-Averaged Path Loss for Horizontally Polarized Directional Antennas

The maximum and minimum path loss curves follow the time-averaged attenuation curve, that is the zero slope points for all three curves are located at the same frequencies.

In Figure 9.96 the time-averaged path loss for the fire and the pre-fire phases are shown in order to assess the effects of fire. Again the minima and maxima of the path loss are located at the same frequencies. This indicates that there is no change in the propagation characteristics of the compartment due to the fire except that there is an increase between 0 and 0.5 dB (depending on the frequency) of the time-averaged path loss.

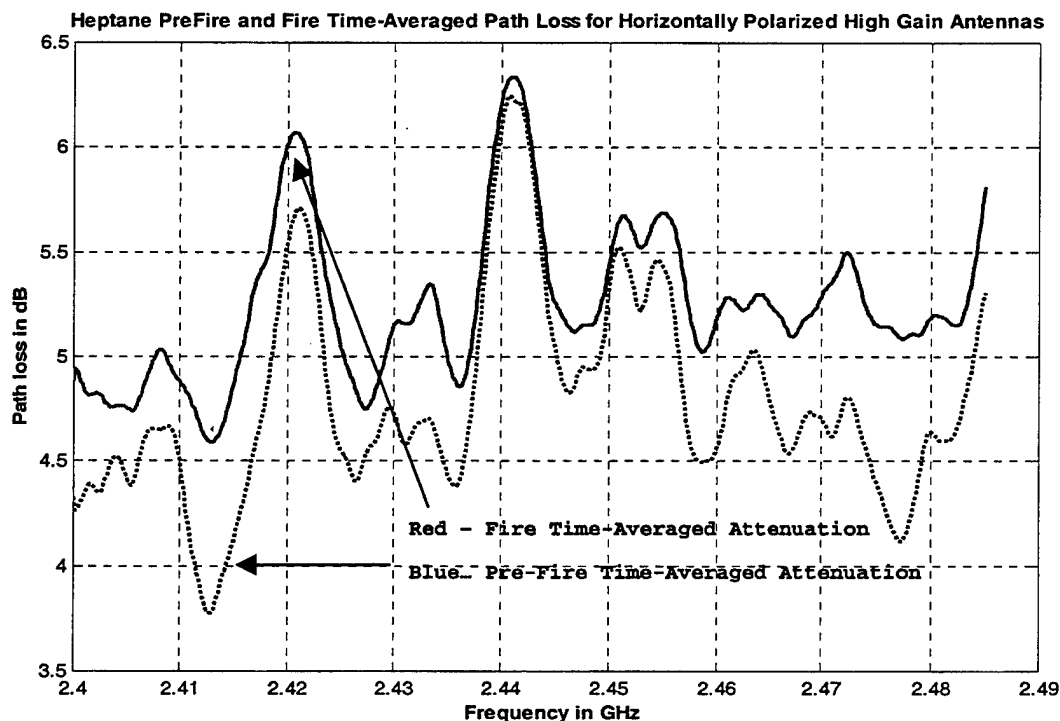


Figure 9.96: Heptane Pre-Fire Time-Averaged Path Loss for Horizontally Polarized High Gain Antennas

h) Heptane Fire Time-Averaged Attenuation for Horizontally Polarized Directional Antennas

The time-averaged attenuation per meter during the fire phase is shown in Figure 9.97. The maximum in attenuation of 0.15 dB/m occurs at 2.477 GHz. The maximum time-averaged attenuation is about 0.13 dB/m.

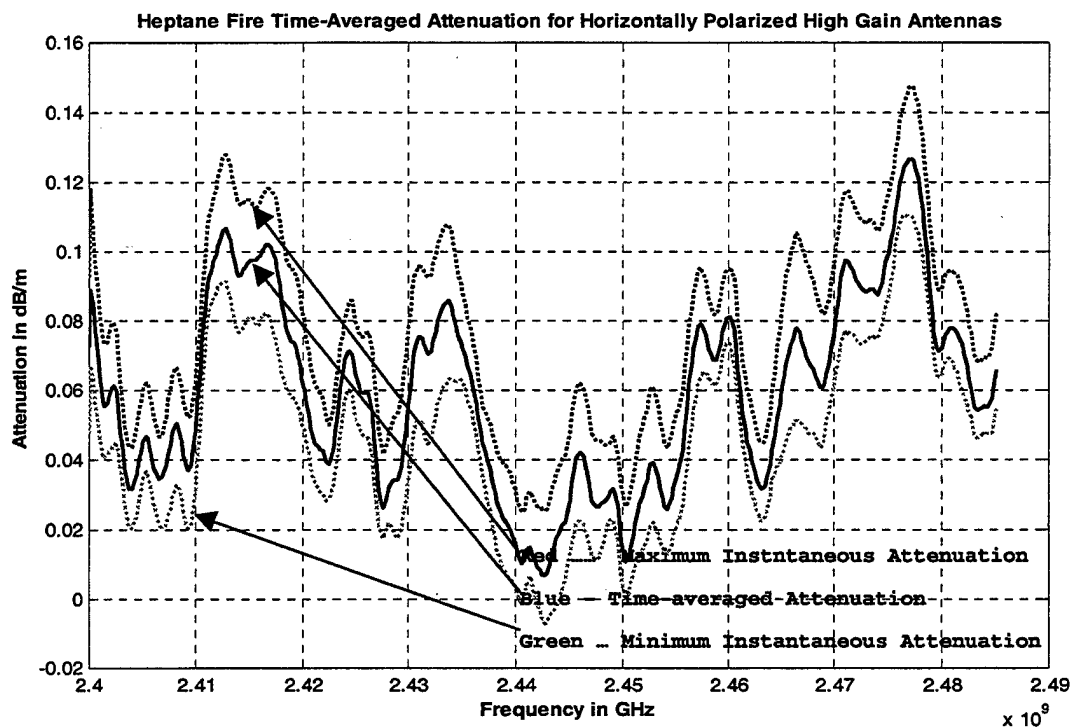


Figure 9.97: Heptane Fire Time-Averaged Attenuation for Horizontally Polarized Directional Antennas

i) Water Mist Phase Time-Averaged Path Loss for Horizontally Polarized Directional Antennas

Our next step was to calculate the time-averaged path loss during the water mist phase. As shown in Figure 9.98 the time-averaged path loss ranged between 4.8 and 6.6dB, a variation close to 2 dB. The maximum time-averaged path loss occurs at 2.442 GHz and the minimum path loss occurs at 2.413 GHz, the same frequencies as for the fire phases. Also the zero slope points for all three curves (min, max and average path loss) occur at the same frequencies.

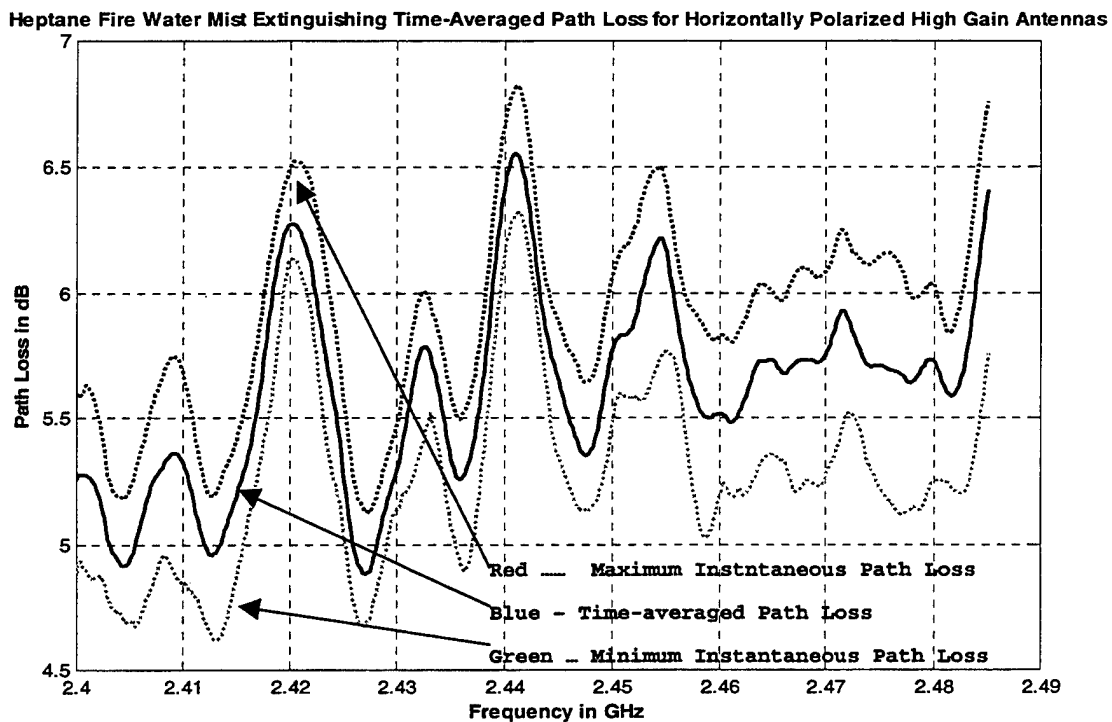


Figure 9.98: Heptane Fire Water Mist Phase Time-Averaged Path Loss for Horizontally Polarized Directional Antennas

The time-averaged attenuation curves for the water mist and the pre-fire phases are shown in Figure 9.99. Again the zero slope points are located at the same frequencies. This indicates that there is no change in the compartment propagation characteristics between the two phases, the only difference being that for the water mist phase there is an increase of about 0.5 to 1 dB for the time-averaged path loss.

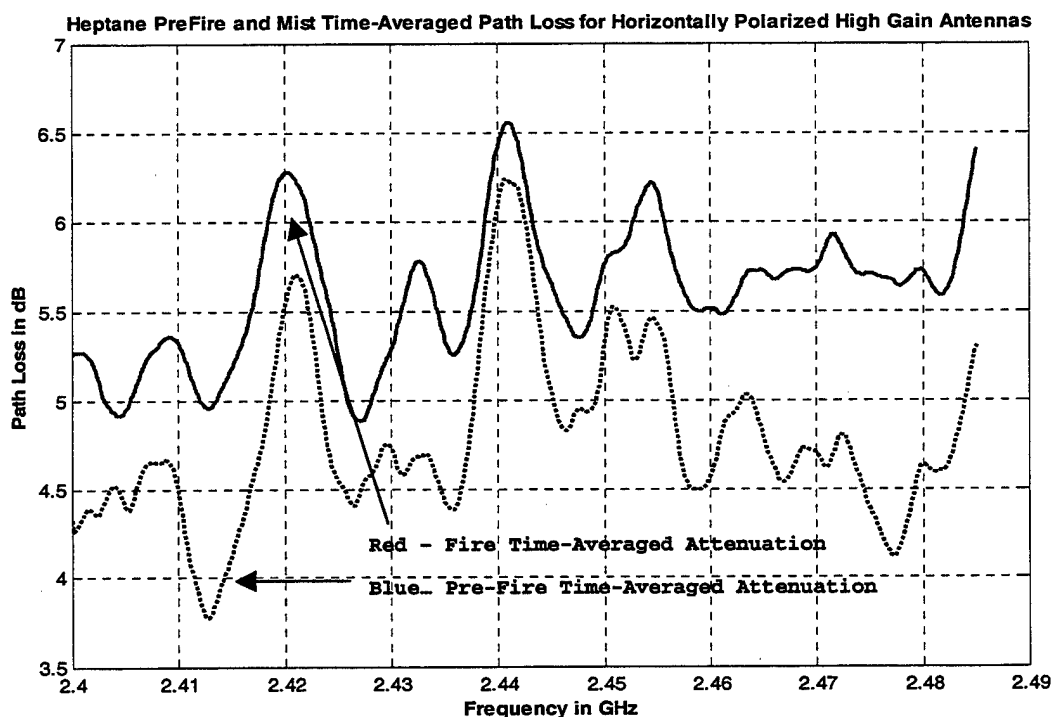


Figure 9.99: Heptane Pre-Fire and Water Mist Time-Averaged Path Loss for Horizontally Polarized High Gain Antennas

j) Water Mist Time-Averaged Attenuation for Horizontally Polarized Directional Antennas

The time-averaged attenuation per meter for the water mist phase is shown in Figure 9.100. The time-averaged attenuation ranges between 0.03 and 0.21 dB/m. The maximum instantaneous attenuation of 0.26 dB/m occurs at 2.442 GHz.

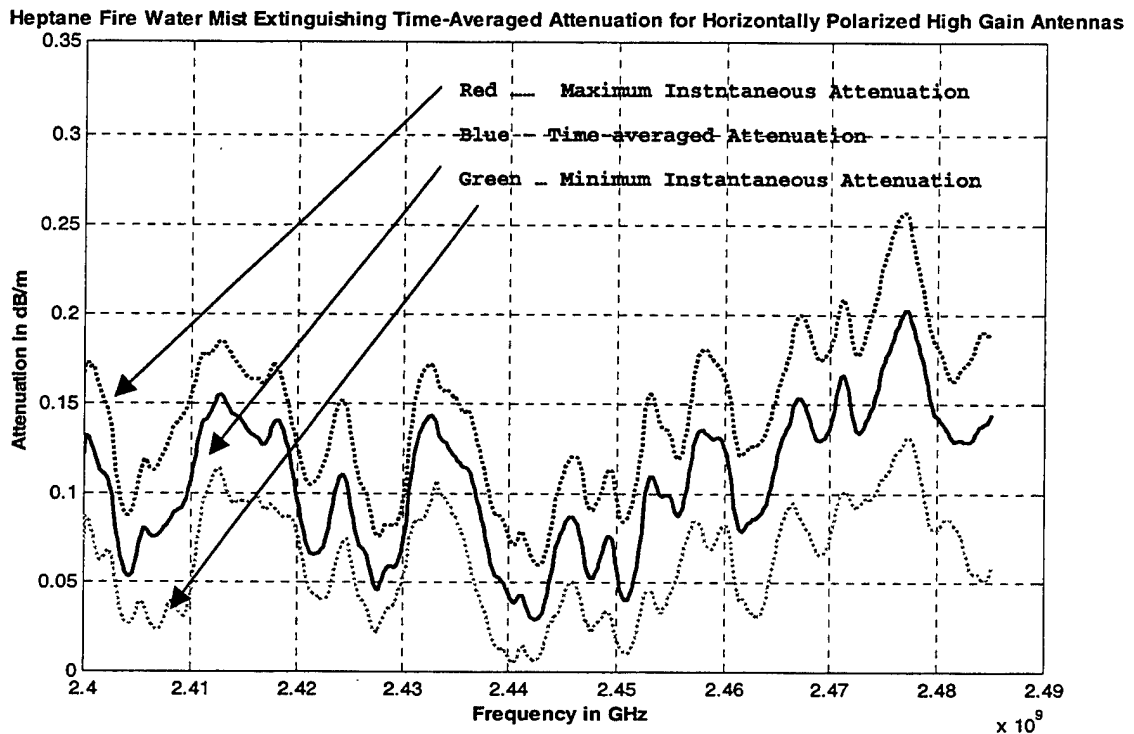


Figure 9.100: Heptane Fire Water Mist Phase Time-Averaged Attenuation for Horizontally Polarized Directional Antennas

k) Steam Build Up Phase Time-Averaged Path Loss for Horizontally Polarized Directional Antennas

Next we calculated the time-averaged path loss during the steam build-up phase. As shown in Figure 9.101 the time-averaged path loss ranged between 4.7 and 6.6 dB.

Also shown on the same plot are the minimum and maximum values of the attenuation for each frequency. The maximum path loss of 6.6 dB occurs at 2.442 GHz and the minimum path loss of 4.75 dB occurs at 2.413 GHz, the same frequencies as for the fire phase. Again the zero slope points for all three curves are located at the same frequencies, indicating that the "frequency response" for the path between the antennas does not change depending on whether there is fire or water mist in the compartment except for the path loss increase or decrease ("scaling").

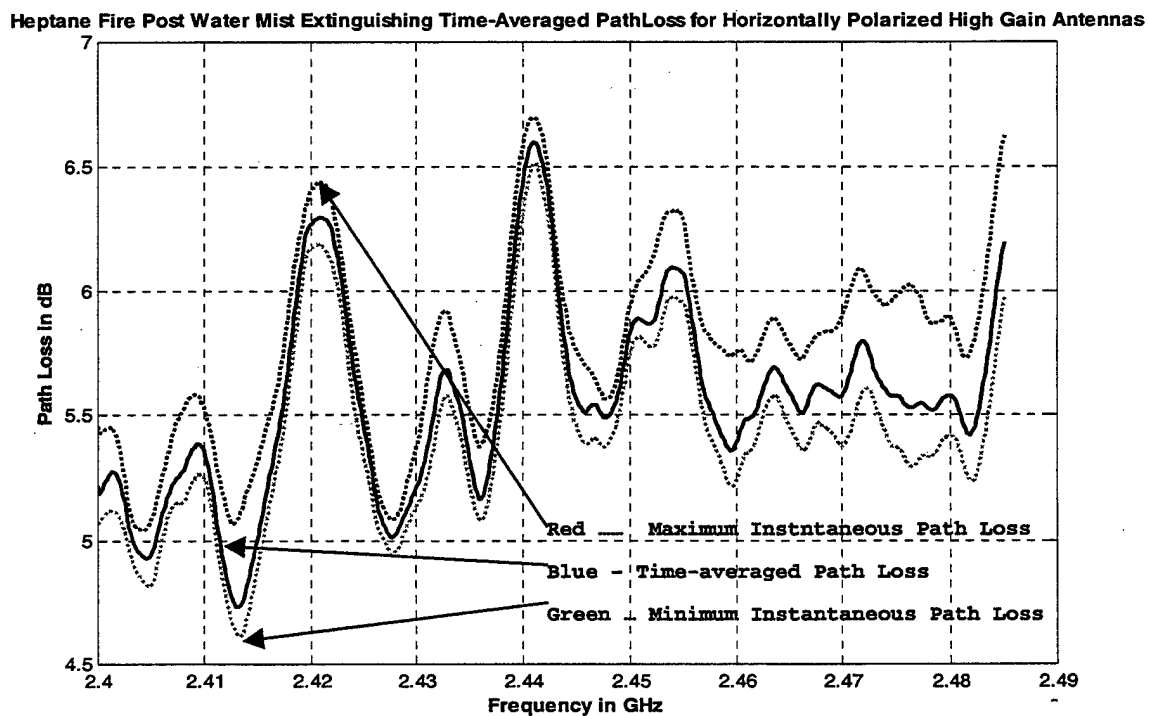


Figure 9.101: Heptane Fire Steam Phase Time-Averaged Path Loss for Horizontally Polarized Directional Antennas

In Figure 9.102 the time-averaged path loss curves for the water mist and the pre-fire phases are shown. Again the zero slope points (maxima and minima) are located at the same frequencies. This indicates that there is no change in the compartment propagation characteristics except for the additional path loss of between 0.4 and 1.3 dB due to the residual steam and smoke in the compartment.

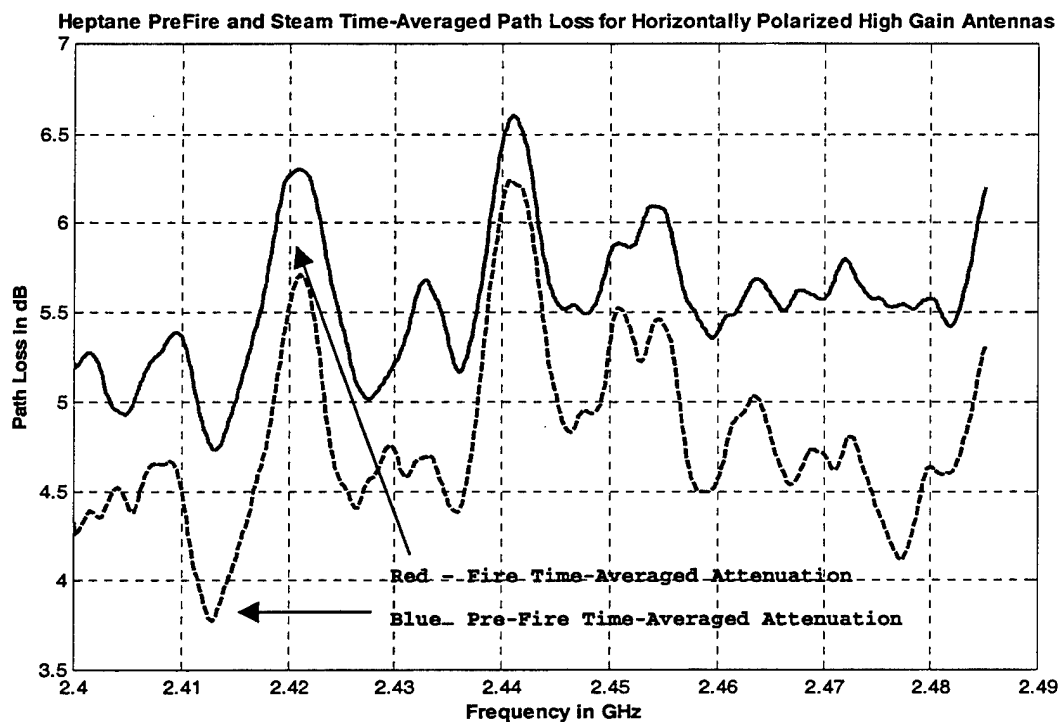


Figure 9.102: Heptane Pre-Fire and Steam Phase Time-Averaged Path Loss for Horizontally Polarized Directional Antennas

1) Steam Build Up Time-Averaged Attenuation for Horizontally Polarized Directional Antennas

In Figure 9.103 the time-averaged attenuation per meter during the steam build-up phase is shown. The values of the time-averaged attenuation per meter vary between 0.04

and 0.17 dB/m, slightly lower than the values measured for the mist build-up phase. The maximum instantaneous attenuation of 0.24 dB/m occurs at 2.475 GHz.

Heptane Fire Post Water Mist Extinguishing Time-Averaged Attenuation for Horizontally Polarized High Gain Antennas

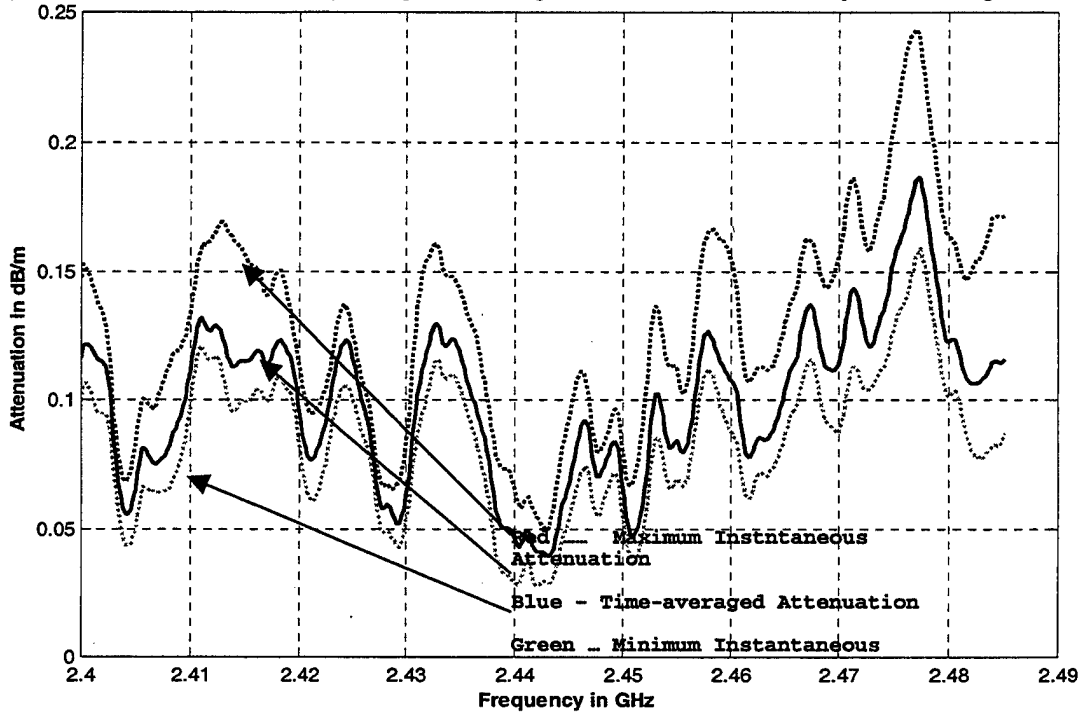


Figure 9.103: Heptane Fire Steam Phase Time-Averaged Attenuation for Horizontally Polarized Directional Antennas

m) Ventilation Phase Time-Averaged Path Loss for Horizontally Polarized Directional Antennas.

Next we calculated the time-averaged path loss for the ventilation phase. As shown in Figure 9.104 the time-averaged path loss ranged between 4.7 and 6.5 dB, approximately 2 dB variation. Also shown on the same plot are the minimum and maximum instantaneous values of the path

loss for each frequency. The maximum path loss of 7.7 dB occurs at 2.442 GHz and the minimum path loss of 4.3 dB occurs at 2.413 GHz, the same frequencies as for the fire phase. Again the zero slope points for all three curves are located at the same frequencies, indicating that the "frequency response" for the path between the antennas does not change depending on whether there is fire or water mist in the compartment except for the path loss increase or decrease ("scaling").

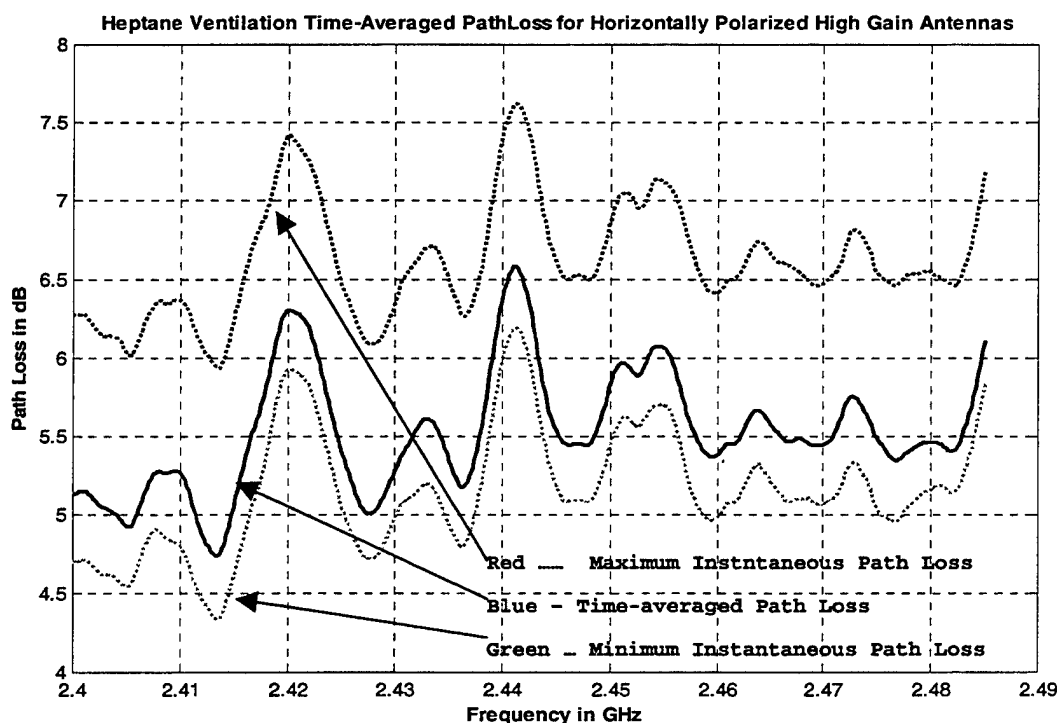


Figure 9.104: Heptane Fire Ventilation Phase Time-Averaged Path Loss for Horizontally Polarized Directional Antennas

In Figure 9.105 the time-averaged path loss curve for the ventilation and the pre-fire phases are shown. Again the zero slope points (maxima and minima) are located at the same frequencies. This indicates that there is no change in the compartment propagation characteristics except of the additional path loss of between 0.4 and 1.3 dB due to the residual steam and smoke in the compartment.

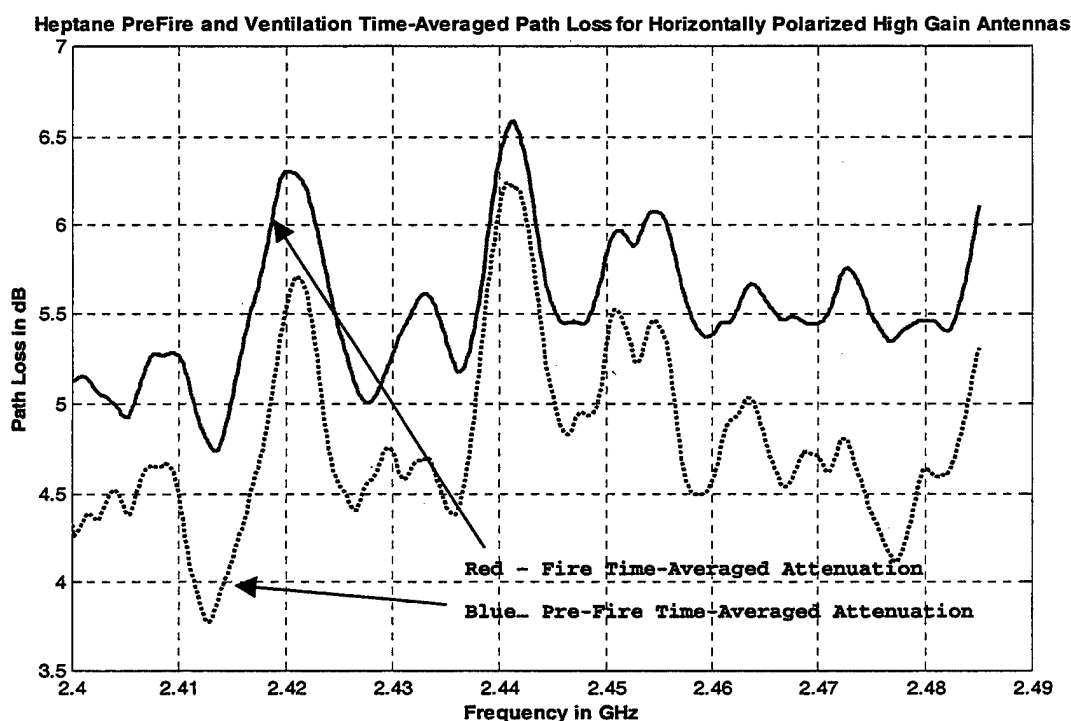


Figure 9.105: Heptane Pre-Fire and Ventilation Phase Time-Averaged Path Loss for Horizontally Polarized Directional Antennas

n) Ventilation Attenuation for Horizontally Polarized Directional Antennas.

In Figure 9.106 the time-averaged attenuation per meter during the ventilation phase is shown. The values of

the time-averaged attenuation per meter vary between 0.02 and 0.16 dB/m, slightly lower than the values measured for the steam build-up phase. The maximum instantaneous attenuation of ~ 0.3 dB occurs at 2.477 GHz.

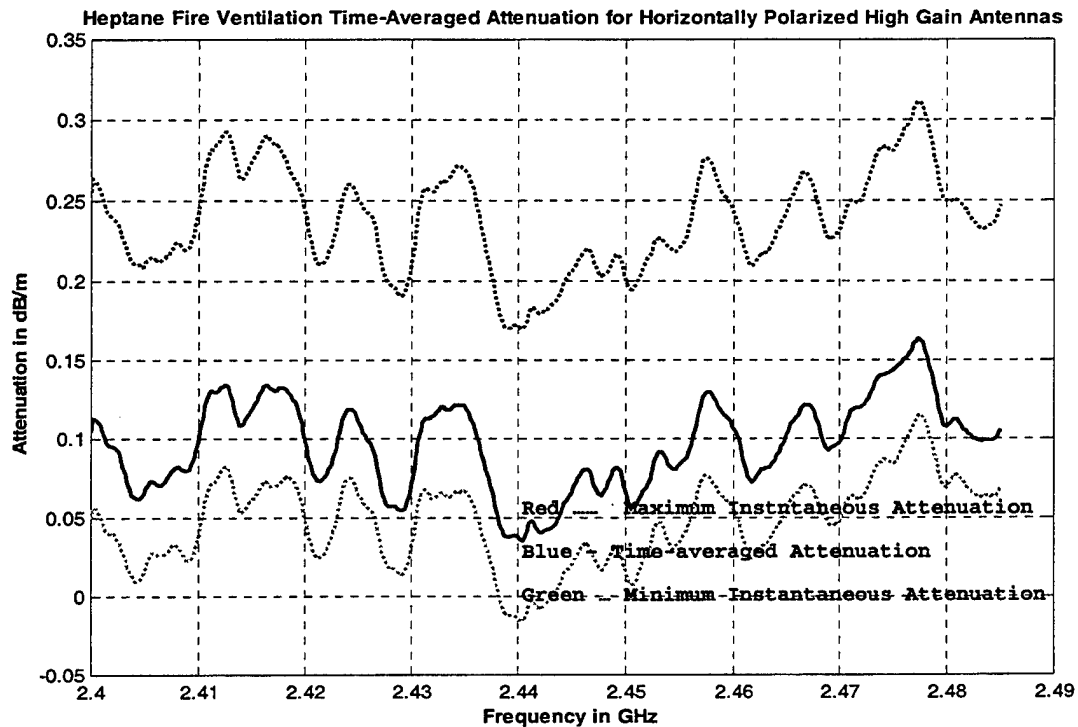


Figure 9.106: Heptane Fire Ventilation Phase Time-Averaged Attenuation for Horizontally Polarized Directional Antennas

o) Attenuation Probability Density Functions for Horizontally Polarized Directional Antennas

The attenuation probability density functions (pdf) for each frequency scan for the horizontally polarized directional antennas are shown in Figure 9.107a. The plot shows that the pdf vary with time and that the attenuation caused by fire and the follow on phases is non stationary.

Initially, when the fire was lit at $t=0$ the attenuation has about 0 dB mean and a large standard deviation. As the fire develops the pdf shifts towards higher attenuation values and the standard deviation of the pdf increases. At $t=1$, when the water mist extinguishing system is turned on, the pdf shifts abruptly towards even higher attenuation values and the standard deviation increases further. At $t=3$, when the water mist extinguishing system is turned off, the pdf

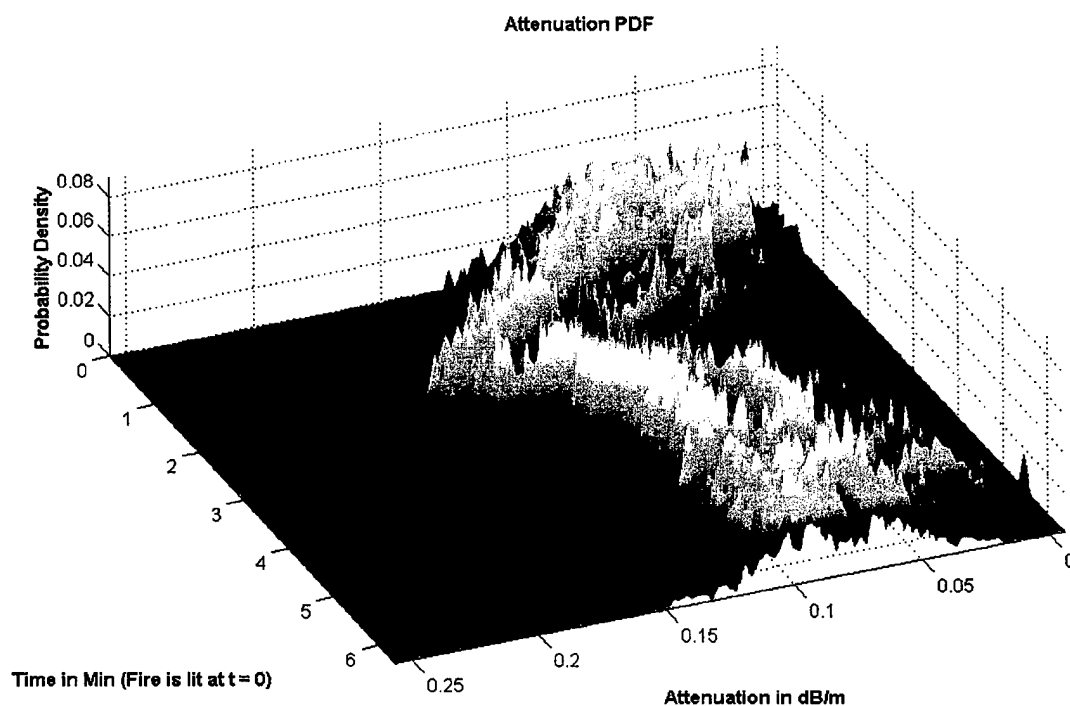


Figure 9.107a: Attenuation Probability Density Functions

starts shifting back towards lower attenuation values, but the standard deviation remains high. Because of the non-stationarity of the pdf's the time-averaged pdf's are presented. For the fire phase, the averaging is done over

the last minute of the fire phase, corresponding to the "fully developed" fire/smoke while for the other phases pdf's for the entire phases are time-averaged.

The attenuation probability density functions for the four phases (fire, water mist, steam build-up, and ventilation) for the horizontally polarized directional antennas during the heptane fire experiments are shown in Figure 9.107b. Also shown, in Figure 9.108, is the "average" attenuation probability density function for all phases. The pdf's for the four phases resemble Gaussian distributions.

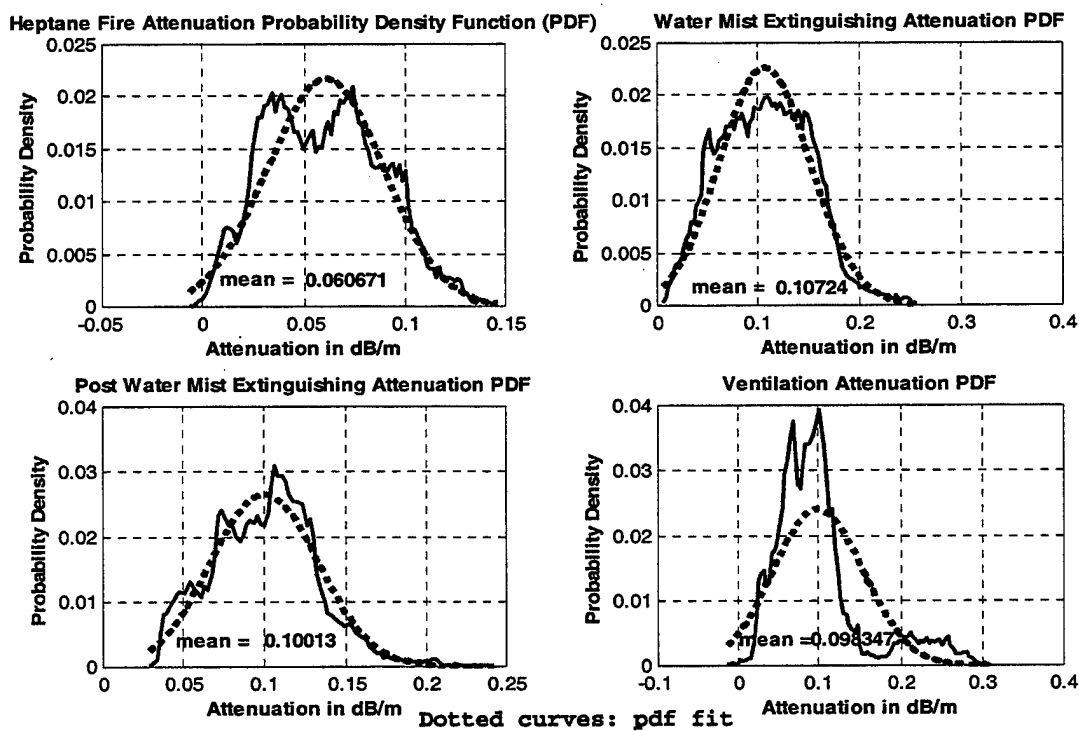


Figure 9.107b: Attenuation Probability Density Functions

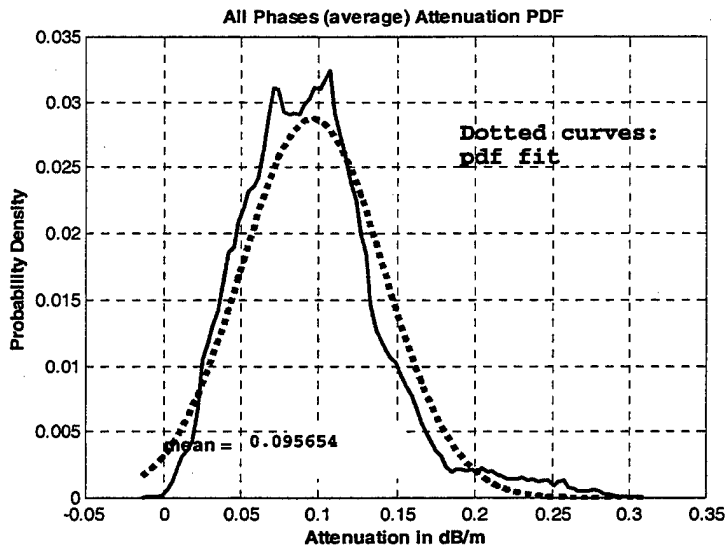


Figure 9.108: Attenuation Average Probability Density Functions

For the fire phase the mean attenuation was 0.060 dB/m. For the water mist phase the mean attenuation was 0.107 dB/m. For the steam build-up phase the mean attenuation was 0.100 dB/m and for the ventilation phase 0.098 dB/m. Finally the all-phases pdf has the average attenuation of 0.095 dB/m. Note that the water mist phase and the steam phase have larger mean attenuation than the fire phase itself.

The cumulative distribution functions for the attenuation for the four phases individually and the overall cumulative distribution function are shown in figures IX-109 and IX-110, respectively. From the fire phase cdf we can determine that there is a 0.95 probability that the attenuation will be lower than 0.1 dB/m. Similarly for the water mist phase there is a 0.95 probability that the attenuation will be less than 0.18 dB/m. For the steam build-up phase there is 0.95 probability that the

attenuation will be less than 0.17 dB/m. This shows that the attenuation of the water mist extinguishing phase causes larger attenuation than the fire itself. For all the phases there is 0.95 probability that the attenuation is going to

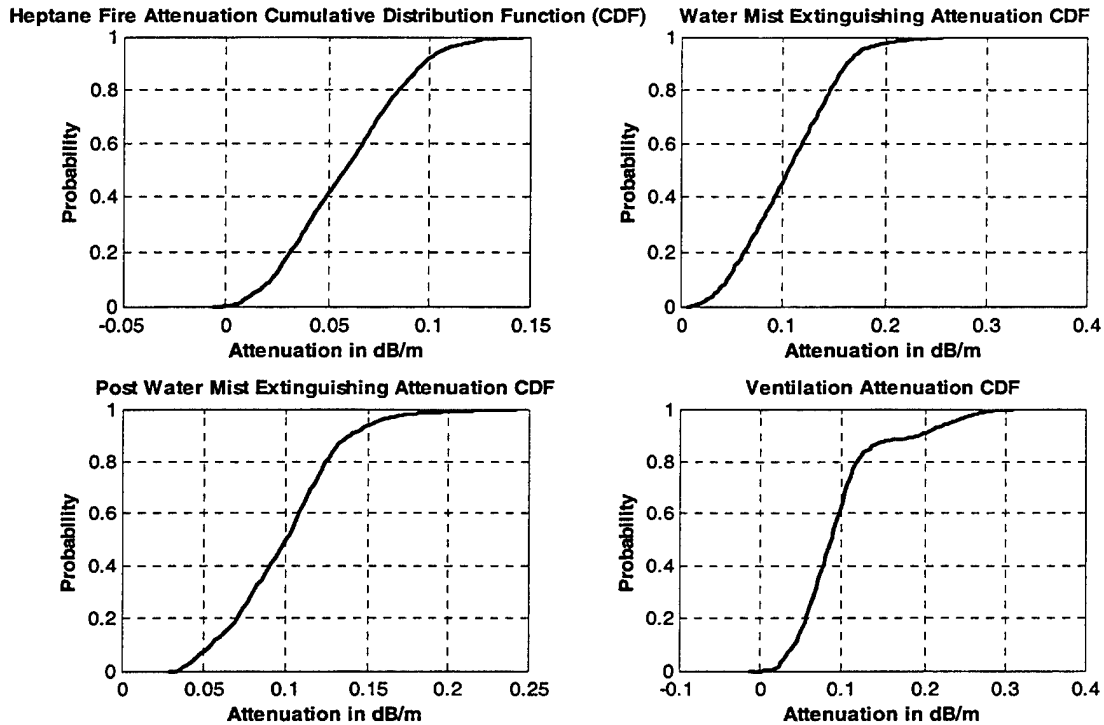


Figure 9.109: Attenuation Cumulative Distribution Functions

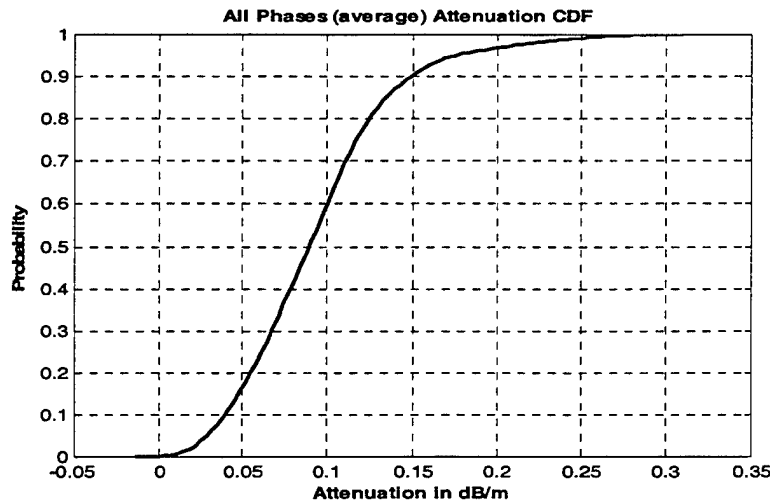


Figure 9.110: Attenuation Cumulative Distribution Functions

be less than 0.22 dB/m. The final ventilation and average cdf values are biased due to the intrusion of the beam.

p) Autocorrelation Functions

Our next step was to determine the attenuation correlation between different frequencies for the different phases of the experiment. Initially we estimated the auto-

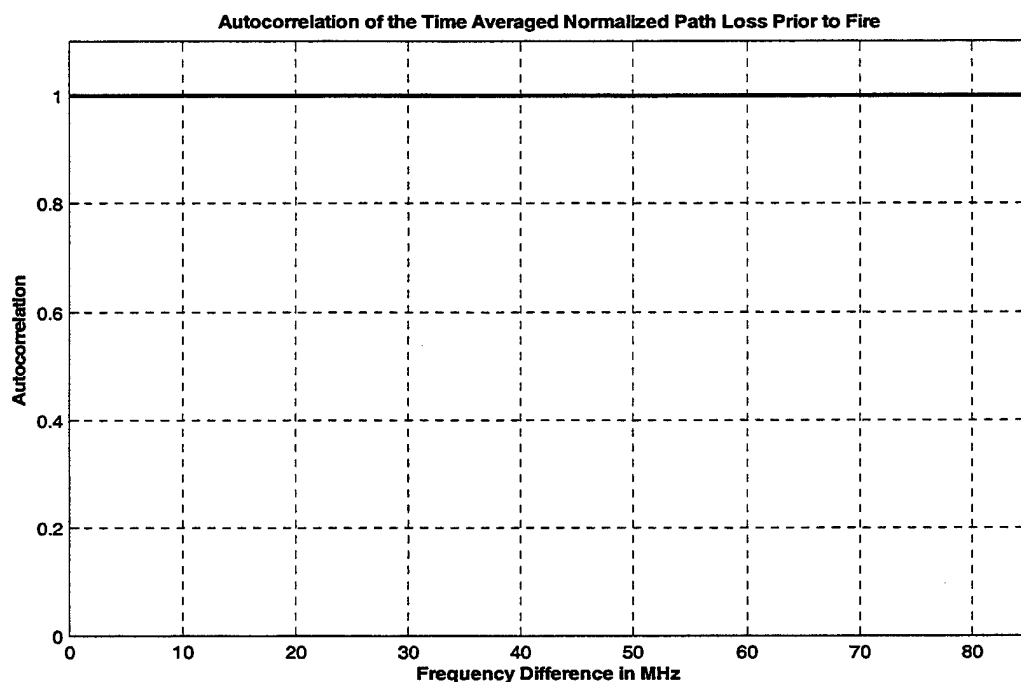


Figure 9.111: Pre-Fire Gain Normalized Autocorellation Function

correlation for the pre-fire phase. In Figure 9.111 the plot of the autocorrelation function indicates a high degree of correlation between attenuation at different frequencies.

This dependency suggests that the attenuation does not vary much with frequency.

The fire phase autocorellation function plot shown in Figure 9.112 is similar to the pre-fire plot. The high values of correlation also follow from the results obtained from the comparison of the pre-fire and heptane fire time-averaged attenuation plots. As shown in Figure 9.96 path loss for all frequency components increased in a similar way and all the minima and maxima remained at the same frequencies.

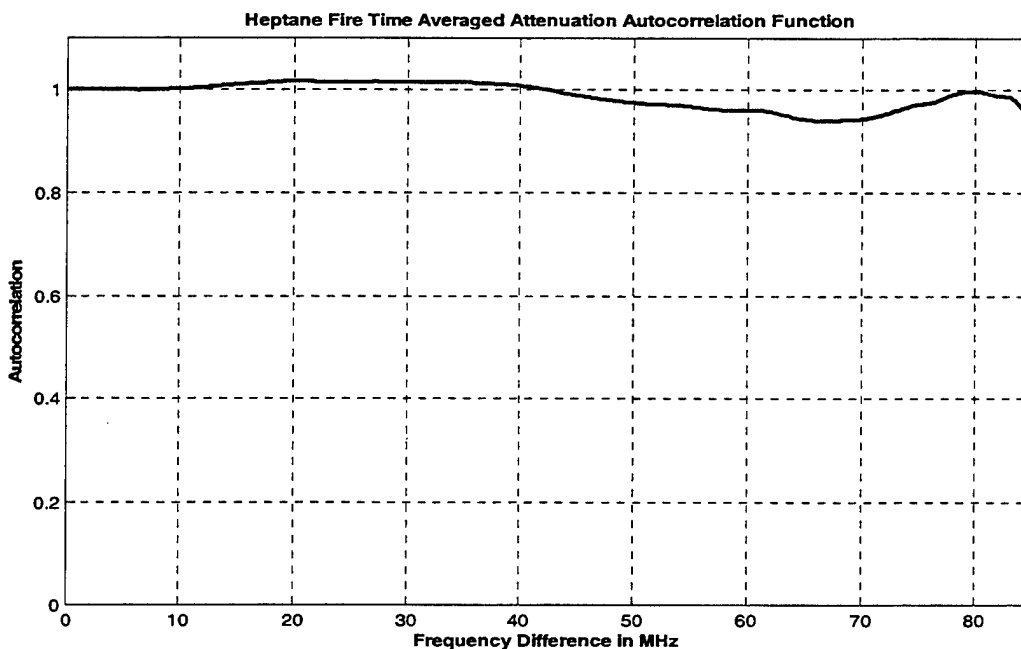


Figure 9.112: Fire Gain Normalized Autocorellation Function

Figures IX-113, IX-114 and IX-115 show the autocorellation function plots for the water mist, steam

build-up, and ventilation phases. These plots are similar to the plots for the pre-fire and heptane fire phases.

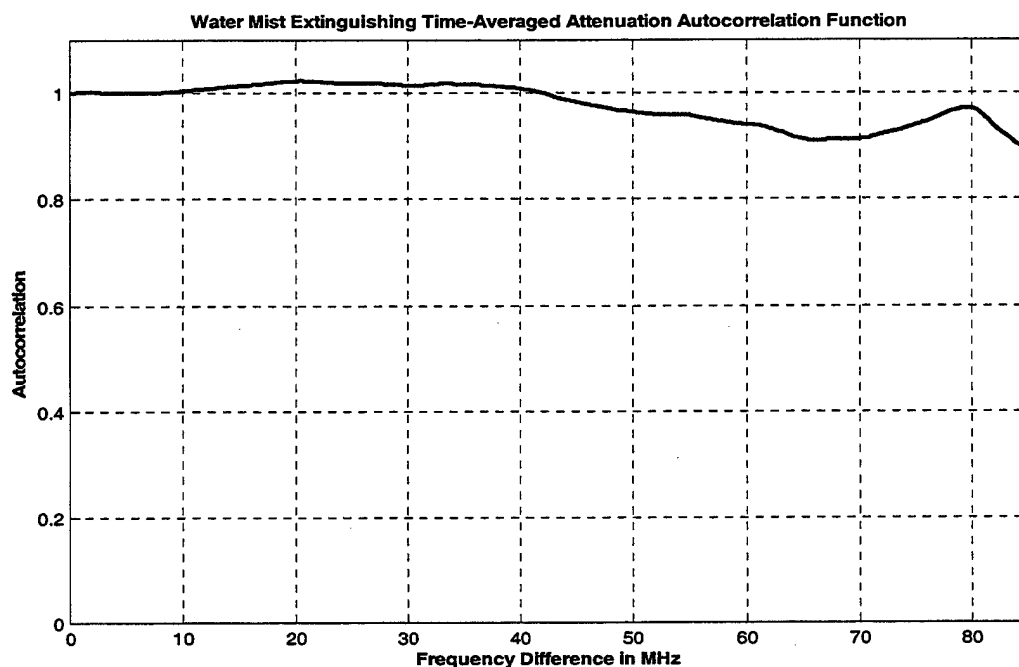


Figure 9.113: Water Mist Gain Normalized Autocorellation Function

This attenuation's relative invariance with frequency is the consequence of using directional antennas for the experiment. There is little effect of the compartment, since the antenna beams are very narrow and a single, line-of-sight path dominates the propagation, and the attenuation due to fire, smoke, and water mist does not vary significantly over the narrow 2.4 GHz ISM frequency band.

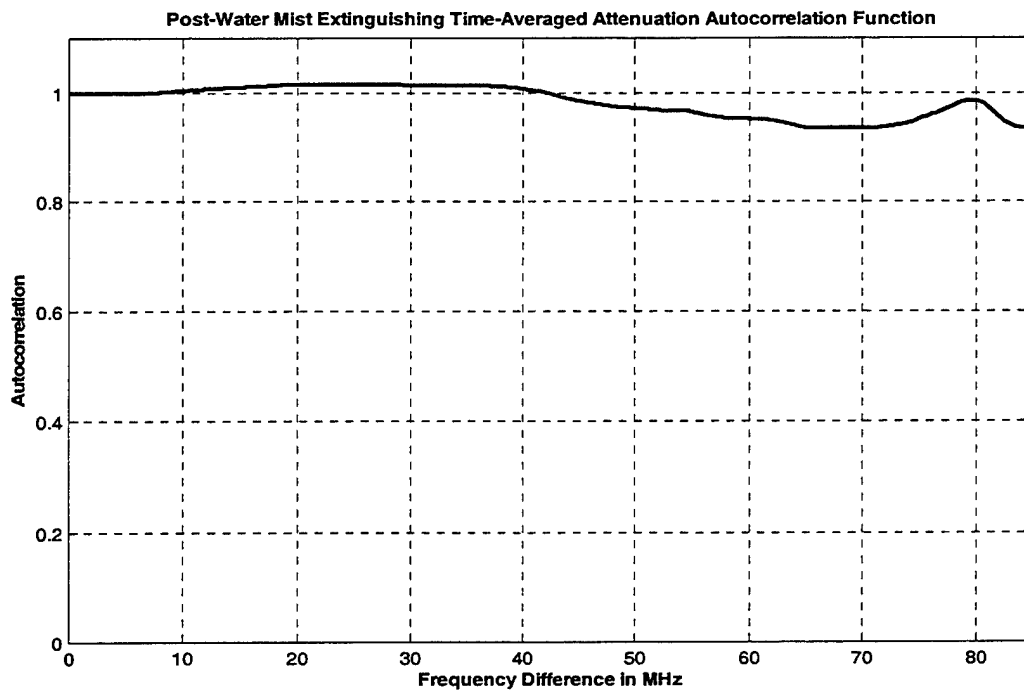


Figure 9.114: Steam Build-Up Gain Normalized Autocorellation Function

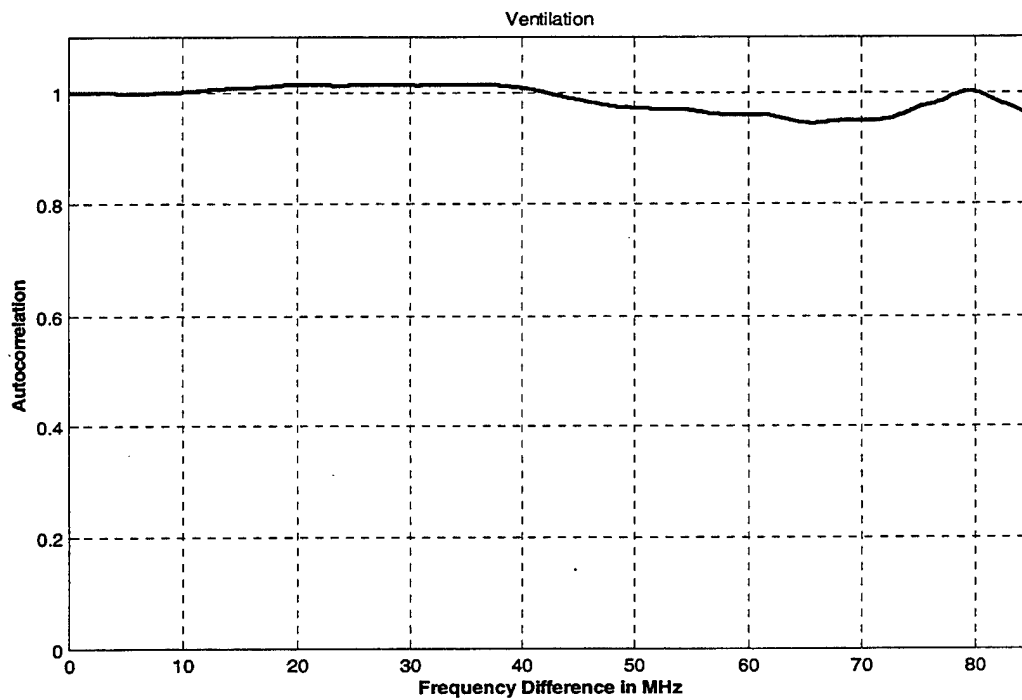


Figure 9.115: Ventilation Gain Normalized Autocorellation Function

q) Estimation of the Best Frequency Difference

The last step was to estimate the frequency difference that, on average, would provide the least combined (sum of) attenuation. This would be useful if a dual-frequency (diversity) transmission system was used. As seen in Figure 9.116 for the horizontally polarized antennas this frequency difference is about 20 MHz, but the changes in combined attenuation are very small. The values close to the full ISM bandwidth (85 MHz) are unreliable because of the diminishing number of frequencies-averaged.

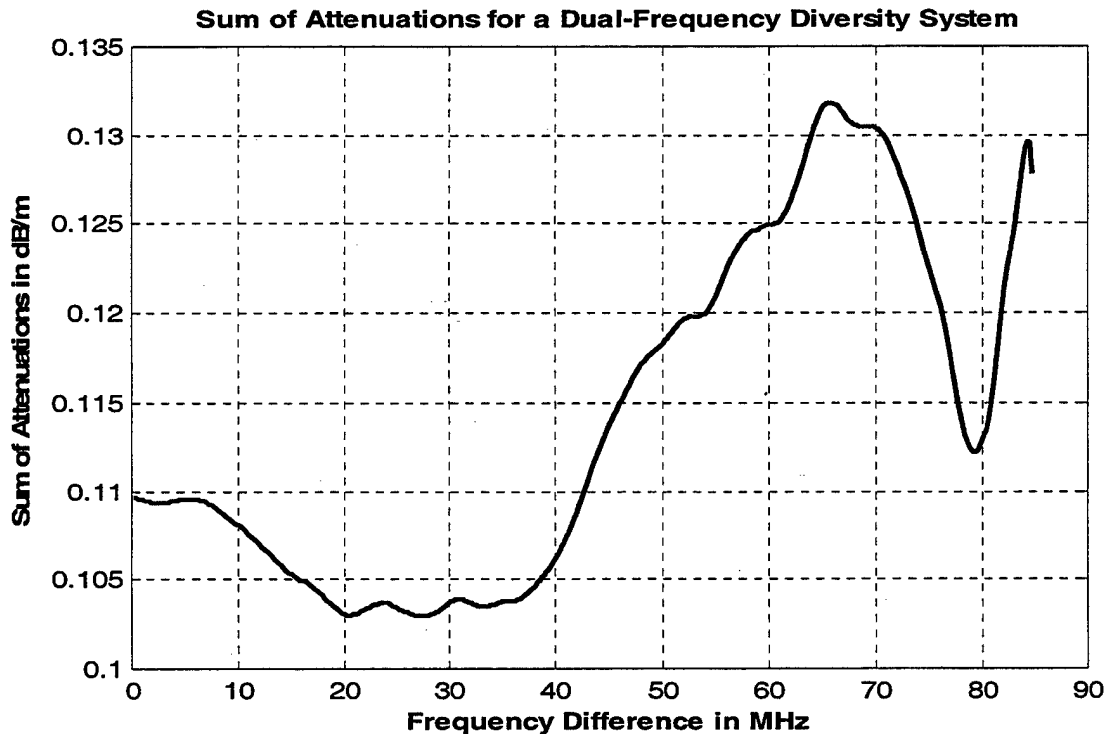


Figure 9.116: Sum of Attenuation for a Dual-Frequency Diversity System

This page has been intentionally left blank

X. NON DIRECTIONAL ANTENNAS

In this chapter we present the measured and processed data for two sets of measurements involving diesel fires and non-directional ("patch") antennas.

A. DIESEL FIRE

There are two sets of measurements for the diesel fire with the non-directional antennas:

- for vertical polarization and
- for Horizontally Polarized

1. Vertical Polarization

a) *Path loss for Vertically Polarized Non-Directional Antennas*

First the measured path loss is presented as a surface plot with the x-axis as the time axis, the y-axis as the frequency axis and the z-axis as the path loss (in dB) axis. In Figure 10.1 the path loss plot is shown for the vertically polarized non-directional antennas. In this figure we have also shown the phase boundary planes. From the plot we see that initially we have an approximately five minutes pre-fire phase. For this phase the time has negative values from -5 to 0. At $t=0$ diesel fire and its measurements begin. The fire lasts for approximately five minutes

(minutes 0-5) followed by a two minute water mist phase (minutes 5-7) and finally a five minute steam build-up phase (minutes 7-12). Finally we see an approximately five-minute post-fire phase. Note that the path loss is much higher than for the directional antennas, because of the lower antenna gain.

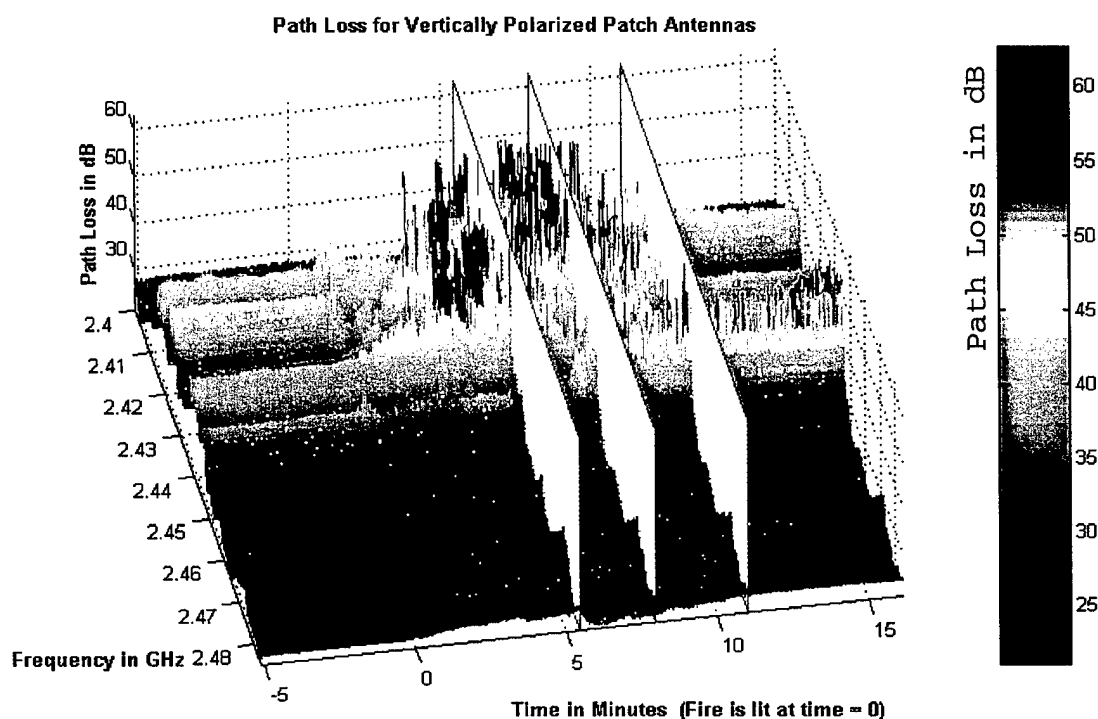


Figure 10.1: Path Loss for Vertically Polarized Patch Antennas

In Figure 10.2 the same surface plot is shown without the phase boundaries. We note the continuity between the fire, water mist and steam build-up phases and a discontinuity between the pre-fire phase ($t=0$) and the fire

phase and between the steam build-up and the post-fire phases ($t=12$). These discontinuities are caused by the "interruptions" in the measurement process to allow for the personnel movement in the compartment to light the fire (at $t=0$) and inspect the completion of the particular experiment run (at $t=12$). Measurements taken during these activities would not be valid since the attenuation changed with people moving between the antennas.

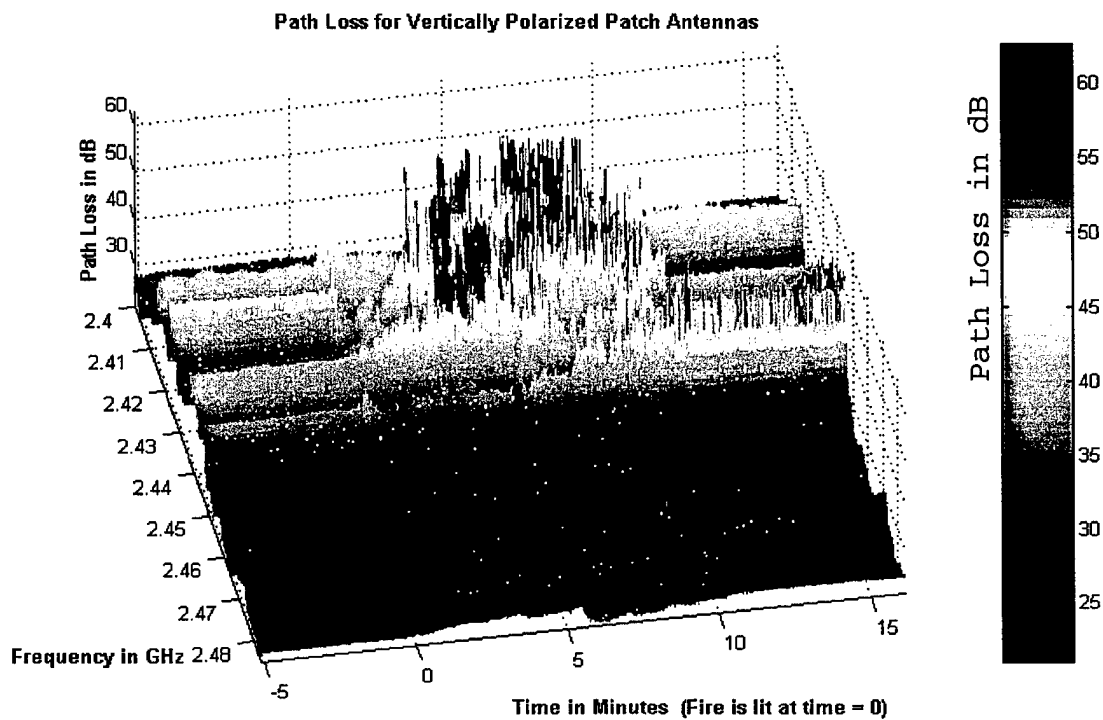


Figure 10.2: Path Loss for Vertically Polarized Patch Antennas

In Figure 10.3 the "bird's eye" view of the path loss is presented. This allows us to visualize how the path loss changes with time and frequency. We note that for the five-minute pre-fire phase the path loss at each frequency

has a constant value with time but is different for different frequencies. The path loss differences are caused by the reflection/absorption characteristics of the portion of the compartment that is "visible" to the two antennas.

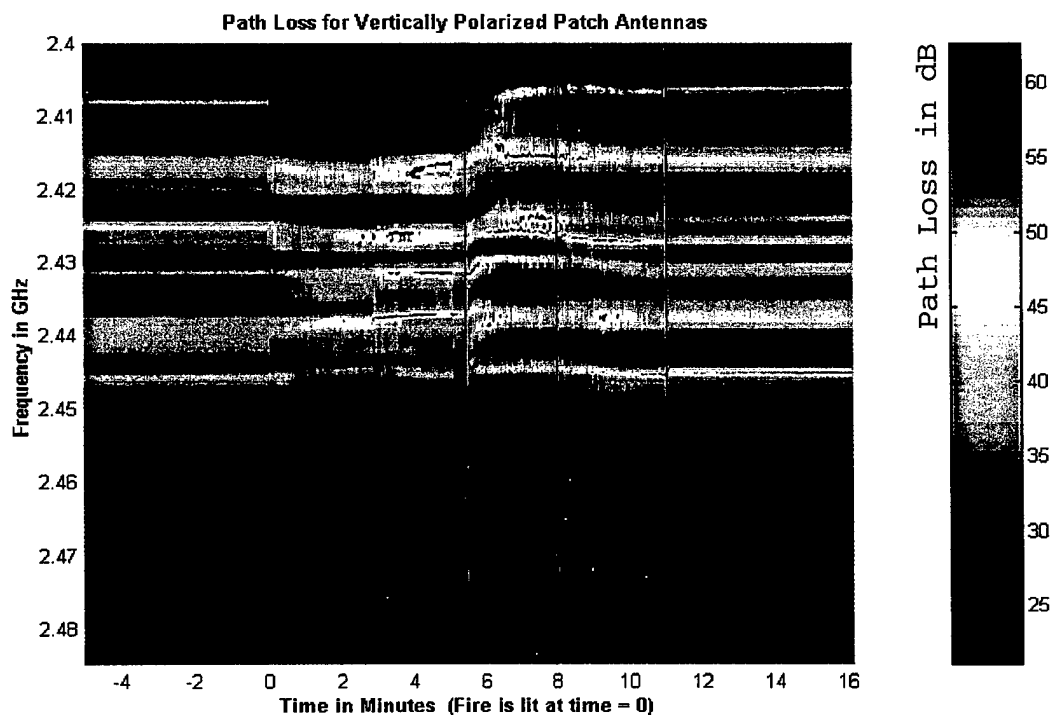


Figure 10.3: Path Loss for Vertically Polarized Patch Antennas

After the fire is lit the path loss increases gradually for all frequencies. We also observe that the locations of the "peaks and valleys" shift towards higher frequencies. During the water mist phase the "peaks and valleys" shift to lower frequencies (opposite to the fire phase) and the path loss reaches its peak value, before decreasing gradually during the steam build-up phase. The

minima/maxima location changes ("shifts") are caused by the changes in the propagation characteristics of the portion of the compartment that is "visible" (within the main beams) to the two antennas. The main cause of the observed changes are the changes in propagation delays for the multipath signal components, and to a much lesser extent from the attenuation caused by fire and its byproducts (as shown by the attenuation results for directional antennas). After the ventilation of the compartment the data for the five minute post-fire phase show that the path loss values are significantly lower than the ones during the fire phase but higher than the values of the pre-fire phase because of the residual water condensation in the compartment and on the antennas. After the ventilation the "peaks" and "valleys" of the path loss shift towards their initial (pre-fire) locations.

b) Attenuation for Vertically Polarized Non-Directional Antennas

We next present the attenuation surface plots. To create these plots we divided each path loss value by the time-averaged pre-fire phase path loss at the corresponding frequency. The result was then divided by the distance between the antennas to obtain the attenuation per unit length. The choice of the distance to obtain the attenuation per unit length (dB/m) requires some explanation. We

selected the distance between the antennas (rather than the fire "depth") for the following reasons:

- The fire depth was ambiguous and changing with time
- The smoke and heat were distributed throughout the compartment and not confined to the "flame" region only
- The antennas were placed close to the fire source (as close as the compartment geometry and the maximum temperature that the antenna could sustain permitted)

In Figure 10.4 the surface plot of the attenuation per meter for the vertically polarized non-directional antennas is shown together with the phase boundary planes. For the pre-fire phase (time between -5 and 0 minutes) the attenuation per meter is approximately 0 dB/m as we would expect since we used the time-averaged path-loss for the pre-fire phase as a reference for each frequency. Therefore, during this phase there are no "peaks and valleys" in the surface plot.

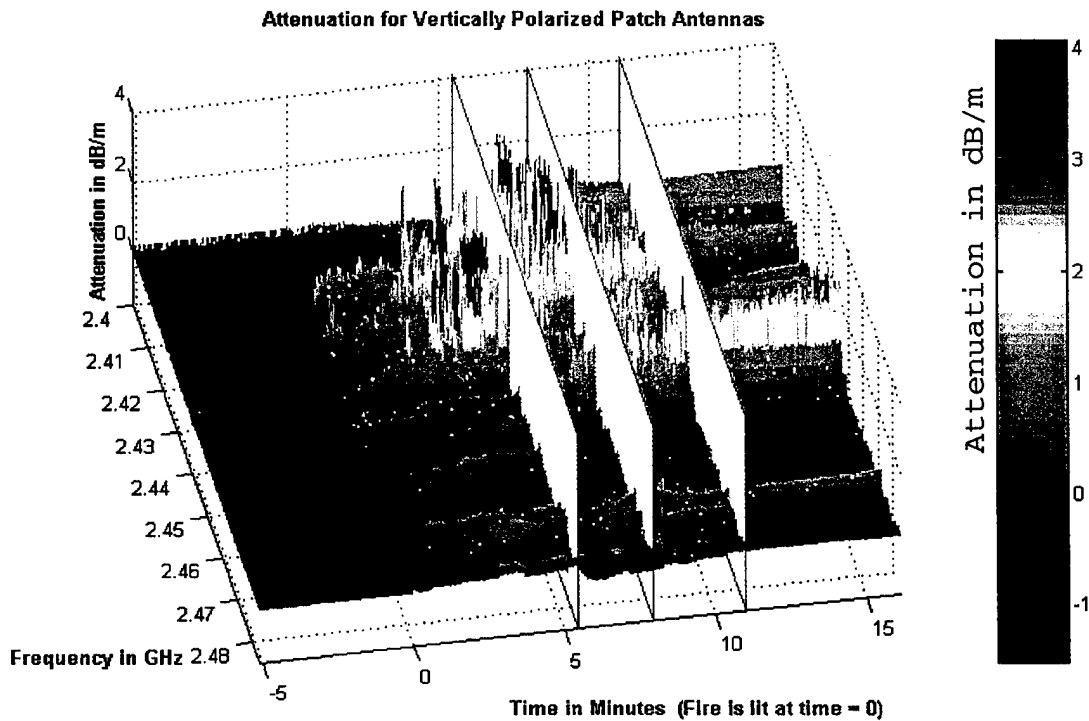


Figure 10.4: Attenuation for Vertically Polarized Patch Antennas

In Figure 10.5 the same surface plot is shown but without the phase boundaries. We note a gradual increase in attenuation during the fire phase, as the heat and smoke build-up in the compartment. Note that near the end of this phase the attenuation is very high for certain frequencies. At about 5 minutes after the fire was lit (for minutes 5-7), there is an abrupt increase in attenuation caused by the activation of the water mist fire-extinguishing system. After two minutes of fire extinguishing the compartment is saturated with steam and smoke (from minute 7 to 12) and the

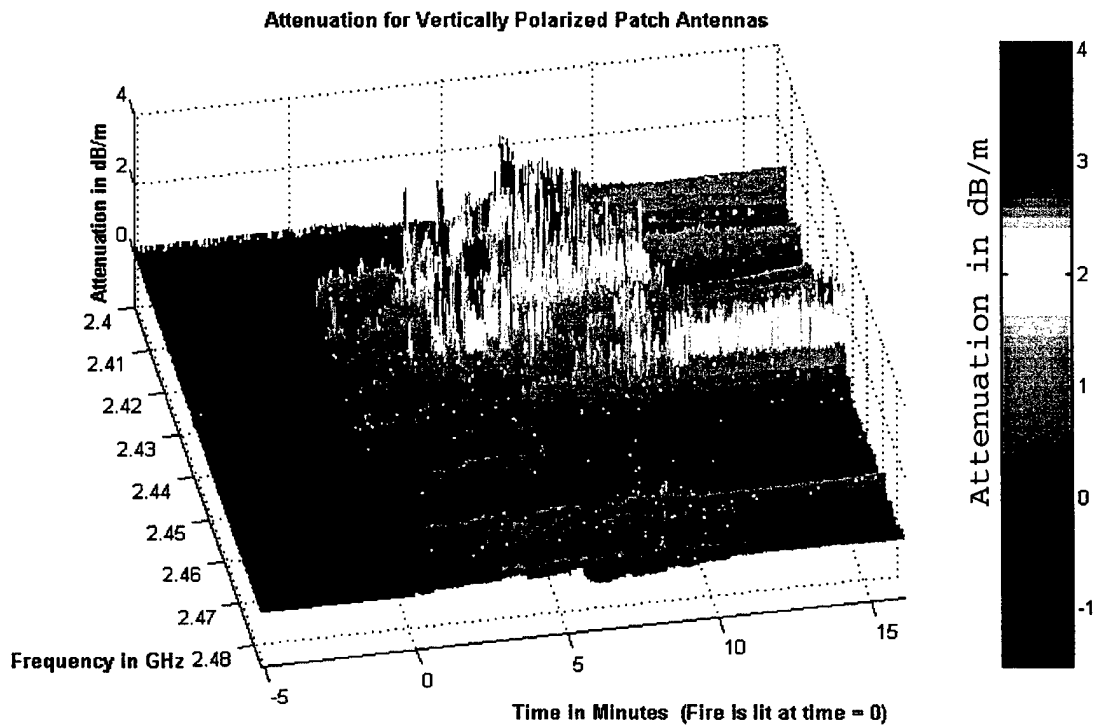


Figure 10.5: Attenuation for Vertically Polarized Patch Antennas

attenuation remains relatively high (but not as high as during the fire-extinguishing phase). Upon ventilation of the compartment the attenuation decreases (from minute 12 on) towards the values prior to the fire (for negative time). Again there are certain frequencies that are significantly attenuated due to the residual water and steam.

In Figure 10.6 the same surface plot is shown, viewed directly from the z-axis (the "bird's-eye" view), clearly showing the attenuation changes for different phases and for different frequencies.

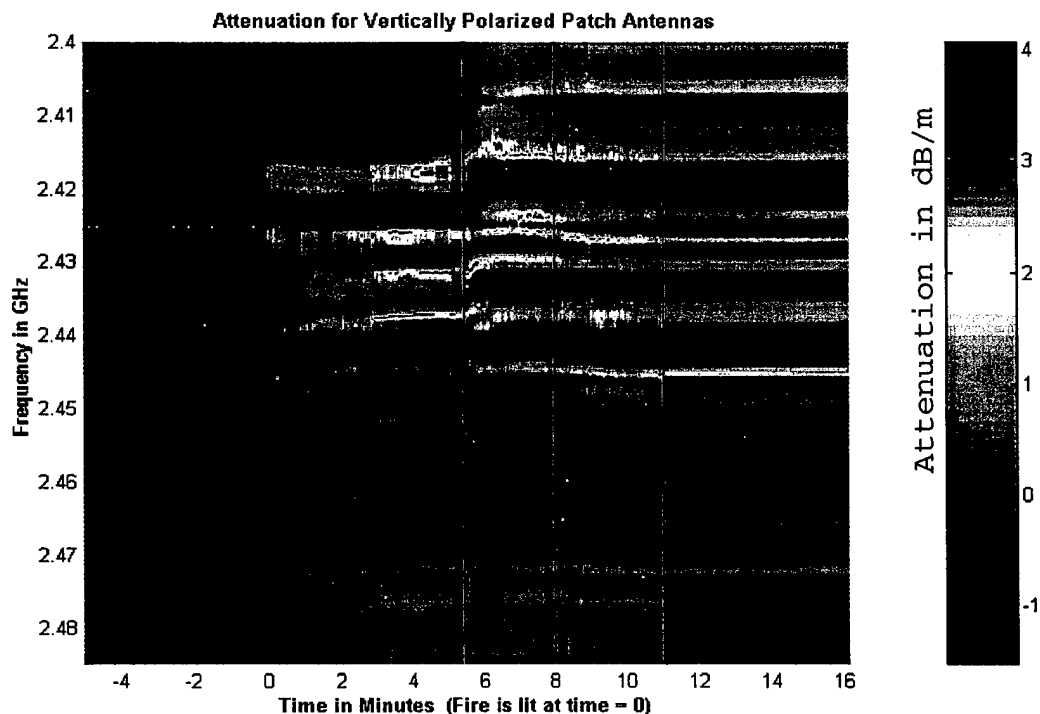


Figure 10.6: Attenuation for Vertically Polarized Patch Antennas

The attenuation per meter reached its maximum value during the water mist fire-extinguishing phase and (for particular frequencies) it was on the order of 4 dB/m. The maximum attenuation for the fire phase was on the order of 2.9 dB/m.

c) Frequency-Averaged Path Loss for Vertically Polarized Non-directional Antennas

The first statistical analysis we performed was to determine the frequency-averaged path loss. As shown in Figure 10.7 the frequency-averaged path loss for the pre-fire phase is almost constant at around 26.4dB. A small

discontinuity is also visible at $t=0$ between the pre-fire and the fire phase due to the door located behind one of the antennas that was open during the pre-fire and closed during the fire phases (the door was used to get access to the compartment by the person starting the fire). After the fire was lit the frequency-averaged path loss increased with time. The rate of increase was fairly constant since we had controlled fire intensity during this phase. After the water mist system was turned on the frequency-averaged path loss initially exhibits a drop, followed by a rapid increase. During the steam build-up phase the frequency-averaged path loss reached its peak value of 27.2 dB and then started to decrease slowly.

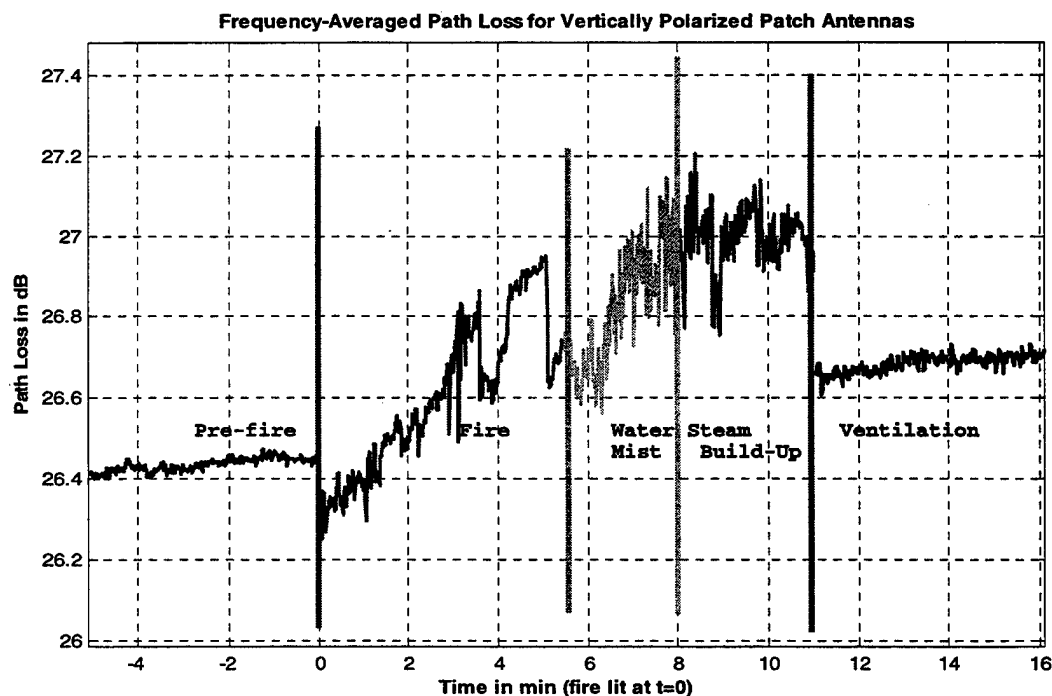


Figure 10.7: Frequency-Averaged Path Loss for Vertically Polarized Patch Antennas

Again, there is a discontinuity between the steam build-up and post-fire phases. This is due to the fact that the post-fire phase measurements were taken approximately ten minutes after the steam build-up phase had ended, the steam was evacuated from the compartment, and the safety personnel inspected the compartment. The frequency-averaged path loss for the post-fire phase is almost constant at about 26.7 dB (slightly higher than for the pre-fire phase).

d) *Frequency-Averaged Attenuation for Vertically Polarized Non-directional Antennas*

Our next step was to determine the frequency-averaged attenuation in dB/m. The shape of the frequency-averaged attenuation as a function of time is exactly the same as for the path loss, as shown in Figure 10.8. The only difference between the frequency-averaged attenuation and the frequency-averaged path loss is the division by a constant distance. During the fire phase the attenuation did not exceed 0.07 dB/m. After the water mist fire extinguishing system was turned on there was a small drop in attenuation (0.01 dB/m) because the smoke and fire were nearly instantaneously suppressed. However as the steam started building up the attenuation per meter increased reaching its maximum value of 0.1 dB/m during the steam build-up phase.

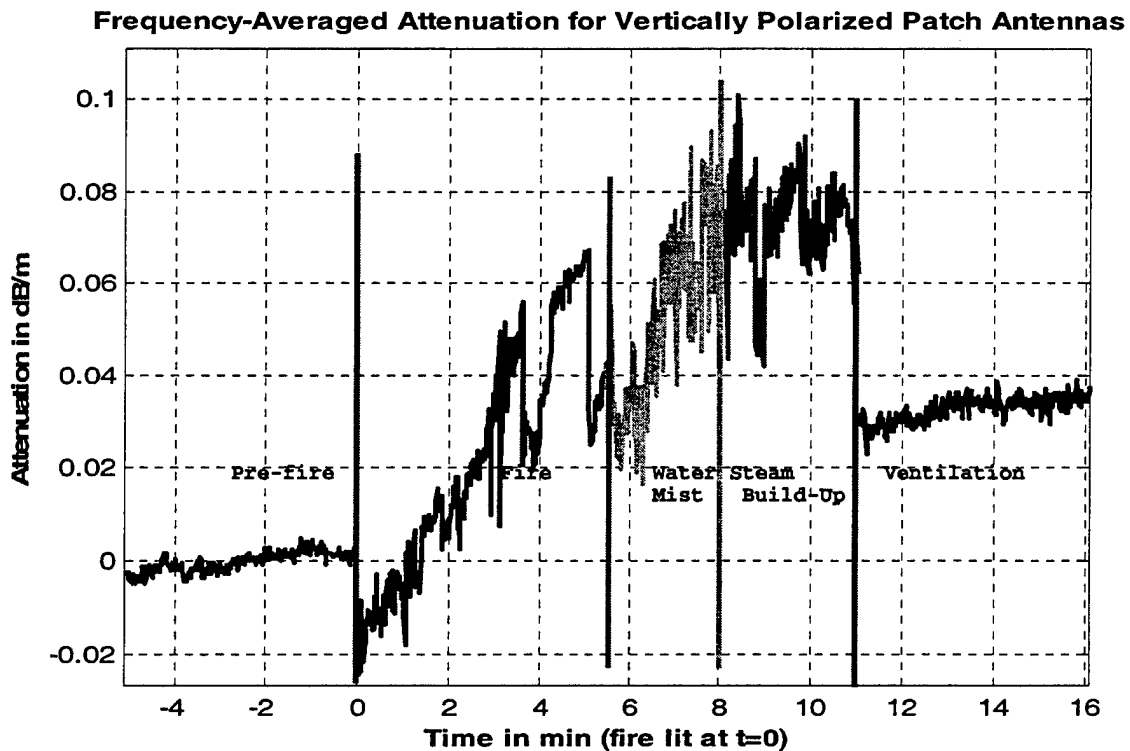


Figure 10.8: Frequency-Averaged Attenuation for Vertically Polarized Patch Antennas

e) Diesel Fire Time-Averaged Path Loss for Vertically Polarized Non-directional Antennas

Our next step was to calculate the time-averaged path loss for the fire phase. As shown in Figure 10.9 the time-averaged path loss ranged between 22 and 42 dB. The plot also shows the minimum and maximum values of instantaneous path loss for each frequency component. The maximum path loss of 62 dB occurs at four frequencies. The path loss value for these four frequencies is about the same because the signal strength at these frequencies was below

the detection threshold of the network analyzer. The minimum path loss of 21 dB occurs at 2.403 GHz. Note the great variation of the path loss with frequency as opposed to a relatively small variation of the frequency averaged path loss with time. This is the direct consequence of the multipath propagation between the two (non-directional) antennas.

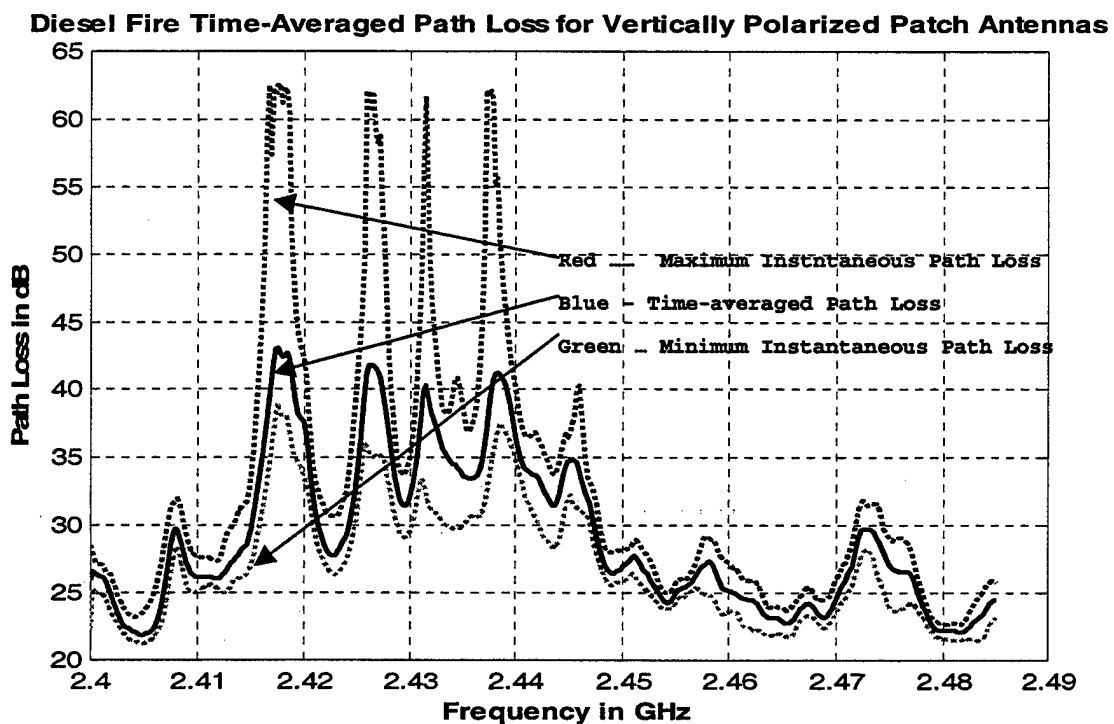


Figure 10.9: Heptane Fire Time-Averaged Path Loss for Vertically Polarized Patch Antennas

The maximum and minimum path loss curves follow the time-averaged attenuation curve, that is the zero slope

points for all three curves are located at the same frequencies.

In Figure 10.10 the time-averaged path loss curve for the fire and the pre-fire phases are shown in order to assess the effects of fire. The minima and maxima of the path loss during the fire shift to higher frequencies by approximately 2 MHz.

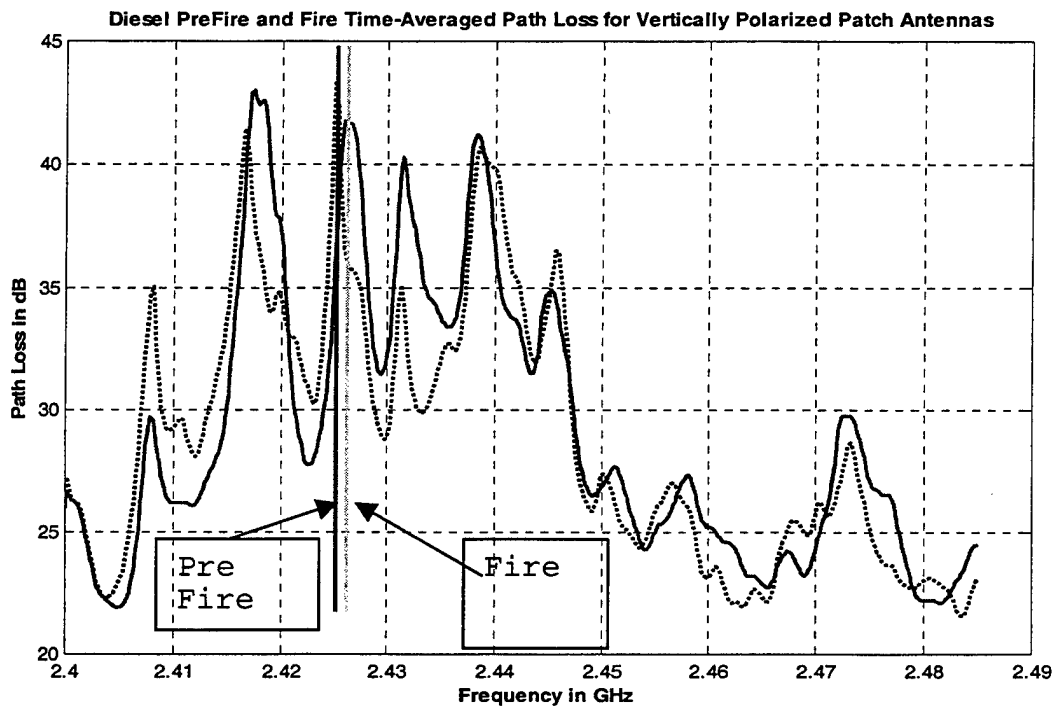


Figure 10.10: Diesel Pre-Fire and Fire Time-Averaged Path Loss for Vertically Polarized Patch Antennas

This shift indicates that there is a change in the multipath propagation characteristics of the compartment due to the fire.

f) Diesel Fire Time-Averaged Attenuation for Vertically Polarized Non-directional Antennas

The time-averaged attenuation per meter during the fire phase is shown in Figure 10.11. The maximum instantaneous attenuation of about 4 dB/m occurs at four frequencies.

Fire Water Mist Extinguishing Time-Averaged Attenuation for Vertically Polarized Patch

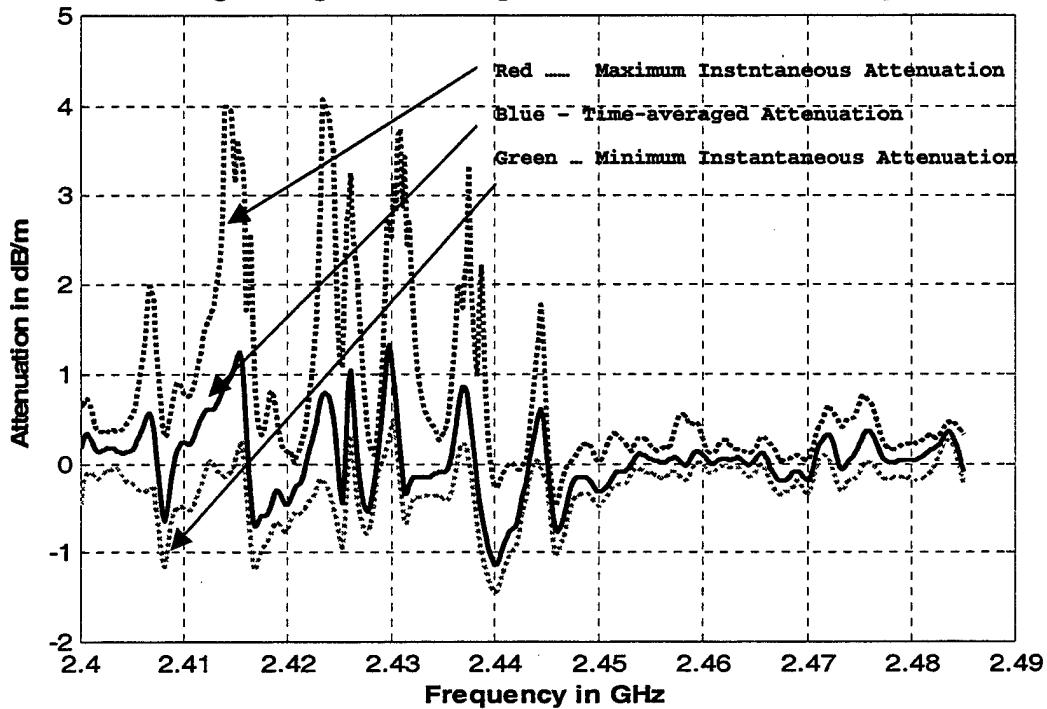


Figure 10.11: Diesel Fire Time-Averaged Attenuation for Vertically Polarized Patch Antennas

The maximum time-averaged attenuation is about 1.1 dB/m. The minimum attenuation for each frequency component is below the 0 dB axis indicating a gain. This is the consequence of the alteration of the compartment multipath propagation characteristics. Due to the shift of the path

loss "peaks and valleys" there are frequencies that are highly attenuated and others that exhibit a transmission gain (compared to the pre-fire phase). Note that these high values of attenuation/gain at certain frequencies are caused by the changes in the propagation velocity (caused by the fire) rather than the losses due to fire.

g) Water Mist Phase Time-Averaged Path Loss for Vertically Polarized Non-directional Antennas

Our next step was to calculate the time-averaged path loss for the water mist phase. As shown in Figure 10.12 the time-averaged path loss ranged between 22 and 45dB. The maximum instantaneous path loss of about 62 dB occurs at four frequencies that are close to the ones for the fire phase. The minimum path loss occurs at 2.404 GHz. Also, the zero slope points for all three curves (min, max and average path loss) occur at approximately the same frequencies.

In Figure 10.13 the time-averaged path loss curves for the water mist and the pre-fire phases are shown. Note that the zero slope points during the water mist phase have shifted to the lower frequencies. This indicates that the changes in the compartment propagation characteristics are opposite for the fire and the water mist extinguishing phases.

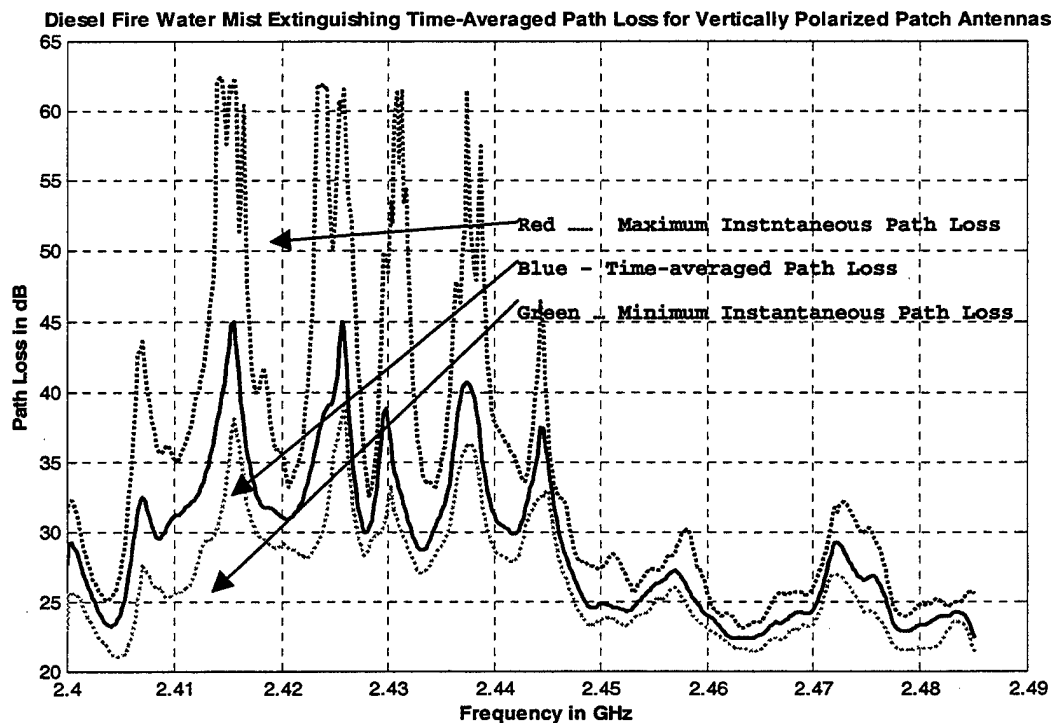


Figure 10.12: Diesel Fire Water Mist Time-Averaged Path Loss for Vertically Polarized Patch Antennas

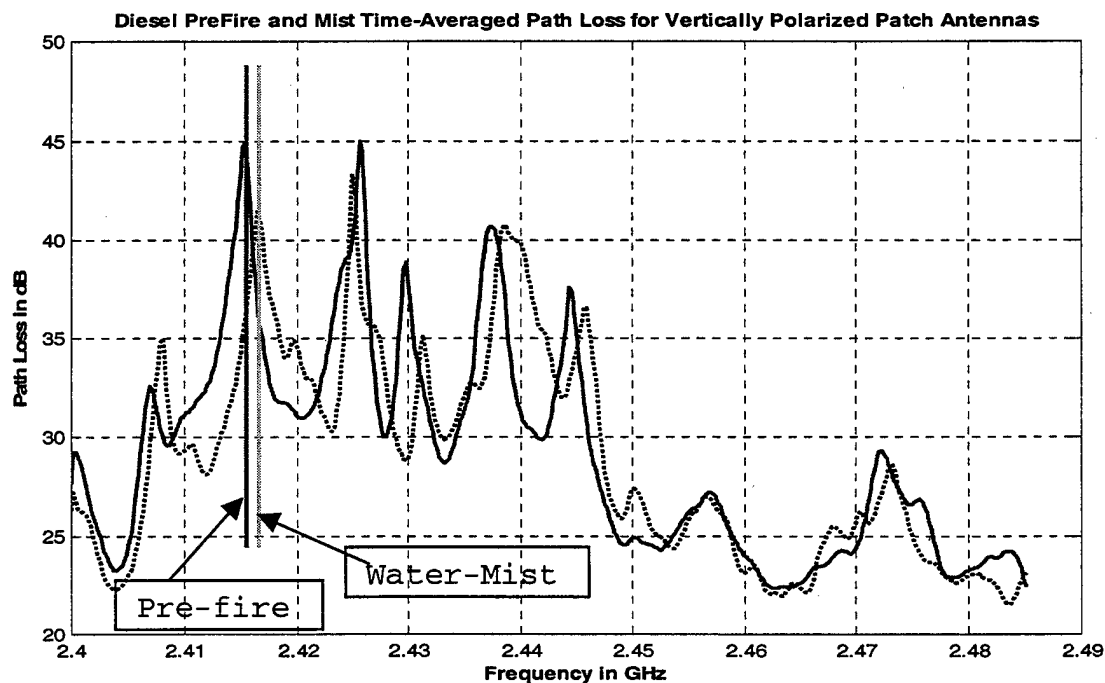


Figure 10.13: Diesel Pre-Fire and Water Mist Time-Averaged Path Loss for Vertically Polarized Patch Antennas

h) Water Mist Time-Averaged Attenuation for Vertically Polarized Non-directional Antennas

The time-averaged attenuation per meter for the water mist phase is shown in Figure 10.14. The time-averaged attenuation ranges between -1.1 and 1.2 dB/m. The maximum instantaneous attenuation is about 4 dB/m. The minimum instantaneous attenuation for each frequency component is below the 0dB axis indicating a gain.

Fire Water Mist Extinguishing Time-Averaged Attenuation for Vertically Polarized Patch

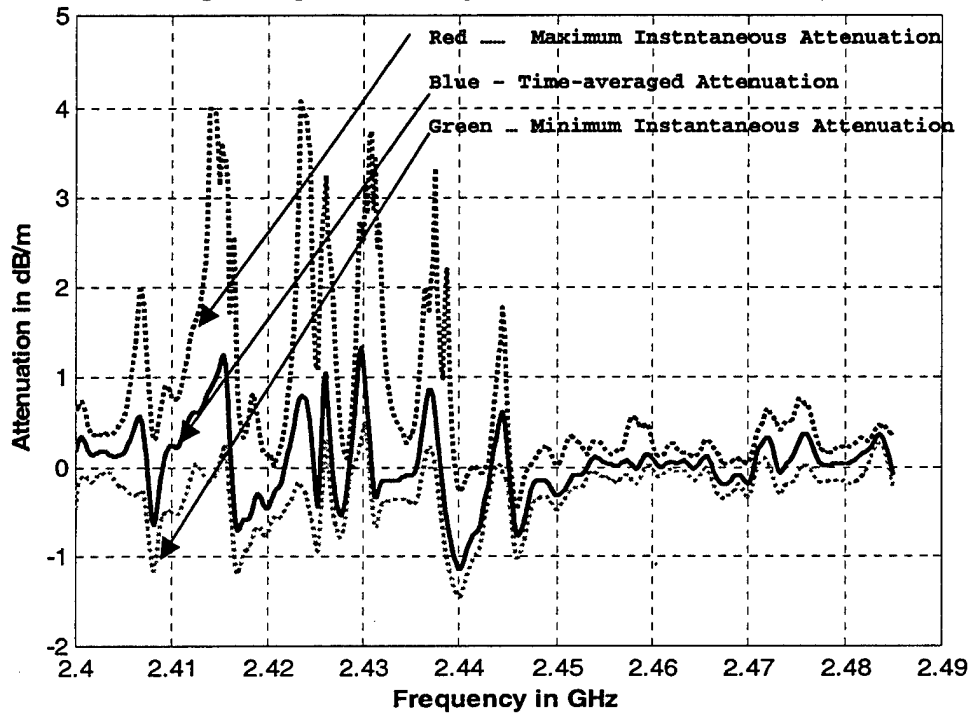


Figure 10.14: Diesel Fire Water Mist Time-Averaged Attenuation for Vertically Polarized Patch Antennas

This is the consequence of the alteration of the compartment multipath propagation characteristics causing the shift of the path loss "peaks and valleys". Therefore there are frequencies that are highly attenuated and others

that exhibit a transmission gain. Again, note that these effects are due to the multipath phase shift changes caused by the effective propagation velocity changes (due to the water mist), rather than the absorption losses of the RF energy by the water particles.

i) Steam Build-Up Phase Time-Averaged Path Loss for Vertically Polarized Non-directional Antennas

Next we calculated the time-averaged path loss for the steam build-up phase. As shown in Figure 10.15 the time-averaged path loss ranged between 24 and 44dB. Also shown on the same plot are the minimum and maximum values of the instantaneous attenuation for each frequency component. The maximum path loss of ~60dB occurs close to the four frequencies for the water mist phase and the minimum path loss occurs at 2.478 GHz.

In Figure 10.16 the time-averaged path loss curves for the steam build-up and the pre-fire phases are shown. Again the zero slope points (maxima and minima) are shifted to lower frequencies by about 4 MHz. The path loss difference is between -5 and 5 dB, due to the steam and residual smoke in the compartment.

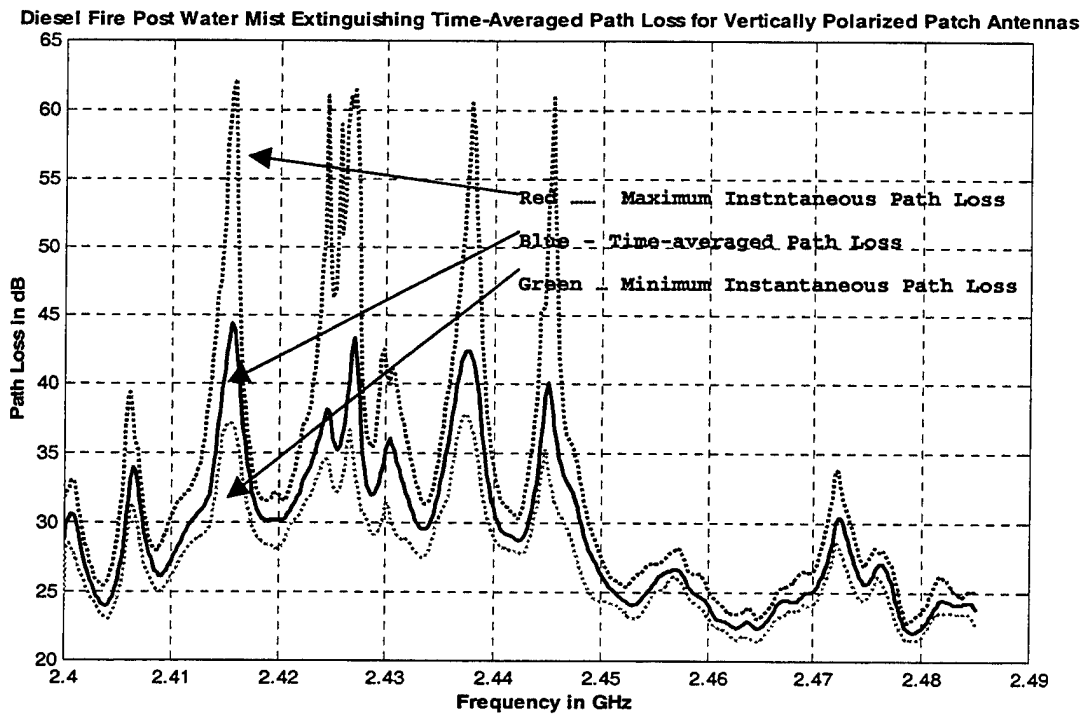


Figure 10.15: Diesel Fire Steam Build-Up Time-Averaged Path Loss for Vertically Polarized Patch Antennas

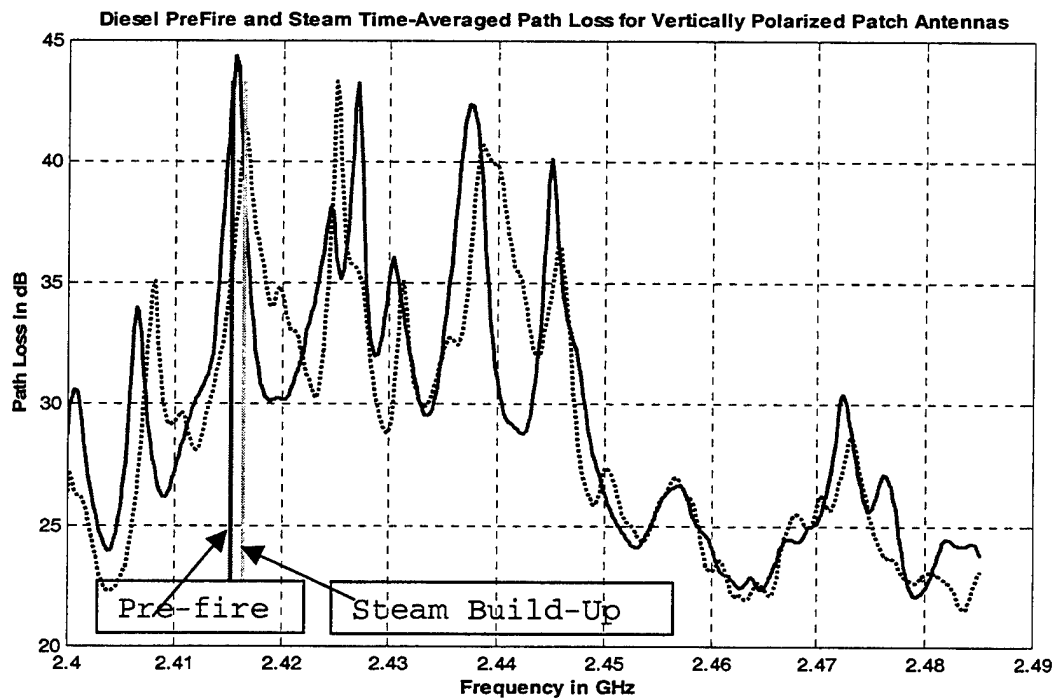


Figure 10.16: Diesel Pre-Fire and Steam Build-Up Time-Averaged Path Loss for Vertically Polarized Patch Antennas

j) **Steam Build Up Time-Averaged Attenuation for Vertically Polarized Non-directional Antennas**

In Figure 10.17, the time-averaged attenuation per meter during the steam build-up phase shows that the values of the time-averaged attenuation per meter vary between -1.1 and 1.02 dB/m, slightly lower than the values measured for the water mist phase.

re Post Water Mist Extinguishing Time-Averaged Attenuation for Vertically Polarized Patch

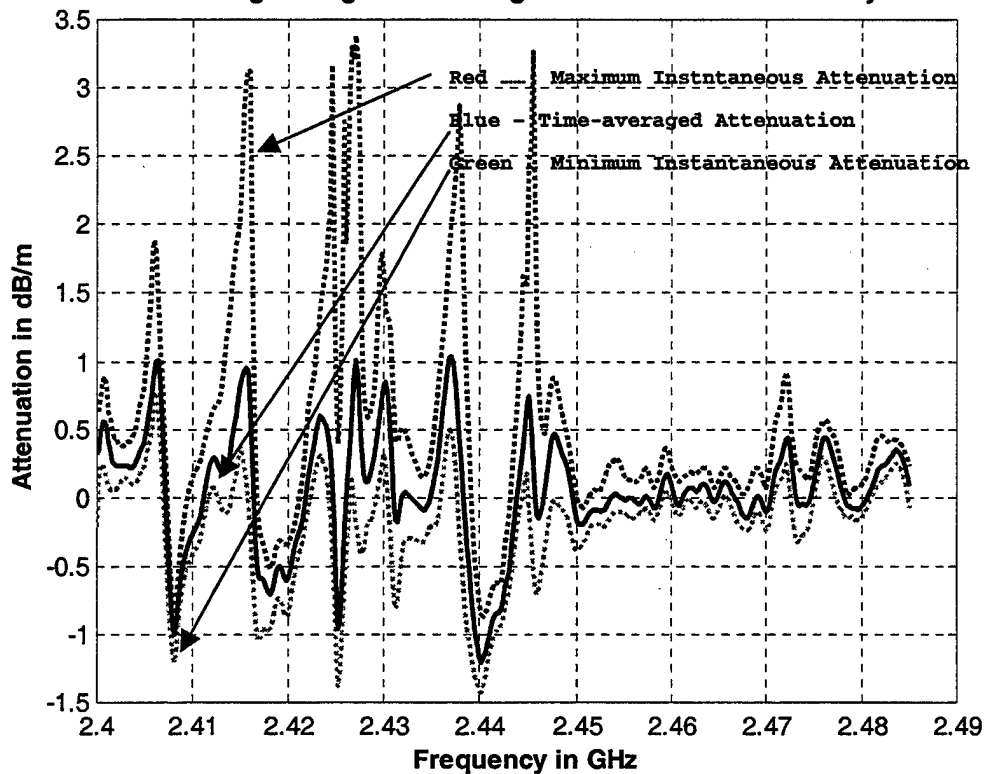


Figure 10.17: Diesel Fire Steam Build-Up Time-Averaged Average for Vertically Polarized Patch Antennas

k) Attenuation Probability Density Functions for Vertically Polarized Non-directional Antennas

The attenuation probability density functions (pdf) for each frequency scan for the vertically polarized non-directional antennas is shown in Figure 9.18a. The plot shows that the pdf vary with time and that the attenuation caused by fire and the follow on phases is non stationary. Initially, when the fire was lit at $t=0$ the attenuation has about 0 dB mean and a small standard deviation. As the fire develops the pdf shifts towards higher attenuation values

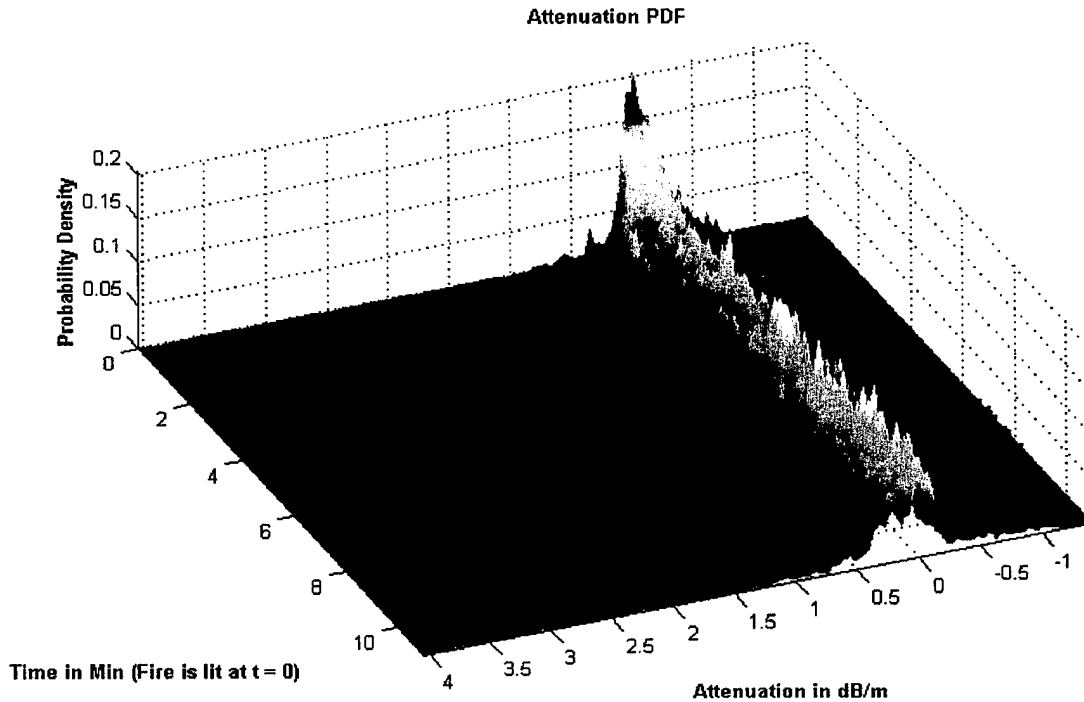


Figure 10.18a: Attenuation Probability Density Function Mesh Plot

and the standard deviation of the pdf increases. At $t=5$, when the water mist extinguishing system is turned on, the

pdf shifts abruptly towards even higher attenuation values and the standard deviation increases further. At $t=7$, when the water mist extinguishing system is turned off, the pdf starts shifting back towards lower attenuation values, but the standard deviation remains high. Because of the non-stationarity of the pdf's the time-averaged pdf's are presented. For the fire phase, the averaging is done over the last minute of the fire phase, corresponding to the "fully developed" fire/smoke; while for the other phases pdf's for the entire phases are time-averaged.

The attenuation probability density functions for the three phases (fire, water mist and steam build-up) for the vertically polarized non-directional antennas during the diesel fire experiments are shown in Figure 10.18b. Also shown is the "average" attenuation probability density function for all phases. The pdf's for the three phases resemble Exponential distributions ($p_x(x) = A \cdot e^{-a|x-b|}$). The mean attenuations are:

- For the fire phase 0.148 dB/m
- For the water mist phase 0.100 dB/m
- For the steam build-up phase 0.083 dB/m
- For all the three phases 0.100 dB/m

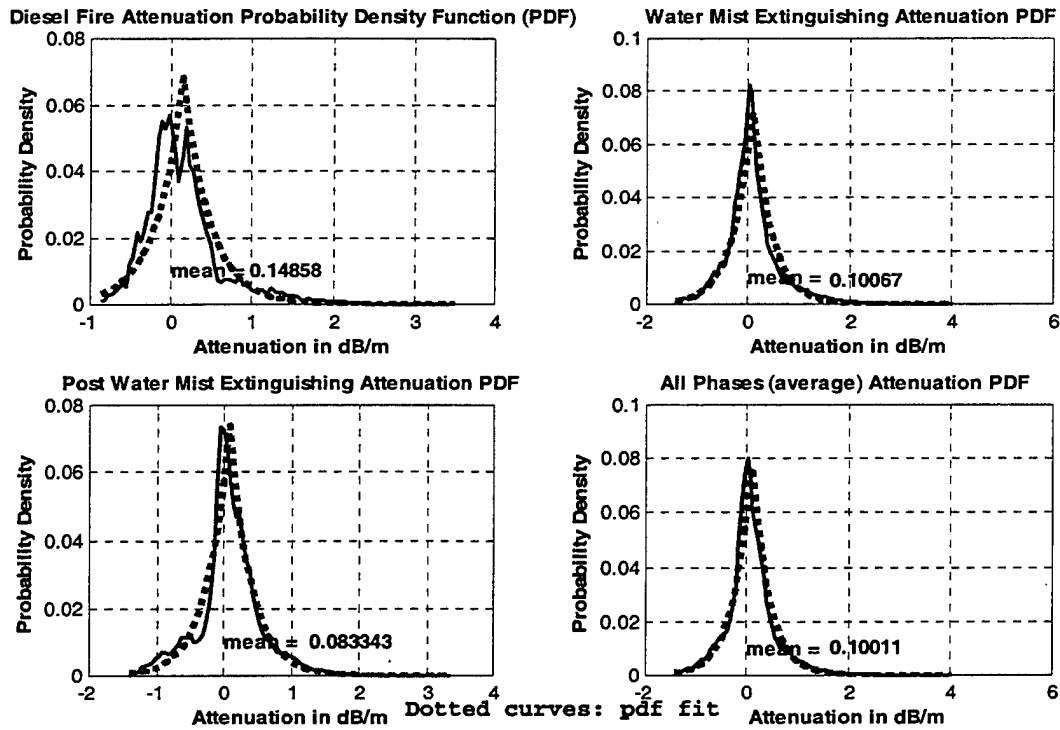


Figure 10.18b: Attenuation Probability Density Functions

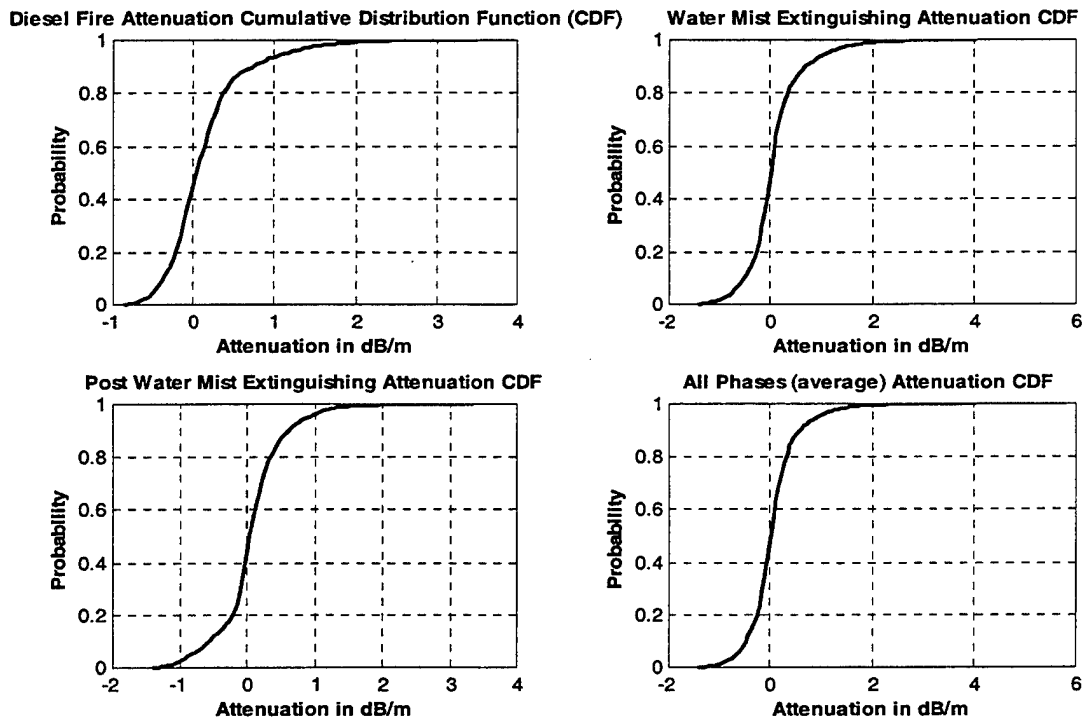


Figure 10.19: Attenuation Cumulative Distribution Functions

The cumulative distribution functions for the attenuation for the three phases individually and the overall cumulative distribution function are shown in Figure 10.19. From the fire phase cdf we can determine that there is a 0.95 probability that the attenuation will be lower than 1.6 dB/m. Similarly for the water mist phase there is a 0.95 probability that the attenuation will be less than 1.8 dB/m. For the steam build-up phase there is 0.95 probability that the attenuation will be less than 1.3 dB/m. This shows that the attenuation for the water mist extinguishing phase causes larger attenuation than the fire itself. For all the phases there is 0.95 probability that the attenuation is going to be less than 1.7 dB/m.

1) Autocorrelation Functions

Our next step was to determine the correlation between different frequencies for the different phases of the experiment. Initially we estimated the autocorrelation for the pre-fire phase. In Figure 10.20 the plot of the autocorrelation function indicates a varying degree of correlation between attenuation at different frequencies. Generally the larger the frequency differences the smaller the correlation. This suggests that the attenuation varies substantially with frequency. Continuing on to the fire phase the autocorellation function plot in Figure 10.21 is

similar to the pre-fire plot, again indicating that different frequency components attenuate differently. This

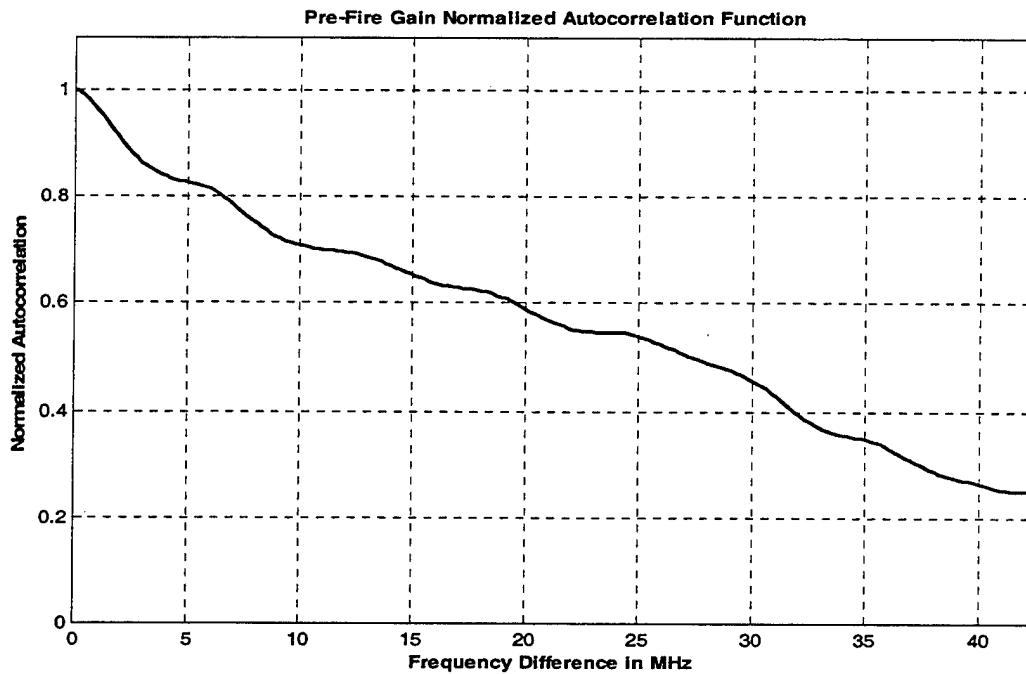


Figure 10.20: Pre-Fire Gain Normalized Autocorellation Function

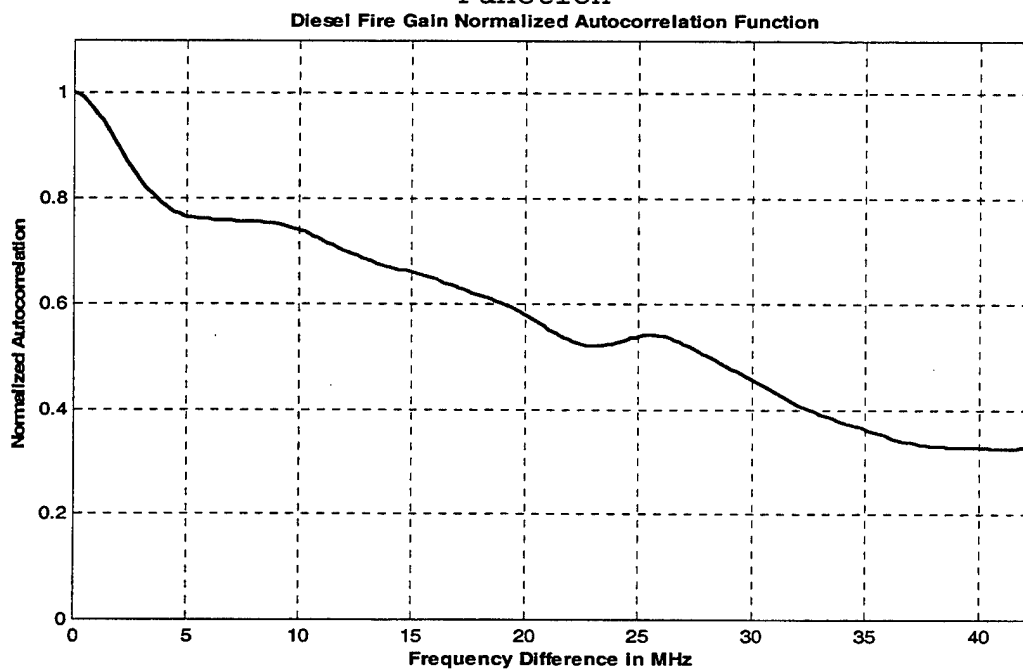


Figure 10.21: Fire Gain Normalized Autocorellation Function

was also evident from Figure 10.10 where path loss for different frequency components increased substantially for some components and decreased for others. Figures X-22 and X-23 show the autocorellation functions for the water mist and steam build-up phases. These autocorellations are similar to the autocorellations for the pre-fire and diesel fire phases.

This type of attenuation variation with frequency is the consequence of using non-directional antennas. There

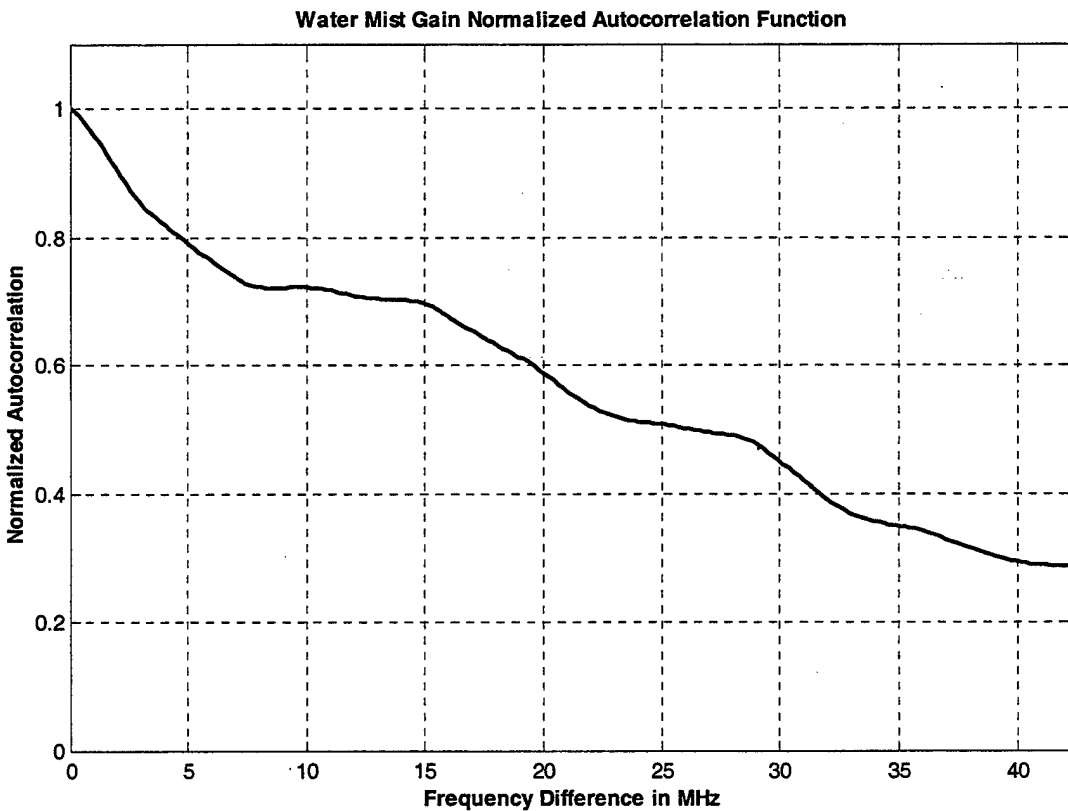


Figure 10.22: Water Mist Gain Normalized Autocorellation Function

is significant effect of the compartment, because of multi path propagation. The multi path causes frequency-selective, non-stationary fading within the 2.4 GHz ISM band.

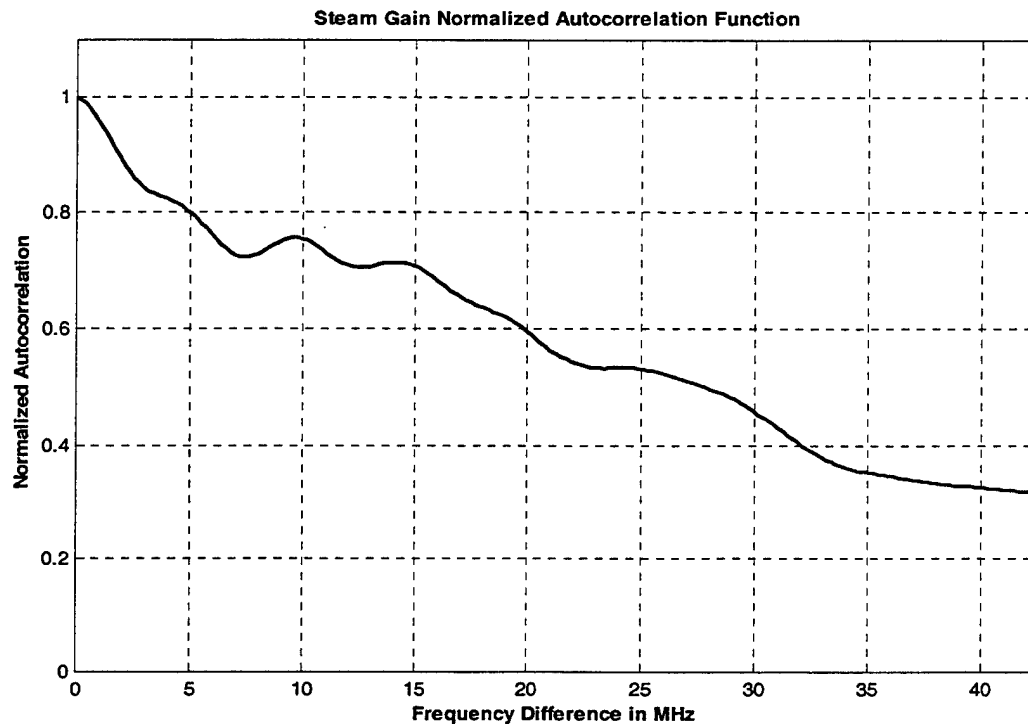


Figure 10.23: Steam Build-Up Gain Normalized Autocorellation Function

m) Estimation of the best frequency difference

The last step was to estimate the frequency difference that, on average, would provide the least combined (sum of) attenuation. This would be useful if a dual-frequency diversity transmission system was used. As seen in Figure 10.24 for the vertically polarized antennas this frequency difference is about 38 MHz. The values close

to the full ISM bandwidth (85 MHz) are unreliable because of the diminishing number of frequencies averaged.

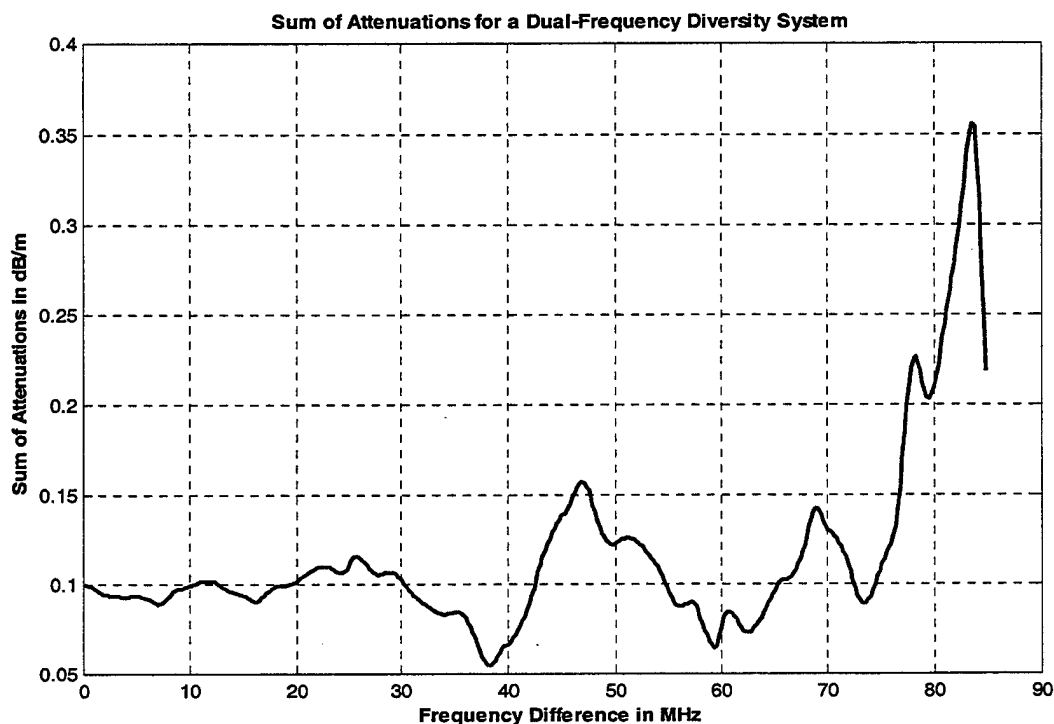


Figure 10.24: Sum of Attenuation for a Dual-Frequency Diversity System

2. Horizontal Polarization

a) *Path loss for Horizontally Polarized Non-directional Antennas.*

First the measured path loss is presented as a surface plot with the x-axis as the time axis, the y-axis as the frequency axis and the z-axis as the path loss (in dB) axis. In Figure 10.25 the path loss plot is shown for the horizontally polarized non-directional antennas, together with the phase boundary planes.

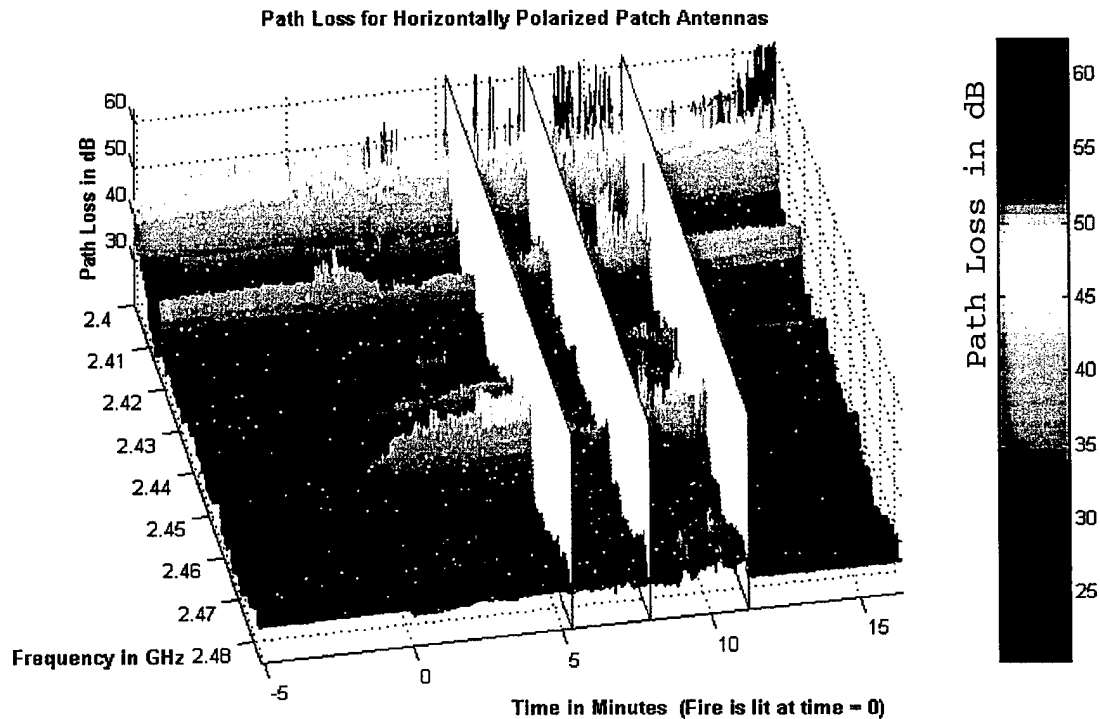


Figure 10.25: Path Loss for Horizontally Polarized Patch Antennas

Initially, we have an approximately five minute pre-fire phase. For this phase the time has negative values from -5 up to 0. Diesel fire measurements begin at $t=0$. The fire last for approximately five minutes (minutes 0-5) followed by a two minute water mist phase (minutes 5-7) and a five minute mist build-up phase (minutes 7-12). Finally we see an approximately five minute post-fire phase.

In Figure 10.26 the same surface plot is shown without the phase boundaries. We note continuity between the

fire, water mist and steam build-up phases. There are discontinuities between the pre-fire phase and the fire

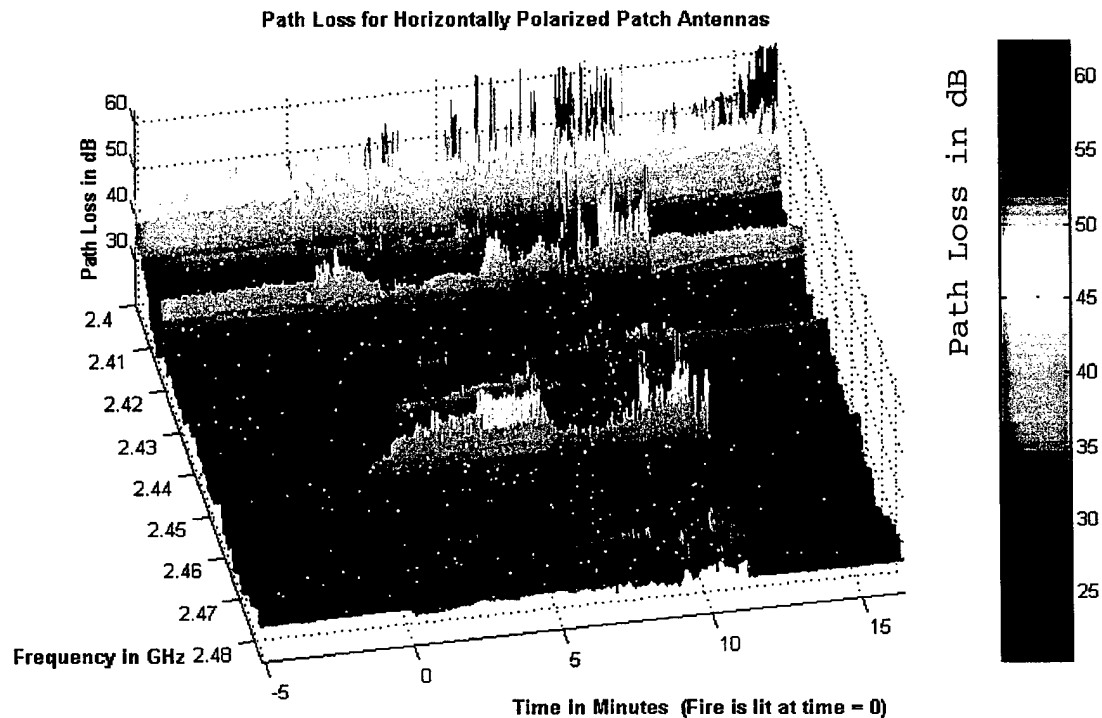


Figure 10.26: Path Loss for Horizontally Polarized Patch Antennas

phase and between the steam build-up and the post-fire phase. These discontinuities are due to the "interruptions" in the measurement process required to allow for the fire personnel to light the fire (at $t=0$) and inspect the completion of the particular experiment run ($t=12$). Measurements taken during this phase would not be valid since the attenuation changed with people moving between the antennas.

In Figure 10.27 the "bird's eye" view of the path loss is presented. This allows us to visualize the path loss

changes with time and frequency. We note that for the five-minute pre-fire phase the path loss at each frequency has a constant value with time but is different for different frequencies, as typical for stationary frequency selective fading.

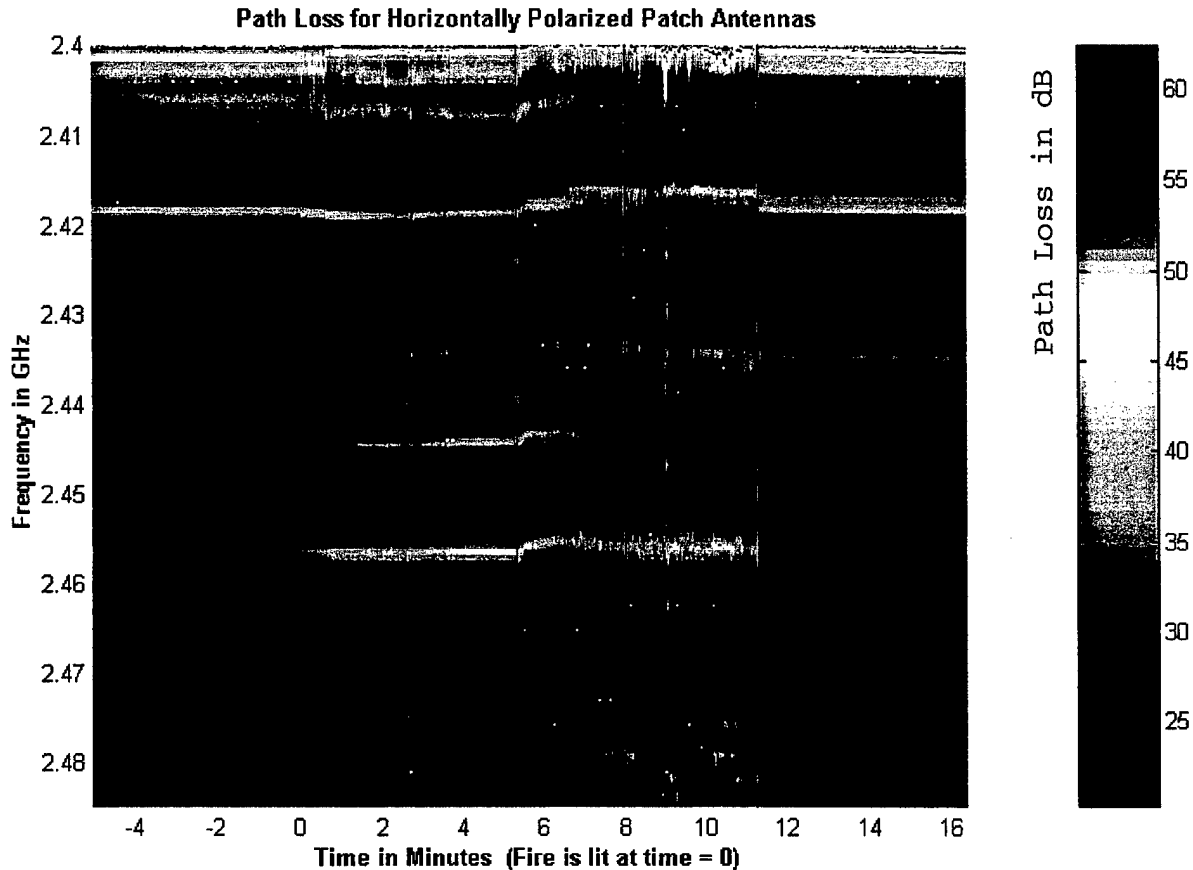


Figure 10.27: Path Loss for Horizontally Polarized Patch Antennas

After the fire is lit the path loss increases gradually for all frequencies. We also observe that the path loss "peaks and valleys" shift towards higher frequencies. During the subsequent water mist phase the "peaks and valleys" shift to lower frequencies and the loss reaches its

valleys" shift to lower frequencies and the loss reaches its peak value of 63 dB. The path loss decreases gradually during the steam build-up phase. The main contribution to the observed path loss changes comes from the changes in relative propagation delays for multipath components, and to a much lesser extent from the attenuation caused by fire and its byproducts. After the ventilation of the compartment, the data for the five minute post-fire phase shows that the path loss values are significantly lower than the ones for the fire phase but higher than the values of the pre-fire phase because of the residual condensation in the compartment and on the antennas. After the ventilation the path loss "peaks and valleys" shift towards their initial locations.

b) *Attenuation for Horizontally Polarized Non-directional Antennas.*

We next present the attenuation surface plots. To create these plots we divided each path loss value by the time-averaged pre-fire phase path loss at the corresponding frequency. The result was then divided by the distance between the antennas to obtain the attenuation per unit length. The choice of the distance to obtain the attenuation per unit length (dB/m) requires some explanation. We selected the distance between the antennas (rather than the fire "depth") for the following reasons:

- The fire depth was ambiguous and changing with time
- The smoke and heat were distributed throughout the compartment and not confined to the "flame" region only
- The antennas were placed close to the fire source (as close as the compartment geometry and the maximum temperature that the antenna could sustain permitted)

In Figure 10.28 the surface plot of the attenuation per meter surface plot for the horizontally polarized non-directional antennas is shown together with the phase boundary planes. For the pre-fire phase (time between -5 and 0 minutes) the attenuation per meter is approximately 0 dB, as expected since the time-averaged pre-fire phase attenuation values for each frequency were used as a reference. Therefore during this phase there are no "peaks and valleys" in the surface plot. In Figure 10.29 the same surface plot is shown but without the phase boundaries. We note a gradual increase in attenuation during the fire phase, as the heat and smoke build-up in the compartment. At about 5 minutes after the fire was lit (for minutes 5-7), there is an abrupt increase in attenuation caused by the activation of the water mist fire-extinguishing system.

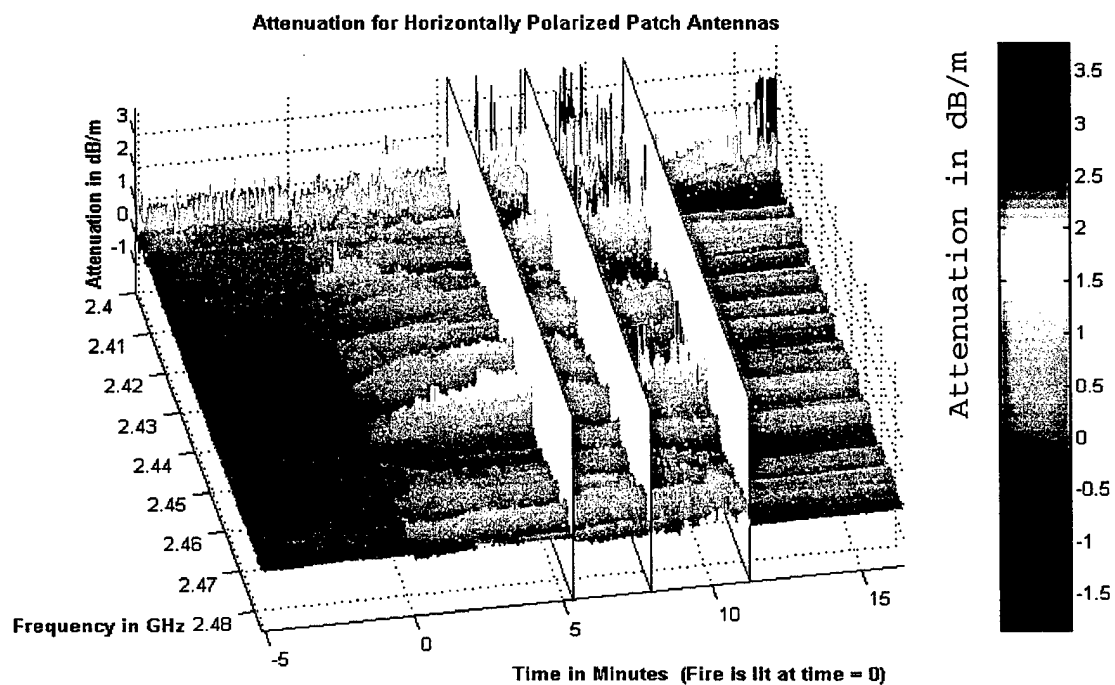


Figure 10.28: Attenuation for Horizontally Polarized Patch Antennas

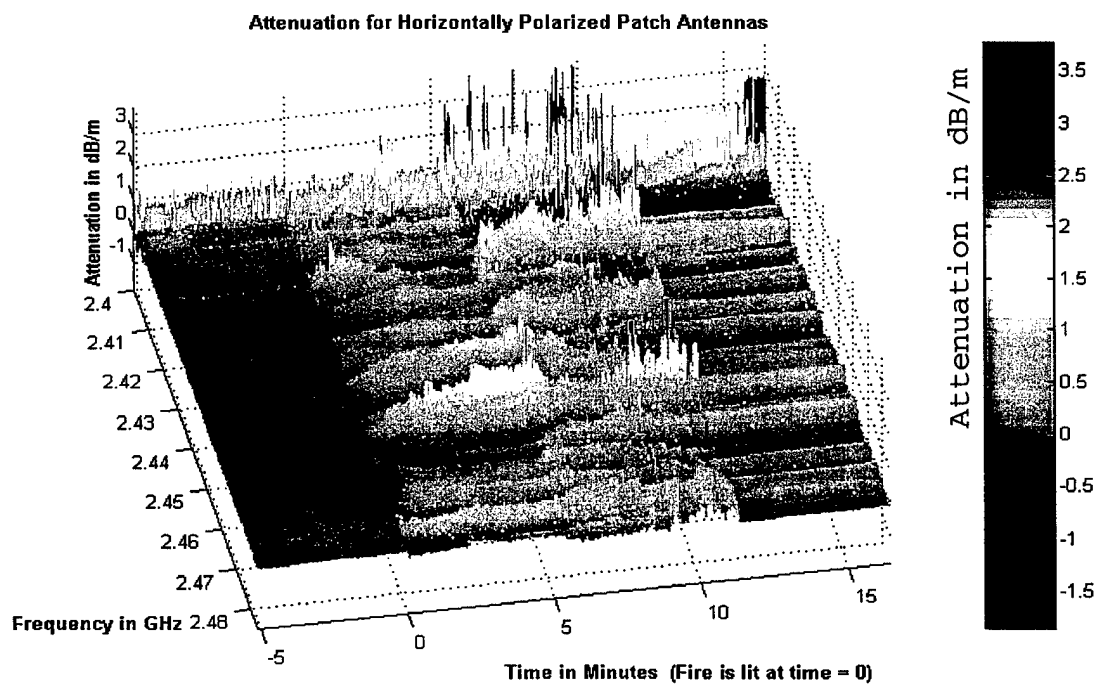


Figure 10.29: Attenuation for Horizontally Polarized Patch Antennas (without phase boundaries)

After the two minutes of fire extinguishing the compartment is saturated with steam and smoke (from minute 7 to 12) and the attenuation remains relatively high (but not as high as during the fire-extinguishing phase). Upon ventilation of the compartment the attenuation decreases (from minute 12 on) towards the values prior to the fire (for negative time).

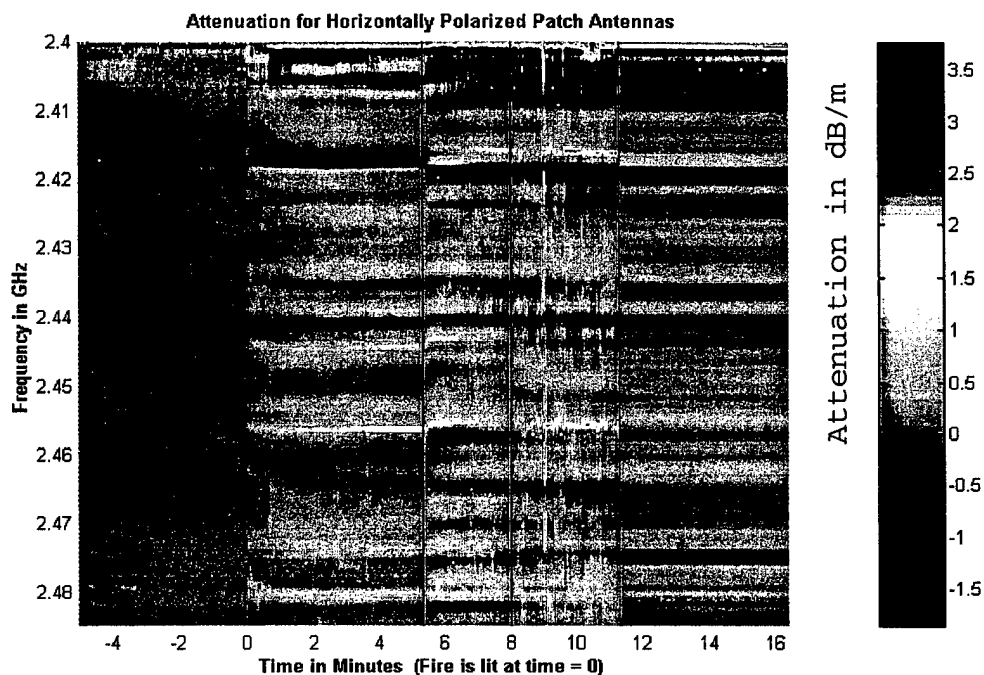


Figure 10.30: Attenuation for Horizontally Polarized Patch Antennas

In Figure 10.30 the same surface plot is shown, viewed directly from the z-axis (the "birds-eye" view) clearly showing the attenuation changes for different phases and for different frequencies. The attenuation per meter reached its maximum value during the water mist fire-

extinguishing phase and (for particular frequencies) it was on the order of 3.7 dB/m. The maximum attenuation for the fire phase was on the order of 0.5 dB/m

c) Frequency-Averaged Path Loss for Horizontally Polarized Non-directional Antennas

The first statistical analysis we performed was to determine the frequency-averaged path loss. As shown in Figure 10.31 the frequency-averaged path loss for the pre-fire phase is almost constant at around 26.6dB. After the fire was lit the frequency-averaged path loss increased with time up to two minutes into the fire when it reached a local maximum. After the water mist system was turned on at about $t=5$ the frequency-average path loss increased rapidly. During the subsequent steam build-up phase the frequency-averaged path loss reached its peak value of about 28 dB. During this phase, at about $t=9$ the time-averaged path loss had a short duration spike of 29.7dB, most likely caused by an intrusion to the space between the antennas by the fire safety personnel. The discontinuity between the steam build-up and post-fire phase is due to the fact that the post-fire phase measurements were taken approximately ten minutes after the steam build-up phase had ended, the steam was evacuated from the compartment, and the compartment was inspected by the safety personnel. The frequency-averaged

path loss for the post-fire phase is almost constant at 26.8 dB (slightly higher than for the pre-fire phase).

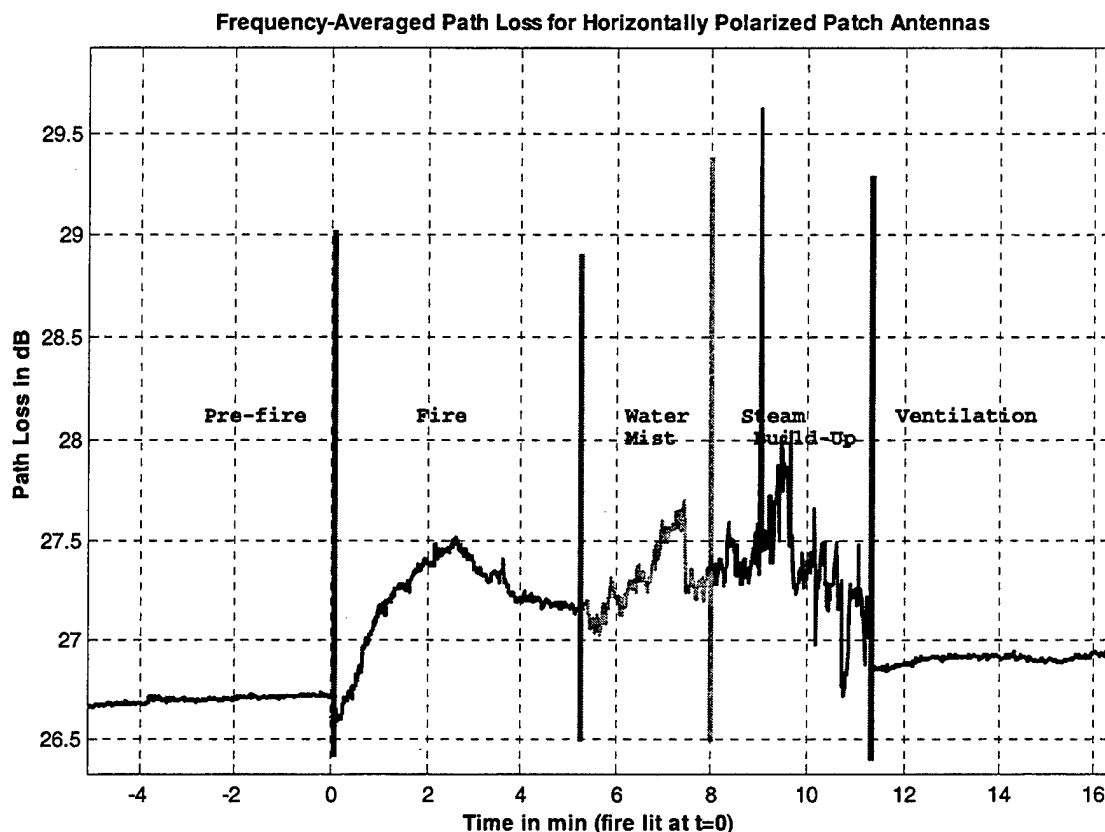


Figure 10.31: Diesel Fire Frequency-Averaged Path Loss for Horizontally Polarized Non-directional Antennas

d) Frequency-Averaged Attenuation for Horizontally Polarized Non-directional Antennas.

Our next step was to determine the frequency-averaged attenuation in dB/m. The shape of the frequency-averaged attenuation as a function of time is exactly the same as for the path loss, as shown in Figure 10.32. The only difference between the frequency-averaged attenuation

and the frequency-averaged path loss is the division by a constant distance.

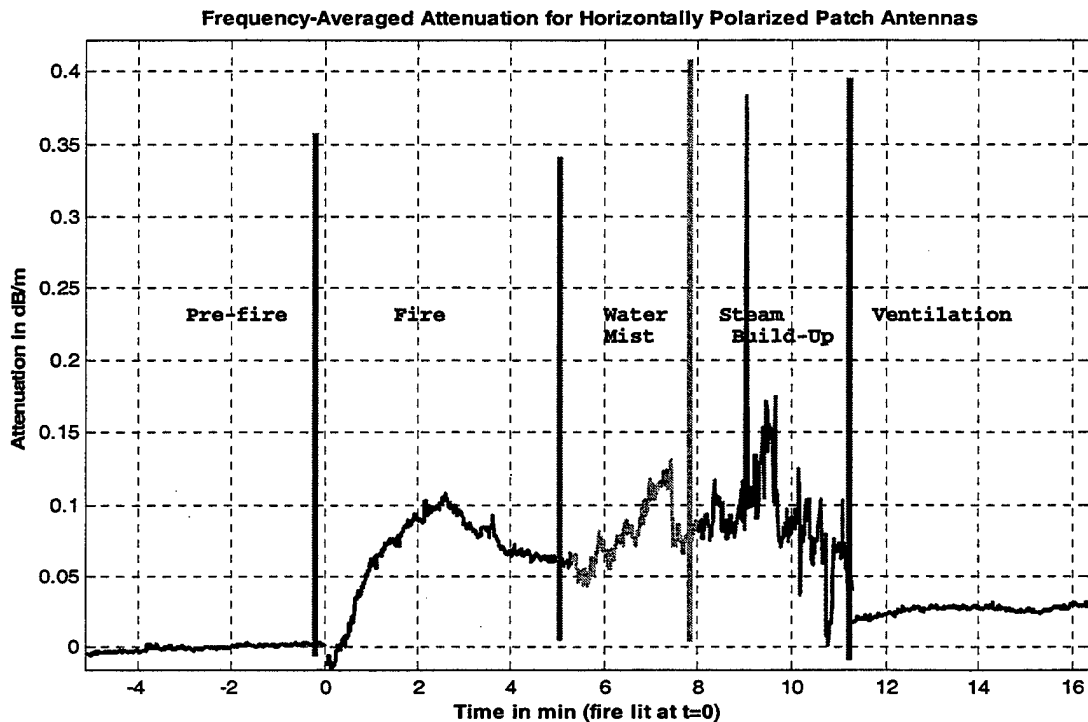


Figure 10.32: Diesel Fire Frequency-Averaged Attenuation for Horizontally Polarized Non-directional Antennas

The maximum frequency-averaged attenuation is approximately 0.17 dB/m. During the fire phase the attenuation did not exceed 0.12 dB/m. After the water mist fire extinguishing system was turned on there was a small drop in attenuation (0.02 dB/m) because the smoke and fire were nearly instantaneously suppressed. However as the steam started building up the attenuation per meter increased, reaching a local maximum after about 1.5 minutes. When the water mist system was turned off, and steam continued building up, the attenuation started to increase again

reaching its maximum before decreasing slowly as the temperature and the steam density gradually decreased.

e) Diesel Fire Time-Averaged Path Loss for Horizontally Polarized Non-directional Antennas.

Our next step was to calculate the time-averaged path loss for the fire phase. As shown in Figure 10.33 the time-averaged path loss ranged between 22 and 43 dB. The plot also shows the minimum and maximum values of instantaneous path loss for each frequency component. The maximum path loss occurs at 2.402 GHz and the minimum path loss occurs at 2.415 GHz.

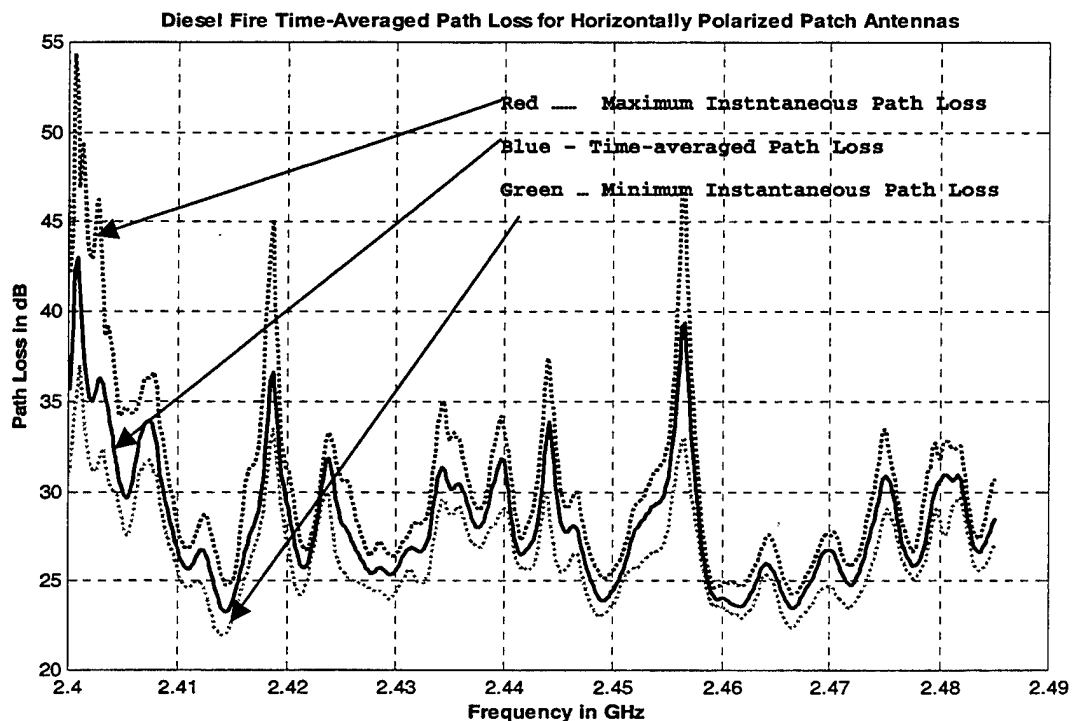


Figure 10.33: Diesel Fire Path Loss for Horizontally Polarized Non-directional Antennas

The maximum and minimum path loss curves follow the time-averaged attenuation curve, that is the zero slope points for all three curves are located at the same frequencies.

In Figure 10.34 the time-averaged path loss curves for the fire and the pre-fire phases are shown. The fire causes the minima and maxima of the path loss to shift (mostly) to higher frequencies.

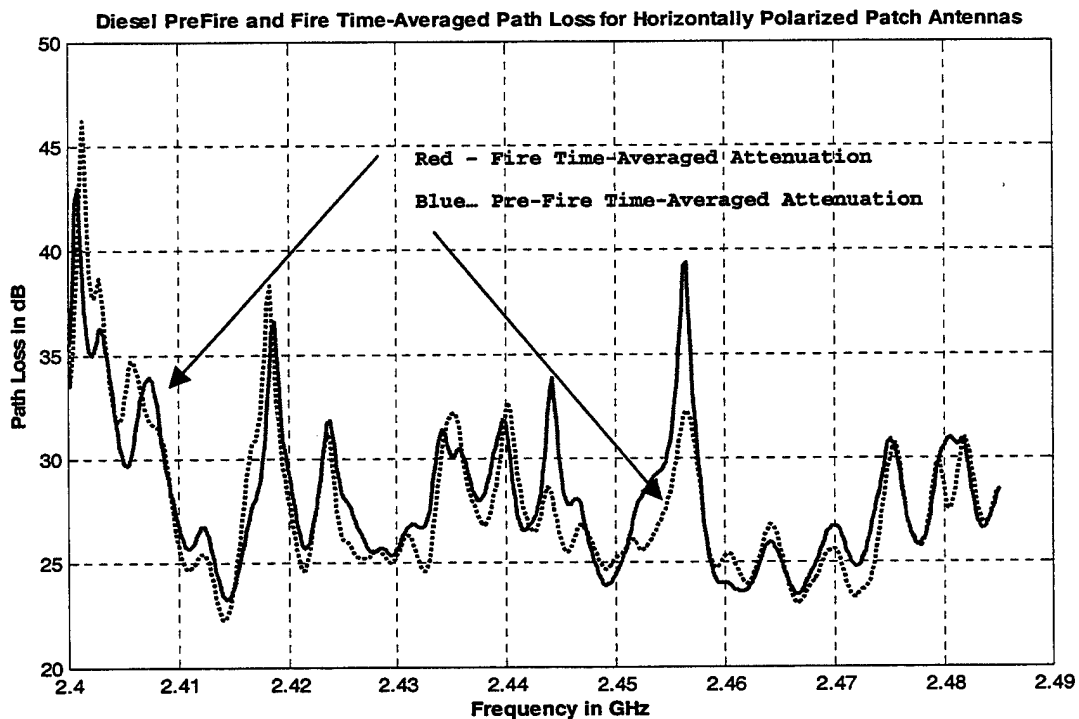


Figure 10.34: Diesel Pre-Fire and Fire Path Loss for Horizontally Polarized Non-directional Antennas

f) Diesel Fire Time-Averaged Attenuation for Horizontally Polarized Non-directional Antennas.

In Figure 10.35 the time-averaged attenuation per meter for the fire phase is plotted. The maximum time-averaged attenuation is 0.7 dB/m. The maximum instantaneous attenuation is again at 2.402 GHz. The minimum instantaneous attenuation for each frequency component is below the 0dB axis indicating a gain. Due to the shift of the path loss "peaks and valleys" there are frequencies with high attenuation and others that exhibit a transmission gain. Note that the relative phase shift changes for the (multipath) propagation paths, rather than the losses due to fire cause this.

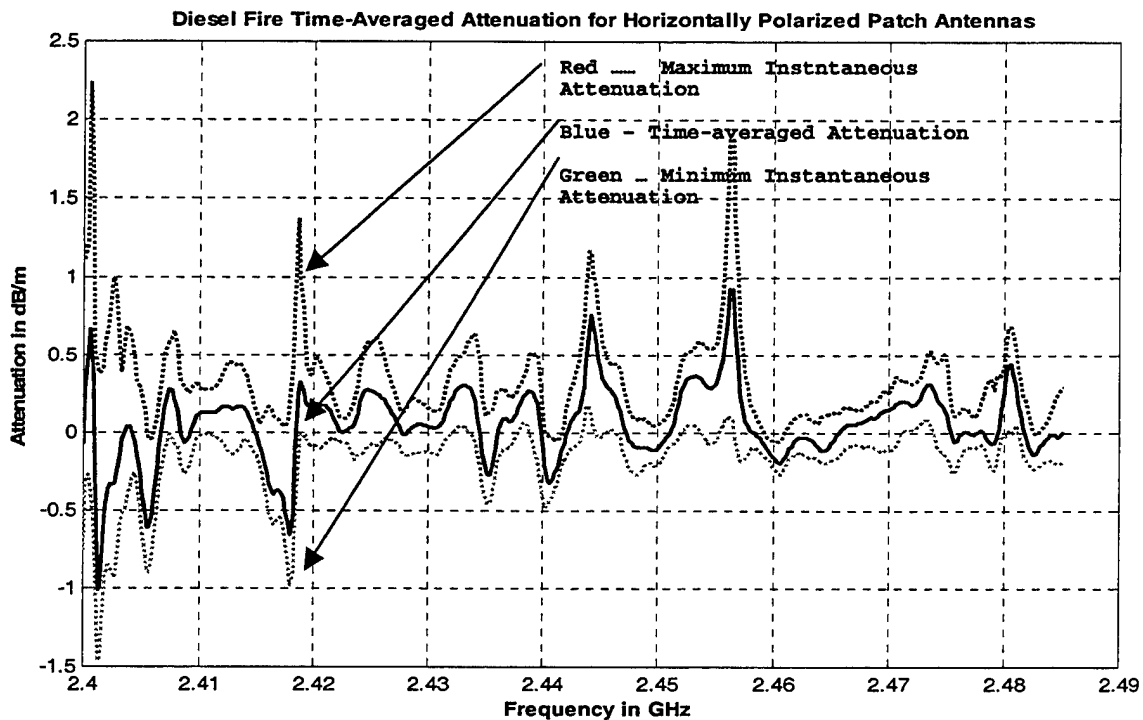


Figure 10.35: Diesel Fire Time-Averaged Attenuation for Horizontally Polarized Non-directional Antennas

g) Water Mist Phase Time-Averaged Path Loss for Horizontally Polarized Non-directional Antennas.

Our next step was to calculate the time-averaged path loss for the water mist phase. As shown in Figure 10.36 the time-averaged path loss ranged between 23 and 43 dB. The maximum path loss occurs at 2.402 GHz and the minimum path loss occurs at 2.413 GHz, the same frequencies as for the fire phases. Also the zero slope points for all three curves (min, max and average path loss) occur at the same frequencies.

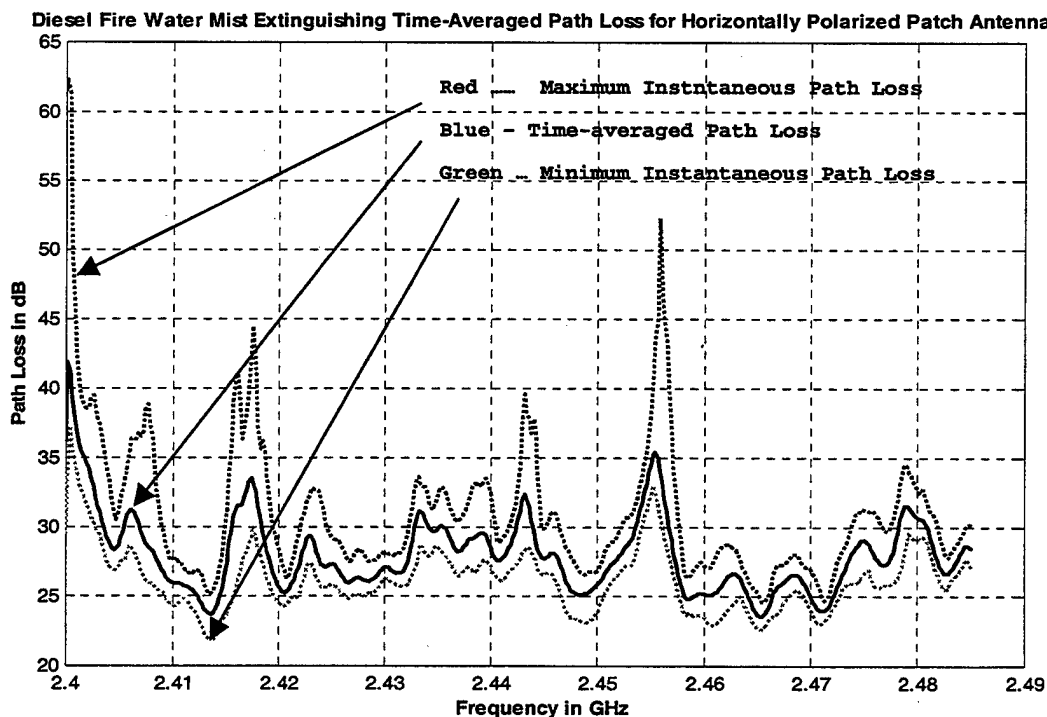


Figure 10.36: Diesel Fire Water Mist Path Loss for Horizontally Polarized Non-directional Antennas

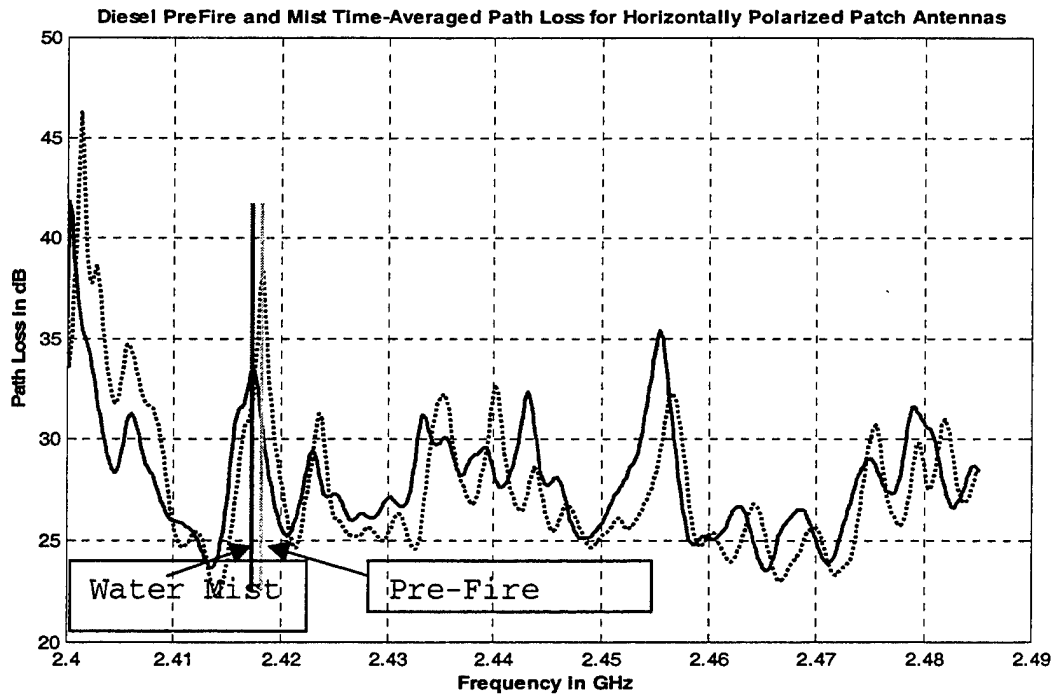


Figure 10.37: Diesel Pre-Fire and Water Mist Path Loss for Horizontally Polarized Non-directional Antennas

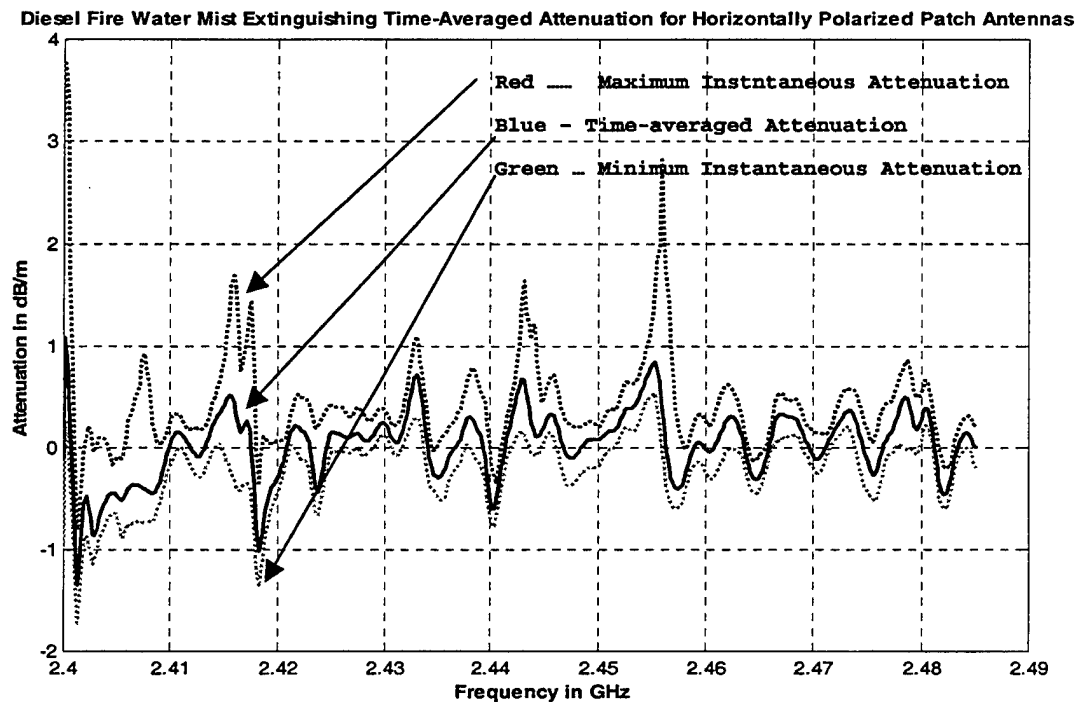


Figure 10.38: Diesel Fire Water Mist Time-Averaged Attenuation for Horizontally Polarized Non-directional Antennas

In Figure 10.37 the time-averaged path loss curves for the water mist and the pre-fire phases are shown. Note that the zero slope points for the water mist phase have shifted to lower frequencies by about 3 MHz. This indicates that there are changes in the compartment propagation characteristics opposite to the changes caused by fire.

h) Water Mist Time-Averaged Attenuation for Horizontally Polarized Non-directional Antennas.

In Figure 10.38 the time-averaged attenuation per meter during the water mist phase is shown. The time-averaged attenuation ranges between -1.1 and 1.1 dB/m and the maximum attenuation occurs at 2.402 GHz. The minimum attenuation for many frequency components is below the 0dB axis indicating a gain. This is the consequence of the alteration of the compartment multipath propagation characteristics. Due to the shift of the path loss "peaks and valleys" there are frequencies that are significantly attenuated and others that exhibit a substantial transmission gain. Note that these effects are caused by the phase shifts changes for multipath propagation paths rather than the losses due to fire.

i) Steam Build Up Phase Time-Averaged Path Loss for Horizontally Polarized Non-directional Antennas.

Next we calculated the time-averaged path loss during the steam build-up phase. As shown in Figure 10.39 the time-averaged path loss ranged between 22 and 42dB. Also shown on the same plot are the minimum and maximum instantaneous values of the attenuation for each frequency component. The maximum path loss occurs at 2.402 GHz and the minimum path loss occurs at 2.465 GHz. Again the zero slope points for all three curves are located at the same frequencies.

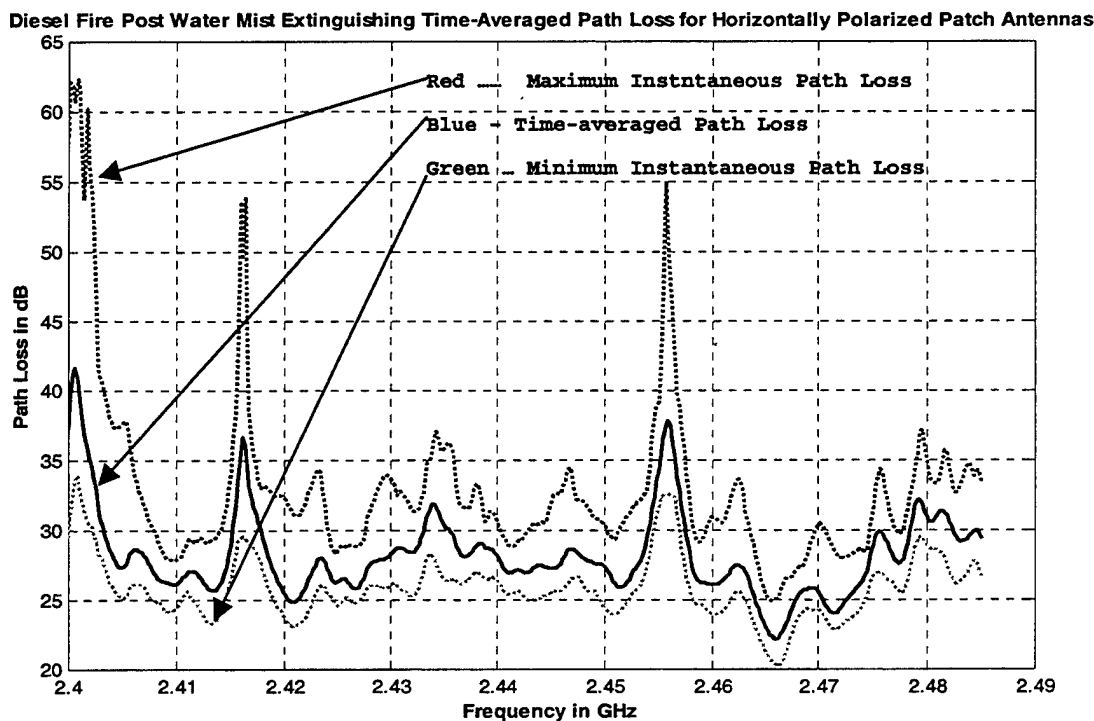


Figure 10.39: Diesel Fire Steam Build-Up Path Loss for Horizontally Polarized Non-directional Antennas

In Figure 10.40 the time-averaged path loss curve for the steam build-up and the pre-fire phases are shown. Again the zero slope points (maxima and minima) during the steam build-up phase are shifted to lower frequencies by about 3 MHz. The additional path loss varies between -7 and +5 dB depending on the frequency.

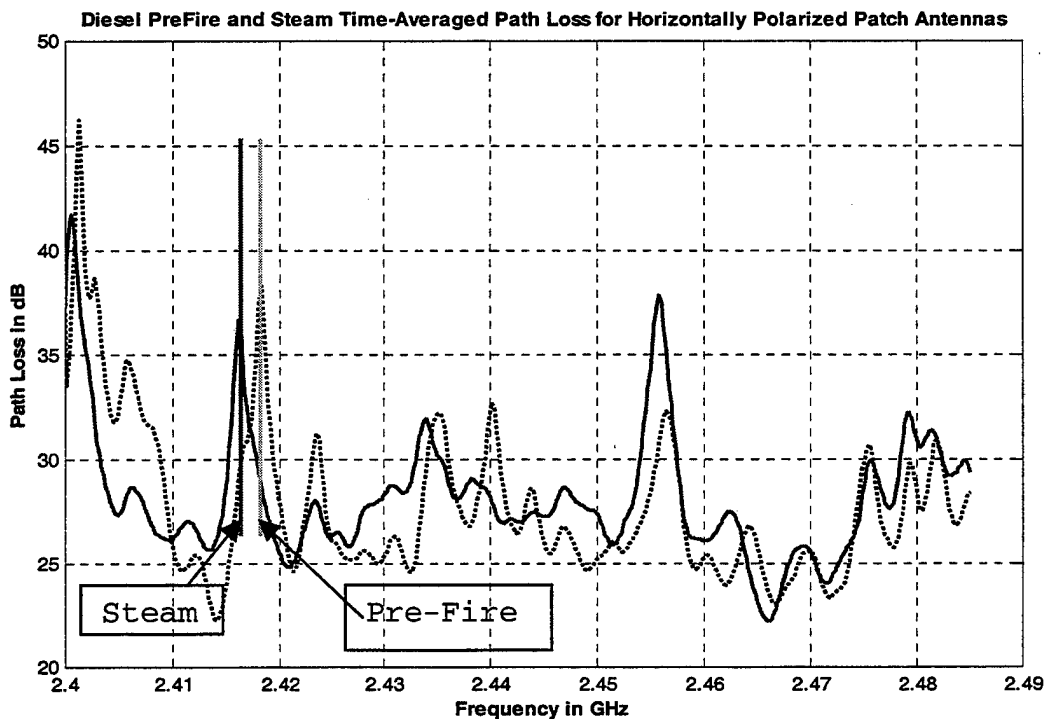


Figure 10.40: Diesel Pre-Fire and Steam Build-Up Path Loss for Horizontally Polarized Non-directional Antennas

j) Steam Build Up Time-Averaged Attenuation for Horizontally Polarized Non-directional Antennas

In Figure 10.41 the time-averaged attenuation per meter during the steam build-up phase shows that the maximum attenuation occurs at 2.402 GHz. The values of the time-

averaged attenuation per meter vary between -1.2 and 0.8 dB/m, slightly lower than the values measured for the water mist phase.

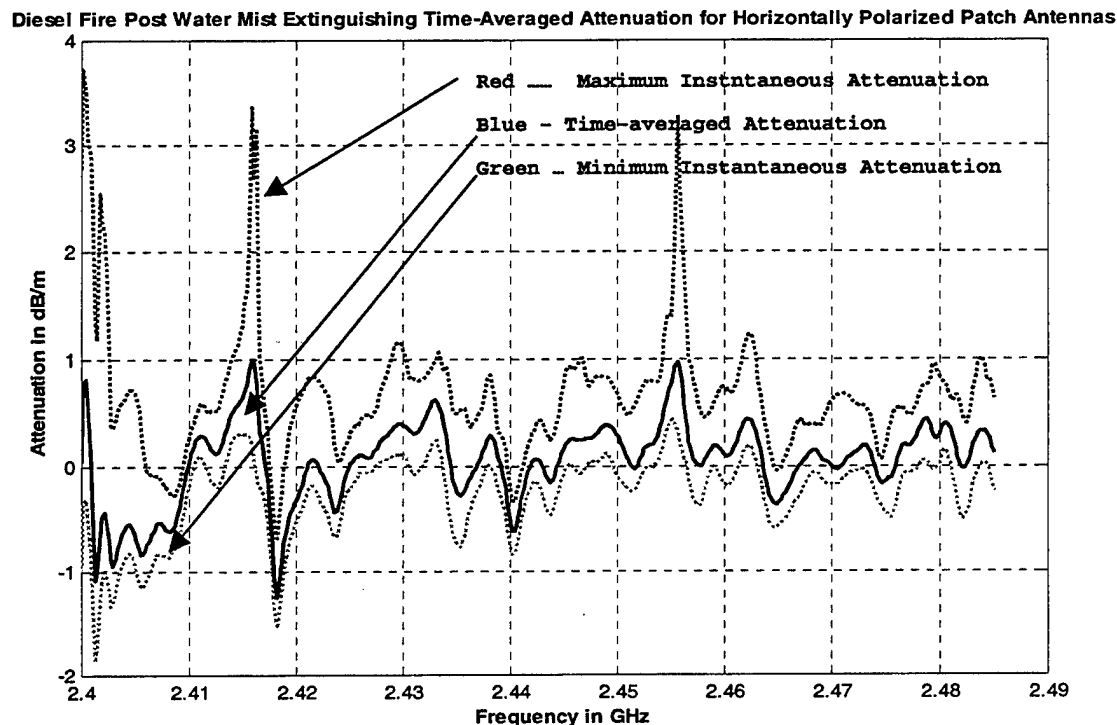


Figure 10.41: Diesel Fire Steam Build-Up Time-Averaged Attenuation for Horizontally Polarized Non-directional Antennas

k) Attenuation Probability Density Functions for Horizontally Polarized Non-directional Antennas

The attenuation probability density functions (pdf) for each frequency scan for the horizontally polarized non-directional antennas is shown in Figure 9.42a. The plot shows that the pdf vary with time and that the attenuation caused by fire and the follow on phases is non stationary.

Initially, when the fire was lit at $t=0$ the attenuation has about 0 dB mean and a small standard deviation. As the fire develops the pdf shifts towards higher attenuation values and the standard deviation of the pdf increases.

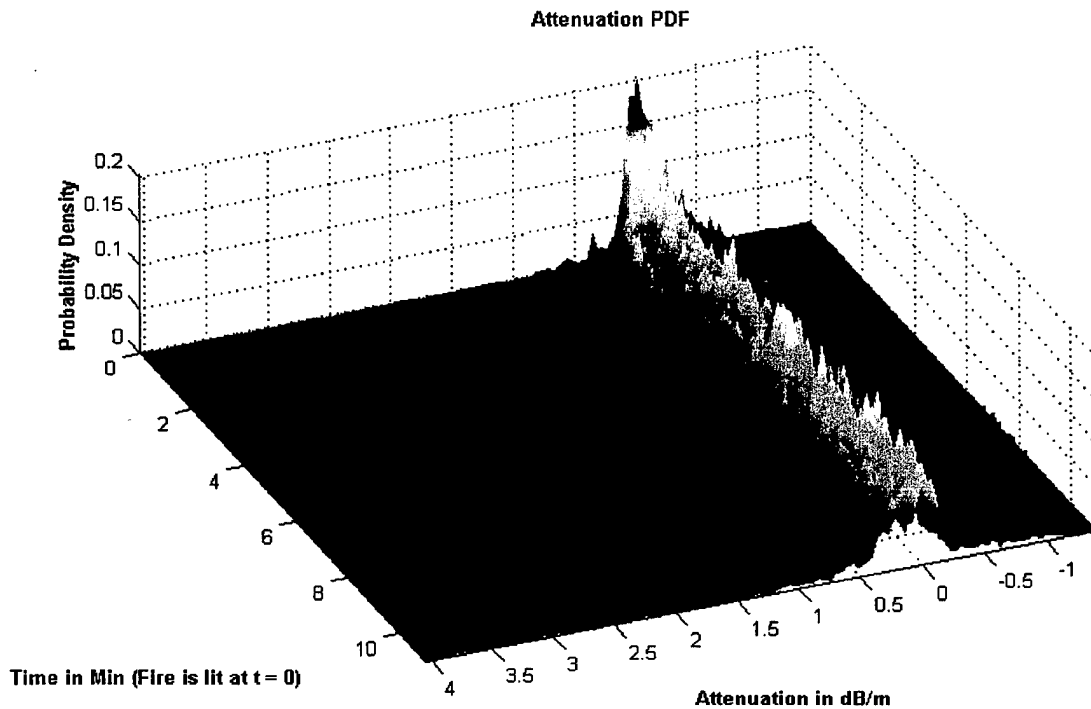


Figure 10.42a: Attenuation Probability Density Function Surface Plot

At $t=5$, when the water mist extinguishing system is turned on, the pdf shifts abruptly towards even higher attenuation values and the standard deviation increases further. At $t=7$, when the water mist extinguishing system is turned off, the pdf starts shifting back towards lower attenuation values, but the standard deviation remains high. Because of the non-stationarity of the pdf's the time-

averaged pdf's are presented. For the fire phase, the averaging is done over the last minute of the fire phase, corresponding to the "fully developed" fire/smoke; while for the other phases pdf's for the entire phases are time-averaged. Furthermore, fire and water mist dynamics cause fading non-stationarity meaning that the fading "depth" and frequency "locations" change with time.

The attenuation probability density functions for the three phases (fire, water mist and steam build-up) of the diesel fire experiments for the horizontally polarized non-directional antennas are shown in Figure 10.42b. Also shown is the "average" attenuation probability density function for all phases.

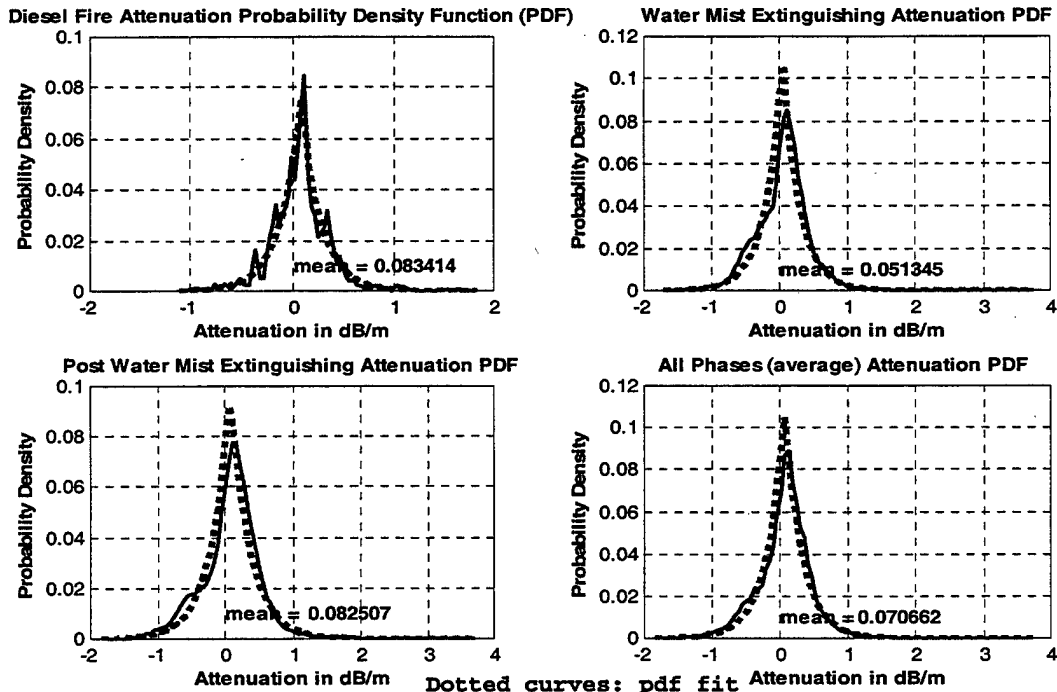


Figure 10.42b: Probability Density Functions

The pdf's for the three phases resemble exponential distributions. The mean attenuations are:

- For the fire phase 0.083 dB/m
- For the water mist phase 0.051 dB/m
- For the steam build-up phase 0.082 dB/m
- For all three phases 0.070 dB/m.

The cumulative distribution functions for the attenuation for the three phases individually and the overall cumulative distribution function are shown in Figure 10.42. From the fire phase CDF we can determine that there

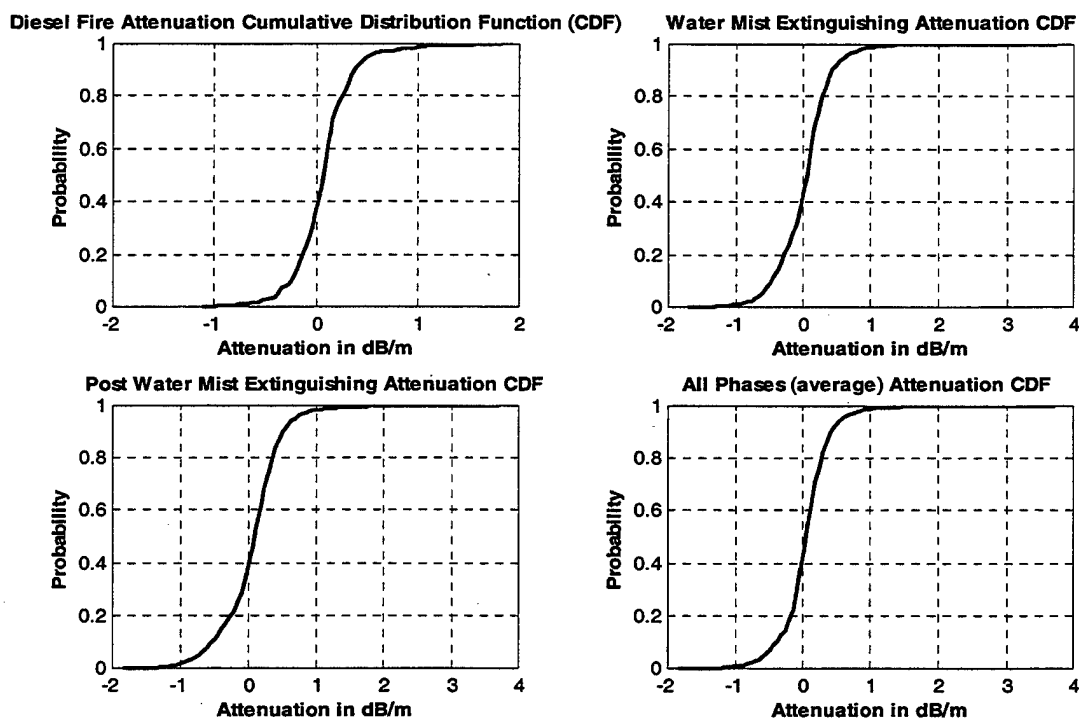


Figure 10.43: Cumulative Distribution Functions

is a 0.95 probability that the attenuation will be lower than 0.9 dB/m. Similarly, for the water mist phase there is a 0.95 probability that the attenuation will be less than 1 dB/m. For the steam build-up phase there is a 0.95 probability that the attenuation will be less than 0.8 dB/m. This shows that the attenuation for the water mist extinguish phase is larger than the attenuation caused by the fire itself. For all the phases there is 0.95 probability that the attenuation will be less than 0.8 dB/m.

1) Autocorrelation Functions

Our next step was to determine the correlation between different frequencies for the different phases of the experiment. Initially we estimated the autocorrelation for the pre-fire phase. In Figure 10.44 the plot of the autocorrelation function indicates a varying degree of correlation between attenuation at different frequencies. Generally the larger the frequency difference the smaller the correlation. This suggests that the attenuation varies substantially with frequency. Continuing on to the fire phase the autocorellation function plot in Figure 10.45 is similar to the pre-fire plot, again indicating that the different frequency components attenuate differently. This was also evident from Figure 10.34, showing that path loss increased substantially for some components and decreased

for others. Figures X-46 and X-47 show the autocorellation functions for the water mist and steam build-up phases.

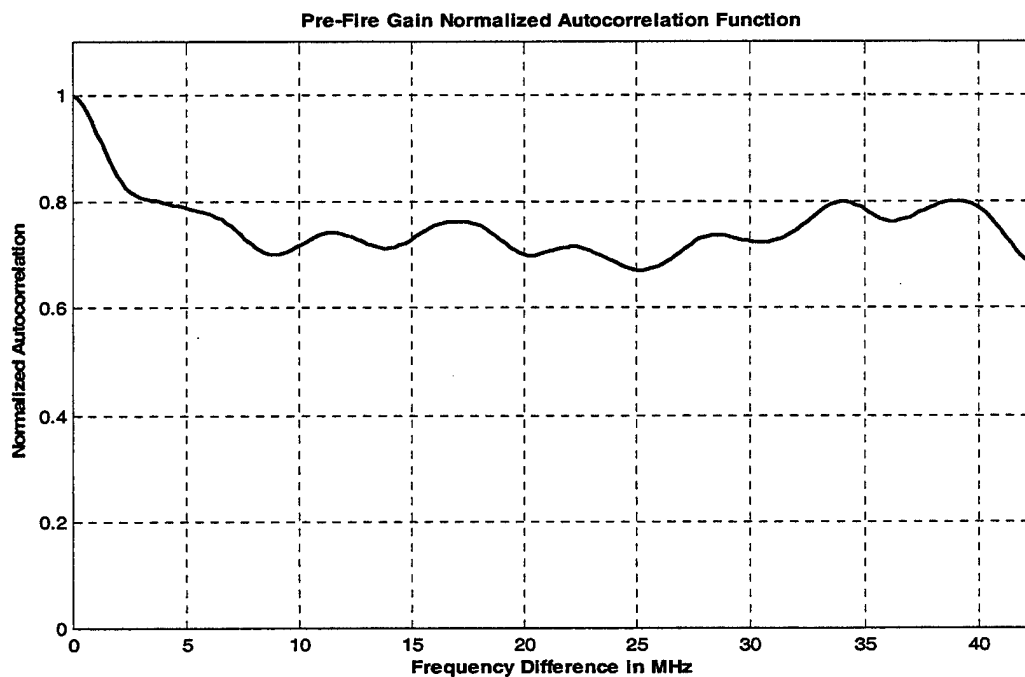


Figure 10.44: Pre-Fire Gain Normalized Autocorellation Function

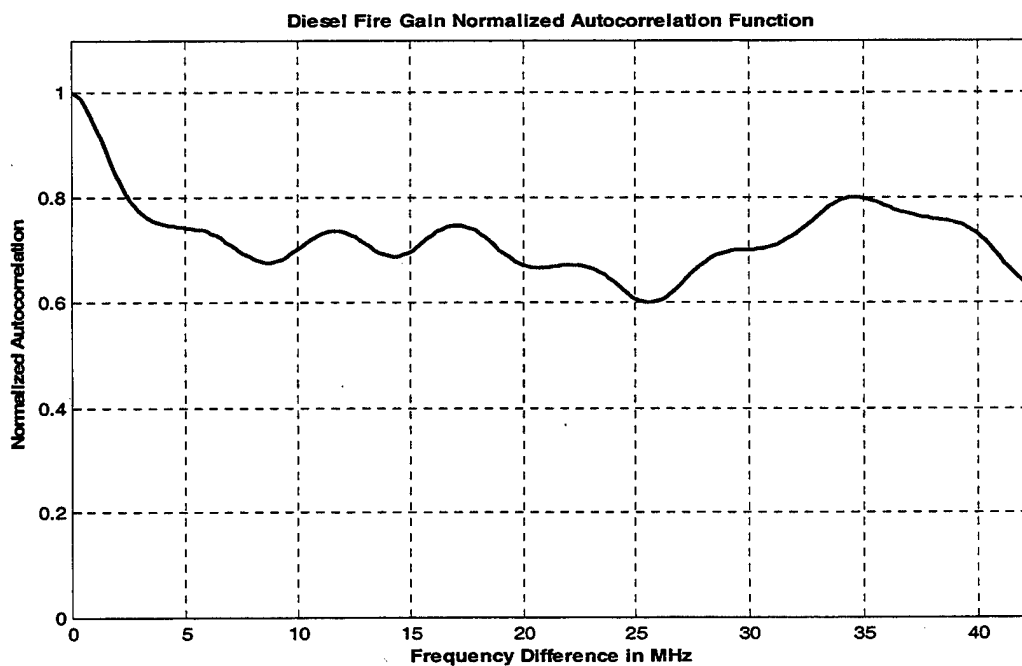


Figure 10.45: Fire Gain Normalized Autocorellation Function

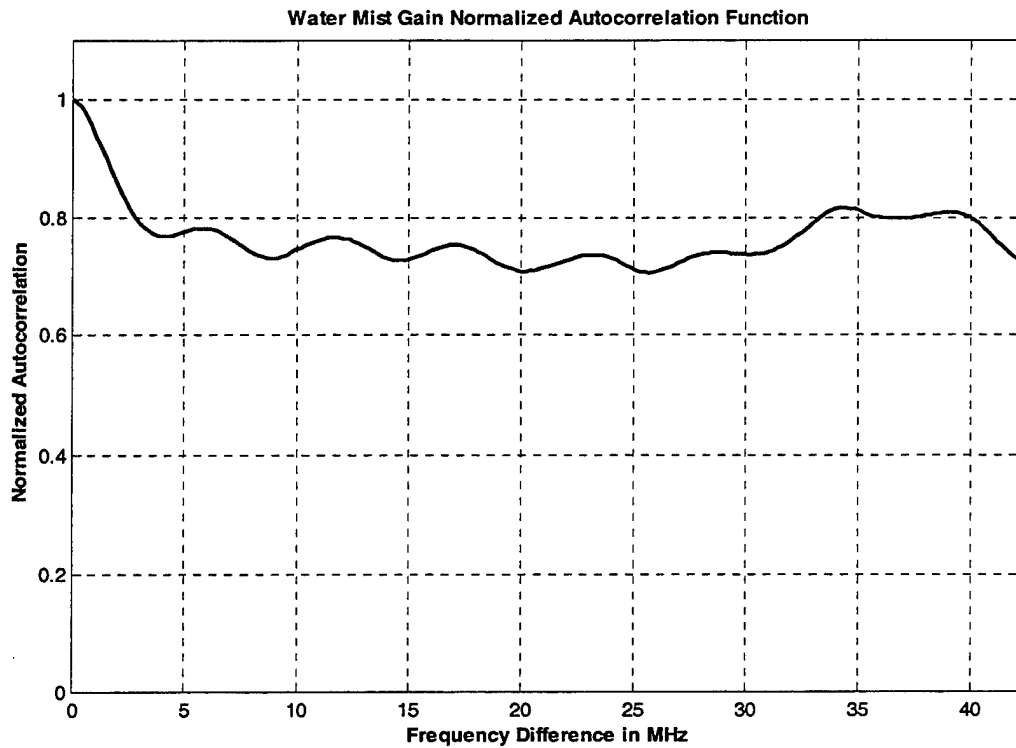


Figure 10.46: Water Mist Gain Normalized Autocorrelation Function

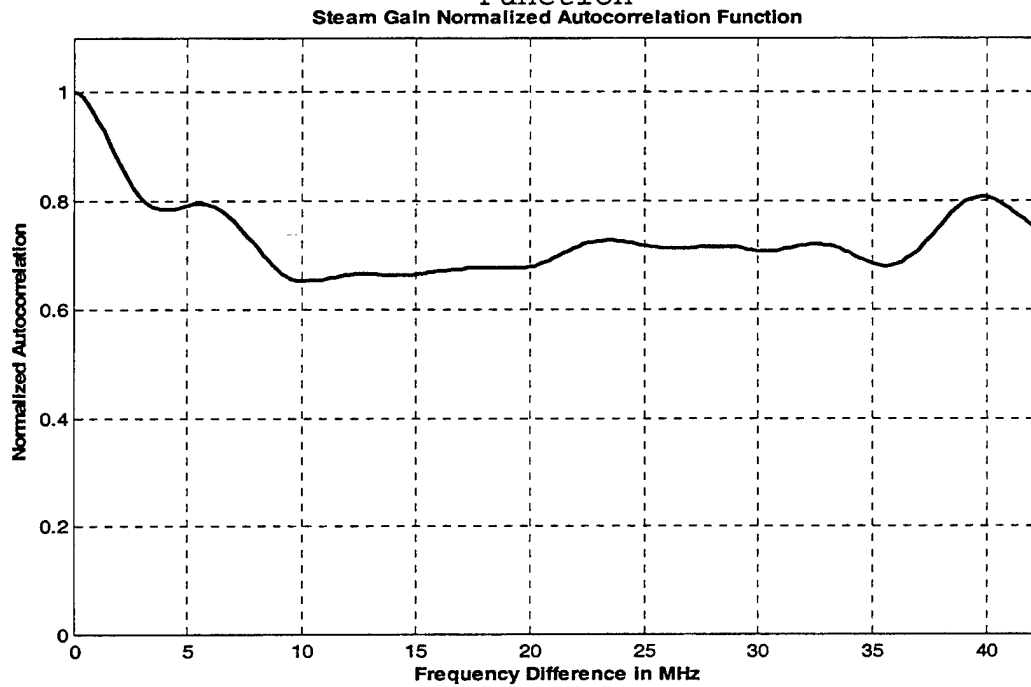


Figure 10.47: Steam Build-Up Gain Normalized Autocorrelation Function

There is significant effect of the compartment, creating multipath propagation. The multipath causes frequency-selective fading over the 2.4 GHz ISM band.

m) Estimation of the Best Frequency Difference

The last step was to estimate the frequency difference that, on average, would provide the least combined (sum of) attenuation. This would be useful if a dual-frequency diversity transmission system was used. As seen in Figure 10.48 for the horizontally polarized antennas this frequency difference is about 74 MHz.

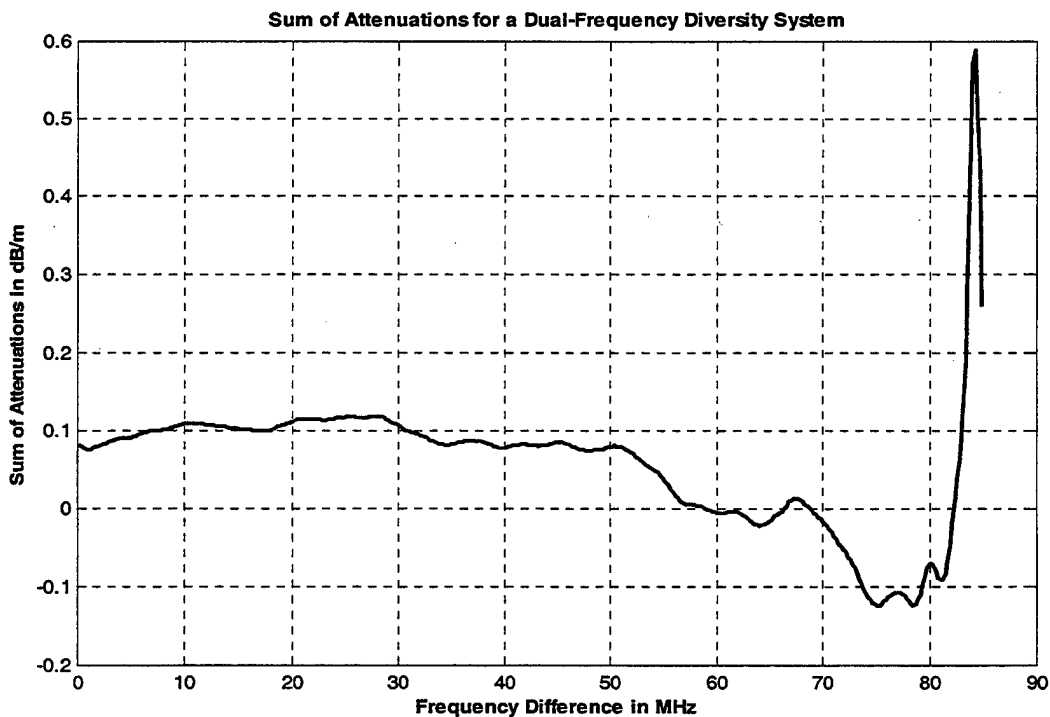


Figure 10.48: Sum of Attenuation for a Dual-Frequency Diversity System

XI. CONCLUSIONS AND RECOMMENDATIONS

A. CONCLUSIONS

The effects of fire and the water mist fire extinguishing are different for the directional (high gain) and the non-directional (low gain) antennas. This difference is caused by the prevalence of a single, direct path for the directional antennas, as opposed to the multipath propagation for the non-directional antennas.

The attenuation for the directional antennas exhibits relatively small variations with time and frequency. The attenuation due to the water mist extinguishing is substantially larger than the attenuation due to the fire itself.

The attenuation for the non-directional antennas exhibits large variations with time and frequency. The attenuation due to the water mist extinguishing is substantially larger than the attenuation due to the fire itself.

The attenuation probability density functions (which are in general functions of time) are also different for directional and non-directional antennas. Gaussian pdf's approximate the experimentally observed pdf's for the directional antennas (for both diesel and heptane fires), whereas exponential pdf's approximate the experimentally

observed pdf's for the non-directional antennas. In addition to the differences in the "shape" of the pdf's, there is a much larger standard deviation of the attenuation for the non-directional antennas. However, despite the substantial differences in the attenuation probability density functions and their standard deviations, the mean attenuations, shown in Table 11-1 for all of the phases of the experiments, are close to each other, regardless of the type of antenna (directional or non-directional) used in the measurements. Since the mean attenuation per meter (averaged over time and frequency) is the measure of the absorption by the medium between the antennas, the relatively close values obtained with two different antenna types (directional and non-directional) increases the confidence in the validity of the measurements.

	DIESEL				HEPTANE	
	HIGH GAIN		LOW GAIN		HIGH GAIN	
	V-POL	H-POL	V-POL	H-POL	V-POL	H-POL
FIRE	0.064	0.050	0.148	0.083	0.0299	0.060
MIST	0.113	0.096	0.100	0.051	0.055	0.107
STEAM	0.110	0.090	0.083	0.082	0.051	0.100
VENT	-	-	-	-	0.050	0.098
AVG	0.105	0.086	0.100	0.070	0.043	0.095

Table 11-1: Mean Attenuation in dB/m

In Table 11-2 the standard deviation of the attenuation for all the phases of the experiments are presented.

	DIESEL				HEPTANE	
	HIGH GAIN		LOW GAIN		HIGH GAIN	
	V-POL	H-POL	V-POL	H-POL	V-POL	H-POL
FIRE	0.025	0.021	0.327	0.195	0.0343	0.028
MIST	0.040	0.030	0.361	0.242	0.040	0.045
STEAM	0.030	0.018	0.319	0.286	0.036	0.033
VENT	-	-	-	-	0.038	0.055
AVG	0.036	0.028	0.337	0.362	0.040	0.045

Table 11-2: Standard Deviation for Attenuation in dB/m

Whereas the mean attenuation is less than 0.12 dB/m regardless of the type of the antenna, the phase of the fire/fire-extinguishing, or the polarization (as evident in Table 11-1), Table 11-2 shows that the standard deviation of attenuation for non-directional antennas is an order of magnitude larger than the standard deviation for directional antennas. This means that much higher attenuation values are possible (with a certain probability) when using non-directional antennas. Again, the physical reason for this is the multipath propagation that for non-directional antennas manifests as severe frequency selective fading,

with the frequencies of deep signal fades affected by fire/smoke, water mist, and steam.

In order to illustrate the effects of multipath, the attenuation values for which there is only 0.05 probability that they will be exceeded (0.95 probability that the attenuation will be less than these values) are shown in Table 11-3 for all the phases of the experiments.

	DIESEL				HEPTANE	
	HIGH GAIN		LOW GAIN		HIGH GAIN	
	V-POL	H-POL	V-POL	H-POL	V-POL	H-POL
FIRE	0.1	0.09	1.6	0.9	0.1	0.1
MIST	0.18	0.14	1.8	1	0.13	0.18
STEAM	0.15	0.12	1.3	0.8	0.12	0.17
VENT					0.11	0.25
AVG	0.16	0.13	1.7	0.8	0.12	0.22

Table 11-3: 0.95 Probability for Attenuation in dB/m

It is again evident (from the table above) that higher values of attenuation are much more likely to occur for non-directional antennas.

For diesel fire/fire-extinguishing and vertically polarized directional antennas, the mean attenuation was 0.107 dB/m, the maximum frequency-averaged attenuation was

0.17 dB/m, and the maximum instantaneous attenuation observed during the experiment was 0.22 dB/m.

For diesel fire/fire-extinguishing and horizontally polarized directional antennas, the mean attenuation was 0.086 dB/m, the maximum frequency-averaged attenuation was 0.21 dB/m and the maximum instantaneous attenuation observed during the experiment was 0.26 dB/m.

The results for the two polarizations for diesel fire are close to each other, with attenuation for the horizontal polarization somewhat larger than the attenuation for the vertical polarization.

For heptane fire/fire-extinguishing and vertically polarized directional antennas, the mean attenuation was 0.043 dB/m, the maximum frequency-averaged attenuation was 0.14 dB/m, and the maximum instantaneous attenuation observed during the experiment was 0.17 dB/m.

For heptane fire/fire-extinguishing and horizontally polarized directional antennas, the mean attenuation was 0.095 dB/m, the maximum frequency-averaged attenuation was 0.21 dB/m and the maximum attenuation observed during the experiment was 0.26 dB/m. The results for heptane fire show more difference between the vertical and horizontal polarizations than the results for diesel fire, the attenuation being larger for the horizontal polarization.

For diesel fire and vertically polarized patch antennas, the mean attenuation was 0.1 dB/m, the maximum frequency-averaged attenuation was 1.2 dB/m, and the maximum instantaneous attenuation observed during the experiment was 4 dB/m. For the vertically polarized antennas 95% of the measured attenuation was less than 1.5 dB/m.

For diesel fire and horizontally polarized patch antennas, the mean attenuation was 0.07 dB/m, the maximum frequency-averaged attenuation was 1.2 dB/m, and the maximum instantaneous attenuation observed during the experiment was 2.5 dB/m. For the horizontally polarized antennas 95% of the measured attenuation was less than 0.8 dB/m.

B. RECOMMENDATIONS

Fire and the follow-on fire-extinguishing phases create non-stationary frequency selective fading. Therefore communication techniques effective against frequency selective fading (non-stationary, but slowly varying) are recommended for use with communication systems intended for shipboard indoors use in order to maintain reliable communications in all situations, including fire and fire-extinguishing. Even in normal conditions, without fire, we have determined that very pronounced frequency selective fading exists. Therefore, a system with anti-fading capability should be used for shipboard indoor use, regardless whether fire and fire extinguishing are of

concern to the user. A narrowband ("single frequency") communications system for indoor shipboard use would be very sensitive to antenna location, changes in the compartment due to equipment relocation and personnel movement, and vulnerable to communications loss due to fire or fire-extinguishing actions. All these are caused by the multipath changes causing severe frequency-selective fading and possibly complete loss of communications.

More experiments should be conducted with low gain antennas to determine the effects of the fire for circular polarization. Also, additional experiments should be conducted with different antenna spacing, relative orientation, and locations (for example, with one of the antennas mounted on the compartment ceiling). In such a manner a more complete statistical description would be obtained for the attenuation caused by fire and fire-extinguishing actions.

APPENDIX A. ANTENNAS SPECIFICATION SHEETS

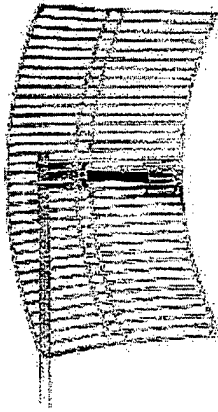
1. High Gain Parabolic Grid Antenna

24 dBi Parabolic Grid 2.4 GHz

List price: \$189.00

USA prices. International prices may vary.

Contact our sales office for reseller and quantity discounts.



2.4 GHz Directional Antenna with wire mesh reflector
Product code WR2400-24

ANTENNA PERFORMANCE

Frequency: 2.4 - 2.485 GHz
Gain: 24 dBi
VSWR: 1.4:1 @ 2.45 GHz
Polarization: Vertical or Horizontal
Impedance: 50 Ohms
Elevation Adjustment: 60° in 10° increments
-3 dB Beamwidth: 7.5°

PHYSICAL CHARACTERISTICS

Dimensions: 24in x 36in x 15in (610mm x 915 mm x 381mm)
Weight: 4.9 lbs (2.22 kg)
Wind Load: 141.5 lbs @ 120 mph
RF Connector: N type female
(available with custom connectors)
Material: Cast magnesium alloy
Mounting: Stainless steel 1 - 2 in (25.4-50.8 mm)

Copyright ©1999 by Winncom Technologies, Inc. - ALL RIGHTS RESERVED

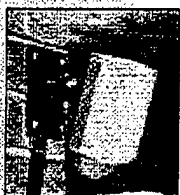
2. Low Gain Patch Antenna

DirectLink™

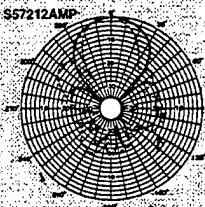
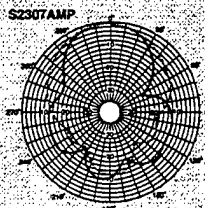
30

CONTEMPORARY PATCH

- Indoor / outdoor
- Attractive styling
- Articulating
- Wall mountable



— E-Plane
— H-Plane



CUSHCRAFT
COMMUNICATIONS ANTENNAS

DirectLink™ Series Antennas

DirectLink has been designed to eliminate concerns over aesthetics in professional workplaces and neighborhoods. DirectLink's contemporary design and neutral color make it a perfect choice for these applications.

Ease of Installation

DirectLink is available in either a Standard Wall Mount or an Articulating Wall Mount Version. The Standard Wall Mount attaches flush to any interior or exterior wall surface. The Articulating Wall Mount allows the antenna to be wall mounted and adds the ability to steer the antenna's main lobe ± 30 degrees in the horizontal plane. Adjustments can be made quickly and easily minimizing installation time while achieving peak performance. DirectLink's versatile mounting hardware kits not only allow the antenna to be mounted to virtually any structure available but they also allow the antenna's pattern to be directed precisely into the desired coverage area.

Both versions allow the feed cable to be routed to a terminal or base station mounted above or below the antenna and even allow the feed cable to be hidden behind the antenna and routed through the wall. In addition, the Standard Wall mount version may be mated with two optional mounting brackets for even greater installation flexibility. The Mast Mount Bracket is used for installations on masts from 1 to 2.5 inches (25 mm to 64 mm) in diameter. The Universal Mount Bracket permits up to 210 degrees of tilt and 360 degrees of rotation for main lobe steering and can be attached to a mast or a flat surface. Both mounts are suitable for indoor and outdoor installations.

Performance and Durability

DirectLink Patch antennas are uniquely designed to provide superior performance. The antenna employs patch technology without the usual reliance on expensive and lossy dielectric substrates. Instead, an air dielectric technology, called MicroAir™ is used to decrease material cost and increase radiation efficiency. Each antenna is provided with a standard low loss cable pigtail. A choice of SMA or TNC connectors is available. Other connector types are available upon request.

Solid brass elements are rigidly supported by the injection molded ultraviolet resistant enclosure. The enclosure components are designed to nest together during assembly creating a moisture barrier. The antenna will provide years of reliable, trouble free service.



FREQUENCY MHz	MODEL	GAIN dBi	3dB Beamwidth, deg. E-Plane H-Plane	VSWR	FB dB	Connector (female)	Articulating Version
2300-2500	S2307AMP10TNE	7.5	50 65	1.5:1	12	TNC	Yes
2300-2500	S2307AMP10TNE	7.5	50 65	1.5:1	12	TNC	No
2300-2500	S2307AMP10SMF	7.5	50 65	1.5:1	12	SMA	Yes
2300-2500	S2307AMP10SMF	7.5	50 65	1.5:1	12	SMA	No
5150-5350	S51510AMP10TNE	10	27 58	1.5:1	15	TNC	Yes
5150-5350	S51510AMP10TNE	10	27 58	1.5:1	15	TNC	No
5150-5350	S51510AMP10SMF	10	27 58	1.5:1	15	SMA	Yes
5150-5350	S51510AMP10SMF	10	27 58	1.5:1	15	SMA	No
5150-5350	S51512AMP10TNE	12	27 45	1.5:1	15	TNC	Yes
5150-5350	S51512AMP10TNE	12	27 45	1.5:1	15	TNC	No
5150-5350	S51512AMP10SMF	12	27 45	1.5:1	15	SMA	Yes
5150-5350	S51512AMP10SMF	12	27 45	1.5:1	15	SMA	No
5725-5825	S57210AMP10TNE	10	27 58	1.5:1	15	TNC	Yes
5725-5825	S57210AMP10TNE	10	27 58	1.5:1	15	TNC	No
5725-5825	S57210AMP10SMF	10	27 58	1.5:1	15	SMA	Yes
5725-5825	S57210AMP10SMF	10	27 58	1.5:1	15	SMA	No
5725-5825	S57212AMP10TNE	12	27 45	1.5:1	15	TNC	Yes
5725-5825	S57212AMP10TNE	12	27 45	1.5:1	15	TNC	No
5725-5825	S57212AMP10SMF	12	27 45	1.5:1	15	SMA	Yes
5725-5825	S57212AMP10SMF	12	27 45	1.5:1	15	SMA	No

COMMON SPECIFICATIONS

Power: 75 Watts (25 Watts at 5 GHz)

Polarization: Linear

Dimensions & Weight:

Standard wall mount -

5.70 x 3.81 x 1.50 in.

(14.48 x 9.68 x 3.80 cm).

5 oz (14 kg)

Articulating wall mt -

5.80 x 3.81 x 2.26 in.

(14.73 x 9.68 x 5.74 cm).

8 oz (23 kg)

Connectors:

SMA, TNC. Other connector types available on special request.

Mounting:

Standard units for wall mounting.

Mast mount bracket kits

available. Custom mount

configurations for volume users.

Cable: Low loss pigtail provided

APPENDIX B. LABVIEW VI CODE

LabVIEW Virtual Instruments (VI) code was used to create the "GPIB THESIS51.vi" program. The program was used during the Shipboard Compartment Fire Experiment (SCFE) to control the GPIB-communication between the PC and the SNA, and to acquire/store the measured data from the SNA for further processing.

The front panel of the VI, which is shown in Figure B.1, simulates the screen of the SNA with additional functions. The program allowed us to observe the following (on the front panel of the VI) during each run of the experiment:

- The current measured values
- The running average (updated continuously) of the values being measured
- The stored average values from the preceding run

In this way, it was possible to observe the current measurements, and also to have a means of comparison with the previous runs.

The software program, as shown in Figure B.2, first initializes the GPIB protocol, informs the GPIB about the SNA's address so as to be able to talk to it, clears the

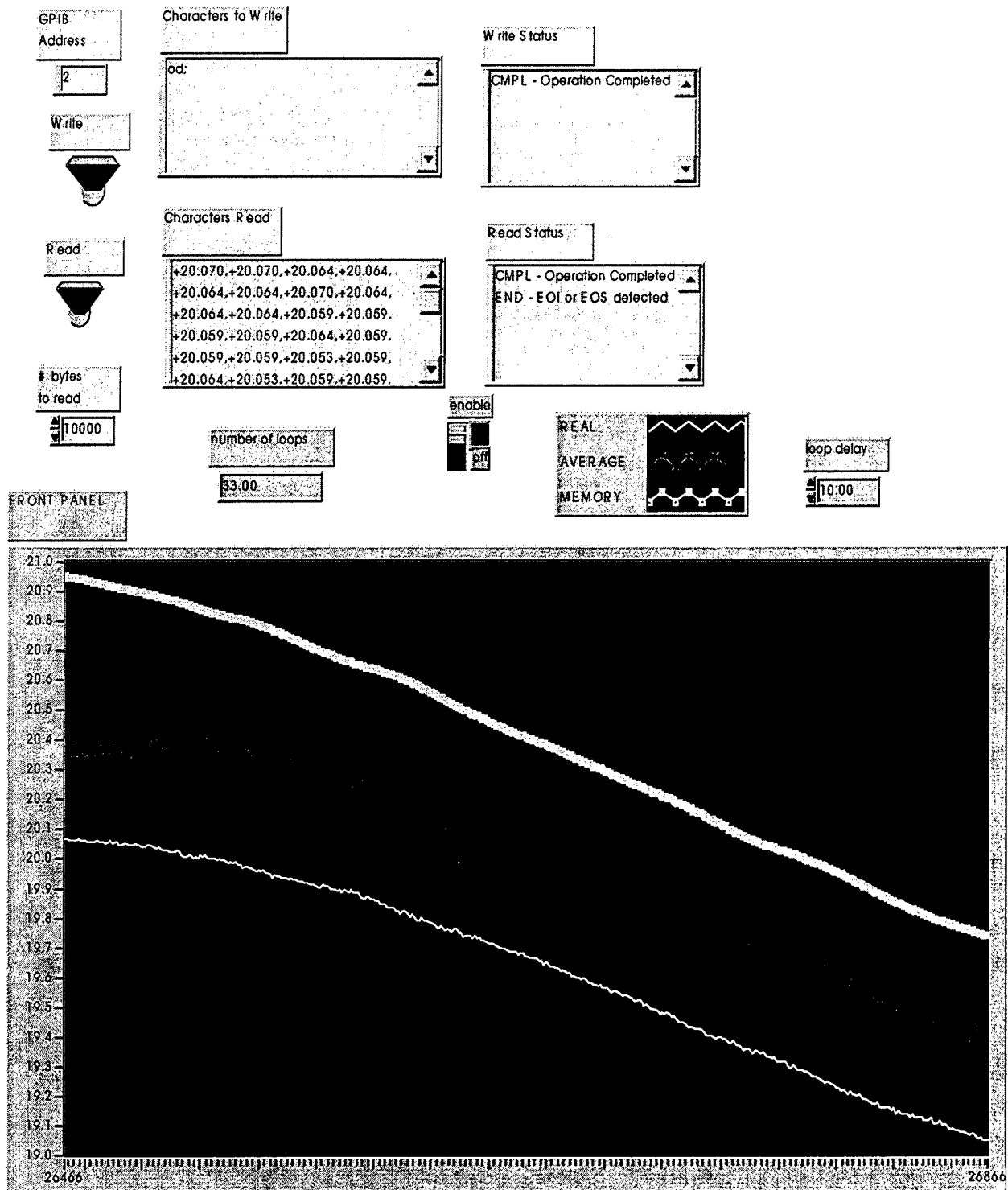


Figure B.1: VI's Front Panel.

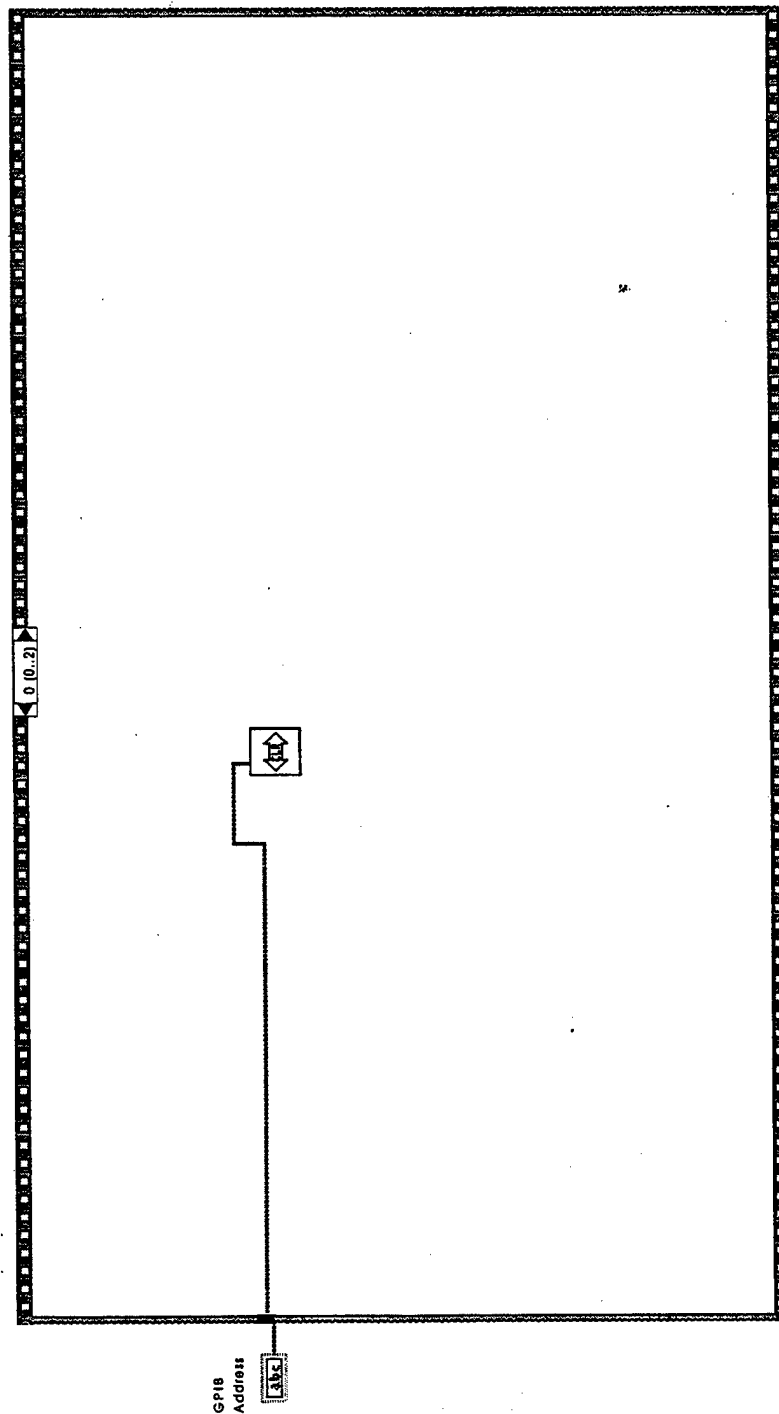


Figure B.2: Initialization of GPIB Protocol.

GPIB from any previous orders stored and sets the SNA and the Sweep Oscillator for remote operation. Next, the program checks if the "write" button is enabled so as to transmit commands to the SNA through the GPIB. If the button is "on", it sends the order, to the GPIB, to read the data having being measured by the SNA. Figures B.3 and B.4 depict this procedure.

The next section of the program, shown in Figures B.5 and B.6, checks if the button "read" is enabled. If it is, it reads 401 values (corresponding to 401 frequencies) measured by the SNA. The SNA divides the measured frequency band (2.4 - 2.485 GHz) in 401 discrete frequencies, and assigns a value to each frequency. If the "read" button is not enabled, or if commands were not sent to the GPIB, then the program reports an error, and asks the operator to abort.

When GPIB finishes with reading the measured values, which are stored in string format, it clears the GPIB as shown in Figure B.7. The measured values are then:

- stored on the hard disk of the PC
- sent to a different VI (VI-6 THESIS)

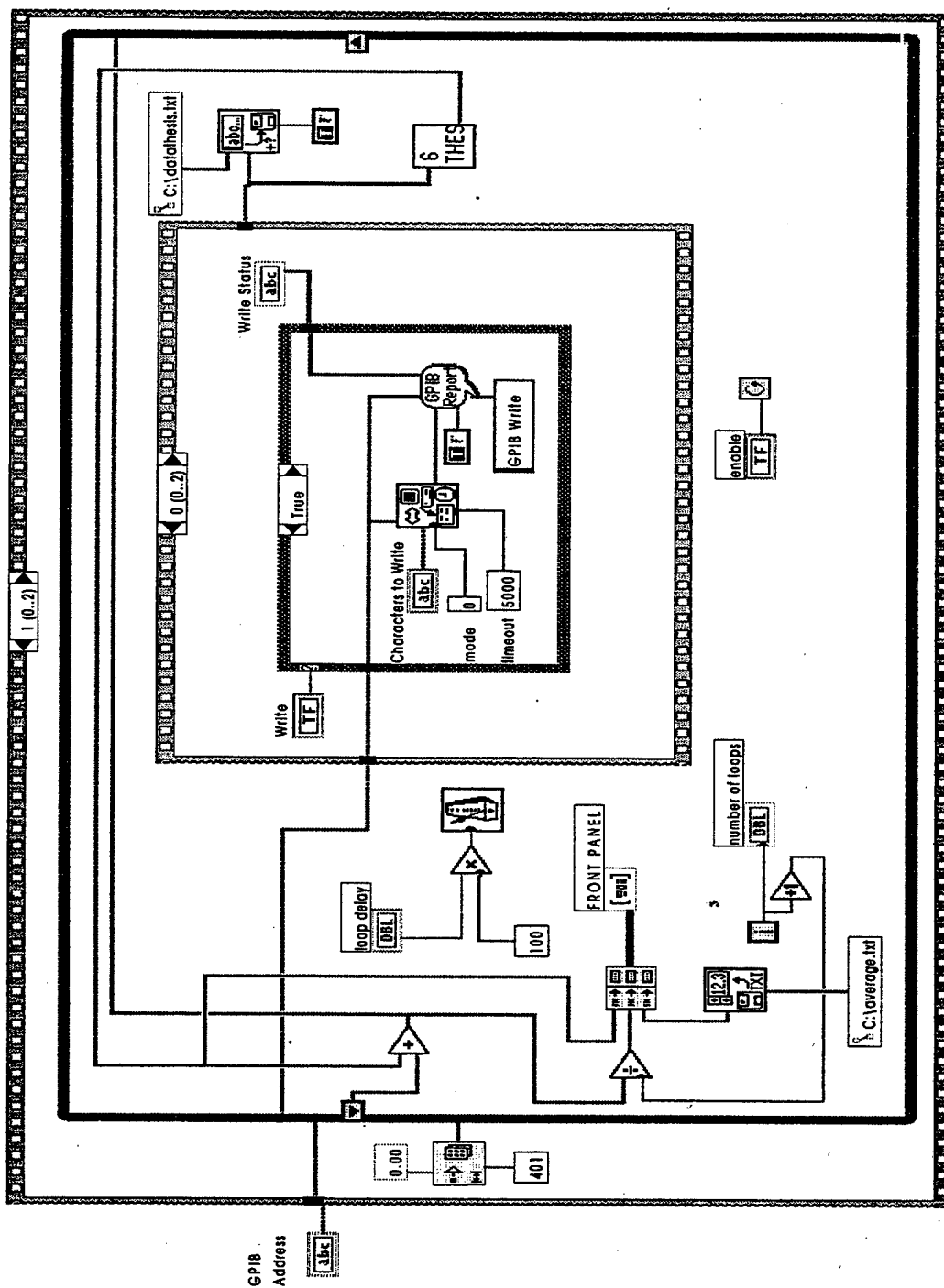
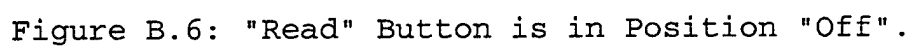


Figure B.3: "Write" Button is in Position "On".



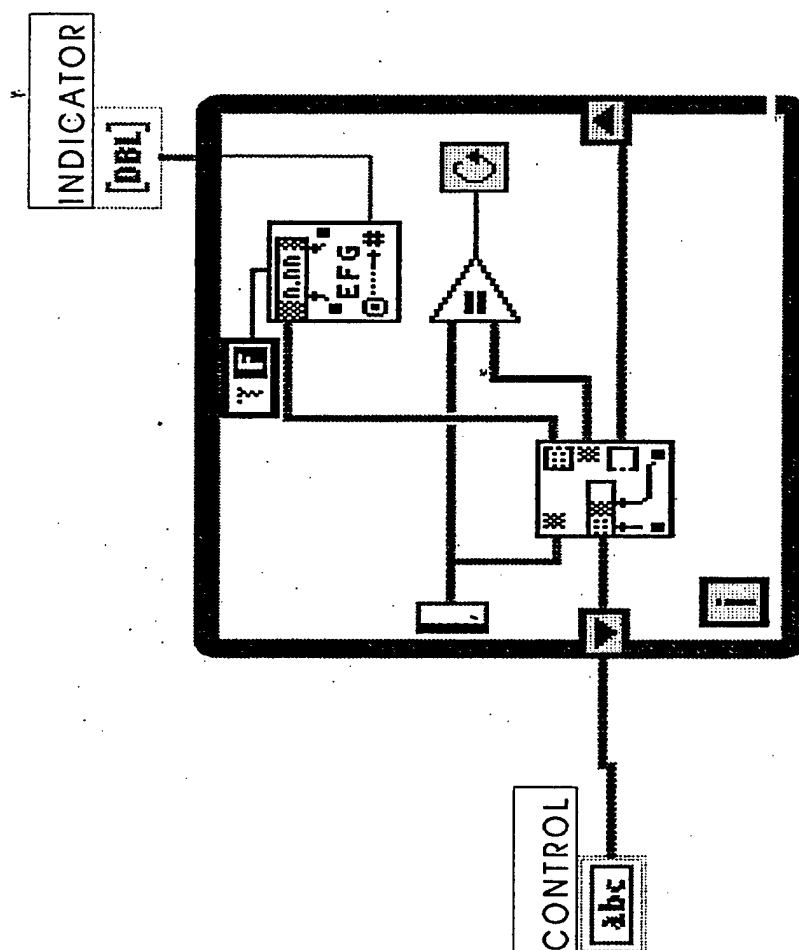


Figure B.8: "VI 6 THESIS" Transforms Data of Strings to Numbers.

"VI-6 THESIS", shown in Figure B.8, transforms the measured data from string format to numbers and sends them to the part of the program, which calculates the running average. After the running average is calculated, it is displayed with the current data and the stored average (from previous experiment) on the front panel of the VI.

After the program sends all the information to the front panel to be displayed, it checks if the "enable" button is "on" or "off". If it is "off" the program sets the SNA and the Sweep Oscillator to local operation, as shown in Figure B.9, and terminates. If the "enable" button is "on", the program waits for the SNA to collect new data, and then starts the procedure of reading the new set of measured values. This loop continues until we decide to stop the measurements and set the "enable" button to "off".

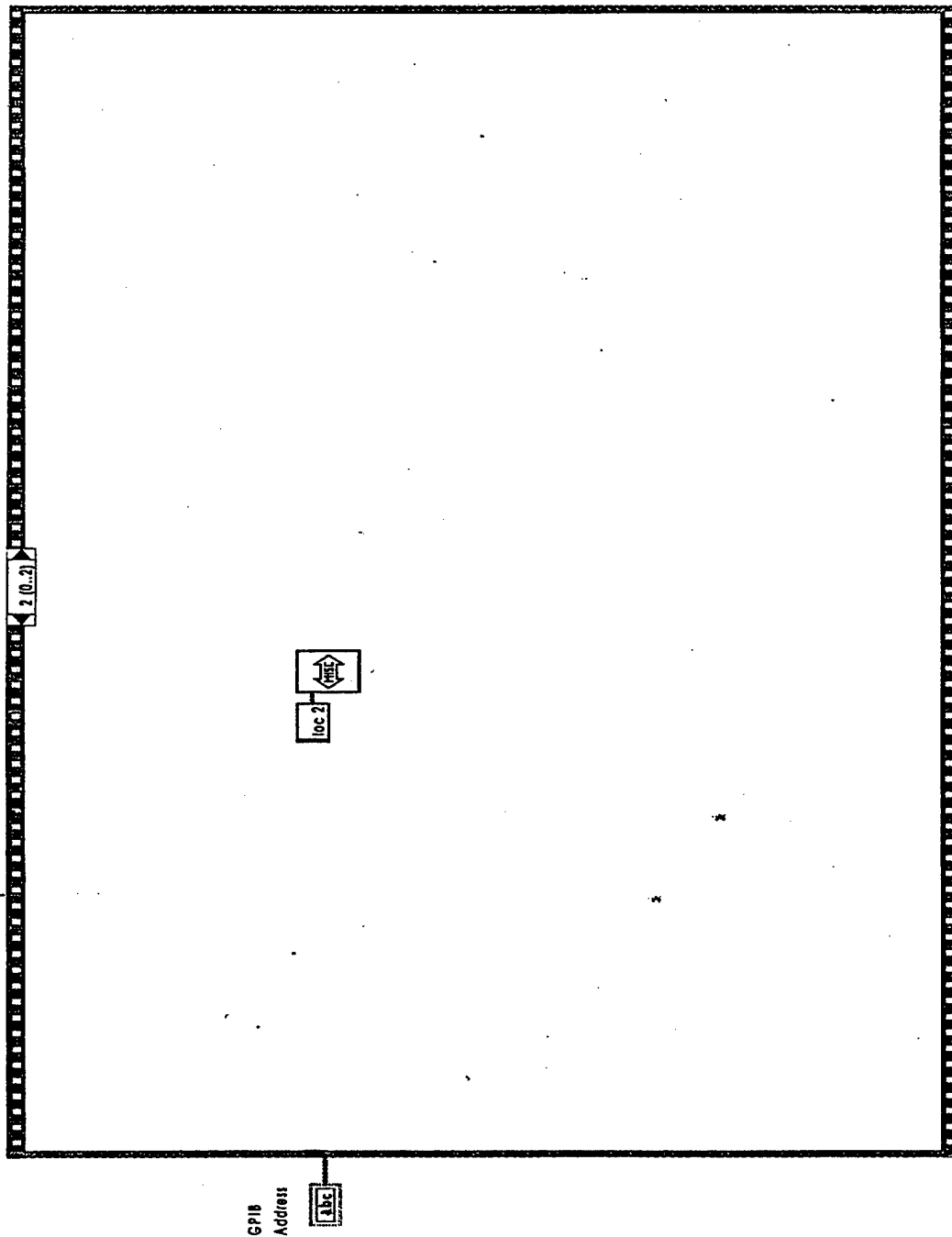


Figure B.9: Program Sets the SNA and the Sweep Oscillator in Local Operation, and Terminates.

APPENDIX C. EX-USS SHADWELL AND SCFE MEASUREMENT COMPARTMENT

The ex-USS SHADWELL is a decommissioned ship that is now used by the Navy as a platform for conducting damage control, firefighting, and survivability investigations and experiments. She is located at the U.S. Coast Guard's Fire and Safety Detachment, beached on Little Sand Island in Mobile, Alabama, under the control of the Navy Technology Center for Safety and Survivability (NTCSS) at the Naval Research Laboratory (NRL). [Ref.21]

The Full Scale Fire Test Facility (ex-USS SHADWELL) is a 457-ft., 9,000-ton landing ship dock. All aspects and ship systems important to damage control are maintained on the ship, and a full complement of instrumentation and computers measure, record and analyze fire behavior, ship systems and personnel reactions during experiments. Photographs of ex-USS SHADWELL are shown in Figure C.1. [Ref.21]

The SCFE was conducted in two compartments located between frames 22 and 29 in the forward part of the fourth and fifth decks of the ship. Figures C.2 and C.3 show the fourth and fifth decks of the ship in the vicinity of the measurements area. The antennas used for the SCFE measurements, were positioned in the lower (fifth deck) part of the "simulated" machine space. The "simulated" machine space consisted of the upper (fourth deck) and lower (fifth deck) parts, and its "Virtual Reality" designed model is

shown in Figure C.4. The "fire source" for the experiment (diesel pan) was located approximately halfway between the transmitting and the receiving antenna. Figure C.5 depicts the details of the measurement compartment.

The measurement equipment was set up in the "engineering station" compartment adjacent to the upper (fourth deck) part of the "machine" space where the hydrocarbon fuel fires were set. In that location (shown in Figure C.2) the equipment where conveniently operated, and windows allowed observation of the measurements compartment.

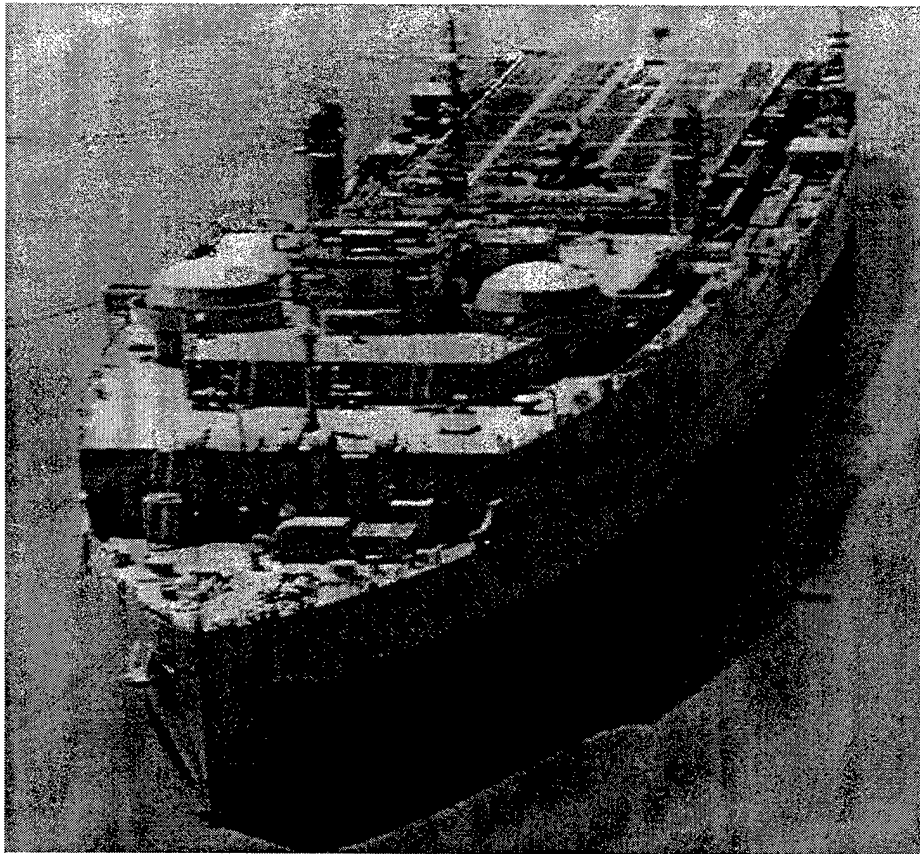
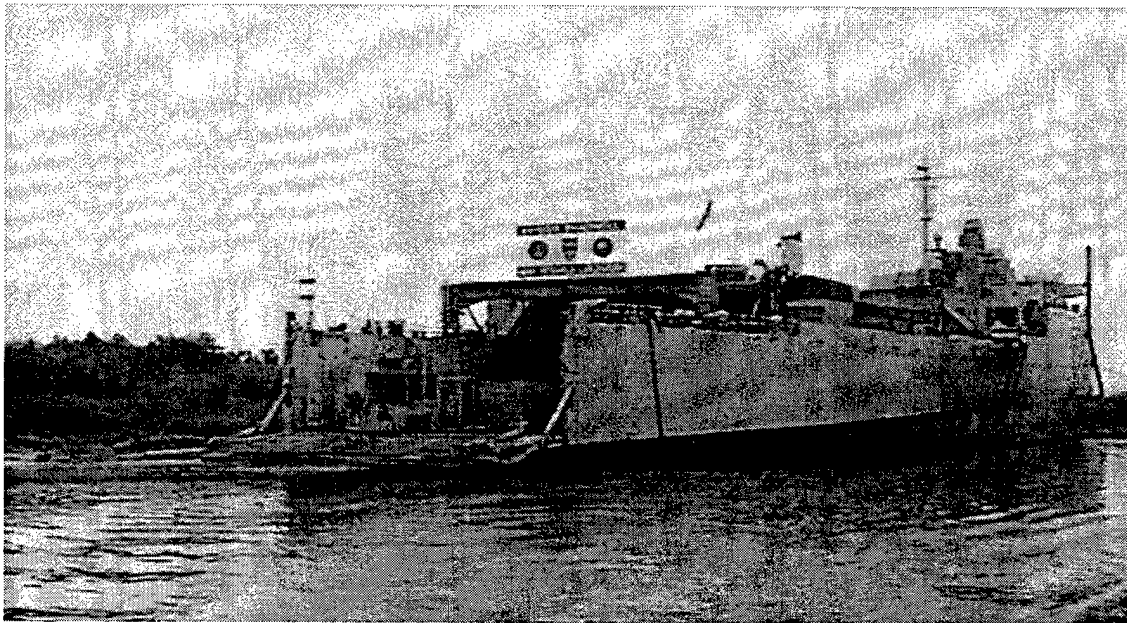


Figure C.1: Photographs of ex-USS SHADWELL.

From Ref. [22]

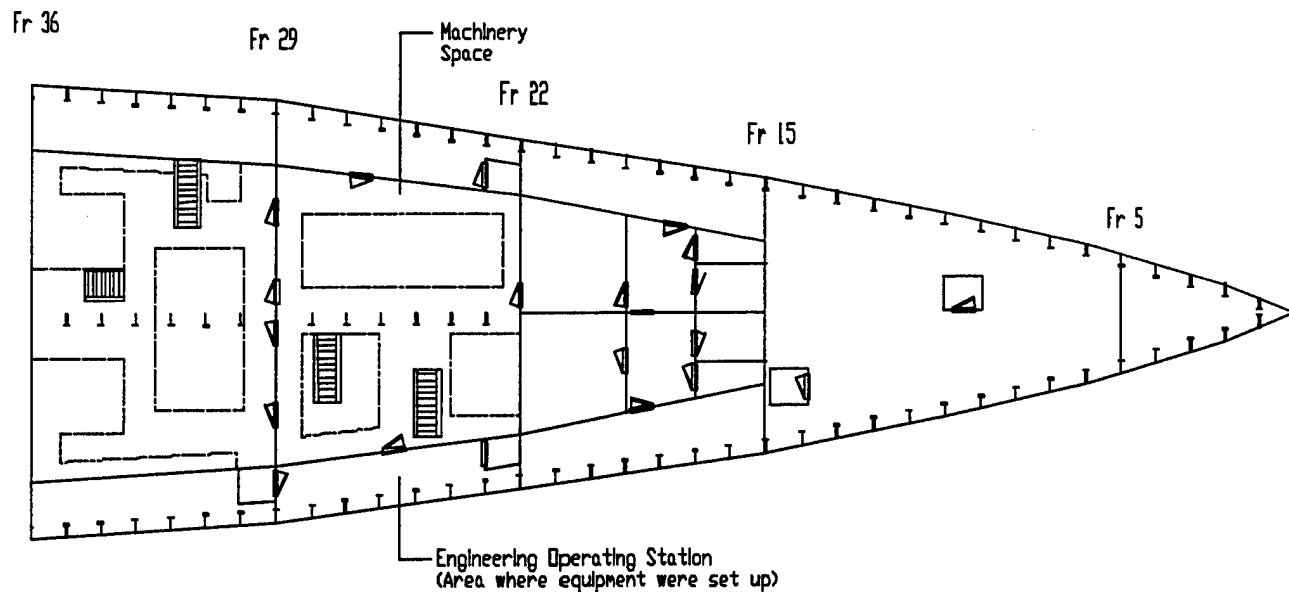


Figure C.2: Forward Part of the Fourth Deck of ex-USS SHADWELL.

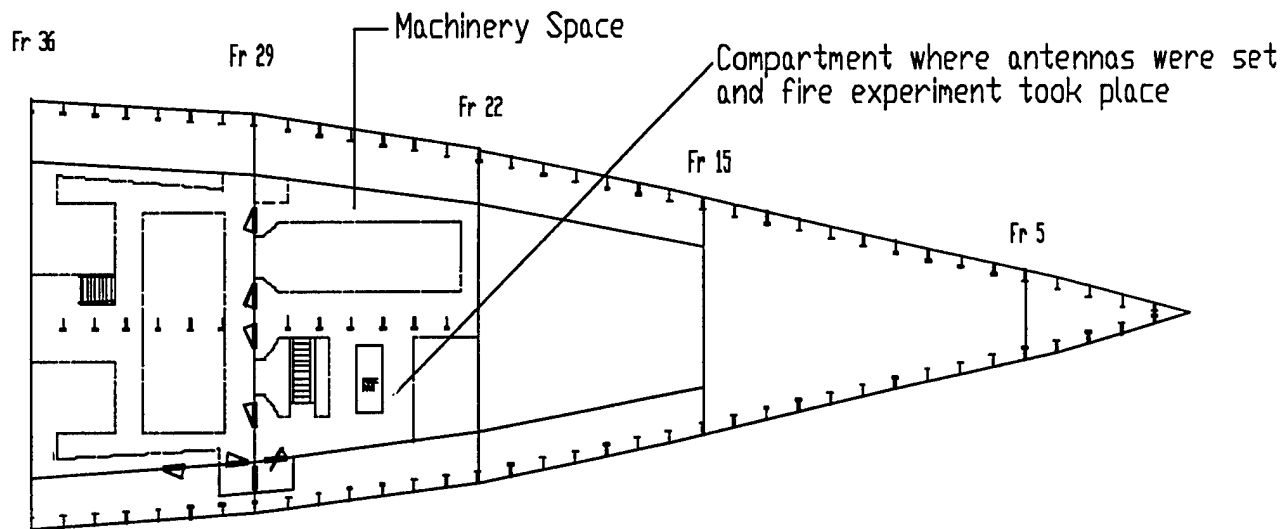


Figure C.3: Forward Part of the Fifth Deck of ex-USS SHADWELL.

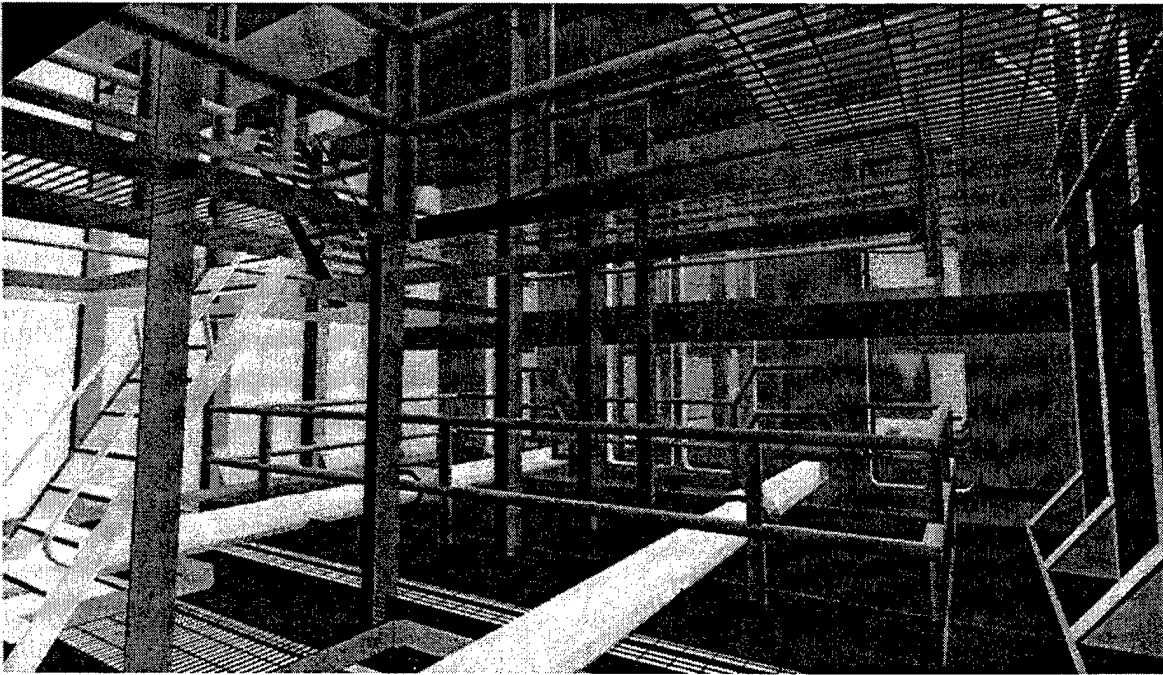


Figure C.4: The ex_USS SHADWELL Mock Machinery Space
"Virtual Reality" Model. From Ref. [23]

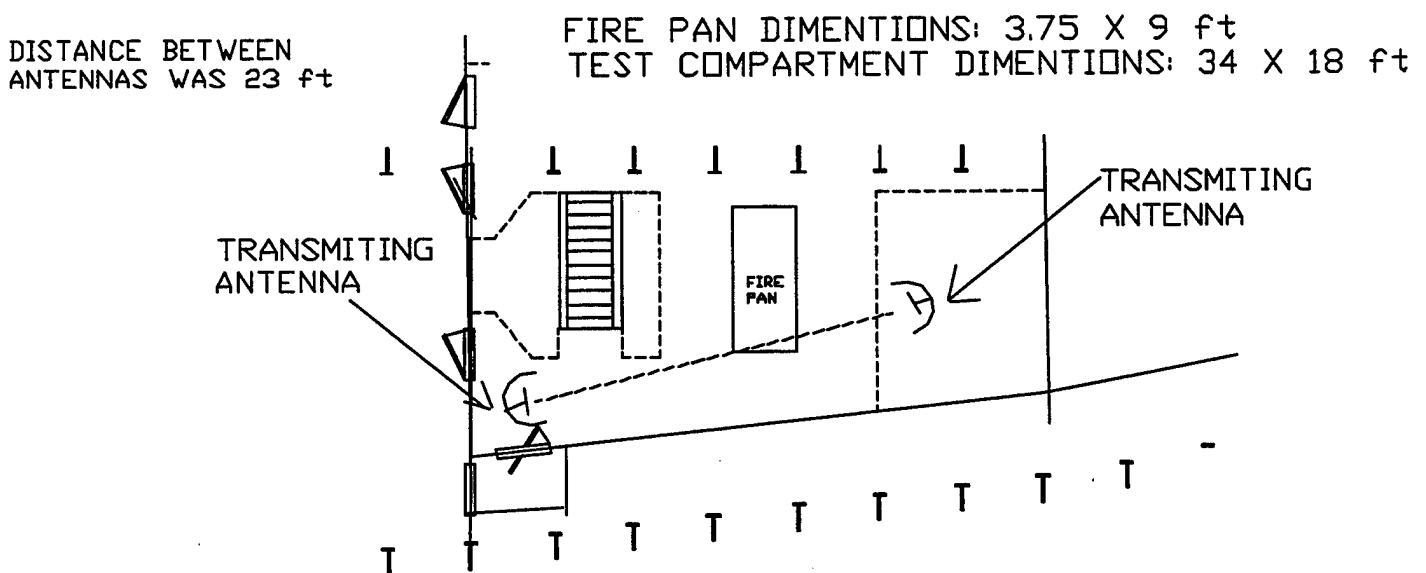


Figure C.5: Measurement Compartment Details.

APPENDIX D. MATLAB DATA PROCESSING CODE

Due to its length, Visiting Professor J. Lebaric, Naval Postgraduate School maintains the MATLAB Code that was developed for the statistical analysis of our data.

LIST OF REFERENCES

1. Naval Research Laboratory, "DC-ARM. Program Objectives, Payoffs and Task Descriptions."
[<http://www.chemistry.nrl.navy.mil/dcarm/objectives.html>]. October 1998.
2. E.L.Mokole, M.Parent, J.Valenzi, E.Tomas, B.T.Gold, and T.T.Street, "Initial Bistatic Measurements of Electromagnetic Propagation in an Enclosed Ship Environment," paper presented at the Antenna Applications Symposium, Allerton Park, Monticello, Illinois, September 15-17 1999.
3. Naval Research Laboratory Report NRL/MR/6180-98-8156, *The Effects of a Fire on Radio Wave Transmissions*, by T.T. Street, F.W. Williams, and B.R. Choquette, April 1998.
4. Parsons, David, *The Mobile Radio Propagation Channel*, John Wiley & Sons, Inc., New York, NY, 1998.
5. Rappaport, T.S., *Wireless Communications. Principles & Practice*, Prentice Hall PTR, Upper Saddle River, NJ, 1996.
6. Kerr, D.E., *Propagation of Short Radio Waves*, McGraw-Hill Book Company, Inc., New York, NY, 1951.
7. Lo, Y.T. and Lee, S.W., *Antenna Handbook. Theory, Applications, and Design*, Van Nostrand Reinhold Company Inc., New York, NY, 1988.
8. Griffiths, D.J., *Introduction to Electrodynamics*, Prentice Hall, Upper Saddle River, NJ, 1989.
9. Demarest, K.R., *Engineering Electromagnetics*, Prentice Hall, Upper Saddle River, NJ, 1998.
10. Hecht, Eugene, *Optics*, Addison Wesley Longman, New York, NY, 1998.
11. Collin, R.E., *Antennas and Radiowave Propagation*, McGraw-Hill, Inc., New York, NY, 1985.
12. Cooper A.W. and Crittenden E.C., *Electro-Optic Sensors and Systems*, course handout Naval Postgraduate School, 1997.

13. Jenn, D.C., *Radar and Laser Cross Section Engineering*, American Institute of Aeronautics, Inc., Washington, DC, 1995.
14. Kong, J.A., *Electromagnetic Wave Theory*, John Wiley & Sons, Inc., New York, NY, 1986.
15. Ginzburg, V.L., *The Propagation of Electromagnetic Waves in Plasmas*, Pergamon Press, New York, NY, 1970.
16. Kruer, W.L., *Frontier in Physics. The Physics of Laser Plasma Interactions*, Addison-Wesley Publishing Company, New York, NY, 1988.
17. Lawton, James and Weinberg, F.J., *Electrical Aspects of Combustion*, Clarendon Press, Oxford, England, 1969.
18. Kruer, W.L., "An Introduction to Plasma Physics", presentation delivered at Lawrence Livermore National Laboratory, course handout, Livermore, CA, 1992.
19. Glanz, James, "The Pervasive Plasma State", *Division of Plasma Physics of the American Physical Society*, Whitley Company, Austin, TX, 1999.
20. National Instruments Company, *LabVIEW Data Acquisition VI Reference Manual*, Prentice Hall, Upper Saddle River, NJ, 1995.
21. Naval Research Laboratory, "Shipboard Fire Scaling." [<http://www.chemistry.nrl.navy.mil/6180/6186.html>]. April 2000.
22. Naval Research Laboratory, "Ex-USS SHADWELL." [<http://www.chemistry.nrl.navy.mil/Images/shadwell.gif>]. April 2000.
23. Naval Research Laboratory, "Shipboard Damage Control and Firefighting Research. Modeling the ex-USS SHADWELL." [<http://www.chemistry.nrl.navy.mil/damagecontrol/vr.html>] December 1998.

INITIAL DISTRIBUTION LIST

	No. Copies
1. Defense Technical Information Center.....2 8725 John J. Kingman Rd., STE 0944 Ft. Belvoir, VA 22060-6218	
2. Dudley Knox Library.....2 Naval Postgraduate School 411 Dyer Rd. Monterey, CA 93940-5101	
3. Engineering and Technology Curricular Office.....1 Code 34 Naval Postgraduate School Monterey, CA 93943-5107	
4. Professor Jeffrey B. Knorr, Code EC/Ko.....1 Chairman, Department of Electrical and Computer Engineering Naval Postgraduate School Monterey, CA 93943-5121	
5. Professor William B. Maier II, Code PH/Mw.....1 Chairman, Department of Physics Naval Postgraduate School Monterey, CA 93943-5117	
6. Professor Jovan Lebaric, Code EC/Lb.....1 Department of Electrical and Computer Engineering Naval Postgraduate School Monterey, CA 93943-5121	
7. Professor James Luscombe, Code PH/Lj.....1 Department of Physics Naval Postgraduate School Monterey, CA 93943-5117	
8. NSWCCD-SSSES, Code 9113.....1 Philadelphia Naval Business Center Philadelphia, PA 19112	

9. Professor Xiaoping Yun, Code EC/Yx.....1
Department of Electrical and Computer Engineering
Naval Postgraduate School
Monterey, CA 93943-5121
10. Embassy of Greece.....1
Naval Attache
2228 Massachusetts Avenue, N.W.
Washington, DC 20008
11. Christos Deyannis.....2
Mavromichali 10, Filothei
Athens, TK 15237
GREECE-HELLAS
12. Dimitrios Xifaras.....2
Evans 2, Ano Patissia
Athens, TK 11143
GREECE-HELLAS